The Dissertation Committee for David Yash Fozdar Certifies that this is the approved version of the following dissertation:

Nanoengineering of surfaces to modulate cell behavior: nanofabrication and the influence of nanopatterned features on the behavior of neurons and preadipocytes

Committee:

Shaochen Chen, Supervisor

Christine E. Schmidt

Li Shi

John R. Howell

John T. McDevitt

Nanoengineering of surfaces to modulate cell behavior: nanofabrication

and the influence of nanopatterned features on the behavior of neurons

and preadipocytes

by

David Yash Fozdar, B.S.; M.S.

Dissertation

Presented to the Faculty of the Graduate School of

The University of Texas at Austin

in Partial Fulfillment

of the Requirements

for the Degree of

Doctor of Philosophy

The University of Texas at Austin

August 2009

UMI Number: 3378697

INFORMATION TO USERS

The quality of this reproduction is dependent upon the quality of the copy submitted. Broken or indistinct print, colored or poor quality illustrations and photographs, print bleed-through, substandard margins, and improper alignment can adversely affect reproduction.

In the unlikely event that the author did not send a complete manuscript and there are missing pages, these will be noted. Also, if unauthorized copyright material had to be removed, a note will indicate the deletion.

UMI®

Dedication

To my parents Connie and Yash,

my brothers and sister, Michael, Roy, and Julie,

my baby nephew and cousin, Austin and Leanna, and

my new baby niece/nephew.

Acknowledgements

I would like to acknowledge the support of my colleagues for their input, generosity, and patience. Special thanks to former Chen group members Shifeng Li (UT PhD) for his assistance in teaching me fabrication, Arvind Battula (UT PhD) for his help learning Comsol Multiphysics, Carlos Aguilar (UT PhD), Matt Hense (UT MS), Yi Lu (UT PhD), Dongbing Shao (UT PhD), and Senthil Theppakuttai (UT PhD), for our conversations. Special thanks to current Chen group members, Wande Zhang for his cleanroom and laser help, Li Hsin Han for his help in deciphering surface chemistry problems, Shaomin Wu, Wei Wang, and Daniel Eils for their input. I would especially like to recognize Jae Young Lee and Dr. Christine Schmidt for our great collaboration on the neuron projects and Xumei Wu and Dr. Charles Patrick for our collaboration on the preadipocyte projects. I would also like to acknowledge Marylene Palard from the UT Microelectronics Research Center, Bill Lackowski, and Mike Tiner from the UT Center for Nano Molecular Science and Technology.

I gratefully acknowledge my committee members: John Howell, John McDevitt, Li Shi, and Christine Schmidt for their ideas, advice, generosity, and patience. Most importantly, I would like to thank my supervisor, Dr. Shaochen Chen, for his unconditional guidance, support, and encouragement throughout my tenure as a graduate student.

Nanoengineering of surfaces to modulate cell behavior: nanofabrication and the influence of nanopatterned features on the behavior of neurons and preadipocytes

Publication No._____

David Yash Fozdar, Ph.D.

The University of Texas at Austin, 2009

Supervisor: Shaochen Chen

Promising strategies for treating diseases and conditions like cancer, tissue necrosis from injury, congenital abnormalities, etc., involve replacing pathologic tissue with healthy tissue. Strategies devoted to the development of tissue to restore, maintain, or improve function is called tissue engineering. Engineering tissue requires three components, cells that can proliferate to form tissue, a microenvironment that nourishes the cells, and a tissue scaffold that provides mechanical stability, controls tissue architecture, and aids in mimicking the cell's natural extracellular matrix (ECM). Currently, there is much focus on designing scaffolds that recapitulate the topology of cells' ECM, *in vivo*, which undoubtedly wields structures with nanoscale dimensions. Although it is widely thought that sub-microscale features in the ECM have the greatest

impact on cell behavior relative to larger structures, interactions between cells and nanostructures surfaces is not well understood.

There have been few comprehensive studies elucidating the effects of both feature dimension and geometry on the initial formation and growth of the axons of individual neurons. Reconnecting the axons of neurons in damaged nerves is vital in restoring function. Understanding how neurons react with nanopatterned surfaces will advance development of optimal biomaterials used for reconnecting neural networks Here, we investigated the effects of micro- and nanostructures of various sizes and shape on neurons at the single cell level.

Compulsory to studying interactions between cells and sub-cellular structures is having nanofabrication technologies that enable biomaterials to be patterned at the nanoscale. We also present a novel nanofabrication process, coined Flash Imprint Lithography using a Mask Aligner (FILM), used to pattern nanofeatures in UV-curable biomaterials for tissue engineering applications. Using FILM, we were able to pattern 50 nm lines in polyethylene glycol (PEG). We later used FILM to pattern nanowells in PEG to study the effect of the nanowells on the behavior preadipocytes (PAs).

Results of our cell experiments with neurons and PAs suggested that incorporating micro- and nanoscale topography on biomaterial surfaces may enhance biomaterials' ability to constrain cell development. Moreover, we found the FILM process to be a useful fabrication tool for tissue engineering applications.

Table of Contents

xiii

List of Tables

List of Figures

Chapter 1: Introduction

1.1. TISSUE ENGINEERING FOR PATHOGENIC TISSUE RESTORATION

The standard in conventional repair strategies for treating damaged tissues has involved extracting healthy autologous tissue from an obscure location in a patient's body and re-inserting or grafting the tissue at the point of defect [1, 2]. Unfortunately, tissue grafting often does not allow the patient to regain function to nominal levels while inflicting additional damage to the donor sites where tissue has been taken. In some instances, synthetic materials can be injected at defect points to produce superficial aesthetic appearance (e.g., collagen injections, breast augmentation, etc.), but, in most circumstances, while volume may be restored, little if any function is recouped. It is out of these limitations, and many others, that researchers in engineering, clinical science, and the life sciences [1] have strived to develop alternative repair strategies, and which has led to the establishment of the field of tissue engineering. Tissue engineering is the development of biological tissue to restore, maintain, or improved damaged tissue and organ functionality [3]. With this fundamental definition of tissue engineering in mind, we narrow the scope of this dissertation to two major sub-fields of tissue engineering, peripheral nerve tissue engineering and adipose tissue engineering, strategies to restore healthy peripheral nerve and adipose (fat) tissue, respectively.

Langer [4] introduced general tenets to the tissue engineering field, which possibly apply to the formation of all types of specialized tissues in the body. Engineering tissue, both soft and nervous, involve three basic components, *(1)* cells, *(2)* a

microenvironment, and *(3)* a tissue scaffold or construct [5]. An appropriate cell source must be identified and an initial cell population, typically found in native tissue in an undifferentiated state, must be isolated and produced in sufficient numbers to facilitate tissue formation. Cells must then be seeded onto a substrate or scaffold that can mechanically support the cell while allowing cells access to nutrients in a timed-release fashion. The scaffold serves to provide cells with a nutrient-rich microenvironment, that ideally should mimic the microenvironment found in the native tissue. The cells, anchored to the scaffold, must then be grown in a bioreactor to form tissue, which can be transplanted into the body. In some cases, additional extracellular cues may be useful in stimulating tissue growth or regeneration, e.g., the application of external stimuli like electrical currents.

Clinical strategies involving the growth of tissue on scaffolds will be implemented based on their efficacy and level of invasiveness, and will most likely consist of either implanting tissue grown, *ex vivo*, or growing tissue *in situ*. Scaffolds serve to provide the three-dimensional tissue architecture of the specialized tissue, and from a clinical point-of-view, give the surgeon better leverage in handling and transplanting the healthy tissue as the point of defect.

Every specialized animal tissue is classified as being *(1)* connective, *(2)* muscle, *(3)* nervous, or *(4)* epithelial tissue. Since the 1970s, specialized tissues representing each of the main tissue-types have been grown, *ex vivo*, for scientific and clinical applications. Along with cell-based therapies consisting of the injection of cell suspensions, which has been done, clinically, to a limited degree, transplantations of cells seeded on simple polymer guidance structures (simple scaffolds) have been shown to

2

help regenerate damaged tissues. Schwann cells isolated from adult nerves were found to stimulate the regeneration of nerves guided in nerve guidance conduits [6]. Schmidt et al. [7] were able to stimulate the outgrowth of neurites from damaged nerves by transplanting schwann cells and applying a small voltage. Epithelial cells have been cultured on surfaces to form two- and three-dimensional (2D and 3D) epithelial sheets to repair corneal tissue and the retinal pigment epithelium [8-12]. A monolayer sheet of retinal pigment epithelial cells (RPECs) transplanted into the subretinal space in rabbits was found to adhere better to surrounding tissues than injected suspensions of RPECs [13]. Other cell-types, including hepatocytes, chondrocytes, smooth muscle cells, endothelial cells, fibroblasts, osteoblasts, etc., have been seeded on polymer scaffolds and transplanted into recipients to coerce the growth of healthy tissue [4].

Nerve and adipose (connective tissue) tissue engineering are two specific tissue engineering applications that have emerged in the last several decades. The molecular biology of nerve and adipose processes like differentiation and proliferation have been largely elucidated, while knowledge of application-based biology, i.e., how various extracellular cues regulate cell behavior, is largely unknown. Accordingly, many studies occurring in the 1990s and 2000s have investigated interactions of nerve cells with various extracellular chemical and physical cues. Fewer studies have been conducted investigating interactions between cells derived from soft tissues like adipose tissue and topographical structures. The introductions in Chapters 4, 5, and 7 review prior studies investigating the interactions of cells with topography. The next few sections in this chapter will introduce the fields of peripheral nerve tissue engineering and adipose tissue

3

engineering, and how advances in these fields will depend on better understanding of how extracellular topographical features modulate cell behavior.

1.2. PERIPHERAL NERVE TISSUE ENGINEERING

Macroscale peripheral nerve cables (Figure 1.1) can be of the order of 1 mm thick. An epineurium sheath bundles together many fascicles. Each fascicle consists of the perineurium, formed by many layers of fibroblasts and collagen, which binds together individual axons, which are wrapped in Schwann cells in myelin. The event in which a peripheral nerve is severed represents the most severe injury to a peripheral nerve, after which, the distal portion of the nerve begins to degrade [2, 14].
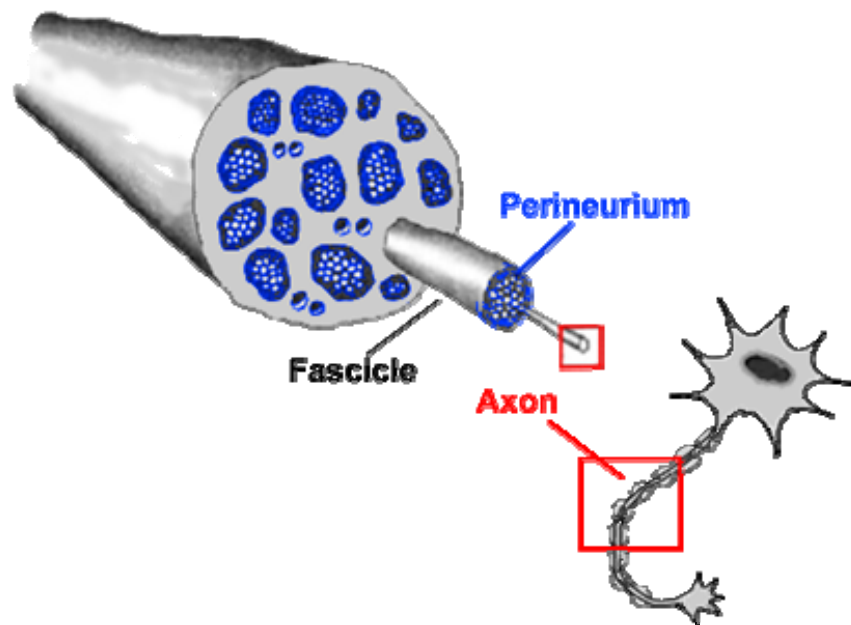
Figure 1.1. The structure of a peripheral nerve. Adapted from ref. [2, 15].

4

Current strategies to repair damaged nerves include suturing nerve endings, implanting autologous nerves, and using nerve guidance conduits. Nerve sutures are useful in repairing damage on a small scale; however, for damage to larger portions of nerve, suturing would require placing a large amount of tension on nerves, which has been shown to inhibit regeneration. Autologous nerve grafts are the standard in terms of treating large scale nerve damage in patients. In a nerve graft, a nerve is taken from one section of a patient's body and re-inserted at the point of injury. Unfortunately, this technique is limited by the fact that new damage is often inflicted at the point were nerve was excised. A newer technique to repairing damaged nerves is by implanting nerve guidance conduits (NGCs), which are simple tubular scaffolds used to guide the regeneration of nerves. NGCs serve to guide axons sprouting from the proximal end of the nerve damage gap, provide access to various growth-facilitating biochemical, and limit the formation of scar tissue [2].

Current research is being focused on advanced scaffolds that recapitulate the structure of peripheral nerves. At this point, current NGCs do not have an architecture that mimics the range of scales inherent to tissue, thus rendering them insufficient at restoring nerve tissue beyond what has been achieved by autologous nerve grafts. The extracellular matrix (ECM) of neurons serves as a mechanical support and introduces various physical topography that modulates cell migration, adhesion, and axon / neurite formation. Major ECM components in the peripheral nervous system, e.g., laminin, have nanoscale dimensions; therefore, to mimic neurons' natural environment, scaffolds will require the incorporation of various cues to promote intimate contact. Ideal NGCs or tissue scaffolds (Figure 6 in ref. [2,16]) will contain porous walls and an internal

biomatrix to provide mechanical support for cells and provide nutrients and the diffusion of growth-facilitating biomolecules. Intraluminal channels will also be incorporated to mimic the fascicles of actual peripheral nerves (Figure 1.1). The walls of the intraluminal channel may contain micro- and nanoscale topography to modulate axon growth. The NGC may be electrically conductive to allow for electrical stimulation for axons.

Creating scaffolds that recapitulate the structure of nerves and that, for instance, present the physical cues compulsory to reliably guiding the regeneration of axons across large injury gaps, will require additional study of the link between physical structures (cues) and neuronal behavior. Chapters 4 and 5 report investigations determining effects of arrays of features of various sub-cellular dimensions and feature shapes on; moreover, further information about cell-surface interactions can be found in their introductions.

1.3. ADIPOSE (SOFT) TISSUE ENGINEERING

Congenital diseases resulting in soft tissue abnormalities like Hemifacial Microsomia, Parry-Romberg's syndrome, and Poland's syndrome can be extremely debilitating from a psychological standpoint. Hemifacial Microsomia is a condition where the lower half of one side of the face is underdeveloped and does not grow as normal. Parry-Romberg's syndrome is a disease where soft tissue, like skin, spontaneously atrophies. Poland's syndrome results in widely-ranging thoracic (mid-section of the body) deformities; such deformities can include the complete lack of development of the pectoralis major (chest muscle) and the hypoplasia (underdevelopment) of soft tissues in the rib cage and even of an arm, hand, or fingers (usually occurs only on one side of the body resulting in extreme asymmetries). Tumor

6

resections, e.g., from breast cancer, also can cause enormous losses in soft tissue (in the case of breast cancer, the entire breast) that can result in loss of functionality and have extreme cosmetic consequences. As you would suspect, these congenital problems and complications related to cancer would be really devastating for any normal human being, psychologically, and in many cases, physically. All these diseases result in extreme defects in the dermis and underlying subcutaneous adipose (fat) tissues [1, 5]. Table 1 in ref. [5] shows several applications where adipose tissue engineering may be useful in the future.

Preadipocytes play a key role in current tissue engineering strategies to restore soft tissue since they can be readily extracted from a patient and cultured *in vitro* [17, 18]. Preadipoctyes (PAs) are fibroblast-like cells that uptake lipid while differentiating into a mature adipocyte (fat cell) [5]. In the body, PAs are surrounded by an ECM that is patterned down to the nanoscale. It has been shown, by studying other types of cells (other than PAs), e.g. smooth muscle cells and nerve cells, that surface topography can affect how cells behave (see section 1.4.). Although the molecular biology of PAs has been largely studied [19-21], the application-based biology of PAs is largely unknown [1]; accordingly, understanding how physical nanostructure surfaces modulate the adhesion, migration, and differentiation of PAs will aid in understanding PAs react with their environment. This will ultimately tissue engineers in implementing physical cues on tissue scaffolds to optimize cell-surface interactions. Chapter 7 gives additional information on PAs and the adipose tissue engineering field and is one of the first studies investigating nanostructure-PA interactions [22].

7

Figure 5 in ref. [5] illustrates an example strategy of how tissue engineering will be implemented in treating breast cancer patients. Adipose tissue will be obtained from a patient for biopsy. From the excised tissue, PAs and cells forming the vasculature to supply blood to tissue will be extracted and cultured *in vitro*. A microvasculature network, the PAs, and additional angiogenic and adipogenic cues will be seeded onto a tissue scaffold with a strategically-designed architecture from the macroscale down to the nanoscale. The macroscale geometry of the scaffold will be determined by a virtual simulator, which can analyze a patient's breast to determine optimal dimensions [5].

1.4. CELL-SURFACE INTERACTIONS

Currently, much attention is being given to optimizing the material, chemical, and physical structure and properties of scaffolds to optimize cell-biomaterial interactions. Ideally, scaffolds will contain features ranging from the millimeter scale (and possibly larger) down to the nanoscale. It has been shown that cells, *in vivo*, interact with sub-microscale / nanoscale features in the extracellular matrix (ECM). It was shown that integrin receptors possess characteristic dimensions on the order of 10 nm [23, 24]. Moreover, the basement membrane of organs has been observed to consist of nanoscale fibers (line topography) and pores (holes) that range in diameter from a few nanometers to several hundred nanometers [24-27]. Collagen has also been observed to consist of tubular fibers with nanoscale dimensions [28]. Laminin has also been observed to have nanoscale texture [29]. Because of the clear evidence that cells' ECM is patterned down to the nanoscale, it is likely that incorporating features of nanoscale dimensions will be necessary in optimizing cell-biomaterial interactions in scaffolds.

8

Features of sub-cellular dimensions may provide the most intimate contact with cells, and are thought to influence the orientation of cells' cytoskeletons [14]. Curtis and Varde were the first to claim that cells respond to topography [30]. Curtis et al. [31] later reviewed studies of the effects of topography on cells. They found that structure depth and width act synergistically to influence cell behavior, and that cell response depended on cell type. At the time their review was published, very few investigations had been conducted regarding the interaction between cells and features of sub-cellular scales. Yim et al. [26, 32, 33] showed that nanofeatures affect the movement, morphology, and proliferation of smooth muscle cells. Cardiomyocytes were found to interact with nanostructures fabricated in polyethylene glycol (PEG). Mesenchymal stem cells and osteoblasts have also been found to interact with their nanostructured ECM [3] and other nanoscale objects like multi-walled carbon nanotubes [34].

A myriad of studies have shown that cells interact with topography with cellular-scale dimensions (greater than a few microns to ~ 100 μm), but it is important that tissue engineers have a greater understand of how physical features of sub-cellular dimensions (a few micrometers and smaller) and morphology affect cell behavior. The contents of this dissertation consist of novel studies investigating the effects of biomimetic surface structures on the behavior of neurons and preadipocytes (see next two sections) to study cell-surface interactions and judge the efficacy of incorporating nanopatterned features on scaffolds [22, 35-37].

9

1.5. THE FABRICATION OF SMALL SCALE STRUCTURES

In order to study cell-surface interactions and design scaffolds with features that mimic the *in vivo* extracellular environment of cells, one must be armed with the capabilities to fabricate small scale features in biocompatible materials. Several advanced micro- and nanofabrication techniques have been used to create nanoscale features to study cell-surface interactions. Moreover, Seidlits et al. [14] reviewed nanofabrication strategies for tissue engineering application, with a focus on neural applications (Table 1 in ref. [14]).

Nanofabrication techniques utilized in the studies reported in this dissertation include reactive ion etching (RIE), photolithography, electron beam lithography (EBL), UV-nanoimprint lithography (NIL), and soft lithographic molding methods. These methods will be discussed in Chapter 2. Chapter 6 presents a novel fabrication method, Flash Imprint Lithograpy Using a Mask Aligner (FILM), used to fabricate nanostructures in UV-curable materials including hydrogels.

1.6. BIOMATERIALS IN CELL STUDIES TISSUE SCAFFOLDS

Many inorganic materials have been used to study cell-surface interactions including silicon and quartz (SiO_2). For the fabrication of two-dimensional nanotopographies for investigating cell-surface interactions, existing hard substrates are still commonly utilized and sometimes preferred. Silicon micro- and nanofabrication technologies have been very well characterized making the process of fabricating nanoscale features quite simple. Moreover, many silicon-based patterning techniques have been adapted for use with polymers for tissue engineering applications.

10

Nanofeatures have been fabricated in a wide variety of polymers (thermoplastics and thermosets) including polymethylmethacrylate (PMMA), polydimethylsiloxane (PDMS), cellulose, polyimide, nylon, cellulose, etc. (see Table 2 in Curtis et al. [31] for references), and even carbon nanotube and nanofiber networks [38, 39]. These materials have been useful in studying the effects of topography on cell-behavior, but they are insufficient as materials in scaffolds as they lack favorable mechanical properties, biocompatibility, and are not biodegradeable. Biomaterials will make use of polymer or hydrogel materials that are cheap, biocompatible, biodegradeable, amenable to biochemical modification, have the desired mechanical and even electrical properties.

Hydrogels represent a class of materials showing quite a bit of promise for use in tissue scaffolds, not only due to their biocompatibility, biodegradability, and cost-effectiveness, but because of their ability to be manipulated as construction materials. Hydrogels, in their liquid precursor state, have relatively low-viscosities (~ viscosity of water) allowing them to flow easily and can also be easily manipulated at the molecular scale to be sensitive to ultraviolet light. These properties make hydrogels quite amenable to new-generation nanoimprint lithography and molding technologies for their conversion to solid structures. Hydrogels that show great promise or have been studied in the past include but are not limited to hyaluronic acid (HA) [40], polyethylene glycol (acrylated) (PEG), polylactic-co-glycolic acid (PLGA), collagen, fibrinogen, chitosan, self-assembling peptides. HA is naturally occurring in the body and has been found to offer many benefits as a scaffold material including being porous for the diffusion of biomolecules and important in the healing of injuries and preventing the formation of scars [41, 42]. PEG is a biocompatible hydrogel that consists of PEG monomer dissolved

in water and a photoinitiator that makes the liquid PEG solidify upon exposure 365 nm *i*-line ultraviolet (UV) light. PEG can be chemically-modified with peptides and other chemicals to promote cell adhesion and render it biodegradable. Chapter 6 demonstrate the use of PEG-dimethacrylate in studying the effects of sub-cellular structures on the behavior preadipocytes [22].

1.7. OVERVIEW OF DISSERTATION

Chapter 2 presents the advanced fabrication technologies utilized for the works discussed in this dissertation, including Chapters 4-7, many of which are commonly used by tissue engineers and scientists. In order to evaluate the significance of the data presented in Chapters 4 and 5, several biostatistical techniques were utilized. Chapter 3 presents these statistical techniques by giving an overview and example of each. The examples presented are related to situations pertaining to Chapters 4 and 5, and are included to give the reader an understanding of how the techniques were applied.

Chapters 4 and 5 present novel studies investigating the effects of arrays of microscale and sub-microscale features (topography) on the differentiation and development of rat hippocampal neurons. The topographies consist of features of an order-of-magnitude smaller dimensions than the characteristic sizes of single neurons, which are proposed to alter the properties of the material as sensed by the neurons. Well-ordered features were patterned in silicon dioxide (SiO_2) (quartz) using advanced microfabrication tools. Chapter 4 presents a study where neurons were cultured on arrays of features of varying size and shape to see how direct intimate contact between individual neurons and features affected the neurons ability to form axons (polarization),

12

which transmit electrical signals from neurons, stimulate the growth of the axons, modulate the spatial orientation of the axons, and to induce changes in conformation of the cell body of the neurons. Chapter 5 presents competition studies on the topographies introduced in Chapter 4 where individual neurons were strategically positioned between two juxtaposing topographies and between a topography and the smooth surface to determine axon preference, which was determined by monitoring onto which topography the axon established itself on. The competitions were conducted in order to determine which particular feature size and shape of those tested, acted as the strongest physical cue affecting axon formation and development.

As mentioned in this chapter, biomaterials play a vital role in tissue scaffolds, providing both the structural framework and microenvironment to cells to facilitate their proliferation. One of the limiting factors in utilizing and incorporating new biomaterials in the construction of tissue engineering scaffolds is the existence and availability of advanced micro- and nanofabrication techniques and technologies that allow manipulation of materials. Chapter 6 presents a novel nanofabrication process, coined Flash Imprint Lithography Using a Mask Aligner (FILM), for the fabrication of features, from the nanoscale to the microscale, in UV-curable biomaterials for tissue engineering applications. The technique allows for the fabrication of small scale structures in biomaterials cheaply, quickly, and easily. Chapter 7 reports the first study incorporating the FILM process to pattern sub-microscale features in polyethylene glycol dimethacrylate (PEGDMA), a biomaterial commonly used a substrate for cell-based applications. In this study, preadipocytes, precursor cells that differentiation into adipocytes (fat cells), were cultured on an array of sub-microscale features to determine

13

the effect of the features on the differentiation and morphology of the preadipocytes. The goals of the investigations of Chapters 4, 5, and 7 was to investigate cell-surface interactions for surfaces containing highly-ordered nanofabricated features order(s)-of-magnitude smaller in dimensions. Chapter 8 contains concluding remarks and details possible future work relevant to the works presented here.

Appendix A includes the t- and χ^2-distribution statistical tables utilized in Chapters 3, 4, and 5. Appendix B summarizes the hippocampal neuron and PA cell culture protocols and staining protocol for the neurons. Appendix C gives sample surface energy calculations using contact angle measurements and calculations for the glass silanization protocol reported in Chapters 6 and 7. Appendix D presents a protocol for converting cell-surface AFM images into Comsol Multiphysics for modeling purposes.

1.8. REFERENCES

1.   Patrick C. W., Tissue engineering strategies for adipose tissue repair, *Anatomical Record*, 2001; **263** pp. 361-366.

2.   Schmidt C. E., Leach J. B., Neural tissue engineering: Strategies for repair and regeneration, *Annual Review of Biomedical Engineering*, 2003; **5** pp. 293-347.

3.   Zhang L. J., Webster T. J., Nanotechnology and nanomaterials: Promises for improved tissue regeneration, *Nano Today*, 2009; **4** pp. 66-80.

4.   Langer R., Tissue engineering, *Molecular Therapy*, 2000; **1** pp. 12-15.

5.   Patrick C. W., Adipose tissue engineering: The future of breast and soft tissue reconstruction following tumor resection, *Seminars in Surgical Oncology*, 2000; **19** pp. 302-311.

6.   Guenard V., Kleitman N., Morrissey T. K., Bunge R. P., Aebischer P., Syngeneic schwann-cells derived form adult nerves seeded in semipermeable guidance channels enhance peripheral-nerve regeneration, *Journal of Neuroscience*, 1992; **12** pp. 3310-3320.

7.   Schmidt C. E., Shastri V. R., Vacanti J. P., Langer R., Stimulation of neurite outgrowth using an electrically conducting polymer, *Proceedings of the National Academy of Sciences of the United States of America*, 1997; **94** pp. 8948-8953.

8.   Teixeira A. I., Abrams G. A., Bertics P. J., Murphy C. J., Nealey P. F., Epithelial contact guidance on well-defined micro- and nanostructured substrates, *Journal of Cell Science*, 2003; **116** pp. 1881-1892.

9.   Liliensiek S. J., Campbell S., Nealey P. F., Murphy C. J., The scale of substratum topographic features modulates proliferation of corneal epithelial cells and corneal fibroblasts, *Journal of Biomedical Materials Research Part A*, 2006; **79A** pp. 185-192.

10.   Lu L. C., Kam L., Hasenbein M., Nyalakonda K., Bizios R., Gopferich A., et al., Retinal pigment epithelial cell function on substrates with chemically micropatterned surfaces, *Biomaterials*, 1999; **20** pp. 2351-2361.

11.   Lu L. C., Yaszemski M. J., Mikos A. G., Retinal pigment epithelium engineering using synthetic biodegradable polymers, *Biomaterials*, 2001; **22** pp. 3345-3355.

12.   Giordano G. G., Thomson R. C., Ishaug S. L., Mikos A. G., Cumber S., Garcia C. A., et al., Retinal pigment epithelium cells cultured on synthetic biodegradable polymers, *Journal of Biomedical Materials Research*, 1997; **34** pp. 87-93.

13. Yaji N., Yamato M., Yang J., Okano T., Hori S., Transplantation of tissue-engineered retinal pigment epithelial cell sheets in a rabbit model, *Biomaterials*, 2009; **30** pp. 797-803.

14. Seidlits S. K., Lee J. Y., Schmidt C. E., Nanostructured scaffolds for neural applications, *Nanomedicine*, 2008; **3** pp. 183-199.

15. Winter J. O., Schmidt C. E., Biomimetic strategies and applications in the nervous system. In *Biomimetic Materials and Design: Biointerfacial Strategies, Tissue Engineering, and Targeted Drug Delivery*, 2002, pp.

16. Hudson T. W., Evans G. R. D., Schmidt C. E., Engineering strategies for peripheral nerve repair, *Clinics in Plastic Surgery*, 1999; **26** pp. 617-+.

17. Hausman G. J., Richardson R. L., Newly recruited and pre-existing preadipocytes in cultures of porcine stromal-vascular cells: Morphology, expression of extracellular matrix components, and lipid accretion, *Journal of Animal Science*, 1998; **76** pp. 48-60.

18. Entenmann G., Hauner H., Relationship between replication and differentiation in cultured human adipocyte precursor cells, *American Journal of Physiology-Cell Physiology*, 1996; **39** pp. C1011-C1016.

19. Macdougald O. A., Lane M. D., Transcriptional Regulation of Gene-Expression During Adipocyte Differentiation, *Annual Review of Biochemistry*, 1995; **64** pp. 345-373.

20. Macdougald O. A., Lane M. D., Adipocyte Differentiation - When Precursors Are Also Regulators, *Current Biology*, 1995; **5** pp. 618-621.

21. Mandrup S., Lane M. D., Regulating adipogenesis, *Journal of Biological Chemistry*, 1997; **272** pp. 5367-5370.

22. Fozdar D. Y., Wu X., Patrick C. W., Chen S., Micro-well texture printed into PEG hydrogels using the FILM nanomanufacturing process affects the behavior of preadipocytes, *Biomedical Microdevices*, 2008; **10** pp. 839-849.

23. Comisar W. A., Hsiong S. X., Kong H. J., Mooney D. J., Linderman J. J., Multi-scale modeling to predict ligand presentation within RGD nanopatterned hydrogels, *Biomaterials*, 2006; **27** pp. 2322-2329.

24. Sniadecki N., Desai R. A., Ruiz S. A., Chen C. S., Nanotechnology for cell-substrate interactions, *Annals of Biomedical Engineering*, 2006; **34** pp. 59-74.

16

25. Abrams G. A., Goodman S. L., Nealey P. F., Franco M., Murphy C. J., Nanoscale topography of the basement membrane underlying the corneal epithelium of the rhesus macaque, *Cell and Tissue Research*, 2000; **299** pp. 39-46.

26. Yim E. K. F., Reano R. M., Pang S. W., Yee A. F., Chen C. S., Leong K. W., Nanopattern-induced changes in morphology and motility of smooth muscle cells, *Biomaterials*, 2005; **26** pp. 5405-5413.

27. Abrams G. A., Murphy C. J., Wang Z. Y., Nealey P. F., Bjorling D. E., Ultrastructural basement membrane topography of the bladder epithelium, *Urological Research*, 2003; **31** pp. 341-346.

28. Curtis A., Wilkinson C., Nantotechniques and approaches in biotechnology, *Trends in Biotechnology*, 2001; **19** pp. 97-101.

29. Hernandez J. C. R., Sanchez M. S., Soria J. M., Ribelles J. L. G., Pradas M. M., Substrate chemistry-dependent conformations of single laminin molecules on polymer surfaces are revealed by the phase signal of atomic force microscopy, *Biophysical Journal*, 2007; **93** pp. 202-207.

30. Curtis A. S., Varde M., Control of cell behavior: Topological factors, *Journal of the National Cancer Institute*, 1964; **33** pp. 15-26.

31. Curtis A., Wilkinson C., Topographical control of cells, *Biomaterials*, 1997; **18** pp. 1573-1583.

32. Miller D. C., Haberstroh K. M., Webster T. J., Mechanism(s) of increased vascular cell adhesion on nanostructured poly(lactic-co-glycolic acid) films, *Journal of Biomedical Materials Research Part A*, 2005; **73A** pp. 476-484.

33. Miller D. C., Thapa A., Haberstroh K. M., Webster T. J., Endothelial and vascular smooth muscle cell function on poly(lactic-co-glycolic acid) with nano-structured surface features, *Biomaterials*, 2004; **25** pp. 53-61.

34. Elias K. L., Price R. L., Webster T. J., Enhanced functions of osteoblasts on nanometer diameter carbon fibers, *Biomaterials*, 2002; **23** pp. 3279-3287.

35. Fozdar D. Y., Zhang W., Palard M., Patrick C., Chen S., Flash imprint lithography using a mask aligner: a method for printing nanostructures in photosensitive hydrogels, *Nanotechnology*, 2008; **19** pp. 1-13.

36. Fozdar D. Y., Lee J. Y., Schmidt C. E., Chen S., Neurons respond uniquely to topographies of various sizes and shapes, *Biomaterials*, 2009; **(submitted)** pp.

17

37. Fozdar D. Y., Lee J. Y., Schmidt C. E., Chen S., Response of neurons to competing topographical features of various sizes and shapes, *Nano Letters*, 2009; **(submitted)** pp.

38. Gheith M. K., Sinani V. A., Wicksted J. P., Matts R. L., Kotov N. A., Single-walled carbon nanotube polyelectrolyte multilayers and freestanding films as a biocompatible platformfor neuroprosthetic implants, *Advanced Materials*, 2005; **17** pp. 2663-+.

39. Firkowska I., Olek M., Pazos-Perez N., Rojas-Chapana J., Giersig M., Highly ordered MWNT-based matrixes: Topography at the nanoscale conceived for tissue engineering, *Langmuir*, 2006; **22** pp. 5427-5434.

40. Seckel B. R., Jones D., Hekimian K. J., Wang K. K., Chakalis D. P., Costas P. D., Hyaluronic-Acid through a New Injectable Nerve Guide Delivery System Enhances Peripheral-Nerve Regeneration in the Rat, *Journal of Neuroscience Research*, 1995; **40** pp. 318-324.

41. Ikeda K., Yamauchi D., Osamura N., Hagiwara N., Tomita K., Hyaluronic acid prevents peripheral nerve adhesion, *British Journal of Plastic Surgery*, 2003; **56** pp. 342-347.

42. Chen W. Y. J., Abatangelo G., Functions of hyaluronan in wound repair, *Wound Repair and Regeneration*, 1999; **7** pp. 79-89.

Chapter 2: Nanofabrication and nanometrology techniques for creating topographical features[1]

2.1. ABSTRACT

Micro- and nanofabrication process are fundamental in the study of cell-interactions as they allow for the fabrication of the small scale features that characterize the nanoscale dimensions of the ECM of cells. This chapter discusses the fabrication and metrology processes utilized in the investigations in this dissertation.

2.2. NANOFABRICATION

2.2.1. Photolithography

As the demands for higher-resolution patterning in the semiconductor industry became more pronounced, limitations in conventional printing methods propelled advancements in optical lithography. The result was the coercion of optical lithography as the primary fabrication tool in micro/nanofabrication, which has been widely adopted in the fabrication of topographical features in inorganic materials, organic polymers, and UV-sensitive biomaterials like hydrogels. Photolithography is the process of transferring features on an optical mask to the surface of a wafer coated with a light-sensitive photoresist. The photolithographic process usually consists of the following steps in the respective order: substrate (wafer) cleaning, photoresist spin-coating, soft-baking, exposure, development and hard-baking. The resist features can be used for a wide

---

[1] Excerpts from [1].

variety of subsequent fabrication processes ranging from micromolding / printing (soft lithography) to subsequent etching and additive steps like chemical vapor deposition and lift-off. For the direct patterning of UV-curable biomaterials like hydrogels, no baking or development are necessary.

In conventional photolithography, a silicon or glass wafer is used as the substrate for subsequent material removal (etching) / additive (deposition) patterning steps. Applications involving the study of the interaction of cells and surface topography are typically done on conventional hard substrates like quartz or silicon; however, in creating two-dimensional and three-dimensional tissue scaffolds, hard substrates serve as a support onto which scaffolds will be fabricated and later delaminated or mechanically peeled or removed from the hard substrate.

To achieve best performance, substrates are usually pre-cleaned in a piranha solution (bath) consisting of hydrogen peroxide and sulfuric acid mixed in a 1:2 volume ratio. The cleaning process removes loosely attached particulate matter and traces of organic, ionic, and metallic impurities from the substrate surface. Depending on the application, it is sometimes desired to subsequently deposit an oxide layer onto the surface of the wafer after the initial cleaning step to serve as a protective barrier for the wafer material in subsequent processing steps. Silicon wafers have a natural oxide layer on their surface, so the oxide deposition step is not always required. Oxide deposition can be accomplished by heating in steam or humidified oxygen at very high temperatures (900-1100 °C) or by other chemical vapor deposition (CVD) processes.

To pattern the substrate, a light-sensitive photoresist is deposited onto the clean wafer surface. A resist whose constituent molecular chains crosslink upon exposure to

20

ultraviolet (UV) light strengthening the polymer is called a negative photoresist; on the contrary, if the molecular chains rupture and the polymer gets weaker by exposure, the resist is called a positive photoresist. Resist deposition is commonly accomplished by spin-coating. The photoresist used is usually in a liquid-phase solution and the viscosity of which can be controllable by additional dilution steps. Spin-coating is the process of utilizing the centrifugal forces associated with spinning at controlled angular velocities for controlled amounts of time. Controlling these two parameters and the properties of the material (i.e. viscosity) to be spin-coated will determine the thickness of the spin-coated layer. The wafer is secured using a vacuum chuck that sucks the wafer onto a metal base (connected to the spinning mechanism) securing it while the wafer spins. The centrifugal forces are responsible for uniformly spreading the resist over the entire wafer and pushing superfluous solution over the edge of the wafer. Resist layers of less than 100 nm have been deposited by tightly controlled spinning processes. Controlling the thickness of spin-coated layers is best conducted on a trial-and-error basis using thin-film thickness measuring techniques like ellipsometry for transparent solutions and a profilometer for measuring the thickness of small structures patterned in the resist. New complexities arise with increasingly complex resist solutions that often preclude the formation of perfectly flat coatings, which are usually very desirable. After the resist coating has been spun onto the wafer, it is soft-baked in an oven at 75-100 ºC for about 10 minutes. Soft-baking removes residual solvents and stresses and enhances the adhesion of the resist to the wafer surface.

Pattern transfer of desired features is accomplished using a photomask that is created from both optically transparent and opaque materials. The type of features

21

desired, the pattern on the mask, will facilitate the type of resist that is most appropriate (positive or negative). Like photoresists, masks are classified in two categories, light and dark field. A light field masks define the features to be transferred with the opaque material while a dark field masks contain the features to be transferred in the transparent material. The pattern is transferred by aligning the wafer with the mask in an aligner. The mask can either be in contact with the substrate (hard contact), slightly raised from the substrate (soft contact), or projection printed where the features on the mask are imaged using a series of lenses that scale down the pattern on the mask. Minimum feature sizes are usually on the order of the wavelength of light used to expose the resist. Hard and soft contact pattern transfer produce patterns with 1:1 feature sizes relative to the mask; projection printing allows the features on the mask to be scaled down 5-10 times. However optical diffraction places a limit on the minimum size of features that can be successfully transferred by traditional photolithography. Features transferred via an i-line (365 nm) UV light are limited at approximately 300 nm, however advances in lithographic light sources have allowed the patterning of features between 150-300 nm by deep ultraviolet (DUV, ~ 200 nm to ~300 nm) and 10-14 nm by extreme ultraviolet (EUV, usually less than 180 nm). After exposure, it is often necessary to treat the surface of the exposed wafer by baking at 100-200 ºC to catalyze the photochemical reactions that continue to occur even after the exposure process has been completed.

After the post-exposure treatment, which is typically of great importance, the exposed wafer is developed in a developer solution. During development the enervated portions of the resist are dissolved in a special solution formulated for specific resist. Developer solutions operate according to a number of mechanisms including: variation

22

of molecular weights, reactivity change, and polarity change. Dry development is also possible using reactive ion etching with a variety of plasmas (e.g. oxygen plasma). Dry developing overcomes adhesion-degradation problems between the resist and wafer characteristic of wet development (using developer solutions). Hard-baking, or post-baking, after development removes residual developer solvents and promotes adhesion between the resist pattern and the wafer that was likely to be weakened during the development process (especially wet–developing).

Moore's Law projected that the number of transistors in an integrated circuit would double every 18 months or so; in other words, the size of transistors would decrease by one-half every three years. Trends in the semiconductor industry have followed this prediction due to the extension of photolithography into the deep and extreme UV (DUV and EUV) range. Using DUV radiation, features as small as 100 nm can be optically patterned; with EUV, features of tens of nanometers can be patterned. As far as conventional photolithography is concerned, EUV radiation represents the limit in which features can be fabricated due to optical diffraction. To reduce feature sizes below this size, either new forms of photolithography (extreme UV) are required or non-photolithographic techniques must be utilized.

2.2.2. Soft Lithography

Many non-photolithographic techniques have been demonstrated for the fabrication of micro/nanofeatures, especially in polymers used for cell-based applications. General printing processes consist of defining and creating a pattern and projecting the pattern onto another substrate by conformal contact. The use of printing

23

techniques for high-resolution patterning regained interests when Whitesides et al. introduced microcontact printing (µCP) [2]. Whitesides et al. were able to pattern a monolayer of an alkanethiol ink to a gold coated surface using a patterned elastomeric stamp of polydimethylsiloxane (PDMS). The stamp, coated with the ink, was pressed onto the gold surface transferring the pattern. The stamp mediated the conformal contact between the ink and the substrate by adapting to the overall shape of the substrate and "intimately" filling the microscopic voids in the substrate associated with surface roughness. µCP has spurred the development of many related high-resolution printing technologies, which, as a conglomeration, make up the set of fabrication techniques described by the term soft lithography. µCP was the first form of soft lithography conducted. The token characteristic behind soft lithography is the formation and usage of elastomeric stamps to transfer the arbitrary pattern of the stamp to a target substrate by incorporating the use of flexible organic biomolecules and materials rather than the rigid inorganic materials characteristic of silicon-based technologies.

Several variations of the general soft lithography technique have been demonstrated including: microcontact printing (µCP) [3], replica molding [4], microtransfer molding (µTM) [5], micromolding in capillaries (MIMIC) [6], and solvent-assisted micromolding (SAMIM) [7]. The advantages and disadvantages of soft-lithographic techniques can be found in reference [2].

2.2.2.1. Replica molding and microcontact printing

In microcontact printing (µCp), a monolayer of molecules is deposited onto a substrate by a patterned elastomeric stamp created by conventional photolithography and

24

injection molding. Polydimethylsiloxane (PDMS), a transparent rubber-like elastomer, is the most commonly used material in stamp fabrication. PDMS is a widely used material because of its many favorable properties at both the microscopic and macroscopic levels. It is commonly used in stamps for printing-based micro/nanofabrication processes, including μCP, and as a material in micro/nanodevices. Additionally, its liquid-phase prepolymer precursor is commercially available at low costs. The elastomeric stamps are traditionally created using rapid prototyping and replica molding technologies [2]. Rapid prototyping is the process of creating 2D masks using CAD software and printing them on cheap transparency films with a 3000 dpi (or higher) high-resolution printer. The masks are then used to create master molds out of photoresist deposited onto silicon substrates. Replica molding is the process of injection-molding the elastomeric stamps using the master mold. Figure 2.1 illustrates the replica molding procedure (REM) [4].

Photolithography is used to create raised patterns of photoresist on the masters using the printed transparencies as masks. Transparency masks are viable for features down to 20 μm; chrome masks are typically required to create features with micron scale dimensions. The master is usually passivated by exposing it to plasma (e.g. oxygen or CF_4 plasma) or to a silanizing vapor in vacuum prior to creating the stamp. To mold the stamp, a liquid-phase prepolymer mixture of PDMS, which consists of a prepolymer formula and a curing agent mixed to a 10:1 ratio by volume, is poured onto the patterned master following surface passivation. The PDMS mixture is then allowed to cure by heating at modest temperatures; the cured elastomer is subsequently peeled from the master transferring the pattern of the master to the solidified PDMS. Passivating the substrate facilitates the easy separation of the PDMS from the substrate which minimizes

25

the risk of damaging the brittle silicon master and the PDMS stamp. In conventional microcontact printing, the raised features on the PDMS stamp are used to transfer a thin-film of ink molecules to a target substrate. The printed ink molecules are arranged according to the pattern on the stamp. The ink molecules chemisorb to the substrate
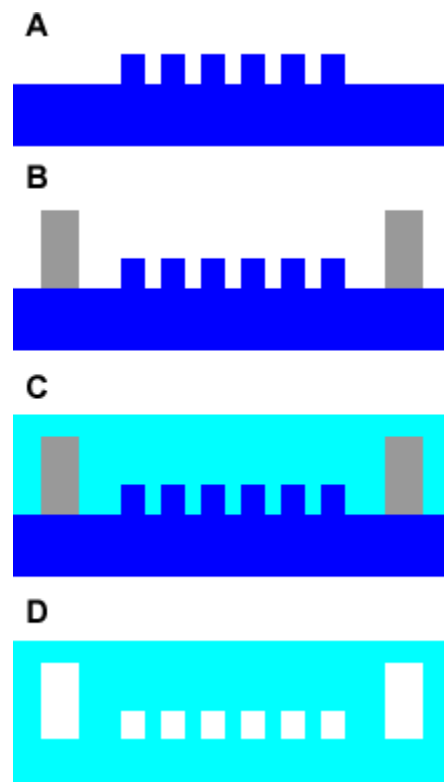
Figure 2.1. The step-by-step replica molding procedure in order from top to bottom [4]. After the master has been formed by rapid prototyping (image A) and vertical posts (pins) have been positioned to create vertical channels (image B), a liquid-phase prepolymer precursor to PDMS is poured onto the raised resist structures on the master (image C). Upon curing, the PDMS (now with the inverted pattern of the master) is removed from the master and bonded to another flat slab of cured PDMS (image D). Oxidation of the contacting surfaces creates a permanent bond between the layers of PDMS. Adapted from ref [4].

forming a self-assembled monolayer (SAM) on the substrate. The most widely used substrate materials for chemisorbing SAMs are metals like gold and silver. The genre of

printing techniques where pressure is applied to a stamp or press to transfer the pattern of the stamp to a target substrate is coined contact printing. µCP is a very convenient form of contact printing because of its low costs, simplicity, and large-scale manufacturing capabilites [3, 8]. Rollers cast in PDMS and coated with a molecular ink are used to print molecular patterns over large areas. Printing on nonplanar surfaces is also possible.

Patterned SAMs of molecular inks are often used as wet-etching masks for subsequent micro/nanofabrication steps. SAMs are very handy in creating metal electrodes since metals like gold and silver chemically react with various wet-enchants that are ineffective at etching SAMs. Functionalized molecular inks can also serve as both intermediates for self-assembling organic layers in additive processes or as passivating layers in patterning techniques requiring the flow of wet-etchants. By attaching various functional groups to a SAM, it is possible to control surface properties like hydrophobicity (surface passivation). Although SAMs are often convenient as masks for wet-etchants, they cannot typically withstand reactive ion etching (RIE) processes.

2.2.3. Nanoimprint lithography (NIL)

Nanoimprinting processes may prove to be the most promising set of fabrication techniques available for mass-producing nanoscale features in inorganic materials, polymers, and biomaterials like hydrogels. Existing high-resolution patterning processes, like electron-beam lithography (EBL), focused ion-beam (FIB) lithography, and X-ray lithography, are either direct-write serial processing tools that have low throughput (E-beam lithography and FIB) or are economically unviable due to enormous capital costs (X-ray lithography). In nanoimprinting, features from a mold are compression molded

27

(embossed) into a soft or liquid-phase polymer substrate material [9, 10]. Fundamentally, the process is simple, relatively economical, and can be performed over large substrate areas (amenable to mass production). Figure 2.2 illustrates the basic nanoimprinting process.
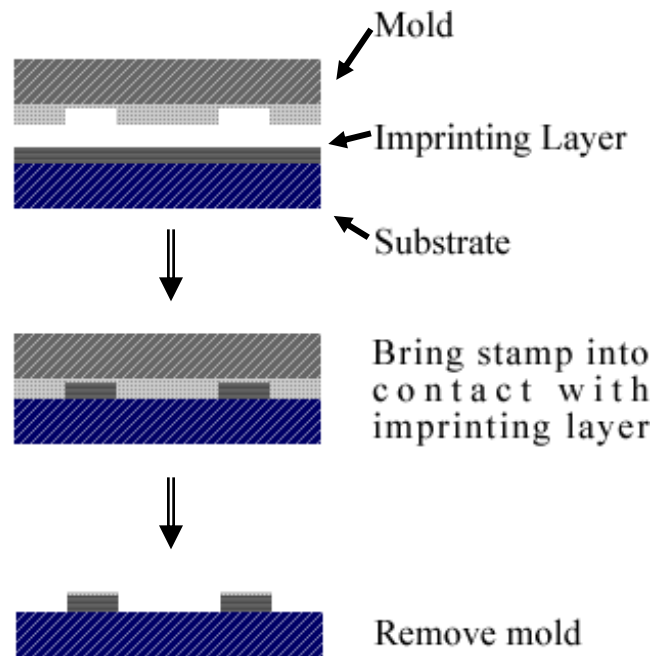
Figure 2.2. An illustration of the nanoimprinting (embossing) process. A relatively rigid mold is pressed onto a soft imprinting layer. An inverted relief pattern remains in the imprinted material when the mold is removed. Adapted from ref. [9].

A rigid mold, created from other fabrication methods like EBL, is used to emboss features into a thin layer of material. The material is melted so that it behaves as a viscous liquid, which can flow into the features of the mold. Once the mold is brought into contact with the substrate material, the material is allowed to fill the features of the

mold. Upon forming the inverse pattern to the mold, the substrate material is cooled so that it solidifies. Upon the solidification of the target substrate, the mold is removed.

The minimum lateral feature size in this particular process was reported to be 25 nm [9], but minimum resolution is highly dependent on the viscosity of the polymer in its melted state. Conventional NIL processes are typically used to pattern structures in thermoplastic materials that are highly viscous upon melting; the higher viscosities limit potential resolution and aspect ratio. In some circumstances, it is necessary to treat the surface of the mold with special chemicals (e.g., fluorinated silanes) to prevent sticking of the target substrate material upon curing. Several variations of nanoimprinting have been developed and detailed information on nanoimprinting processes can be found in references [9-18].

2.2.3.1. *UV-nanoimprint lithography (UV-NIL)*

In UV-NIL, a substrate is coated with a viscous liquid-phase UV-curable resin (or hydrogel). The resin is pressed against a mold and cured by irradiation with UV light [12, 14]. Either the mold or the substrate has to be transparent to UV light so that the photosensitive material can be exposed. UV-NIL has been widely adopted for fabrication nanofeatures in UV-curable hydrogels like PEG [19]. The FILM process (Chapter 6) is a novel form of UV-NIL that takes advantage of the control and automation of optical aligners to do the imprinting.

The fidelity of structures printed by UV-NIL depend on the surface hydrophobicities of the molds and hard substrates (e.g., silicon or glass) that harbor the

29

UV-curable resin. For molding high aspect-ratio features, quartz has shown to be an ideal material due to it's relatively low contact angle, allowing small capillary-like features to suction in fluid by capillary forces. Because the materials typically patterned in UV-NIL have lower viscosities than those used in conventional NIL, feature resolutions are much higher and features with large aspect-ratios can be readily produced.

2.2.4. Electron beam lithography (EBL)

Electron-beam lithography (EBL) is a high-resolution patterning technique in which high-energy electrons, typically of energies between 10 and 100 keV, are focused into a narrow beam and used to expose electron-sensitive resists [20].

The mask fabrication process in EBL is significantly simpler than photolithography because a computer uses the information from a software mask to control the electron beam (e-beam). Physical masks are not required. The e-beam is scanned across an entire wafer coated with an electron-sensitive resist. The beam transfers information, i.e. the image, from the software mask to the resist to form a latent image. EBL is a pixel-by-pixel serial process whose resolution directly correlates to beam size; however, proximity effects from electron scattering limit the resolution of EBL, especially in exposed regions containing densely packed features. Proximity effects are primarily a mechanism of e-beam scattering in the resist, electron backscattering from the substrate, and the scattering of secondary electrons ejected from the resist. E-beams are easy to manipulate through the use of external electric and magnetic fields; their energy and dosage (C/cm^2) are highly controllable as well.

30

Maximum electron current is delivered within the pixel area being exposed with very high contrast. The maximum dosage deliverable by a particular beam is given by Equation 2.1:

$$D_{max} = \frac{it}{A} \left\{ \begin{array}{l} D_{max} = \text{maximum dosage} \ (\text{C/cm}^2) \\ i = \text{current} \ (\text{C/s}) \\ t = \text{time} \ (\text{s}) \\ A = \text{pixel area} \ (\text{cm}^2) \end{array} \right. \tag{2.1}$$

The beam current is related to numerical aperture and the diameter of the focused spot by the following relationship (Equation 2.2):

$$I = \beta \left(\frac{\pi d^4}{4} \right) \left(\pi \alpha^2 \right) \left\{ \begin{array}{l} \alpha = \text{numerical aperture} \ (\text{rad}) \\ d = \text{diameter of the focused spot} \ (\text{m}) \\ \beta = \text{brightness of the source} \ (\text{A} \cdot \text{cm}^{-2} \cdot \text{sr}^{-1}) \end{array} \right. \tag{2.2}$$

Having resists that are particularly sensitive to electrons to form a latent or direct image is necessary. Choice of resist, exposure dosage, electron energy, feature density, etc., all contribute to the best obtainable resolution of EBL. Currently, the main drawback of EBL is its low-throughput since it is a direct-write process. Greater details about EBL can be found in the next section describing scanning electron microscopy (section 2.3).

31

2.3. NANOMETROLOGY

2.3.1. Scanning electron microscopy (SEM) [21, 22]

The SEM is one of the most widely-utilized tools in science. An SEM consists of three subsystems[2]:

1. Electron optical column

2. Vacuum system

3. Display system

The electron optical column consists of an electron gun, electronic lenses, and other electronics. Images are created by a beam of electrons produced by the electron gun[3]. The electrons are emitted from a metal filament in the gun[4] and focused by a Wehnelt cylinder. The filament acts as a cathode propelling the emitted electrons to an anode aperture, which further defines the structure of the beam while recycling electrons that do not traverse the aperture. The anode aperture is typically a disk grounded to the earth with a concentric hole (aperture) in its center. The potential difference between the filament and the anode aperture must be tightly controlled and held extremely stable to ensure that a majority of the accelerated electrons traversing the aperture have the same energy. In a real SEM, the electrons at any cross-section in the beam (relative to the beam's direction of propagation) will actually have a distribution of energies referred to as chromatic aberration. Though chromatic aberration is an undesirable phenomenon that has to be minimized as much as possible, it is impossible to completely avoid. The Wehnelt filter is maintained at a slightly more negative potential than the filament

---

[2] A layout of a conventional SEM is shown in Fig. 1.2a on p. 2 of ref [22]

[3] A cross-sectional view of a conventional electron gun is shown in Fig. 1.2b on p. 3 of ref [22].

المنارة للاستشارات

www.manaraa.com

causing electrons to be emitted only towards the tip of the filament focusing the beam through the anode aperture.

One of the main limitations to resolution is beam diameter, which can typically be demagnified to around 1-5 nm in high-resolution systems. The beam is demagnified through a series of electronic condenser lenses and a final objective lens. Choice of resist and electron scattering also heavily influence resolution. The choice of electrically-sensitive resist usually effects scattering properties.

2.3.1.1. *Major SEM components and function*

The electron optical column and display system of an SEM consist of several components that synergistically work together to produce the very high-resolution images. Table 2.1 lists the components of the electron optical column and display system. The vacuum system (not shown in Table 2.1) is responsible for generating high vacuum in the electron optical column.

Table 2.1. Components of an SEM (and an EBL system). Adapted from ref. [22].

Electron Optical Column	Display System
1. Electron Gun 2. Anode Disc 3. Condenser Lenses 4. Scan Coils 5. Objective Lens 6. Specimen 7. Electron Detector	1. Signal Amplifier 2. Waveform Generator 3. Magnification Control 4. Scan Coils 5. LCD Brightness Control 6. LCD Monitor

---

[4] See inset 1.22 on p. 54 in ref. [20]

As mentioned before, the beam is generated from the electron gun and focused through the anode aperture (disk). The condenser and objective lenses demagnify the beam and scan coils are responsible for rastering the beam across the specimen surface.

2.3.1.2. Image Processing

When the beam bombards the surface of the specimen, electrons (among other things) are emitted from the specimen and captured by a detector that eventually converts collected scattered electrons into an image on a computer screen. Images are created from a conglomeration of fundamental imaging units called pixels, referring to single points on the specimen and on the computer monitor. The pixels are very small, so to create an entire image, a large number of pixels enshrouding an area have to be sampled. The electron-beam is systematically moved, point-by-point along a line, and the electrons emitted from the specimen are collected. After completing a line, the beam moves back to the start of the scanned line and displaces one line-width down. The electron beam then rasters another line; this process occurs over and over until a complete frame (image) has been imaged consisting of approximately 1000 lines containing approximately 1000 pixels each. The scan coils in the electron-optical column raster the electron-beam. Information controlling the scan coils is supplied by the waveform[5] generator.

The image is displayed on a computer monitor. Scan coils in the monitor are fed the same waveform from the waveform generator as the scan coils in the electron-optical

---

[5] Waveform refers to the series of instructions that govern the deflection of the electron-beam by the scan coils.

column; thus, the scans in both sets of coils are synchronized so that the same scan occurs on the monitor. Signals from the detector, which collects electrons emitted by the specimen, are fed to an amplifier. The amplified signals are passed to the monitor's brightness control. The strength of the signal determines the brightness of the pixels of the image on the monitor. Image frames on the computer monitor are often produced at a rapid 25 frames per second, which appears as a flicker free image; thus, the scan rates of the electron-beams in the electron-optical column and the computer monitor are very high in order to produce flicker-free images. Magnification is produced by reducing the scan area on the specimen. Since the scanned area on the computer monitor stays the same, reducing the rastered area on the specimen increases magnification.

Additional electron optics are usually included in the electron-optical column to correct for certain aberrations like astigmatism. Also, adjustable specimen stages are necessary to orient the specimen for scanning purposes.

2.3.1.3. *Electron-specimen interactions in SEM imaging*

Scattered electrons generated by the interaction of the beam electrons and the specimen are chiefly responsible for generating the signals that lead to SEM image formation. The number of scattered electrons collected by the detector at each location on the specimen's surface determines the intensity of the signals necessary for creating image contrast. Two types of electron scattering are of primary important in SEM imaging, elastic and inelastic scattering.

Elastically scattered electrons–backscattered electrons (BSEs)–are very important to image processing. The negatively charged beam electrons interact and are deflected in

35

different directions by passing closely to the positively charged nuclei of the atoms in the specimen; the elastically scattered electrons lose very little energy (< 1 eV) in the scattering process, but the electrostatic attraction causes their trajectories to curve at an angle. The angle of deflection depends on the energy of the electron and how close the electron passes by the nuclei. The number of BSEs emitted from the specimen is dependent on the angle between the incident electron beam and the specimen surface. Consequently, BSEs are very useful in mapping surfaces containing very fine features. BSEs are also highly sensitive to changes in specimen atomic number even when surface topography is rather smooth; thus, BSEs can be used to map the chemical composition of a finely polished specimen. In regard to mapping composition, elastic scattering is more likely to occur in atoms of high atomic number and of electron beams of lower energy while inelastic scattering is more likely to occur in low atomic number elements.

Inelastically scattered electrons lose a large portion of their energy upon interacting with the specimen. Collisions between electrons in the beam and atoms in the specimen tend to be very complex producing any number of products depending on the amount of energy transmitted from the incident electrons. One very important product of electron-specimen interactions are secondary electrons, which are electrons knocked out of the conduction band of atoms in the specimen. Secondary electrons (SEs) are of relatively low energy (relative to unscattered electrons and BSEs) and typically only escape from the specimen when they are released within very short distances of the surface (approximately 10 nm). Like with BSEs, the intensities of the signals produced by SEs depend on the angle between the incident beam and the specimen surface; thus, SEs are widely used in image processing.

36

Some electrons in the beam have sufficient energy to pass through the sample unscattered; they have no information regarding specimen topography and are consequently not used in SEM image processing. However, unscattered electrons are of primary importance in other imaging techniques like transmission electron microscopy (TEM). Other products like Auger electrons, X-rays, photons (cathodoluminescence), and phonons result from electron-specimen interactions; however, these products are not used in topographic SEM image processing. The efficiency of electron-specimen interactions is very low, and most of the energy absorbed by the specimen is converted into heat rather than producing the radiative products useful in imaging.

2.3.1.4. Operating parameters in SEM imaging

Resolution and magnification **-** Resolution is the smallest possible feature size discernible by a particular imaging technique and measuring device. In SEM imaging, resolution is mainly limited by the diameter of the focused electron beam–spot size. Other factors reduce resolution in SEM imaging, and typically, spot size is limited by extraneous noise generated by nuances like chromatic and spherical aberration; thus, although spot size can be decreased to a great degree, a point is reached where other factors limit resolution. An important aspect to SEM imaging is the signal-to-noise (S/N) ratio, which decreases proportionally with spot size.

The maximum achievable magnification is related to resolution by Equation 2.3. Display resolution is variable to a small degree, but is similar for the displays used in most SEMs. Spot size is the most important parameter in determining the maximum achievable magnification, but the relation between resolution and magnification

37

determines the useful magnification threshold. Images at magnifications above this threshold provide no additional topographical information.

$$\text{Max Mag} = \frac{\text{Display Resolution}}{\text{Spot Size}} \qquad (2.3)$$

Real-time magnification is determined by dividing the size of a line of pixels in the SEM display by the size of a line rastered by the electron beam over the specimen (Equation 2.4).

$$\text{Real - Time Mag} = \frac{\text{Display Line Size}}{\text{Sample Line Size}} \qquad (2.4)$$

Line size in the SEM display is effectively constant so magnification is determined solely by the size of the area scanned over the specimen by the electron beam. The electron beam is rastered over the specimen point-by-point along a line. Upon scanning an entire line, the beam shifts to the initial point in the line and down one line-width before proceeding to raster another line. The process is continued until an entire frame–the point-by-point and line-by-line raster of the specimen–is completed. The number of frames scanned per second determines whether a flicker free image is produced or not; frame rate is more crucial to conventional CRT displays than modern LCDs.

38

Accelerating voltage - Electron accelerating voltages in SEM imaging are commonly around 20 keV. Higher voltages reduce chromatic aberration provided they remain stable. To achieve the best possible resolution, the highest useful accelerating voltage should be used; however, because excessively high voltages can lead to significant specimen charging and damage, a balance must be established to maximize resolution and preserve the specimen. As the voltage is increased, the depth of penetration and interaction volume of the beam electrons increases significantly; these important parameters increase for specimens of decreasing atomic number.

Scan Speed - The speed at which the electron beam is rastered over the specimen can be varied over a pretty large range. High scan speeds are necessary for real-time imaging because the image on the display must be updated quickly; however, high scan speeds generate images with more noise than those generated by lower scan speeds. Lower scan speeds are not amenable to real-time imaging, but rather, to generate topographical still images.

2.3.3. Tapping-mode atomic force microscopy (AFM)

Scanning probe microscopy (SPM) is a general form of microscopy where a sharp probe is scanned across a surface and interactions between the probe tip and specimen are monitored. Tapping mode atom force microscopy (AFM) is a form of SPM where a small tip attached to the end of an oscillating cantilever is scanned across the surface of a sample specimen. The cantilever and tip assembly, usually silicon or silicon nitride, oscillates near its resonance frequency. The resonating tip taps the surface of the sample while scanning across it, line-by-line, mapping various properties of the surface, like

39

topographic height and phase. A feedback loop maintains a constant amplitude of oscillation of the tip by collecting data from a laser that is focused on the cantilever. The laser beam reflects off the cantilever and is retrieved by a photodiode detector. Changes in various properties of the surface change the angle of reflection of the laser beam. Topological height data is captured by recording the vertical z-position of a piezoelectric scanner at each x,y location, i.e., pixel, which changes to maintain a constant amplitude of oscillation as the tip encounters features on the surface at different heights or different chemical composition (if the surface is smooth enough).

Laser light reflected from the oscillating cantilever is captured by a photodiode detector, which measures the RMS of the amplitude of oscillation signal. The RMS signal is filtered through a feedback loop that maintains a constant amplitude of oscillation (via the controller). The scanner on an AFM is made from piezoelectric materials, which expand and contract proportionally to an applied voltage; whether the materials elongate or contract depends on the polarity of the applied voltage. A typical piezo scanner incorporates independently operated piezo electrodes for $x,y,$ and z translation into a hollow tube configuration. The tube scanner can accurately move in all three spatial dimensions when AC voltages are applied to the different piezo electrodes. Applying voltages to the x,y electrodes causes the scanner to raster in the x,y directions.

Despite being a bit more time-consuming, tapping mode AFM has many advantages over conventional contact mode AFM where a tip is simply scanned across a sample surface. Tapping mode AFM has higher resolution than contact mode. Tapping mode measurements also exert smaller forces on soft surfaces including tensile, compressive, and lateral (torsional) forces that can scrape a surface.

40

2.3.4. Phase Mapping with Tapping-Mode AFM

Phase imaging is an additional capability of tapping-mode AFM tip that can detect variations in chemical composition of a surface (or slightly below). In phase mapping, the phase difference of the cantilever oscillation relative to the signal sent to the cantilever's piezo is mapped pixel-by-pixel over the scanned surface area. The oscillating piezo is responsible for inducing the resonant vibration of the cantilever. Interactions of the cantilever probe with a surface dampen the oscillations of the probe. Changes in properties of a surface, e.g. chemical composition, cause different degrees of dampening. A signal is sent in response to the damping phenomenon to the driving piezo to preserve a constant amplitude of oscillation of the probe. A phase image is produced by monitoring the phase lag between the simultaneous vibrations of the cantilever and the changing oscillating signal sent to the driving piezo. Contrast by phase mapping is very sensitive allowing for the visualization of very fine structures on a surface that would normally not be imaged by height measurements alone.

2.4. NANOPROCESSING

2.4.1 Reactive ion etching (RIE)

A few other nanofabrication processes are commonly utilized in fabricating nanopatterned substrates. RIE is the process of removing material from a substrate by bombarding it with ions from a plasma discharge. The sample is placed on one of two electrodes in an etching chamber. As combinations of gases are flowed into the chamber, a voltage is applied across the electrodes forming the plasma. RIE is synergistic chemical / physical dry etching technique that is anisotropic and selective. Controlling

the sidewall profile of features and etch rates is possible by controlling etch gas flow rates, the energy of the plasma (power), and the combinations of gases used in the etch. The etch chamber must be at very low pressures in order to ensure proper etching. One of the main advantages of dry-etching is that it is also safer than wet-etching. The major drawback is that dry-etch processes can be expensive. A good review on RIE can be found in ref. [20].

2.4.2. Chemical vapor deposition (CVD)

CVD is utilized to grow thin-films on substrates inside a CVD chamber. In conventional CVD, hot carrier gases are transported into the CVD chamber to react with the surface of the substrate to deposit a solid film. Energy needed to drive the reaction causing pattern transfer can be supplied optically, electronically, or thermally. The CVD process is inherently a diffusive process governed by momentum and mass transport laws. Pattern transfer occurs in several steps: *(1)* The hot carrier gases are transported into the CVD chamber, (2) film precursors in the gas are transported to the substrate, (3) the film precursors are adsorbed to the substrate where they (4) react to form film-initiating precursors, which initiate growth of the film to be deposited, and (5) the film begins to nucleate and grow. Throughout the process the chemical reactions at the surface of the substrate produce by-products that must be removed from the chamber. By-products also form in the bulk of the gas flow region in the CVD chamber. Further details of CVD can be found in ref. [20].

2.4.3. Thermal evaporation of metals

Thermal evaporation is a rather simple technique used to deposit metals on substrates in a deposition chamber. The deposition chamber consists of a sample stage holder directly centered above the area where a source metal is loaded. In most cases, the source metal consists of metal pellets or wire, which are put inside a conducting crucible-like container, which fits snugly into a holder in the chamber. The holder consists of electrodes, which emit a current that traverses the sample holder and the source material during deposition At a certain voltage, the source metal heats up to the point where it evaporates. For the metal to adequately reach the substrate, the metal deposition process requires that the deposition chamber be pumped down to extremely low pressures. Additionally, the substrate must be positioned in clear view of the evaporated metal since deposition is based on having a line-of-sight with the source material. Because deposition is a line-of-sight technique, step coverage can be poor compared with other deposition processes like CVD. Attached to the substrate holder is a shutter that can be closed at any time during deposition process to cut the line-of-sight with the source material and stop the deposition (along with turning down the voltage causing the metal to evaporate).

2.4.4. Lift-off

Lift-off is the process of depositing a material, e.g., a metal, on a patterned sacrificial layer, usually a photo- or electronic polymer resist, and lifting off parts of the material by dissolving the sacrificial layer in a solvent or wet-etchant. Lift-off creates the inverse of the pattern incorporated into the sacrificial layer. Polymethylmethacrylate

43

(PMMA) is one of the most commonly utilized sacrificial materials in lift-off because it easily dissolves in relatively benign organic solvents like acetone.

2.5. REFERENCES

1.   Fozdar D. Y., Lu Y., Shao D. B., Chen S., Nano/Microfabrication Techniques for Organic Electronics and Photonics. In *Handbook of Organic Electronics and Photonics*, American Scientific Publishers, Valencia, CA, 2008, pp.

2.   Xia Y., Whitesides G. M., Soft lithography, *Angewandte Chemie International Edition*, 1998; **37** pp. 551-575.

3.   Xia Y. N., Zhao X. M., Whitesides G. M., Pattern transfer: Self-assembled monolayers as ultrathin resists, *Microelectronic Engineering*, 1996; **32** pp. 255-268.

4.   Duffy D. C., McDonald J. C., Schueller O. J. A., Whitesides G. M., Rapid prototyping of microfluidic systems in poly(dimethylsiloxane), *Analytical Chemistry*, 1998; **70** pp. 4974-4984.

5.   Zhao X. M., Xia Y. N., Whitesides G. M., Fabrication of three-dimensional micro-structures: Microtransfer molding, *Advanced Materials*, 1996; **8** pp. 837-&.

6.   Kim E., Xia Y. N., Whitesides G. M., Polymer Microstructures Formed by Molding in Capillaries, *Nature*, 1995; **376** pp. 581-584.

7.   Kim E., Xia Y. N., Zhao X. M., Whitesides G. M., Solvent-assisted microcontact molding: A convenient method for fabricating three-dimensional structures on surfaces of polymers, *Advanced Materials*, 1997; **9** pp. 651-654.

8.   Wilbur J. L., Kumar A., Kim E., Whitesides G. M., Microfabrication by Microcontact Printing of Self-Assembled Monolayers, *Advanced Materials*, 1994; **6** pp. 600-604.

9.   Chou S. Y., Krauss P. R., Renstrom P. J., Imprint of Sub-25 Nm Vias and Trenches in Polymers, *Applied Physics Letters*, 1995; **67** pp. 3114-3116.

10.   Chou S. Y., Krauss P. R., Renstrom P. J., Imprint lithography with 25-nanometer resolution, *Science*, 1996; **272** pp. 85-87.

11.   Lawrence J. R., Turnbull G. A., Samuel I. D. W., Polymer laser fabricated by a simple micromolding process, *Applied Physics Letters*, 2003; **82** pp. 4023-4025.

12.   Riechel S., Kallinger C., Lemmer U., Feldmann J., Gombert A., Wittwer V., et al., A nearly diffraction limited surface emitting conjugated polymer laser utilizing a two-dimensional photonic band structure, *Applied Physics Letters*, 2000; **77** pp. 2310-2312.

13. Wang J., Sun X. Y., Chen L., Chou S. Y., Direct nanoimprint of submicron organic light-emitting structures, *Applied Physics Letters*, 1999; **75** pp. 2767-2769.

14. Kallinger C., Hilmer M., Haugeneder A., Perner M., Spirkl W., Lemmer U., et al., A flexible conjugated polymer laser, *Advanced Materials*, 1998; **10** pp. 920-+.

15. Schlereth K. H., Bottner H., Embossed Grating Lead Chalcogenide Distributed-Feedback Lasers, *Journal of Vacuum Science & Technology B*, 1992; **10** pp. 114-117.

16. Emmelius M., Pawlowski G., Vollmann H. W., Materials for Optical-Data Storage, *Angewandte Chemie-International Edition in English*, 1989; **28** pp. 1445-1471.

17. Rodia C. M., Precision Electroforming for Optical Disk Manufacturing, *Proceedings of the Society of Photo-Optical Instrumentation Engineers*, 1985; **529** pp. 69-75.

18. Lehmann H. W., Widmer R., Ebnoether M., Wokaun A., Meier M., Miller S. K., Fabrication of Sub-Micron Crossed Square-Wave Gratings by Dry Etching and Thermoplastic Replication Techniques, *Journal of Vacuum Science & Technology B*, 1983; **1** pp. 1207-1210.

19. Kim P., Kim D. H., Kim B., Choi S. K., Lee S. H., Khademhosseini A., et al., Fabrication of nanostructures of polyethylene glycol for applications to protein adsorption and cell adhesion, *Nanotechnology*, 2005; **16** pp. 2420-2426.

20. Madou M. J., *Fundamentals of Microfabrication: The Science of Miniaturization*, CRC Press, Boca Raton, 2002.

21. Goldstein J., Newbury D., Echlin P., Joy D., Jr. A. D. R., Lyman C., et al., *Scanning Electron Microscopy and X-Ray Microanalysis: A Text for Biologists, Materials Scientists, and Geologists*, Plenum Press, New York, 1992.

22. Lawes G., *Scanning Electron Microscopy and X-Ray Microanalysis*, John Wiley and Sons, Hoboken New Jersey, 1987.

Chapter 3: Biostatistical methods for quantifying neuronal behavior

3.1. ABSTRACT

This chapter covers the basic statistical methods utilized in chapters 4 and 5 to determine statistical significance. Additional information can be found in Christensen [1]. Six techniques are discussed including t-tests for the cases of one and two sample populations, for binomial and measurement data, ANOVA, and χ^2-tests. The tests allow comparisons between two sample means and between a sample mean and a baseline probability. Statistical charts used in the analysis here, and in Chapters 4 and 5, can be found in Appendix A.

3.2. ONE SAMPLE BINOMIAL *T*-TEST - Determining the statistical significance of a single stochastic sample (count data) containing n independent measurements [2]

Statistical tests were mandatory in determining whether cell data was mathematically significant based on the number of measurements and null hypothesis per sample (experiment). In cases where samples were not statistically significant, or in cases where typical statistical tests were deemed inappropriate, observational trends considered interesting were noted as a lack of mathematical significance does not always preclude a lack of absolute significance.

Sample variances were calculated using mean values and are the average of the squared distances between the individual measurements in the sample and sample mean.

The degrees of freedom in the sample is the number of measurements, *n,* minus one. Standard error (SE) is calculated by dividing the variance by *n* and taking the square root. The statistical parameter, to be compared with published tabulated *t*-distribution data, is determined by dividing the difference between the sample mean and null hypothesis by the standard error of the sample. The test statistic should be compared with the *t*-distribution assuming a particular confidence interval (%) described by the expression, $(1-\alpha)100\%,$ where, by standard practice, the α-parameter is given a value of 0.05 (~ 95% confidence). Small samples should not be considered normally distributed so that the points of comparison from the statistical charts are determined using the degrees of freedom [~ *t*(*n*-1)].

Binomial count (stochastic) data (i.e., yes / no, % data) has to be treated slightly differently than measurement data. Binomial count data is best described as data having a yes / no outcome or % of positive outcomes. As stated above, SE is calculated by taking the square root of the variance (Var) of the estimate where the variance is determined by Equation 3.1.

$$\text{Var}(\hat{p}) = \frac{\hat{p}(1-\hat{p})}{n} \tag{3.1}$$

where $\hat{p}$ = the percentage of positive outcomes (e.g., % yes) and *n* is the number of samples. Observed t-values are calculated by dividing the difference between $\hat{p}$ and a baseline probability (*p*) (null hypothesis), e.g., 50% ($p = 0.50$), by the standard error

48

(Equation 3.2). By comparing the observed t-values to a standard t-distribution tabulation, considering the degrees of freedom ($n-1$) and confidence level (e.g., 95% confidence where $\alpha = 0.05$), p-values can be linearly interpolated to determine whether the data is statistically different relative to the baseline probability.

Example 3.1. Neurons polarizing on a smooth quartz surface

	Polarized	Not-Polarized	Total
Smooth	230	770	1000

$$\hat{p} = \frac{230}{1000} = 0.23 \rightarrow \text{Var}(\hat{p}) = \frac{0.23(1-0.23)}{1000} = 0.000171 \rightarrow$$

$$\text{SE}(\hat{p}) = \sqrt{\text{Var}(\hat{p})} = \sqrt{0.000171} = 0.0138 \rightarrow$$

$$t_{\text{obs}} = \frac{\hat{p}-p}{\text{SE}(\hat{p})} = \left| \frac{0.23-0.50}{0.0138} \right| = 19.57 \tag{3.2}$$

where p is the null hypothesis. From the above observed t-statistic, a p-value can be determined by linearly interpolating from a t-distribution tabulation. p-values are defined according to Equation 3.3.

$$p = \Pr\left[|z| \geq 19.57\right] \tag{3.3}$$

were Pr means "the probability of". Equation 3.2 states that the p-value is the probability of seeing data as or more extreme than those that were actually observed. If α is less than the p-value, we can conclude immediately that the null hypothesis IS NOT rejected.

49

If α is greater than the p-value, we can conclude immediately that the null hypothesis IS rejected.

Example 3.1 continued…

degrees of freedom $df = n - 1 = 999 \sim \infty$

$\alpha = 0.05$

From Table A.1 we can immediately see that **p < 0.001** for a two-sided test.[1]

3.3. TWO-SAMPLE *T*-TEST - Determining statistical differences between two sets of measurement data containing n independent measurements [3]

Here we consider the situation where we desire to compare the means of two independent samples to determine whether the means are mathematically distinguishable based on the variances of the samples. Probably the most commonly used method of comparing two sample means involves assuming that the inherent variance in the two sets of data (experimental variance) is equal. Again, we want to calculate a test statistic, which we can use to determine a p-value using t-tabulation data (t-test). Measurement data has to be considered slightly differently than binomial data when considering the calculation of individual sample means (Equation 3.4) and variances (Equation 3.5). A pooled estimation of variance is drawn from the variances of the individual samples and is calculated according to Equation 3.6.

---

[1] A two-sided test is used to determine if the observed quantity differs from the null hypothesis. A one-sided test is used to determine if the observed quantity is higher (or lower) than the null hypothesis.

50

$$\bar{y}_i = \frac{1}{n_i} \sum_{j=1}^{n_i} y_{ij} \tag{3.4}$$

$$\text{Var}_i = \text{SD}^2 = \frac{1}{n_i - 1} \sum_{j=1}^{n_i} \left(y_{ij} - \bar{y}_i\right)^2 \tag{3.5}$$

$$\text{Var}_{\text{pool}} = \frac{1}{n_1 + n_2 - 2} \sum_{i=1}^{2} \sum_{j=1}^{n_i} \left(y_{ij} - \bar{y}_i\right)^2 \tag{3.6}$$

i denotes the sample and $i = 1,2$ and j describes the elements in each sample, n_i is the total number of elements in sample i, and SD is the standard deviation; thus y_{ij} denotes the jth element in data set i. SE is calculated using the pooled variance (Equation 3.6) according to Equation 3.7.

$$\text{SE}(\bar{y}_1 - \bar{y}_2) = \sqrt{\text{Var}_{\text{pool}}\left(\frac{1}{n_1} - \frac{1}{n_2}\right)} \tag{3.7}$$

The observed test statistic is calculated by subtracting the null hypothesis from the difference in the means for each sample and dividing by SE (Equation 3.8). In most cases, like in Chapters 4 and 5, the null hypothesis assumes that the means of two samples undergoing a comparison are equal, i.e., $\mu_1 = \mu_2 \rightarrow \mu_1 - \mu_2 = 0$. The degrees of freedom in the calculation equal the total number of elements of both samples minus 2 $\left(n_1 - n_2 - 2\right)$.

51

$$\frac{\left|\left(\bar{y}_1 - \bar{y}_2\right) - \left(\mu_1 - \mu_2\right)\right|}{\text{SE}(\bar{y}_1 - \bar{y}_2)} \sim t(n_1 - n_2 - 2) \tag{3.8}$$

Example 3.2: Axon length of neurons on topography and smooth surface.

i		Mean Axon Length (μm)	SD	n
1	Smooth	25	18	49
2	xyz	52	32	55

    Consider the situation where it is desired to determine whether mean axon length is statistically different among neurons on smooth surface relative to those on topography xyz. In the table above, the mean values and standard deviations have been given (determined by Equations 3.4 and 3.5).

$$\text{Var}_i = \text{SD}^2 = \frac{1}{n_i - 1}\sum_{j=1}^{n_i}\left(y_{ij} - \bar{y}_i\right)^2 \to \text{SD}^2 \cdot (n_i - 1) = \sum_{j=1}^{n_i}\left(y_{ij} - \bar{y}_i\right)^2 \to$$

$$\text{Var}_{\text{pool}} = \frac{1}{n_1 + n_2 - 2}\sum_{i=1}^{2}\sum_{j=1}^{n_i}\left(y_{ij} - \bar{y}_i\right)^2 =$$

$$\text{Var}_{\text{pool}} = \frac{1}{n_1 + n_2 - 2}\left[\text{SD}_1^2 \cdot (n_1 - 1) + \text{SD}_2^2 \cdot (n_2 - 1)\right]$$

$$\to \text{Var}_{\text{pool}} = \frac{1}{49 + 55 - 2}\left[18^2 \cdot (49 - 1) + 32^2 \cdot (55 - 1)\right] = 694.59 \to$$

$$\text{SE}(\bar{y}_1 - \bar{y}_2) = \sqrt{\text{Var}_{\text{pool}} \cdot \left(\frac{1}{n_1} - \frac{1}{n_2}\right)} \to \text{SE}(\bar{y}_1 - \bar{y}_2) = \sqrt{694.59 \cdot \left(\frac{1}{49} - \frac{1}{55}\right)} = 1.244$$

52

We can now use Equation 3.8 to calculate the observed test statistic. Because we want to see if the means of each sample are statistically different, we take our null hypothesis as being that the sample means are equal, i.e., $\mu_1 = \mu_2 \rightarrow \mu_1 - \mu_2 = 0$.

$$t_{obs} = \frac{\left|\left(\bar{y}_1 - \bar{y}_2\right) - \left(\mu_1 - \mu_2\right)\right|}{\mathrm{SE}(\bar{y}_1 - \bar{y}_2)} = \frac{\left|(25 - 52)\right| - 0}{1.244} = 21.7$$

where the number of degrees of freedom $= t\left(n_1 - n_2 - 2\right) = t(102)$

$$\alpha = 0.05$$

From Table A.1 we can immediately see that **p < 0.001** for a two-sided test, which shows that our means are statistically different (significant) relative to one another to a confidence level of better than 99.9%. In essence, topography xyz appears to affect axon length relative to the smooth surface. Very rarely if ever would we see behavior that resembles the null hypothesis.

3.4. TWO SAMPLE BINOMIAL *T*-TEST - Determining statistical differences between two sets of binomial data containing n independent measurements [4]:

If we want to do a similar calculation to the one presented in A.2., but with binomial data, we can determine the pooled variance using Equation 3.9.

$$\mathrm{Var}_{pool}\left(\hat{p}_1 - \hat{p}_2\right) = \frac{\hat{p}_1 \cdot \left(1 - \hat{p}_1\right)}{n_1} + \frac{\hat{p}_2 \cdot \left(1 - \hat{p}_2\right)}{n_2} \tag{3.9}$$

53

From the variance estimate, one can calculate SE by simply taking the square root. The

observed test statistic can be calculated using Equation 3.8 (see Example 3.3).

Example 3.3: Axon formation on smooth surface versus topography

i		Axons	No Axons	% Neurons Forming Axons	n
1	Smooth	25	64	28.1 %	89
2	xyz	34	33	45.3 %	75

Consider the situation where it is desired to determine whether the fraction of neurons

(%) that formed axons on surface xyz is statistically different than neurons on smooth

surface.

$$\text{Var}_{\text{pool}}(\hat{p}_1 - \hat{p}_2) = \frac{\hat{p}_1 \cdot (1 - \hat{p}_1)}{n_1} + \frac{\hat{p}_2 \cdot (1 - \hat{p}_2)}{n_2} \rightarrow$$

$$\text{Var}_{\text{pool}}(\hat{p}_1 - \hat{p}_2) = \frac{0.281 \cdot (1 - 0.281)}{89} + \frac{0.453 \cdot (1 - 0.453)}{75} = 0.005574 \rightarrow$$

$$\text{SE}(\hat{p}_1 - \hat{p}_2) = \sqrt{\text{Var}_{\text{pool}}} = \sqrt{0.005574} = 0.07466 \rightarrow$$

We take the null hypothesis to be that the fraction of cells forming axons should be equal,

i.e., $\mu_1 = \mu_2 \rightarrow \mu_1 - \mu_2 = 0$.

$$t_{\text{obs}} = \frac{\left|(\hat{p}_1 - \hat{p}_2) - (\mu_1 - \mu_2)\right|}{\text{SE}(\hat{p}_1 - \hat{p}_2)} = \frac{\left|(0.281 - 0.453) - 0\right|}{0.07466} = 2.3038$$

54

where the number of degrees of freedom $= t(n_1 - n_2 - 2) = t(162)$

$$\alpha = 0.05$$

From Table A.1 we can immediately see that **0.02 < p < 0.04** for a two-sided test, which shows that our means are statistically different (significant) assuming our α of 0.05. Topography xyz appears to impact axon formation relative to the smooth surface. Rarely would we see behavior that resembles the null hypothesis.

3.5. ONE-WAY BALANCED ANALYSIS OF VARIANCE (ANOVA) - Determining statistical differences in multiple samples [5]

ANOVA is useful in situations requiring comparisons of means from more then two data sets. When each data set consists of the same number of observations or elements, i.e., $n_1 = n_2 = ... = n_i$, the ANOVA is coined a balanced ANOVA. Like with the statistical technique describe in A.2., ANOVA assumes equal variance among the samples and utilizes a pooled variance in the calculation of SE. The pooled variance is referred to as the mean-squared error (MSE) and can be determine by Equation 3.10.

$$\text{MSE} = \frac{1}{n-a} \sum_{i=1}^{a} \sum_{j=1}^{n_i} (y_{ij} - \bar{y}_i)^2 \qquad (3.10)$$

where a = the total number of samples. The degrees of freedom of the MSE are called the degrees of freedom for error dfE and can be determined by Equation 3.11.

55

$$dfE = \sum_{i=1}^{a} n_i - 1 \tag{3.11}$$

Using the mean-squared error, SE can be calculated using Equation 3.12.

$$\text{SE}(\bar{y}_1 - \bar{y}_2) = \sqrt{\left(\frac{\text{MSE}}{n_1} + \frac{\text{MSE}}{n_2}\right)} \xrightarrow{\text{balanced ANOVA}} \text{SE}(\bar{y}_1 - \bar{y}_2) = \sqrt{\left(\frac{2 \cdot \text{MSE}}{n_1}\right)} \tag{3.12}$$

Example 3.4: Axon preference to topography based on distance

	Distance (µm)	
	>30	**0-30**
300-nm Lines - single	16.7%	53.8%
300-nm Lines - multiple	0.0%	50.0%
300-nm Holes	0.0%	85.7%
2-µm Lines - single	0.0%	72.7%
2-µm Lines - multiple	100.0%	62.5%
2-µm Holes	0.0%	57.7%
n_i	6	6
$\bar{y}_i$	19.4%	63.7%
Var	0.1602	0.0178

Assume that we have six different topographies discussed in Chapter 4, which vary from one another according to feature shape, size, and/or boundary type (single- and multiple-type) and we want to see how the topographies influence axon extension, in general, based on distance neglecting topography type. We classify individual neurons based on distances either greater than or less than 30 µm from the topography boundaries

56

and say that a positive outcome has occurred if the axon of a neuron extends towards and touches the topography.

We can immediately recognize that we have an equal number of samples per data set, i.e., $n = 6$. Once again, we are interested in seeing how distance influences the number of positive outcomes as defined above regardless of topography type. Using Equation 3.10, we first calculate the MSE from the number of elements per sample (n_i), average $\bar{y}_i$, and variance (Var).

$$\text{MSE} = \frac{1}{n-a} \sum_{i=1}^{a} \sum_{j=1}^{n_i} (y_{ij} - \bar{y}_i)^2 \rightarrow \text{MSE} = \frac{1}{n-a} \cdot \left[\text{Var}_{<30} \cdot (n_{<30} - 1) + \text{Var}_{>30} \cdot (n_{>30} - 1) \right]$$

$$\text{where } \text{Var}_i \cdot (n_i - 1) = \sum_{j=1}^{n_i} (y_{ij} - \bar{y}_i)^2 \quad \text{(From Example A.2.)} \rightarrow$$

$$\text{MSE} = \frac{1}{12-2} \cdot (0.1602 \cdot 5 + 0.0178 \cdot 5) = 0.0890 \rightarrow$$

$$\text{SE}(\bar{y}_1 - \bar{y}_2) = \sqrt{\left(\frac{2 \cdot \text{MSE}}{n_1} \right)} = \sqrt{\left(\frac{0.0890}{3} \right)} = 0.1722 \rightarrow$$

We take our null hypothesis to be that distances of less than or greater 30 microns have no effect on the number of positive outcomes, i.e., $\mu_1 = \mu_2 \rightarrow \mu_1 - \mu_2 = 0$.

$$t_{\text{obs}} = \frac{\left| (\bar{y}_1 - \bar{y}_2) - (\mu_1 - \mu_2) \right|}{\text{SE}(\bar{y}_1 - \bar{y}_2)} = \frac{\left| (0.194 - 0.637) - 0 \right|}{0.1722} = 2.5726$$

degrees of freedom for error $dfE = 10$ (Equation 3.11)

57

$$\alpha = 0.05$$

From Table A.1 we can immediately see that **0.02 < p < 0.04** (p = 0.0295 by linear interpolation) for a two-sided test, which shows that our means are statistically different (significant) assuming our α of 0.05. We see that distance does have an effect on sequestering the axon of polarized neurons, i.e., on the number of positive outcomes. Rarely would we see behavior that resembles the null hypothesis.

3.6. SINGLE SAMPLE X^2-TEST - Determining statistical differences between a single multinomial sample and a baseline probability distribution by chi-square (χ^2) tests [6]

Consider a similar situation to that presented in section 3.1 where we want to determine if the percentage of positive outcomes in a binomial sample of n independent measurements, is statistically different from a baseline probability. χ^2-tests require the use of chi-distribution tabulations in order to determine p-values. In using the tables (Tables A.2.), we must calculate a χ^2 test statistic, which is determined by finding the Pearson residuals. The χ^2 test statistic can be calculated by Equation 3.13.

$$\chi^2 = \sum_q \left(\frac{O - E}{\sqrt{E}} \right)^2 \tag{3.13}$$

where O is the observed count and E is the expected count q based on the null hypothesis or baseline probability distribution. The quantities inside the parentheses in Equation 3.13 are Pearson residuals. We must sum the squared Pearson residuals calculated for

each outcome. In determining p-values, we must once again consider the degrees of freedom in our data set, which are determined by Equation 3.14.

$$df = q - 1 \qquad (3.14)$$

where q is the number of outcomes that each measurement in the data set can have. For binomial data $q = 2$ so that there is only a single degree of freedom inherent to the data set.

Example 3.5: Competition between topographies for axon sequestration

2-µm Lines
0
6
300-nm Lines

Consider the situation where we micropositioned six individual cells exactly between two line topographies, 2-µm lines and 300-nm lines (groove dimensions) (see Chapter 4). We want to determine which topography serves as a stronger stimulus modulating axon formation and extension based on feature dimensions rather than shape. We believe that the topography in which a neuron's axon establishes itself upon serves as a stronger stimulus influencing axon development. After analyzing the cells we found that all six cells chose the smaller 300-nm lines over the larger 2-µm lines. We want to use a χ^2-test to determine if, based on our relatively small sample size ($n = 6$), our data shows that neuron's actually prefer the 300-nm lines. In essence, we want to run the χ^2-

test assuming a null hypothesis of 50% (a 50% baseline probability distribution) to determine whether the observed data shows that cell preference statistically differs from a 50/50 chance that the neurons will choose the 300-nm lines. We must calculate the χ^2 test statistic using Equation 3.13.

$$\chi^2 = \sum_q \left(\frac{O - E}{\sqrt{E}}\right)^2 = \left(\frac{O - E}{\sqrt{E}}\right)^2_{300-nm} + \left(\frac{O - E}{\sqrt{E}}\right)^2_{2-\mu m} \rightarrow$$

$$\left(\frac{6 - 3}{\sqrt{3}}\right)^2_{300-nm} + \left(\frac{6 - 3}{\sqrt{3}}\right)^2_{2-\mu m} = 6$$

where the expected count for each topography is 50% of the total number of data points ($n = 6$), i.e., $E_{300-nm} = E_{2-\mu m} = 3$. Because our count data has two outcomes, i.e., the neurons have to pick between the 300-nm lines or 2-μm lines, we must sum the two squared Pearson residuals for each outcome. Based on the degrees of freedom in the problem we can use χ^2-tables (Table A.2 in the appendix) to determine a p-value.

$$\chi^2\text{-test statistic} = 6$$

$$\text{degrees of freedom} = 1 \quad (\text{Equation 3.14})$$

$$\alpha = 0.05$$

From Table A.2 we can immediately see that **0.02 < p < 0.04** for a two-sided test, which shows that our means are statistically different (significant) assuming our α of 0.05. Our calculations indicated that neurons prefer the smaller 300-nm lines and that there is not a 50/50 chance that cells will choose one of the two line topographies, rather cells are biased towards the 300-nm lines.

Note: χ^2-tests are usually utilized to analyze polytomous data, i.e., count data with more than two possible outcomes. Binomial tests are special cases of the χ^2-test where data has only two possible outcomes.

3.7. TWO SAMPLE χ^2-TEST USING MULTINOMIAL DATA - Determining statistical differences between two independent multinomial samples chi-square (χ^2) tests [7]

If we want to compare whether the distribution of multinomial count data among the different outcomes between two separate sample populations, we must utilize a slightly more complex procedure than the one presented in section 3.5. This statistical test is best illustrated using an example. First we must introduce a modified version of the Pearson residual shown in Equation 3.15.

$$r_{ij} = \frac{O_{ij} - E_{ij}}{\sqrt{E_{ij}}} \qquad (3.15)$$

61

where i represents each outcome and j each sample population. O and E represent the number of observed and expected outcomes so that O_{ij} and E_{ij} represent the number of observed and expected outcomes for outcome i of sample population j. The χ^2 test statistic can be determined from Equation 3.16.

$$\chi^2 = \sum_{ij} r_{ij}^2 = \sum_{ij} \left(\frac{O_{ij} - E_{ij}}{\sqrt{E_{ij}}} \right)^2 \tag{3.16}$$

Example 3.6: Axon alignment on topographies

Consider the situation where we seeded cells on the 300-nm lines and 2-μm lines and we wanted to analyze and compare axon alignment relative to the lines based on line dimensions. We defined alignment by angle θ, the angle between a line approximating the direction of the axon (a straight line drawn through the axon) and direction of the lines (grooves) where θ = 0-90° (see Figure 4.4 in Chapter 4). We classified axon alignment as being parallel, unaligned, or perpendicular for angles of 0-30°, 30-60°, and 60-90°, respectively. Our problem consists of two sample populations (j = 1,2) consisting of the cells on the 300-nm lines and those on the 2-μm lines. Each axon can have one of the three alignments, so three possible outcomes are possible (i = 1,2,3). The table below summarizes the data.

62

	j	1	2	*
i		300-nm Lines	2-μm Lines	Total
1	0-30°	47	35	82
2	30-60°	14	4	18
3	60-90°	12	6	18
*	Total	73	45	118

To determine whether the distribution of angles is statistically different for neurons on the 300-nm lines relative to those on the 2-μm lines, we employ a two sample χ^2-test for $i = 1,2,3$ and $j = 1,2$. The first thing we need to do is pool together the proportion of axons exhibiting a particular alignment outcome over all topographies, according to Equation 3.17.

$$p_i^0 = \frac{O_{i*}}{O_{**}} \tag{3.17}$$

where * indicates that the observed values (O) must be summed over the respective indice, e.g., O_{i*} indicates the sum of the observed values over all sample populations for outcome i and O_{**} is the sum total of the observed values over all outcomes and sample populations. Equation 3.17 yields the proportion (%) of neurons observed to choose a particular alignment i summed over both topographies $j = 1,2$ relative to the overall number of observations over all alignments and topographies. The superscript 0 indicates that the proportions are estimated under the null hypothesis that alignment should be identical for each topography. Using the proportions calculated from Equation 3.17, we have to estimate the expected number of neurons that should have exhibited each

63

alignment on each topography. Equation 3.18 can be used to determine the estimated values.

$$E_{ij} = O_{*j} p_i^0 \qquad (3.18)$$

where the observed values O are summed overall on i for each j (topography). From the expected values we can calculate the Pearson residuals given by Equation 3.15. The following table shows a tabulation of the values given by Equations 3.17 and 3.18. We calculate the highlighted cells in the table as sample calculations.

i	p_i	E_{i1}	E_{i2}
	j	1	2
1	0.695	50.73	31.27
2	0.153	11.14	6.86
3	0.153	11.14	6.86

$$p_1^0 = \frac{\sum\limits_{j=1}^{2} O_{1j}}{\sum\limits_{i=1}^{3}\sum\limits_{j=1}^{2} O_{ij}} = \frac{O_{11}+O_{12}}{O_{11}+O_{12}+O_{21}+O_{22}+O_{31}+O_{32}} = \frac{47+35}{47+35+14+4+12+6} = 0.695$$

$$\rightarrow E_{i1} = 0.695 \cdot \sum\limits_{i=1}^{3} E_{i1} = 0.695 \cdot (O_{11}+O_{21}+O_{31}) = 0.695 \cdot (47+14+12) = 50.73 \rightarrow$$

$$E_{i2} = 0.695 \cdot \sum\limits_{i=1}^{3} E_{i2} = 0.695 \cdot (O_{12}+O_{22}+O_{32}) = 0.695 \cdot (35+4+6) = 31.27 \rightarrow$$

64

We use Equation 3.15 to find the Pearson residuals. The table below tabulates the residuals. Below the box is a sample calculation of the highlighted cell. We can use the residuals and calculate the χ^2 test statistic.

	r_{ij}^2	
i (down), *j* (right)	1	2
1	-0.52	0.67
2	0.86	-1.09
3	0.26	-0.33

$$r_{32} = \frac{O_{32} - E_{32}}{\sqrt{E_{32}}} = \frac{6 - 6.86}{\sqrt{6.86}} = -0.33 \rightarrow$$

$$\chi^2 = \sum_{ij} r_{ij}^2 = \sum_{i=1}^{3}\sum_{j=1}^{2} r_{ij}^2 = r_{11}^2 + r_{12}^2 + r_{21}^2 + r_{22}^2 + r_{31}^2 + r_{32}^2 =$$

$$(-0.52)^2 + 0.67^2 + 0.86^2 + (-1.09)^2 + 0.26^2 + (-0.33^2) = 2.82$$

χ^2-test statistic = 2.82

degrees of freedom = 1 (Equation 3.14)

$\alpha = 0.05$

From Table A.2 we can immediately see that **p < 0.10** for a one-sided test, which shows that our means are distributions are NOT statistically different (significant) assuming our α of 0.05. If we were to change our requirement for significance, then our measurements would be deemed to be statistically different; thus, our choice of α greatly

65

effects the interpretation of the results. Our calculations indicate that there is probably a difference in axon alignment for neurons seeded on 300-nm lines relative to 2-µm lines, but the difference is not marked.

3.8. REFERENCES

1.   Christensen R., In *Analysis of Variance, Design and Regression*, Chapman & Hall, Great Britian, 1996, pp. 1-587.

2.   Christensen R., One binomial sample. In *Analysis of Variance, Design and Regression*, Chapman & Hall, Great Britian, 1996, pp. 227-230.

3.   Christensen R., Two independent samples with unequal variance. In *Analysis of Variance, Design and Regression*, Chapman & Hall, Great Britian, 1996, pp. 95-98.

4.   Christensen R., Two independent binomial samples. In *Analysis of Variance, Design and Regression*, Chapman & Hall, Great Britian, 1996, pp. 231-233.

5.   Christensen R., One-way analysis of variance. In *Analysis of Variance, Design and Regression*, Chapman & Hall, Great Britian, 1996, pp. 114-123.

6.   Christensen R., One multinomial sample. In *Analysis of Variance, Design and Regression*, Chapman & Hall, Great Britian, 1996, pp. 233-235.

7.   Christensen R., Two independent multinomial samples. In *Analysis of Variance, Design and Regression*, Chapman & Hall, Great Britian, 1996, pp. 235-239.

Chapter 4: Hippocampal neurons respond uniquely to topographies of various sizes and shapes[1]

4.1. ABSTRACT

A number of studies have investigated the behavior of neurons on microfabricated surfaces for the purpose of developing better biomaterials for use in neural applications; however, there have been few methical studies exploring the effects of topographies of various feature sizes and shapes on neural growth and differentiation. Accordingly, here we investigated the effects of arrays of lines (ridge-grooves) and holes of microscale (~2 μm) and sub-microscale (~300 nm) dimensions, patterned in quartz (SiO₂), on the *(1)* adhesion, *(2)* axon establishment (polarization), *(3)* axon length, *(4)* axon alignment, and *(5)* cell morphology of rat embryonic hippocampal neurons, to study the response of the neurons to feature dimension and geometry. The neurons were cultured for 24 hours and analyzed using optical and scanning electron microscopy. The topographies were found to have a negligible effect on cell attachment, but to cause a marked increase in axon polarization, occurring more frequently on sub-microscale features than on microscale features. Neurons were observed to form longer axons on lines than on holes and smooth surfaces; axons were either aligned parallel or perpendicular to the line features. Analysis of cell morphology indicated that the surface features impacted the morphologies of the soma, axon, and growth cone. Results suggest that incorporating

---

[1] This work been submitted. Conditional reference [1].

microscale and sub-microscale topographies on biomaterial surfaces may enhance the biomaterials' ability to modulate nerve development and regeneration.

4.2. INTRODUCTION

Much of the focus within the nerve tissue engineering field has been dedicated to engineering stimulative microenvironments to regenerate damaged nerve tissue by modulating the responses by individual neurons. The microenvironment consists of various chemical and physical cues produced naturally or synthetically, which influence the behaviors of cells [2]. Tissue engineering scaffolds have been fabricated to provide a permissive microenvironment capable of facilitating cell growth and differentiation, forming tissue with the desired architecture [3]. Improvements in biomaterials can be achieved by introducing extracellular physical and chemical cues, or a combination thereof, on biomaterial surfaces to influence tissue development on scaffolds [2].

Structures with dimensions of the same scale as individual cells have been shown to modulate cell differentiation, migration, and shape. Accordingly, the incorporation of cellular-scale (micron-scale) topography on tissue scaffolds may be important in better regulating tissue growth by providing cells with an interface that simulates cells' natural extracellular environment. Requisite to introducing the necessary microscale physical stimuli to cells to control tissue formation is understanding the link between specific surface-bound physical cues and cell response at the single-cell level.

69

Over the last few decades, there has been a growing interest in applying microfabrication techniques to strategically pattern surfaces with the goal of either altering biomaterial surface properties or simply improving a biomaterials' ability to provoke particular cell responses [4]. In the late 1990s, Curtis et al. fabricated surfaces with grooved structures and deemed that groove dimensions highly affected cell behavior [5]. They also stressed that cell response depends heavily on cell-type, where cell-surface interactions between observed for one type of cell were different from those for another cell-type exposed to identical structures. Dalby et al. [6, 7] cultured fibroblasts on an array of groove-ridges in which the grooves had a 12.5 μm width and 2.5 μm depth. They found that the fibroblasts tended to embed and align themselves within the grooves or on top of the ridges. Berry et al. [8] monitored the proliferation of fibroblasts on arrays of circular holes ranging from 7-25 μm in diameter at spacings of 20 and 40 μm. They found that the fibroblasts proliferated to a greater degree on holes with smaller diameter and smaller pitch. Teixeira et al. [9, 10] found that the elongation and alignment of human corneal epithelial cells (HCECs) cultured on lines of 70-nm width (width of ridges) and 400-nm pitch depended heavily on feature depth. The HCECs were markedly more aligned for lines with a 600-nm depth than those of 150-nm depth. Increases in feature pitch from 400 nm up to 2 μm showed little effect on alignment and the HCECs did not align with the lines when the pitch was increased to 4 μm. Teixeira et al. emphasized the importance and direct link between feature size and the behavior of HCECs.

Rudimentary investigations have been conducted to study the behavior of neurons on micropatterned substrates. Goldner et al. [11] cultured dorsal root ganglion neurons

70

on ridge-groove structures of width and depth in the tens of microns. They observed the neurons anchoring on the ridges and forming neurite bridges across the grooves. Rajnicek et al. [12, 13] investigated the effects of ridge-groove structures of microscale dimension on the contact guidance of rat hippocampal neurons. They investigated groove widths of 1, 2, and 4 μm at various depths ranging from 14 nm to 1.1 μm. Axons were found to align perpendicularly to the lines as groove width and depth decreased. Deep wide channels that were 4 μm wide and 1.1 μm deep guided the neurons to migrate into the grooves and align their axons parallel to the lines. Rajnicek et al. did not study neuronal differentiation, such as initial axon formation (i.e., polarization) and axon elongation, for neurons cultured on different features.

Gomez et al. [14, 15] were the first to study the effects of micropatterned topography on axonal establishment and elongation. They showed that polarization was more likely to occur on synthetically patterned lines of 1-μm and 2-μm widths than on smooth surfaces. Yet, they did not study interactions between neurons and topography for features of varying shape, including circular holes, or features with sub-microscale dimensions (< 1 μm).

In attaining a more thorough understanding of the influence of physical surface structures on neurons, it is pivotal that cell-surface interactions be studied for different feature sizes and shapes (in the same set of experiments). Here, we investigate the effects of feature size and shape among various micropatterned topographies on *(1)* cell-substrate adhesion, *(2)* axon establishment (neuron polarization), *(3)* axon length, *(4)* axon alignment, and *(5)* cell morphology of rat embryonic hippocampal neurons after 24 h in culture. We conducted experiments on four different homogeneous topographies

71

including *lines* (i.e., ridge-groove structures) of 300-nm and 2-µm width (width of grooves) and 1-µm spacings (ridges) and *holes* of 300-nm and 2-µm diameter and 1-µm spacings in both the horizontal and vertical directions. All structure depths were approximately 400-500 nm.

4.3. MATERIALS AND METHODS

4.3.1. Quartz substrate fabrication

25 mm^2 square quartz substrates were exposed to an oxygen plasma (50 sccm O_2, 300 Watts, 150 mTorr, 25 °C; Plasma-Therm 790, Plasma-Therm, Inc., St. Petersburg, FL, USA) for 10 min and immersed in a mixture of 25% hydrogen peroxide (30% H_2O_2 in water) (v/v) in sulfuric acid (piranha bath) for 10 min (hydrogen peroxide 30%, sulfuric acid 96%, JT Baker, Phillipsburg, NJ, USA). The substrates were removed from the bath, thoroughly rinsed in deionized water, dried with N_2 gas, and dehydrated on a hot plate at 200 °C for 5 min.

After cleaning, a thin 30-nm layer of chromium was thermally evaporated onto the quartz at a rate of 5 Å/sec (Explorer, Denton Vacuum, Moorestown, NJ, USA). ZEP-520A (Zeon Chemicals, Louisville, KY, USA) positive electronic resist was coated onto the chromium layer to a thickness of approximately 200 nm by spinning at 4000 rpm for 40 sec; nominal layer thickness was reduced by diluting the ZEP in anisole to a concentration of 50% (v/v). After spin-coating, the resist was baked on a hot plate at 180 °C for 150 sec.

Arrays of structures were patterned in the ZEP using electron beam lithography (JEOL 6000 FSE, JEOL Ltd., Tokyo, Japan; Raith 50, Raith GmbH, Dortmund,

72

Germany) with a beam fluence of 100 $\mu C/cm^2$ and subsequently developed in ZED-N50 (Zeon Chemicals, Louisville, KY, USA). Isopropyl alcohol (Thermo Fisher Scientific, USA) was used as the etch-stop during the developing process. The substrate was dried with a slow stream of N_2 gas. The ZEP resist served as a dry-etch mask for the underlying chromium layer, which provided a selectivity close to 3:1 chromium:ZEP. A two-step reactive-ion-etching (RIE) (Trion Technology, Clearwater, FL, USA) process was used to etch through the chromium. The first step was a descum O_2 plasma treatment to remove residual resist from developed regions. The second step was the chromium etch step, which etched completely through the chromium layer to the quartz. The remaining ZEP resist was stripped during the following quartz etch. The chromium layer served as the etch mask for the underlying quartz with a selectivity of over 10:1 quartz:chromium. The quartz was etched down about 400 nm. After quartz etching, the remaining chromium was stripped with a chromium wet-etchant (Etchant 1020, Transene Company, Danvers, MA, USA) at 40 °C for 2 min. The quartz was then thoroughly washed in a piranha bath for 10 min and stored in DI water for later experimentation.

4.3.2. Design and characterization of topographies

Topographies consisting of either lines or holes were strategically chosen based on previous results in the literature [5, 9, 12, 14]. Structure arrays are shown in Figure 4.1 with dimensions summarized in Table 4.1. Four topographies were designed *(1)* holes with a 2-μm diameter and horizontal and vertical spacings of 1 μm, *(2)* lines of 2-μm width and a spacing of 1 μm, *(3)* holes with a 300-nm diameter and horizontal and vertical spacings of 1 μm, and *(4)* lines of 300-nm width and a spacing of 1 μm. We

73

refer to the 300-nm structures as "sub-microscale" since we believe that the syntax more accurately depicts the size of the structures relative to the larger microscale structures (> 1 μm) and smaller nanoscale structures (< 100 nm, though nanoscale in many bio-applications is considered < 1 μm). The depth of all structures was approximately 400-500 nm.

Atomic force microscopy (AFM) and scanning electron microscopy (SEM) were used to characterize the quartz substrates. AFM images were taken to ensure precise dimensions of topography. AFM images were acquired with a Dimension 3100 with Nanoscope IV controller (Digital Instruments & Veeco Metrology Group, Santa Barbara, CA, USA) using a silicon tip in tapping-mode (Tap300, Budget Sensors, Sophia, Bulgaria). SEM images were acquired with a Zeiss SUPRA 40 VP Scanning Electron Microscope (Carl Zeiss, Peabody, MA, USA) after depositing a 10-nm layer of platinum/palladium (208HR, Cressington Scientific Instruments, Watford, UK).

4.3.3. In vitro hippocampal cell culture

Square wells of 1.5 cm^2 inner area were molded in polydimethylsiloxane (PDMS) (Slygard 184, Dow Corning, Midland, MI, USA). The wells were placed on each patterned quartz substrate and sterilized by exposure to ultraviolet (UV) radiation for 2 h. Sterilized substrates were incubated in 0.1 mg/mL poly-D-lysine (Sigma-Aldrich Corporation, St. Louis, MO, USA) overnight and subsequently washed twice with sterile

74
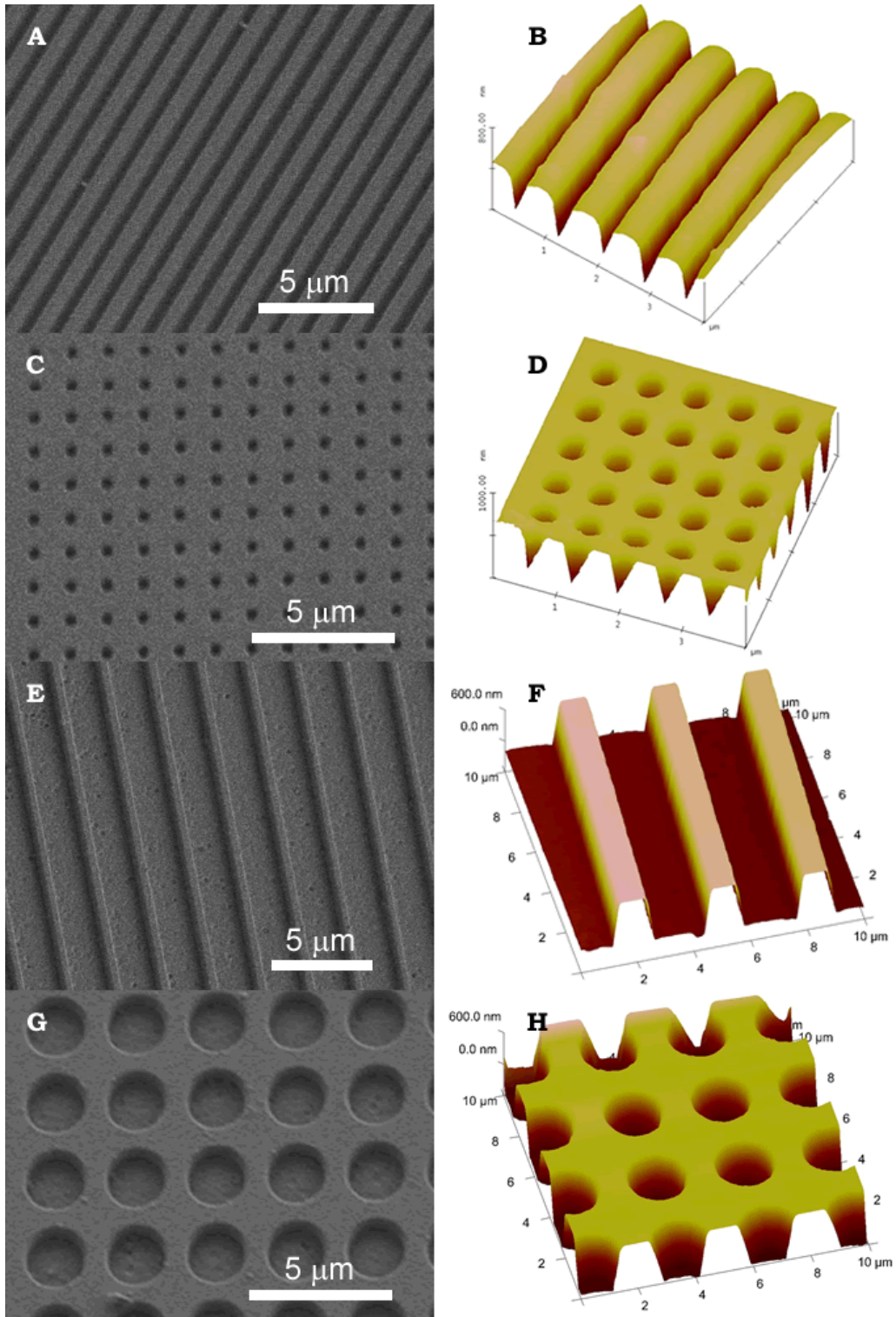
Figure 4.1. Quartz surfaces patterned with arrays of structures to form topographies. (A,B) Grooves (lines) of 300-nm width with a spacing of 1 µm (1.3 µm pitch); (C,D) holes with a 300-nm diameter with horizontal and vertical spacings of 1 µm (1.3 µm pitch); (E,F) grooves (lines) of 2-µm width with a spacing of 1 µm (3 µm pitch); (G,H) holes with a 2-µm diameter with horizontal and vertical spacings of 1 µm (3 µm pitch). All topographies consist of structures with 400-500 nm depth.

Table 4.1. Dimensions of the topographies used in the nerve cell experiments (Chapters 4 and 5).

Shapes	Dimensions		
Lines	Ridge (μm)[a]	Groove (μm)	Depth (nm)
300-nm Lines	1	0.3	400
2-μm Lines	1	2	500
Holes	Spacing (μm)[b]	Diameter (μm)	Depth (nm)
300-nm Holes	1	0.3	400
2-μm Holes	1	2	500

a) Pitch: 1.3 μm for 300-nm Lines and 3 μm for 2-μm Lines
b) Pitch: 1.3 μm for 300-nm Holes and 3 μm for 2-μm Holes in x- and y-directions

double-deionized water. Samples were dried in a sterile laminar flow bench and stored at 4 °C until used in cell culture experiments.

Rat embryonic hippocampal neurons (E18) were isolated from commercial rat hippocampal tissue (BrainBits, Springfield, IL, USA) according to the manufacturer's protocol. The hippocampus was incubated in 4 mg/mL papain solution (Worthington, Lakewood, NJ, USA) in Hibernate E medium (BrainBits, Springfield, IL, USA) at 30 °C for 20 min. A fire-polished Pasteur pipette was used to triturate the hippocampal tissue, followed by centrifugation at 200g for 1 min. A cell pellet was suspended in 1 mL of warm culture medium consisting of Neurobasal medium (Invitrogen, Gaithersburg, MD, USA) supplemented with 2% B-27 supplement (Invitrogen), 0.5 mM L-glutamine (Fisher Scientific, Pittsburgh, PA, USA), 0.025 mM glutamic acid (Sigma-Aldrich), and 1% antibiotic-antimycotic solution (Sigma-Aldrich). Cells were seeded on the quartz substrates with a seeding density of 2 x 10^4 cells/cm^2 in the culture medium and incubated at 37 °C and 5% CO_2 for 24 h.

4.3.4. Immunofluorescence and image analysis

Embryonic hippocampal neurons cultured on the substrates were fixed with 4% paraformaldehyde (Sigma-Aldrich) and 4% sucrose (Sigma-Aldrich) in phosphate-buffered saline (PBS) ($pH = 7.2$) for 20 min at room temperature. Fixed samples were permeabilized with 0.1% Triton X-100 (Fluka, St. Louis, MO, USA) and 3% goat serum (Sigma-Aldrich) in PBS for 20 min, washed twice with PBS, and treated with a blocking solution of 3% goat serum in PBS for 1 h at 37 ºC. Tau-1, a microtubule protein expressed in axons, was labeled as an axonal marker. Mouse tau-1 antibody (Chemicon, Temecula, CA, USA) was diluted to 1:200 in blocking solution, and added to the culture samples. After overnight incubation at 4 ºC, the samples were washed with PBS two times, treated with a secondary antibody solution of Alexa 488-labeled goat anti-mouse IgG (Invitrogen) (1:200 dilution in blocking solution) at 4 ºC for 5 h, and rinsed in PBS for 5 min two times. Samples were stored at 4 ºC while awaiting further analysis.

Fluorescence and optical images of cells and axons were acquired using a fluorescence microscope (IX-70, Olympus). The images were captured using a color CCD camera (Optronics MagnaFire, Goleta, CA, USA). Cell images were analyzed using Image J software (National Institutes of Health). Axon length was measured as the linear distance between the soma junction (point of axon initiation from the soma) and the distal tip of the axon. When several neurites branched from a single neuron, the length of the longest axon was measured and recorded. A neuron was considered to be polarized only when the axon was approximately two times longer than the characteristic diameter of the cell body, as previously described [16]. Only individually isolated cells were analyzed in our experiments. Axon alignment relative to the line topographies was

77

determined by measuring the angle subtended by a line extending from the soma junction to the growth cone and the direction of the edges of the lines.

4.3.5. Examination of cellular morphologies

SEM was utilized to evaluate cell and axon morphology on the topographies. Fixed hippocampal neurons were dehydrated by treating with ethanol in water at successively increasing concentrations of ethanol; cells were treated at concentrations (v/v) of 30% for 45 min, 50% for 30 min, and 70%, 85%, 90%, 95%, and absolute ethanol (100%) (Pharmco, Brookfield, CT, USA) for 10 min each. Water was completely removed by adding hexamethyldisilazane (HMDS) (Sigma-Aldrich) and drying in air at ambient conditions. The dried samples were coated with a thin 10-nm layer of platinum/palladium by sputter coating (208HR, Cressington Scientific Instruments, Watford, UK). SEM images were acquired with a Zeiss SUPRA 40 VP Scanning Electron Microscope.

4.3.6. Statistical analysis of experimental data

Data were analyzed using a combination of balanced one-way analysis of variance (ANOVA) [17] and standard two-sided t-tests for measurement [18] and binomial [19] data. p-values were calculated from a standard t-distribution tabulation and reported where applicable. The criterion for statistical significance was $p < 0.05$, although p-values less than 0.20 were noted.

78

4.4. RESULTS

4.4.1. Design and fabrication of topographical substrates

We define a homogeneous topography as a surface formed when a single structural formation is arrayed over the entire area. Fundamental structural *shapes* include ridge-grooves (i.e., lines) and holes, which represent structures arrayed in one direction and two directions. In addition to fundamental changes in shape, order-of-magnitude changes in feature dimensions represent another major modification to topography. Accordingly, we fabricated features of different scales, i.e., microscale (> 1 μm) and sub-microscale (< 1 μm), which can provide intimate contact with cellular components such as the soma, axon, and growth cone of neurons (Table 4.1). Since the cell body of neurons is approximately 5-10 μm in diameter, a 2-μm feature has dimensions of the same order-of-magnitude as a typical neuron [20]. A 300-nm feature has dimensions of an order-of-magnitude smaller than those characterizing the size of a neuron. Features having sizes in the tens of microns and larger represent topography with dimensions of orders-of-magnitude larger than those characterizing the size of neurons. Surfaces with structures of orders-of-magnitude larger dimensions than the neurons may be not recognized by the neurons in the same way as topography with dimensions of cellular (~1-10 μm) and sub-cellular (sub-microscale) scales. Consequently, we fabricated microscale sub-microscale topographical holes and lines (Table 4.1) to investigate their interactions with individual neurons.

79

4.4.2. Cell adhesion to topographies

Cell adhesion to each of the topographies was determined by counting the total number of anchored cells on the patterns 24 h after seeding (Figure 4.2). The number of adhered cells on each topography was determined to be 117, 123, 90, 102, and 119 cells/mm^2 for the 300-nm lines, 300-nm holes, 2-μm lines, 2-μm holes, and smooth surface, respectively. Adhesion was statistically the same on the topographies as on the smooth surfaces. Trends showed that adhesion appeared to actually decrease on the microscale topography relative to the sub-microscale and smooth surfaces. It has been
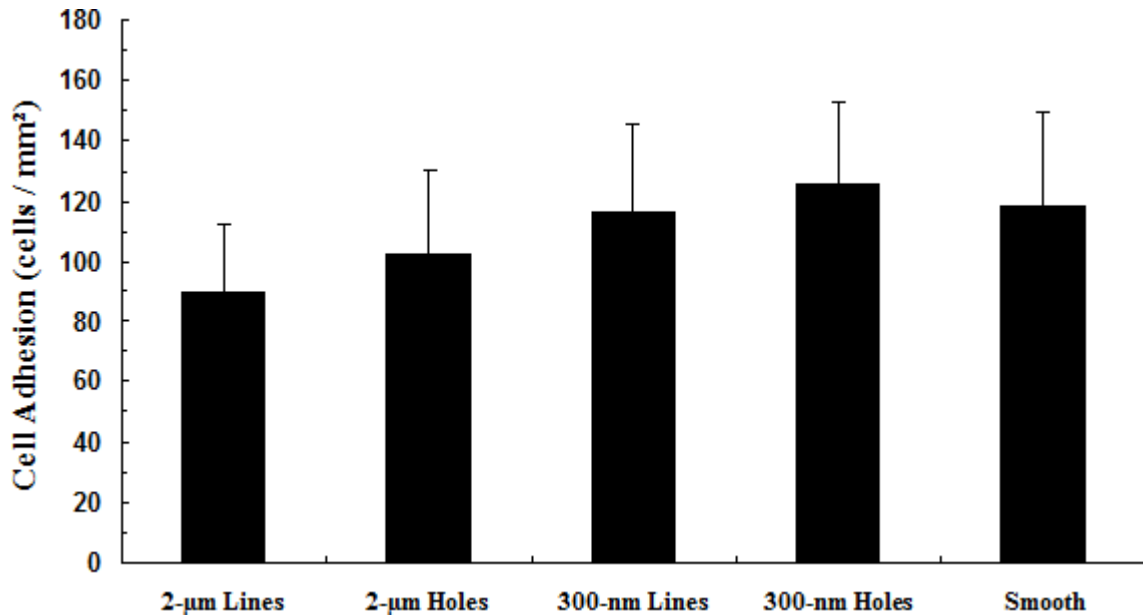
Figure 4.2. Adhesion of neurons to topography and smooth surface calculated by dividing the total number of cells sampled (polarized and unpolarized) and dividing by surface area. Differences in adhesion on topography were similar to smooth surface. Error bars = sem.

proposed in the literature that cell adherence depends on the proportion of ridge area on patterned surfaces, which is consistent with the fact that the proportion of ridge area on the sub-microscale topographies is quite a bit greater than on the microscale topographies.

4.4.3. Axon formation on topographies

We investigated the influence of the topographies on initial axon establishment (i.e., polarization) (Figure 4.3A). Polarization on all the topographies was statistically greater than on smooth quartz (29.3%). Polarization was greater on the 300-nm holes (56.2%) than on the 2-µm holes (46.5%) ($p < 0.20$) but similar to the 300-nm lines (51.9%). Also, polarization was smaller on the 2-µm lines (46.3%) than on the 300-nm lines ($p < 0.20$), but similar to the 2-µm holes. Results indicate that topography had a markedly positive impact on polarization relative to the smooth surface. Moreover, trends showed that polarization was influenced more by structure size than shape, where sub-microscale features appeared to stimulate polarization to a slightly greater degree than microscale features.

4.4.4. Axon elongation on topographies

Axon length was measured for each polarized cell (Figure 4.3B). Mean axon length was 50.1 µm, 38.7 µm, 44.4 µm, 31.0 µm, and 31.8 µm, on the 2-µm lines, 2-µm holes, 300-nm lines, 300-nm holes, and smooth surface, respectively. Longer axons were observed on the 2-µm ($p < 0.05$) and 300-nm ($p \approx 0.05$) lines compared to the axons on the smooth surfaces. However, no significant differences in axon length were observed

81
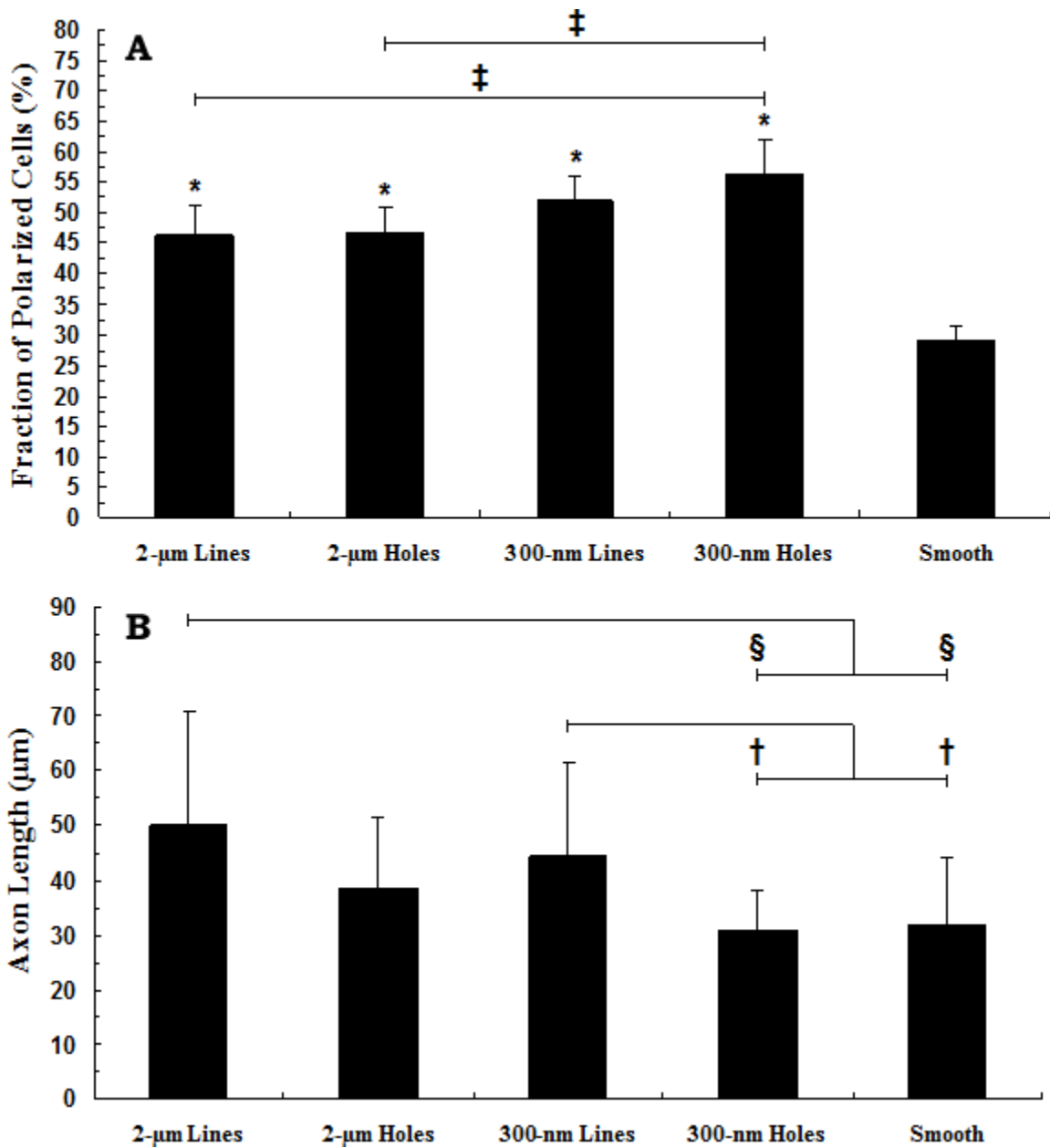
Figure 4.3. **(A) Fraction of neurons polarized (%) relative to the total cell count on each topography and smooth surface; (B) Mean axon length (μm) of polarized neurons on topography and smooth surface. Error bars = sem.** *****Statistically significant relative to smooth surface ($p \leq 0.05$), §p $\leq$ 0.50, †$p \leq 0.10$, ‡$p \leq 0.20$. At least 100 neurons were analyzed on each topography (except 300-nm Holes, # cells = 73).**

82

between any hole topography and the smooth surfaces. Axon length on the 2-µm lines (50.1 µm) was statistically greater than on the 300-nm holes (31.0 µm) ($p \approx 0.05$) but not statistically greater than on the 2-µm holes (38.7 µm) or 300-nm lines (44.4 µm). Axon lengths appeared greater on the 300-nm lines than on the 300-nm holes, although the data was not statistically significant.

Overall, axon length was the longest on the 2-µm lines and the shortest on the 300-nm holes, indicating that feature shape and size on substrates appeared to synergistically influence axonal elongation; however, trends showed that cells developed more elongated axons on the lines than on holes or the smooth surface, which suggests that axon elongation depends more on feature shape than feature size, in contrast to what was seen for axon polarization.

4.4.5. Axon alignment on lines

Axon alignment was analyzed and reported in terms of axonal angle θ and axon length (Figure 4.4). Angles took on values between 0-90° and axons having angles between 0-30°, 30-60°, or 60-90° were classified as having parallel, indeterminate (unaligned), or perpendicular alignment, respectively. We have not included data of axon alignments on holes and smooth surfaces because these topographies were found not to have a directionality capable of guiding axon alignment. Axons predominately aligned in a parallel fashion for both sizes of lines; however, the smaller 300-nm lines resulted in more perpendicular alignment (Figure 4.4A). 77.8% of axons exhibited parallel alignment on the 2-µm lines compared to 64.4% of axons on the 300-nm lines. We observed a marked difference in the degree of "complete alignment" of axons on the

83

different line sizes, which were axons having extreme values of θ between 0-10° (completely parallel) or 80-90° (completely perpendicular). 55.6% of cells on the 2-µm lines demonstrated completely parallel alignment compared to 37.0% on the 300-nm lines ($p < 0.05$). No cells on the 2-µm lines demonstrated completely perpendicular alignment whereas 9.6% of cells on the 300-nm lines exhibited completely perpendicular alignment ($p < 0.05$).

We found relationships between axonal angles and axon lengths, where average axon length was sensitive to alignment relative to the grooves (Figure 4.4B and Figure 4.4C). On the 300-nm lines, the average axon length for neurons with perpendicular alignment (60-90°, 75.9 µm) was statistically greater than those with parallel alignment (0-30°, 40.7 µm) or those with axons having indeterminate alignment (30-60°, 42.8 µm). On the other hand, no statistical differences in mean axon length were observed for axons in each of the angle groups for the 2-µm lines (Figure 4.4B). Interestingly, "extensively" elongated axons (defined as axons >100 µm in length) were mostly found to have parallel or perpendicular alignment depending on groove dimensions. On the 2-µm lines, extensively elongated axons only formed with parallel alignment (0-30°). On the other hand, extensive elongation appeared to be most prevalent for perpendicular alignment (60-90°) on the 300-nm lines.

Figure 4.5 shows representative images of hippocampal cells with elongated axons exhibiting both parallel and perpendicular alignment in response to the presence of the lines. In Figure 4.5, images 4.5(A,B) show cells exhibiting parallel alignment relative to the 2-µm lines and images 4.5(C-E) show perpendicular alignment relative to the 300-nm lines.

84
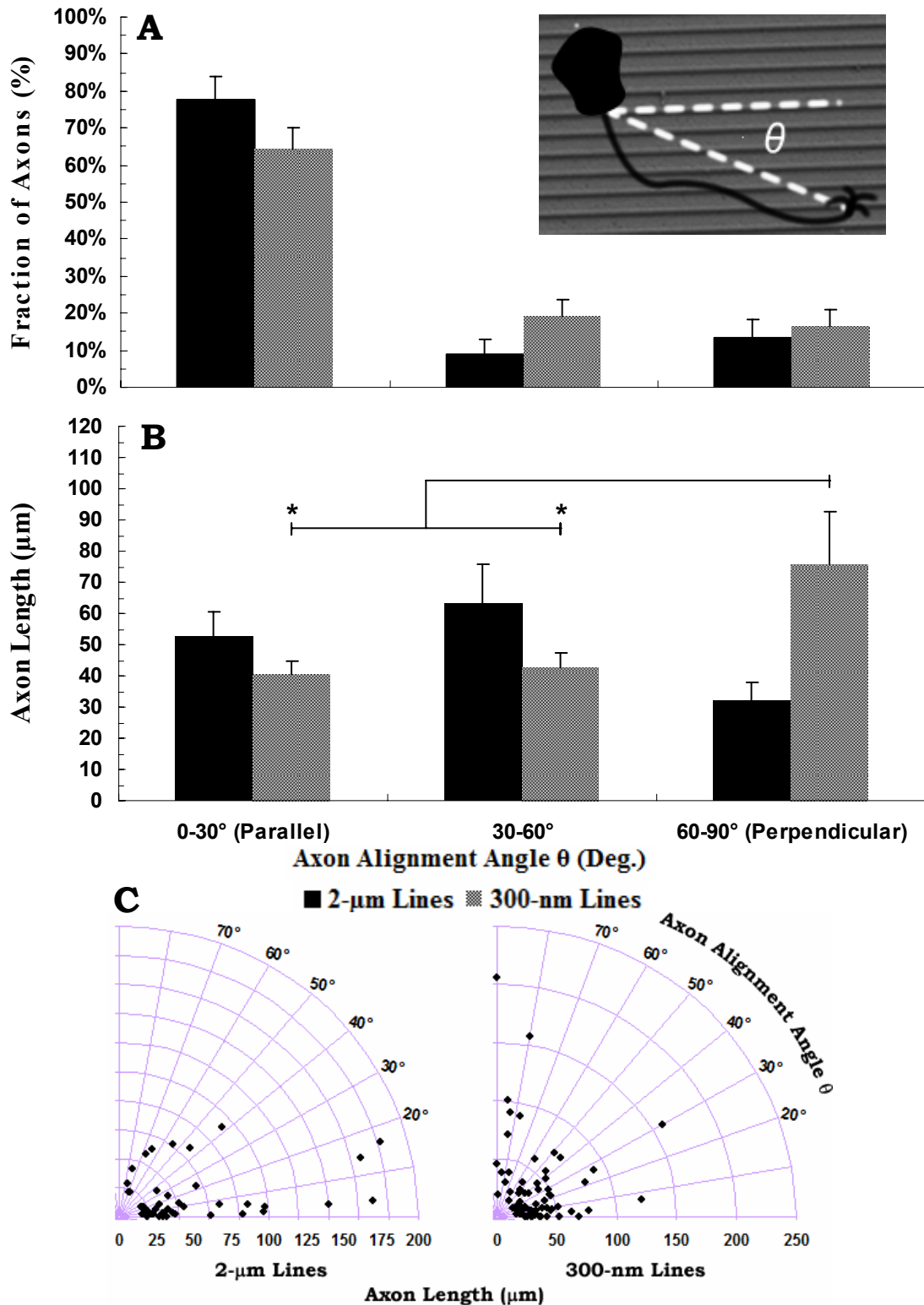
Figure 4.4. (A) Histogram showing the percentage of axons having an alignment, *θ*, of 0-30° (parallel), 30-60° (unaligned), and 60-90° (perpendicular) on the 2-μm and 300-nm lines. (Inset) Axon orientation angle *θ*. Average *θ* for all angles 0-90° for the 2-μm and 300-nm Lines was 19.1° (# *cells* = 45) and 28.9° (# cells = 73), respectively (*p* < 0.05). (B) Average axon length for axons of various alignments. (C) Axon alignment plotted against axon length for the data represented in (A). Error bars = sem. *p < 0.05.

85
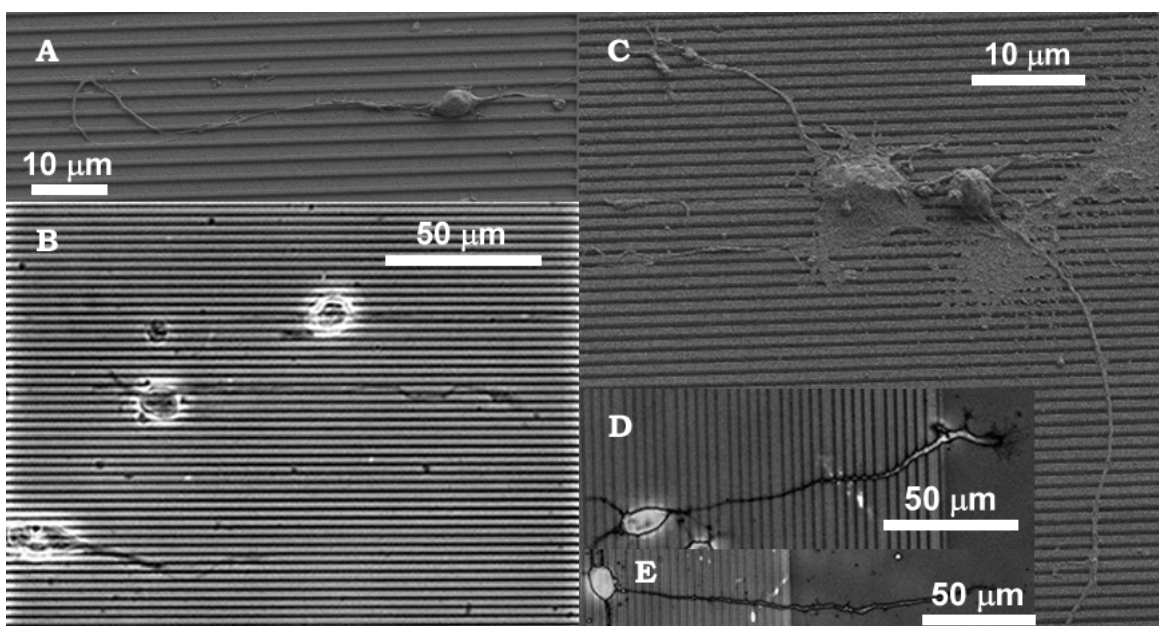
Figure 4.5. SEM and optical images showing the influence of line width on the orientation of elongated axons seeded on arrays of microfabricated lines (line topographies). (A,B) parallel alignment on the 2-µm lines; (C-E) perpendicular alignment on the 300-nm lines.

4.4.6. Cellular morphologies on topographies

Figure 4.6 shows representative images of cells grown on various topographies. For all topographies, the soma tended to sit on the ridges between holes or lines and form an elliptical shape; however, the soma was usually found embedded in the grooves of the 2-µm lines and having an elliptical shape. In addition to the soma, filopodia and growth cones appeared to interact differently with each of the topographies (Figure 4.6). In general, growth cones were more spread out on the sub-microscale topographies and smooth surfaces than on the larger microscale topographies. Filopodia, which play a role in contact guidance and pathfinding [21], appeared to grow from the periphery of the growth cones as well as the axons (i.e., lateral fillpodia).

86
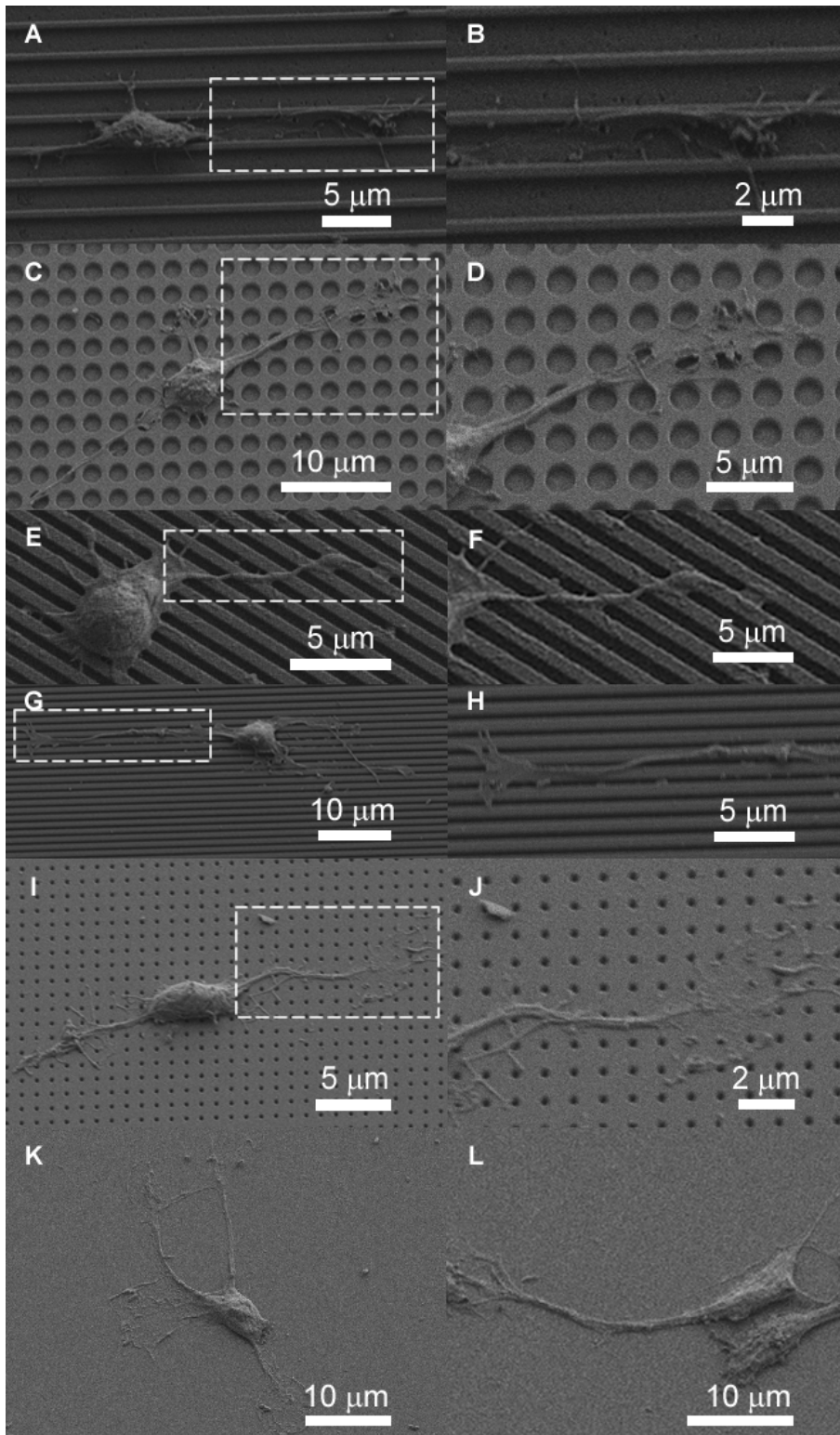
Figure 4.6. Soma and axon orientation and morphology based on topography. The images in the right column show the enlarged areas indicated in the white boxes shown in the juxtaposing images in the left column. Sample cells on (A-D) 300-nm lines, (E,F) 300-nm holes, (G,H) 2-µm lines, (I,J) 2-µm holes, and (K,L) smooth surface.

87

On the 300-nm lines, axons crossed the ridges at orthogonal angles and extended lateral filopodia at regular intervals on each of the ridges that were bridged by the axon; however, when axons aligned parallel to the lines, few lateral filopodia were observed. On the 2-μm lines, filopodia were observed at the growth cone and at random locations along the length of the axons. On the 300-nm holes, the growth cone formed filopodia around its periphery while lateral filopodia were found at random locations along the axons. On the 2-μm holes, the growth cone tended to have filopodia around its periphery and often appeared flattened and sprawled while lateral filopodia did not appear along the length of axons in most cases. Interestingly, axons tended to almost always cross the 2-μm holes and were rarely observed to anchor to the sidewalls or bottom surfaces of the holes.

4.5. DISCUSSION

The mechanisms by which surface texture affects neuron behavior are not clearly understood. However, it has been proposed that topography exerts mechanical stresses on the cell cytoskeleton analogous to texture or roughness on surfaces that enhance traction [5]. The mechanical stresses ultimately provoke specific cellular responses, possibly by transducing changes in gene expression [7]. Microscale and sub-microscale topography introduce physical discontinuities in surface area that apply mechanical forces to neurons. These discontinuities seem to affect the morphologies of filopodia, the growth cone, and the soma, which, overall, act to provoke cellular responses, like neurite initiation, rate of growth, and alignment.

88

We note that the cells may sense the sub-microscale and microscale topographies differently, at a fundamental level, due to the order-of-magnitude difference in size scale. Because of their relatively small size, densely packed sub-microscale features are largely inaccessible by cellular structures, thus, rendering the surfaces heterogeneous in terms of material properties where the trough regions (grooves) represent pockets of fluid (culture medium). The pockets of fluid, in combination with the solid surface, collectively would change the properties of the surface recognized by cells having sizes of larger scale. On the other hand, since cells are able to access the grooves of larger microscale features, the microscale features may serve to introduce physical discontinuities in surface area, but not to change material properties from the perspective of individual cells [22-24]. Teixeira [9] found that HCECs on different patterns (i.e., smooth surface, microscale and nanoscale lines) displayed different focal adhesion numbers and sizes. As ridge-widths decreased, focal adhesion sizes decreased, commensurately, altering the adhesive properties of the topographies.

We speculate that our tested features might not be sufficient at altering cell adhesion; however, future studies with other features may allow us to better understand the role of topography on the adherence of neurons. We found that the adhesion of neurons to the topographies relative to a smooth surface was similar; however, trends showed that cells appear to adhere better on surfaces with sub-microscale features relative to those with microscale features. Adhesion appears to depend on ridge area, where ridge area on surfaces with smaller features is greater than those with larger features. Changes in adhesion based on feature size may be related to what has been observed for surfaces with varying surface roughness. Sapelkin et al. [25] observed that

89

immortalized rat hippocampal neurons preferentially adhered to porous silicon than crystalline silicon.

Polarization was markedly enhanced on all topographies relative to smooth quartz. Additionally, sub-microscale features induced axon formation more than microscale features regardless of feature shape. Our results are consistent with previous studies [14, 26]. Gomez et al. [14] found that rat embryonic hippocampal neurons on PDMS microchannels of 1-μm and 2-μm width enhanced axon formation compared to smooth PDMS after 20 hours in culture. Lee at al. [26] cultured hippocampal neurons on various PLGA fibers having diameters of 400 nm – 2.2 μm and found that a greater number of neurons polarized on smaller PLGA fibers while differences in fiber orientation for similar fiber diameters had a negligible effect on polarization. The authors proposed that the topography caused alterations in focal adhesions and provided distortions in the cytoskeleton that triggered the intracellular mechanisms controlling axon initiation.

Unlike axon polarization, we found that overall axon length was more feature-shape dependent than feature-size dependent. Additionally, the lines were observed to promote axon elongation, especially in cases where axons exhibited either parallel or perpendicular alignment. These results suggest that topography may play different roles in influencing neuronal development at different developmental stages, such as initial axon formation and subsequent axon elongation.

It is thought that axon alignment to lines may reflect naturally occurring axonal alignments to neurite bundles [27, 28]. We observed axon alignment to be predominately parallel on both sizes of lines; however, we observed more perpendicular alignment on

90

the smaller 300-nm lines (Figure 4.4A). Similar axon alignments were reported by Rajnicek et al. [12]. They found that line depth and width seem to play a combined role in promoting alignment. For a given line width, they showed that alignment became less parallel and more orthogonal for decreasing depth. We found that decreasing line width while maintaining depth also promoted more perpendicular alignment. It has been claimed that hippocampal neurites appear to use different mechanisms for perpendicular and parallel contact guidance and that lines present separate signals that provoke parallel and perpendicular responses, depending on feature dimensions [13].

4.6. CONCLUSIONS

Here we reported the results of our investigation determining the effects of micro- and nanopatterned topography of various sizes and shapes on *(1)* cell-substrate adhesion, *(2)* axon establishment (neuron polarization), *(3)* axon length, *(4)* axon alignment, and *(5)* cell morphology of rat embryonic hippocampal neurons. For this purpose, we fabricated arrays of 300-nm holes, 2-µm holes, 300-nm lines, and 2-µm lines in quartz (SiO_2); all structures forming the arrays had a depth of approximately 400-500 nm. We found that hippocampal neurons responded differently to topographies of different sizes and shapes. Topography (holes and lines) enhanced axon formation and the degree of axon formation was found to be feature size-dependent, with polarization being greater on sub-microscale features than microscale features. Lines were found to increase axon elongation where elongation was observed to be feature shape dependent rather than size dependent. Lines also influenced axon alignment, and a connection between alignment and axon length was found to exist in certain circumstances.

91

Finally, topography was found to alter cellular morphologies (i.e., soma, axons, growth cones, filopodia) where size and shape were both important factors influencing cell behavior. Our findings heighten our understanding of neuronal behavior on topography in the early developmental stages of individual neurons and may aid in designing biomaterials for neural applications such as neural probes and tissue engineering scaffolds.

4.8. REFERENCES

1. Fozdar D. Y., Lee J. Y., Schmidt C. E., Chen S., Neurons respond uniquely to topographies of various sizes and shapes, *Biomaterials*, 2009; **(submitted)** pp.

2. Li G. N., Hoffman-Kim D., Tissue-engineered platforms of axon guidance, *Tissue Engineering Part B-Reviews*, 2008; **14** pp. 33-51.

3. Liu C. Y., Westerlund U., Svensson M., Moe M. C., Varghese M., Berg-Johnsen J., et al., Artificial niches for human adult neural stem cells: Possibility for autologous transplantation therapy, *Journal of Hematotheraphy & Stem Cell Research*, 2003; **12** pp. 689-699.

4. Norman J., Desai T., Methods for fabrication of nanoscale topography for tissue engineering scaffolds, *Annals of Biomedical Engineering*, 2006; **34** pp. 89-101.

5. Curtis A., Wilkinson C., Topographical control of cells, *Biomaterials*, 1997; **18** pp. 1573-1583.

6. Dalby M. J., Riehle M. O., Yarwood S. J., Wilkinson C. D. W., Curtis A. S. G., Nucleus alignment and cell signaling in fibroblasts: response to a micro-grooved topography, *Experimental Cell Research*, 2003; **284** pp. 274-282.

7. Dalby M. J., Topographically induced direct cell mechanotransduction, *Medical Engineering & Physics*, 2005; **27** pp. 730-742.

8. Berry C. C., Campbell G., Spadiccino A., Robertson M., Curtis A. S. G., The influence of microscale topography on fibroblast attachment and motility, *Biomaterials*, 2004; **25** pp. 5781-5788.

9. Teixeira A. I., Abrams G. A., Bertics P. J., Murphy C. J., Nealey P. F., Epithelial contact guidance on well-defined micro- and nanostructured substrates, *Journal of Cell Science*, 2003; **116** pp. 1881-1892.

10. Teixeira A. I., Abrams G. A., Murphy C. J., Nealey P. F., Cell behavior on lithographically defined nanostructured substrates, *Journal of Vacuum Science & Technology B*, 2003; **21** pp. 683-687.

11. Goldner J. S., Bruder J. M., Li G., Gazzola D., Hoffman-Kim D., Neurite bridging across micropatterned grooves, *Biomaterials*, 2006; **27** pp. 460-472.

12. Rajnicek A. M., Britland S., McCaig C. D., Contact guidance of CNS neurites on grooved quartz: influence of groove dimensions, neuronal age and cell type, *Journal of Cell Science*, 1997; **110** pp. 2905-2913.

93

13. Rajnicek A. M., McCaig C. D., Guidance of CNS growth cones by substratum grooves and ridges: effects of inhibitors of the cytoskeleton, calcium channels and signal transduction pathways, *Journal of Cell Science*, 1997; **110** pp. 2915-2924.

14. Gomez N., Lu Y., Chen S.C., Schmidt C., Immobilized Nerve Growth Factor and Microtopography Have Distinct Effects on Polarization Versus Axon Elongation in Hippocampal Cells in Culture, *Biomaterials*, 2006; **Accepted** pp.

15. Gomez N., Chen S. C., Schmidt C. E., Polarization of hippocampal neurons with competitive surface stimuli: contact guidance cues are preferred over chemical ligands, *Journal of the Royal Society Interface*, 2007; **4** pp. 223-233.

16. Dotti C. G., Sullivan C. A., Banker G. A., The Establishment of Polarity by Hippocampal-Neurons in Culture, *Journal of Neuroscience*, 1988; **8** pp. 1454-1468.

17. Christensen R., One-way analysis of variance. In *Analysis of Variance, Design and Regression*, Chapman & Hall, Great Britian, 1996, pp. 114-123.

18. Christensen R., Two independent samples with unequal variance. In *Analysis of Variance, Design and Regression*, Chapman & Hall, Great Britian, 1996, pp. 95-98.

19. Christensen R., Two independent binomial samples. In *Analysis of Variance, Design and Regression*, Chapman & Hall, Great Britian, 1996, pp. 231-233.

20. Seidlits S. K., Lee J. Y., Schmidt C. E., Nanostructured scaffolds for neural applications, *Nanomedicine*, 2008; **3** pp. 183-199.

21. Bentley D., Toroianraymond A., Disoriented Pathfinding by Pioneer Neuron Growth Cones Deprived of Filopodia by Cytochalasin Treatment, *Nature*, 1986; **323** pp. 712-715.

22. Cassie A. B. D., Baxter S., Wettability of Porous Surfaces, *Transactions of the Faraday Society*, 1944; **40** pp. 546 - 551.

23. Kim P., Kim D. H., Kim B., Choi S. K., Lee S. H., Khademhosseini A., et al., Fabrication of nanostructures of polyethylene glycol for applications to protein adsorption and cell adhesion, *Nanotechnology*, 2005; **16** pp. 2420-2426.

24. Adamson A. W., The Solid-Liquid Interface - Contact Angle. In *Physical chemistry of surfaces*, John Wiley and Sons, New York, 1982, pp. 338-342.

94

25. Sapelkin A. V., Bayliss S. C., Unal B., Charalambou A., Interaction of B50 rat hippocampal cells with stain-etched porous silicon, *Biomaterials*, 2006; **27** pp. 842-846.

26. Lee J. Y., Bashur C. A., Gomez N., Goldstein A. S., Schmidt C. E., Enhanced polarization of embryonic hippocampal neurons on micron scale electrospun fibers, *Journal of Biomedical Materials Research - Part A*, 2009 (in press); pp.

27. Nagata I., Nakatsuji N., Rodent Cns Neuroblasts Exhibit Both Perpendicular and Parallel Contact Guidance on the Aligned Parallel Neurite Bundle, *Development*, 1991; **112** pp. 581-590.

28. Nagata I., Kawana A., Nakatsuji N., Perpendicular Contact Guidance of CNS Neuroblasts on Artificial Microstructures, *Development*, 1993; **117** pp. 401-408.

Chapter 5: Response of neurons to competing topographical features of various size and shape[1]

5.1. ABSTRACT.

Understanding how surface features influence the establishment and outgrowth of the axon of developing neurons at the single cell level may aid in designing implantable scaffolds for the regeneration of damaged nerves. Past studies have shown that micropatterned ridge-groove structures did not only instigate axon polarization, alignment, and extension, but are also preferred over smooth surfaces and even neurotrophic ligands. Here, we performed tournament-style competition axonal-growth assays on a proprietary topography grid (four quadrants) to determine the relative preferences for various topographies (microscale and sub-microscale lines and holes), where each topography in the grid consisted of an array of microscale (~2 μm) or sub-microscale (~300 nm) holes or lines with variable dimensions. Individual rat embryonic hippocampal cells were positioned between two arrays of different topographies or along the outer borders of the arrays on unpatterned surface, cultured for 24 hours, and analyzed with respect to axonal selection using conventional imaging techniques. Sub-microscale features were found to have a notably unique effect on preferential axonal growth relative to microscale features, while both sizes and shapes of features exhibited enhanced responses relative to smooth surface.

---

[1] This work has not yet been submitted. Conditional reference [1].

5.2. INTRODUCTION

Advances in nerve tissue engineering may ultimately lead to the development of relatively non-invasive procedures for treating peripheral nerve damage. Much focus is being placed on the development of biomaterials that can present combinations of various stimulative cues, e.g., endogenous cells and physical and chemical stimuli) to damaged tissue [2, 3]. The biomaterials will likely be used to construct tissue scaffolds that provide nerve tissue with a realistic microenvironment containing chemical / physical cues that induce and sustain or enhance tissue development and viability. A variety of cues will be incorporated onto scaffolds, either in isolation or synergistically, including chemical ligands and physical structures, which will be implemented based on their efficacy and level of invasiveness. Schmidt et al. [4] provided a comprehensive review of tissue engineering strategies for the repair and regeneration of damaged nerve tissue.

In the body, neurons are naturally encompassed within a myriad of physical and biochemical cues and boundary conditions that signal the formation and extension of neural processes in highly aligned fashions [5]. Because typical laboratory cell cultures do not provide cells with microenvironments that recapitulate the conditions found *in vivo*, it has been exceedingly difficult to stimulate the establishment of inter-neuronal connectivities that are necessary to form nerve tissue with the proper architecture and function. Utilizing cues on scaffolds effectively may enhance our capabilities to modulate specific nerve cell responses by providing cells with realistic microenvironments [6, 7].

97

Microfabrication techniques have been adopted to pattern surfaces with well-ordered features to study the effects of topography on neuronal behavior [8-12]. Studies on the interactions between microfabricated topographical cues and neurons have revealed the important role of physical cues in inciting a myriad of cellular behaviors, including adhesion, migration, and differentiation. Rajnicek et al. [13, 14] performed one of the first in-depth studies on the effects of line arrays on the alignment of axons of hippocampal neurons. They showed that topography and its dimensions heavily affect axonal alignment. Gomez et al. [15] performed novel competition axon guidance assays by culturing individual hippocampal neurons between two micropatterned polydimethylsiloxane (PDMS) surfaces, one containing microscale lines and the other various neuroactive biomolecules, such as nerve growth factor (NGF) and laminin. They found that embryonic hippocampal neurons extended their axons preferentially toward the 2-µm line topographies relative to smooth PDMS surfaces or PDMS patterned with NGF and laminin, emphasizing the ability of topography to stimulate axonal growth. To date, their have not been similar competition studies evaluating preferential axonal growth among topographies of varying feature shape and size. Therefore, we investigated the ability of microscale and sub-microscale lines and holes to influence axonal guidance by performing competitive assays. First, preferential axon guidance was evaluated between each topography and smooth surface composed of identical materials. Second, axon preference was evaluated between the different topographies.

98

5.3. MATERIALS AND METHODS:

5.3.1. Quartz Substrate Fabrication

25 mm^2 square quartz substrates were exposed to an oxygen plasma (50 sccm O$_2$, 300 Watts, 150 mTorr, 25 °C; Plasma-Therm 790, Plasma-Therm, Inc., St. Petersburg, FL, USA) for 10 min and immersed in a mixture of 25% hydrogen peroxide (30% H$_2$O$_2$ in water) (v/v) in sulfuric acid (piranha bath) for 10 min (hydrogen peroxide 30% #2190, sulfuric acid 96% #9684, JT Baker, Phillipsburg, NJ, USA). The substrates were removed from the bath, thoroughly rinsed in deionized water, dried with N$_2$ gas, and dehydrated on a hot plate at 200 °C for 5 min. After cleaning, a thin 30-nm layer of chromium was thermally evaporated onto the quartz at a rate of 5 Å/sec (Explorer, Denton Vacuum, Moorestown, NJ, USA). ZEP-520A (Zeon Chemicals, Louisville, KY, USA) positive electronic resist was coated onto the chromium layer to a thickness of approximately 200 nm by spinning at 4000 rpm for 40 sec; nominal layer thickness was reduced by diluting the ZEP in anisole to a concentration of 50% (v/v). After spin-coating, the resist was baked on a hot plate at 180 °C for 150 sec.

Arrays of structures were patterned in the ZEP using electron beam lithography (JEOL 6000 FSE, JEOL Ltd., Tokyo, Japan; Raith 50, Raith GmbH, Dortmund, Germany) with a beam fluence of 100 μC/cm^2 and subsequently developed in ZED-N50 (Zeon Chemicals, Louisville, KY, USA) by double-spray-puddle for 15 + 15 sec using standard pipettes. IPA was used as the etch-stop during the developing process. The substrate was dried with a slow stream of N$_2$ gas. The ZEP resist served as a dry-etch mask for the underlying chromium layer, which provided a selectivity close to 3:1 chromium:ZEP. A two-step reactive-ion-etching (RIE) (Trion Technology, Clearwater,

99

FL, USA) process was used to etch through the chromium. The first step was a descum O₂ plasma treatment to remove residual resist from developed regions. The second step was the chromium etch step, which was timed to etch completely through the chromium layer to the quartz. The ZEP resist did not have to be stripped after etching through the chromium layer since remaining resist was stripped rather quickly during the following quartz etch. The chromium layer served as the etch mask for the underlying quartz with a selectivity of over 10:1 quartz:chromium. The quartz was etched down about 400 nm. After quartz etching, remaining chromium was stripped with a chromium wet-etchant (Etchant 1020, Transene Company, Danvers, MA, USA) at 40 °C for 2 min. The quartz was then thoroughly washed in a piranha bath for 10 min and stored in DI water for later experimentation.

5.3.2. Design of topographies

Topographies consisted of single structures arrayed in either one (lines) or two dimensions (holes) and were strategically chosen based on results obtained by Gomez et al. [15] and on additional design rules. Four topographies were designed and combined to form a 4-grid competition grid to facilitate data acquisition.

We define a homogeneous topography as a surface formed when a single structural formation is arrayed over the entire area to be patterned in a single-step with minor to no subsequent modifications. Fundamental structural shapes include groove-ridge (i.e., lines) and hole / pillar, which represent structures arrayed in one direction and two directions with a particular pitch (i.e., distance between common points among two identical adjacent structures), respectively. According to our definition of homogeneous,

100

combinations of structures or structural gradients based on size would render the resulting topography inhomogeneous. Several variations of the two fundamental shapes of homogeneous topographies (lines and holes) exist, but we believe that those modifications are simply variations of simple lines and holes and do not represent major changes in shape.

The arrays of 300-nm structures were patterned using a special method that reduced the electron beam writing time (Raith 50 EBL system) significantly, convenient for writing dense structure arrays over relatively large areas, ranging in scale from square micrometers to centimeters. Patterning structures over a large area is a commonplace requirement for patterning dense arrays of sub-microscale features (critical dimension < 1 µm) for performing cell studies. Typically, objects are patterned with EBL as closed polygons bounded by a finite number of vertices. While straight edges simply connect two vertices, curved features can consist of a very large number of vertices (a curved edge is essentially the serial aggregate of tiny lines attached end-to-end). Increasing the accuracy of edge curvature requires the specification of a greater number of vertices; thus, defining an edge with a seemingly continuous curvature, like a simple circle, can require the specification of tens to hundreds of vertices. A circular structure (e.g., a hole) created with an insufficient number of vertices would appear as a regular polygon with distinct edges instead of a circle with a continuously curved edge. Unfortunately, increasing the number of vertices defining a feature's boundaries involves a disproportionate increase in writing time. Accordingly, writing accurate sub-microscale (and nanoscale) structures in terms of a closed polygon (area), regardless of boundary curvature (though curved objects take longer), typically takes a significant amount of

101

time and depends both on the density of the structures in the array (structures / area) and the overall area to be patterned.

To reduce writing times significantly, the 300-nm holes and lines were patterned by single-pixel dot and line exposures in place of conventional area exposures. Individual pixels were essentially points (tiny areas) defined by the focused spot of the electron beam (usually a few nanometers in diameter). When single pixels were exposed, interactions between the electron beam and the electronically-sensitive resist were allowed to spread symmetrically outward in a radial fashion to form a circle whose diameter depended on the fluence of the electron beam and the time at which each pixel was exposed (dwell time). Longer dwell times resulted in circles of larger diameters. Circles were formed by discrete single-pixel exposures using the beam shutter (blanker) while lines were formed by rastering the beam to form a continuous line of single pixels. For the 300-nm holes, dot fluence was set to 0.7 μC. For the 300-nm lines, line fluence was set to 2000 μC/cm. Due to the larger dimensions of the 2-μm structures, pattern density was small enough that the structures could be written as polygons with an area fluence of 100 μC/cm^2; circular holes were drawn as regular polygons with 64 vertices. One thing to note is that the diameter of circles produced by irradiating single pixels expands slightly after the completion of the exposure as residual chemical reactions persist for short durations upon the blanking of the electron beam. Line-widths from line exposures also expand slightly for the same reasons.

Arrays of simple objects, like holes or lines, can be written rather easily by implementing a strategically premeditated spatial arrangement of points or lines and appropriately setting beam parameters (i.e., beam fluence and dwell time), which can be

102

altered from pixel-to-pixel or line-to-line, over the area to be patterned. Arrays of more complex objects can be drawn by single-pixel writes as well, by creating the individual objects making up the array from a local compilation of dots and lines and copying the area to be patterned in the horizontal and vertical directions (*x*- and *y*-directions in a Cartesian coordinate system). Many modern EBL tools include computer-aided drafting (CAD) tools that make it possible to graphically setup exposures while permitting easy access to beam parameters. Dot and line exposures are quite useful for more hastily patterning arrays of sub-microscale features on surfaces over large areas, which is often required of surfaces serving as substrates for biological cells. Such was the case for our 4-quadrant grid system; moreover, dot and line exposure could also be quite convenient in the fabrication of photonic crystal devices for *opto-biological* applications.

5.3.3. Chemical pretreatment of quartz substrates

Square-shaped cell culture dishes of 1.5 cm^2 inner area (the walls of the dish enclosures had a lateral thickness of several millimeters) were molded in polydimethylsiloxane (PDMS) (Slygard 184, Dow Corning, Midland, MI, USA). The rings were placed on each patterned quartz substrate, and sterilized by exposure to ultraviolet (UV) radiation for 2 h. The PDMS rings were used to confine liquids on the substrates, which allowed us to conserve our liquid media, including the cell culture media containing the cell suspensions. Sterilized substrates were incubated in 0.1 mg/mL poly-D-lysine (Sigma-Aldrich Corporation, St. Louis, MO, USA) overnight and subsequently washed with sterile double-deionized water. Hydrated samples were dried in a sterile laminar flow bench and stored at 4 °C until used in cell culture experiments.

103

5.3.4. Isolation of rat hippocampal cells

E18 rat embryonic hippocampal neurons were isolated from commercial rat hippocampal tissue (BrainBits, Springfield, IL, USA) according to the manufacturers protocol. The hippocampus was incubated in 4 mg/mL papain solution (Worthington, Lakewood, NJ, USA) in Hibernate E medium (BrainBits, Springfield, IL, USA) at 30°C for 20 min. A fire-polished Pasteur pipette was used to triturate the hippocampal tissue, followed by centrifugation (@ 200 g's for 1 min). A cell pellet was suspended in 1 mL of warm culture medium containing Neurobasal medium (Invitrogen, Gaithersburg, MD, USA), 2% B-27 supplement (Invitrogen), 0.5 mM L-glutamine (Fisher Scientific, Pittsburgh, PA, USA), 0.025 mM glutamic acid (Sigma-Aldrich), and 1% antibiotic-antimycotic solution (Sigma-Aldrich).

5.3.5. Cell micropositioning for performing competition assays

Micropositioning techniques were employed to place cells in precise locations on the quartz substrates. Hippocampal neurons were randomly seeded on the quartz substrates with a seeding density of 2 x 10^4 cells/cm^2. Individual cells were re-positioned in unpatterned gaps between the topographies (quadrants) in the 4-grid competition system or at the borders of the topographies juxtaposing smooth surface using micropipettes and a specialized micropositioning system.

Tapered micropipettes were formed by pulling glass capillaries (single-barrel standard borosilicate glass tubing 1 mm outer dia., 0.58 mm inner dia., World Precision Instruments, Sarasota, FL, USA) with a vertical pull type puller (PC-10, Narishige

104

International, East Meadow, NY, USA). The pulled micropipettes were connected to a pneumatic microinjector (IM-9C, Narishige International) and tightened to an XYZ movable micromanipulator (MN-151, Narishige International). This set-up was mounted on a reflectance upright microscope (BX51WI, Olympus, Center Valley, PA, USA) inside a horizontal laminar airflow workstation to guarantee sterility in the procedure.

A patterned quartz substrate was placed inside a PDMS ring, which was placed in the center of a sterile Petri dish of 10-cm diameter. The size and thickness of the square ring was small enough so that space was left between the outside wall of the ring and the circular wall of the Petri dish. Triturated neurons in culture medium (2×10^4 cells/mL) were added in the space outside the ring and allowed to settle for 5 min. Single neurons were identified on the Petri dish (outside the PDMS ring), aspirated with the micropipette by creating suction with the injector, moved with the micromanipulator, and repositioned inside the rings in desired locations on the quartz substrate by releasing from the pipette. After micropositioning, Petri dishes were incubated at 37 °C and 5% CO_2 for 24 h.

5.3.6. Immunofluorescence

Embryonic hippocampal neurons cultured on the substrates were fixed with 4% paraformaldehyde (Sigma-Aldrich) and 4% sucrose (Sigma-Aldrich) in phosphate buffered saline (PBS) (*pH = 7.2*) for 20 min at room temperature. Fixed samples were permeabilized with 0.1% Triton X-100 (Fluka, St. Louis, MO, USA) and 3% goat serum (Sigma-Aldrich) in PBS buffer for 20 min, washed twice with PBS, and treated with a blocking solution of 3% goat serum in PBS for 1 h at 37 ºC. Tau-1, a microtubule protein expressed in axons, was labeled as an axonal marker. Mouse tau-1 antibody (Chemicon,

105

Temecula, CA, USA) was diluted to 1:200 in blocking solution, and added to the culture samples. After overnight incubation at 4 ºC, the samples were washed with PBS two times, treated with a secondary antibody solution of Alexa 488-labeled goat anti-rat IgG (Invitrogen) (1:200 dilution in blocking solution) at 4 ºC for 5 h, and rinsed in PBS for 5 min two times. Samples were stored at 4 ºC while awaiting further analysis.

5.3.7. Distance measurements based on immunofluorescence

Fluorescence images of cells and axons were acquired using a fluorescence microscope (IX-70, Olympus). The images were captured using a color CCD camera (Optronics MagnaFire, Goleta, CA, USA). Cell images were analyzed using Image J software (available from National Institute of Health website). Distance was routinely measured as the linear distance between the center of the cell body and the edge of the topography associated with the measurement. When several neurites branched from a single nerve cell, the longest neurite was used in the measurement. A neuron was considered to be polarized only when the axon was approximately two times longer than the characteristic diameter of the cell body (~ 15 µm).

5.3.8. Examination of topography and cells

Fixed hippocampal neurons were dehydrated by treating with ethanol in water at successively increasing concentrations; cells were treated at concentrations (v/v) of 30% for 45 min, 50% for 30 min, and 70%, 85%, 90%, 95%, and absolute ethanol (100%) (Pharmco, Brookfield, CT, USA) for 10 min each. Water was completely removed by adding hexamethyldisilazane (HMDS) (Sigma-Aldrich) and drying in air at ambient

conditions. The dried samples were coated with a thin 10-nm layer of platinum/palladium by sputter coating (208HR, Cressington Scientific Instruments, Watford, UK). SEM images were acquired with a Zeiss SUPRA 40 VP Scanning Electron Microscope (Carl Zeiss, Peabody, MA, USA). AFM images were taken to ensure precise dimensions of topography. AFM images were acquired with a Dimension 3100 with Nanoscope IV controller (Digital Instruments & Veeco Metrology Group, Santa Barbara, CA, USA) using a silicon tip in tapping-mode (Tap300, Budget Sensors, Sophia, Bulgaria).

5.3.9. Statistical analysis of experimental data

Cell count data was analyzed using a combination of balanced one-way analysis of variance (ANOVA) [16], one- and two-sample binomial t-tests [17, 18], and chi-squared (χ^2) tests [19]. A 50% probability distribution was assumed in calculating test statistics in the one-sample binomial and χ^2-tests. One-sample binomial t-tests were performed in lieu of χ^2-tests when sample sizes were small. In all other cases where data was compared with a 50% probability, only χ^2-tests were performed. Both the two-sample binomial t-tests and one-way ANOVAs were performed together to determine whether individual averages were statistically different; in most cases, results for the tests are presented together. *P*-values were interpolated from standard t- and χ^2-distribution tables using the observed test statistics. Averages were deemed statistically different if significant to greater than a 90% confidence level according to the *P*-value. Significance close to but less than a 90% confidence level was deemed mildly significant (e.g., *P*-

107

values ≈ 0.1 – 0.2). In cases where samples were not statistically significant, or in cases where typical statistical tests were deemed inappropriate, observations and trends were noted.

5.4. RESULTS AND DISCUSSION

5.4.1. Competitions between topography and the smooth surface

To conduct the competitions, structure arrays were patterned into a proprietary four-quadrant competition grid on quartz (Figure 5.1). Each quadrant consisted of an array of homogeneous structures separated by unpatterned rectangular regions of 20-µm width. Each competition scheme was defined as a competition between two juxtaposing topographies vying to sequester the axon of a polarized nerve cell. In this study, topographies included *(1)* holes with a 2-µm diameter with horizontal and vertical spacings of 1 µm, *(2)* lines of 2-µm width with a spacing of 1 µm, *(3)* holes with a 300-nm diameter with horizontal and vertical spacings of 1 µm, and *(4)* lines of 300-nm width with a spacing of 1 µm. Throughout the paper, we sometimes refer to the 300-nm structures as "sub-microscale", though structures having dimensions less than 1 µm are often called "nano" in bio-applications (as opposed to 100 nm).

To determine whether topography could promote axon formation and guidance directionality relative to unpatterned surface, individual embryonic hippocampal neurons were positioned at the outer fringes of the topographies. Neurons were micro-positioned close to the boundaries of each of the topographies (under 50 µm) and cultured for 24 hours. The neurons were then stained with anti-Tau-1 antibody and DAPI, and visualized by conventional optical and fluorescence microscopy. When a neuron extended and

108
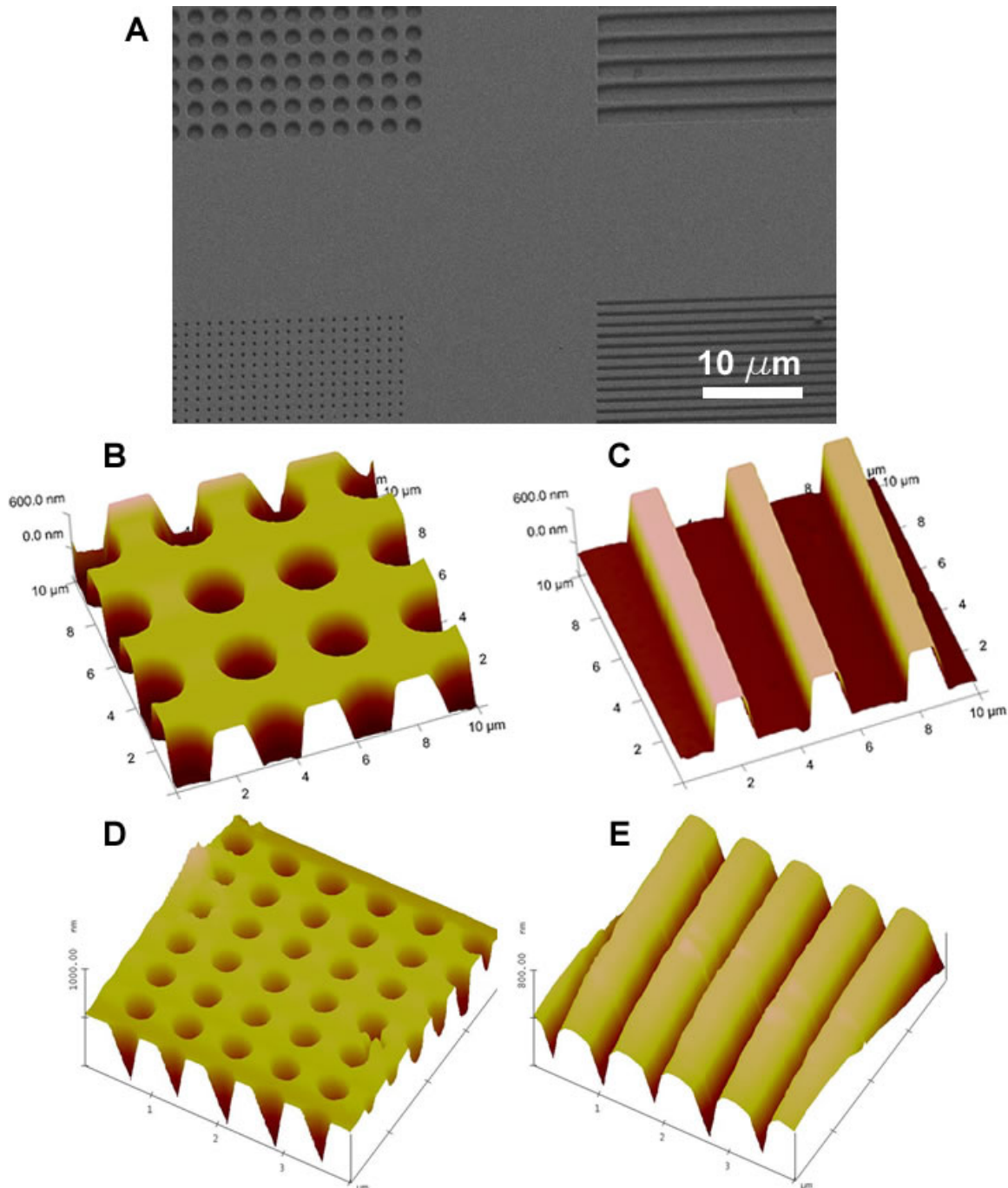
Figure 5.1. (A) 4-quadrant grid competition system. The grid competition system consists of four competition schemes, where each scheme is a competition between two topographies. The 4-quadrant system incorporates homogeneous arrays of (B) *(top left of 1A)* holes with a 2-μm diameter with horizontal and vertical spacings of 1 μm (3 μm pitch), (C) *(top right of 1A)* lines of 2-μm width with a spacing of 1 μm (3 μm pitch), (D) *(bottom left of 1A)* holes with a 300-nm diameter with horizontal and vertical spacings of 1 μm (1.3 μm pitch), and (E) *(bottom right of 1A)* lines of 300-nm width with a spacing of 1 μm (1.3 μm pitch). Structures all consisted of a depth of between 400-500 nm. The unpatterned regions between each scheme are 20-μm in width and are the areas where cells were positioned in the competition experiments.

109

established its axon onto a certain topography, the topography was considered to be preferred over the smooth surface. Multiple cells were positioned around each topography and statistical analysis (one-way analysis of variance (ANOVA) [16], one- and two-sample binomial t-test [17, 18], chi-squared (χ^2) test [19]) was used to determine whether results were significant. If statistical tests showed a preference for particular topographies, then those topographies were considered to influence axon polarization. Polarized cells were only analyzed when their axons were elongated enough to make contact with the neighboring topography. On the other hands, when an axon was sufficiently long, but did not touch topography, bare surface was regarded as a preferential substrate. Distance between the center of the cell body and the edge of the pattern was measured and reported as the "cellular distance". A distance of zero means that the center of the cell body of a neuron coincided with the pattern boundary.

Figure 5.2A depicts the results from the competitions for axon sequestration between smooth surface and topography based on feature shape, size, and boundary type. The solid grey and striped areas represent bare and patterned surface, respectively, and are divided by the vertical line, which represents the boundary between the two regions. Each point in the plot represents an individual cell where the horizontal distance between the point and the vertical line represents the distance between the center of the cell body and the boundary. Line-patterns were divided into two types, single-type and multiple-type, as growing neurons and axons can face grooves on a substrate in different ways (Figure 5.2B). The single-type (or perpendicular) boundary represented lines in which

110
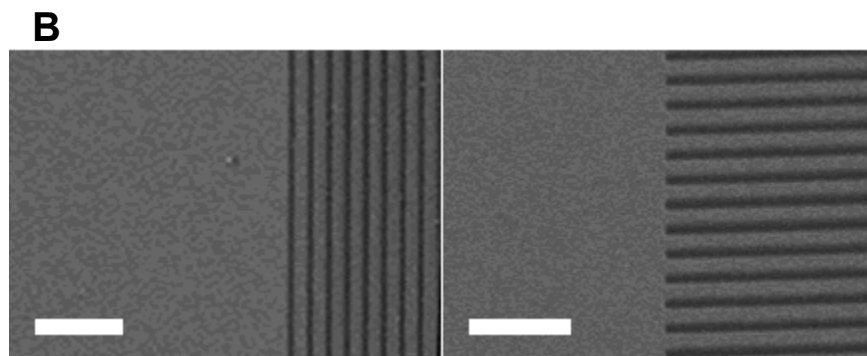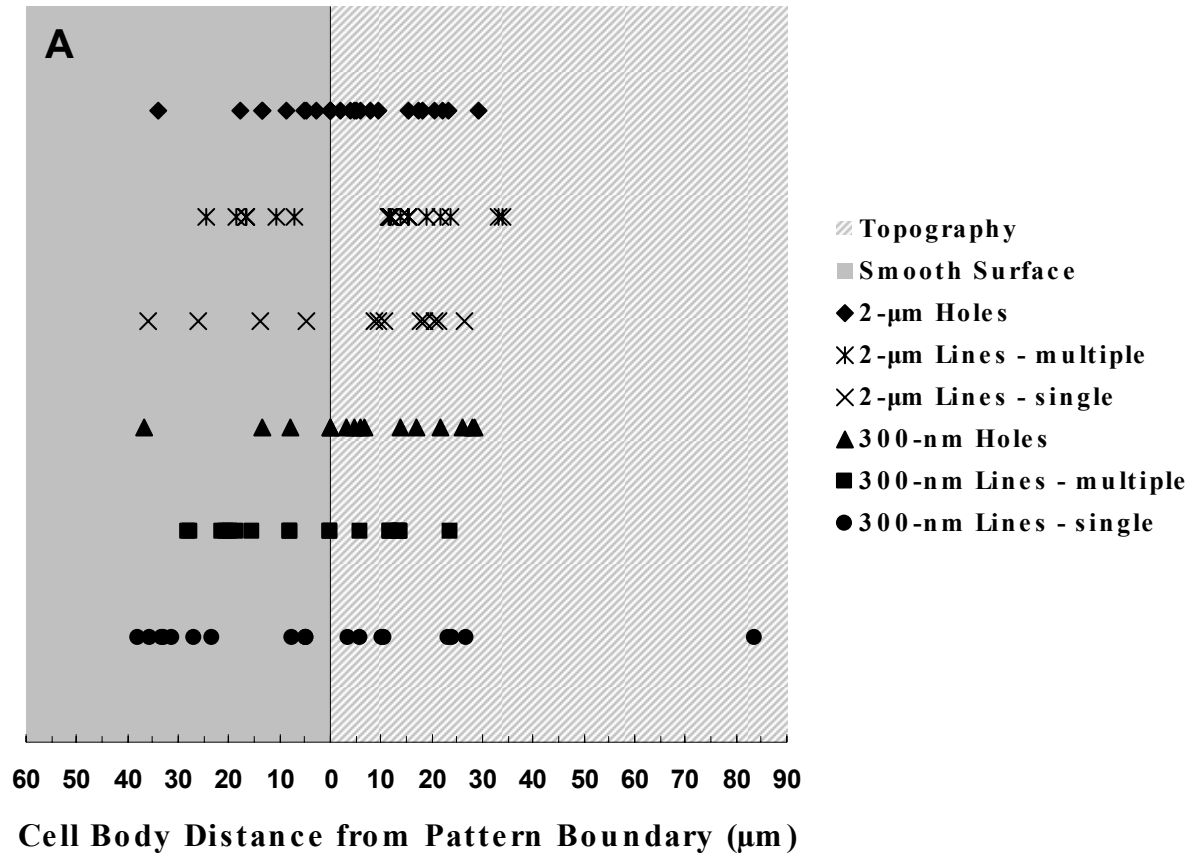
Figure 5.2. (A) Results from the competition experiments between topography and smooth surface. The solid grey and striped areas represent the bare and patterned surfaces, respectively. Each data point represents axon preference of an individual cell. The vertical line represents the boundary of the pattern and the horizontal distance between each point and the line represents the distance between the center of the cell body and the boundary. **(B)** Single- (Left) and multiple-type (Right) boundary of line topographies (300-nm lines shown). Scale bars = 5 µm. Sample sizes (n = no. of cells): 300-nm Lines – single, n = 19; 300-nm Lines – multiple, n = 18; 300-nm Holes, n = 15; 2-µm Lines – single, n = 12; 2-µm Lines – multiple, n = 18; 2-µm Holes, n = 27.

111

the boundary between the unpatterned and patterned region was created by a single line. The multiple-type (or parallel) boundary represented the other case where the boundary between the unpatterned and patterned region consisted of the ends of several lines. Therefore, four categories were studied for the lines, including single- and multiple-type for each size-scale.

We determined overall axonal preference to the topographies relative to the smooth surfaces based on distance regardless of feature shape, size, and boundary orientation (Figure 5.3). 55.3%, 65.7%, 68.0%, and 27.3% of neurons chose topography over smooth surface for distances between 0-10, 10-20, and 20-30, and >30 μm, respectively. Preference in every range under 30 μm was statistically significant relative to preference at a distance greater than 30 μm. Relative to a 50% probability distribution, where cells equally prefer topography and smooth surface (i.e., no preferential axon growth), preference was different than 50% in the ranges of 10-20 and 20-30 μm but not within the range of 0-10 μm. These results suggest that a distance of around 30 μm served as a limit over which the topographies became less influential as a stimuli enhancing cell response and as a minimal distance for growing neurites and axons to sense and respond to topography. In particular, neurons growing close to surface features (< 30 μm) appeared to enable an immature neurite, near or on topography, to become an axon. An axon develops from one of the multiple neurites found on an immature neuron (stages 2 and 3). Selection of a neurite to form into axon is considered random; however, external cues such as topography may provide an inductive signal to a specific neurite on or close to the topography coercing it to form into an axon and elongate.
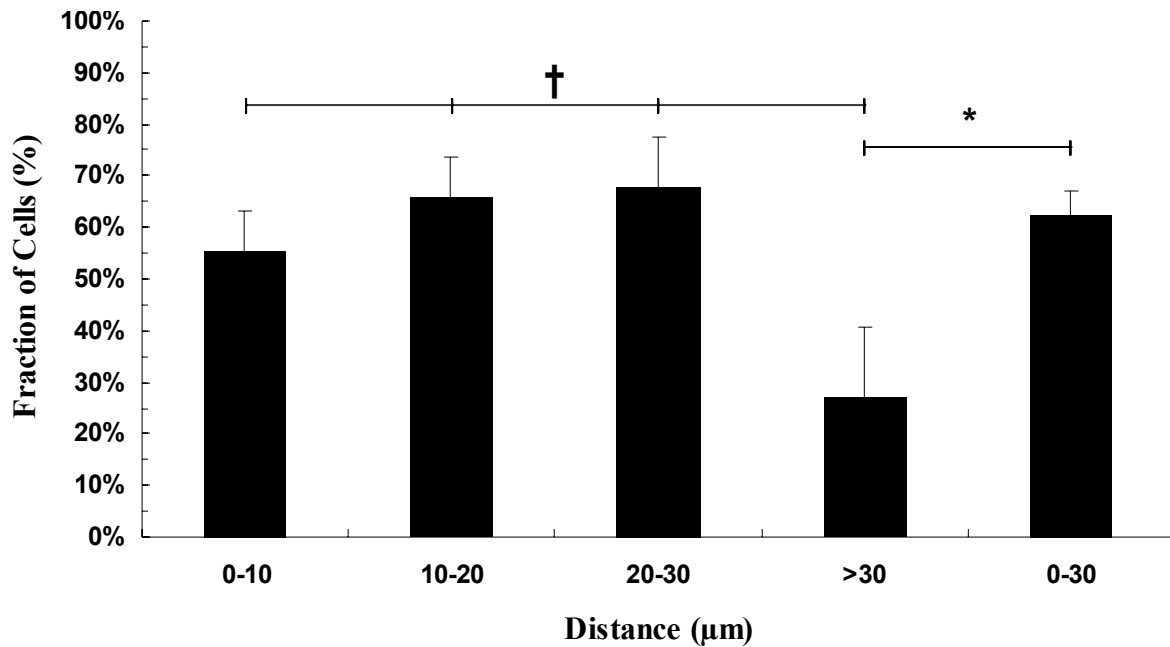
Figure 5.3. Fraction of cells (%) choosing topography over smooth surface based on the distance measured from the center of the cell body to the topography boundary (using the shown data of Figure 5.2). Scale bars = sem; distance units = μm. One-way ANOVA and two-sample binomial _t_-tests were used to compare the data for statistical significance. χ^2-tests were conducted to determine whether preference was statistically different than a 50% probability choice. _P_-values are indicated for each competition. *0-30 vs. >30: _P_ < 0.05 (ANOVA and binomial); χ^2-tests: 0-30, _P_ < 0.05, >30, not significant. †Preferences in the 0-10, 10-20, and 20-30 ranges were not significant relative to one another, but each range <30 was statistically different than >30 (_P_ ≤ 0.10, ANOVA and binomial); χ^2-tests: 0-10, not significant, 10-20, _P_ = 0.0669, 20-30, _P_ = 0.0765. Sample sizes (_n_ = no. of cells): 0-10, _n_ = 38; 10-20, _n_ = 35; 20-30, _n_ =25; 0-30, _n_ = 98; >30, _n_ = 11.

Overall, preference for topography over smooth surface for neurons at distances

under 30 μm was found to statistically vary from a 50% probability distribution. Based

on this observation that the critical distance from a neuron to topography was close to 30

μm, we analyzed the preference data for each of the topographies for neurons positioned

at distances under 30 μm (using two-sample binomial _t_-tests) (Figure 5.4). The portion

of neurons extending axons to topography was 57.5% and 85.7%, for the 2-μm holes and

the 300-nm holes, respectively. For the 300-nm lines, 53.8% and 50.0% of neurons

113

chose the 300-nm lines of single-type and multiple-type boundaries over smooth surface, respectively. 72.7% and 62.5% of neurons extended axons to the 2-μm lines of single-type and multiple-type boundaries, respectively.

According to χ^2-tests and one-sample binomial t-tests (50% reference), only the preference for the 300-nm holes was statistically significant relative to a 50% probability
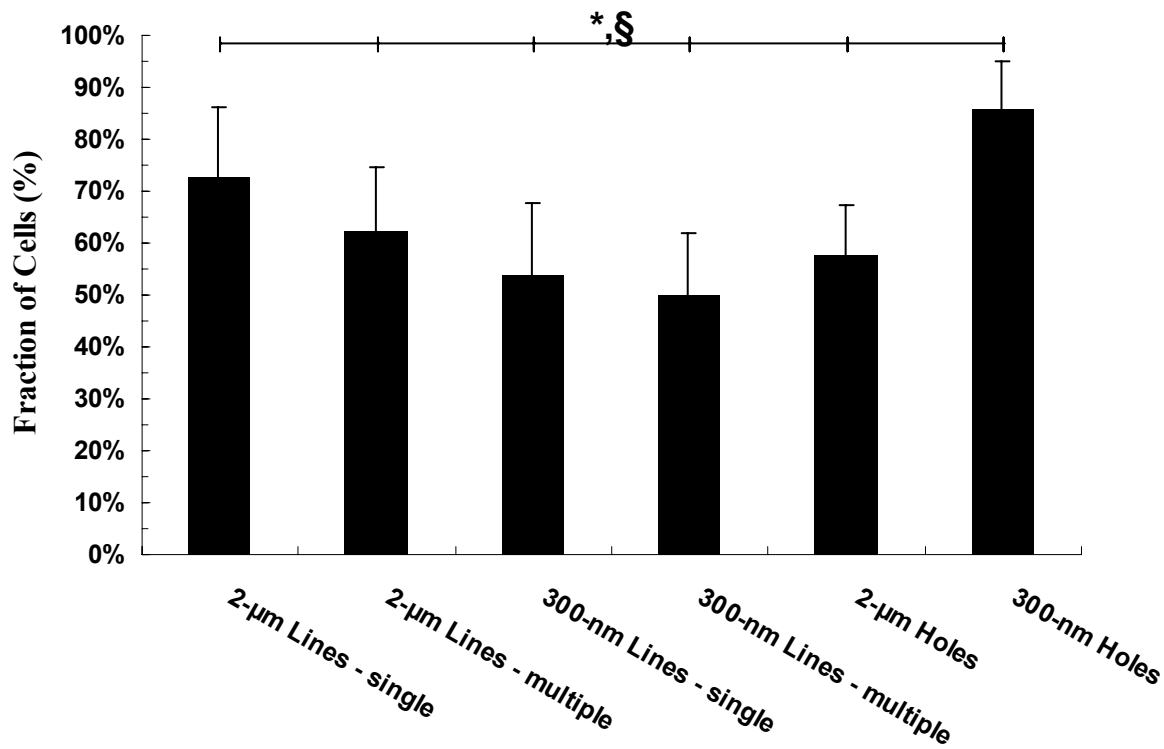
Figure 5.4. Fraction of cells choosing topography (%) based on feature size, shape, and boundary type (single- and multiple-type for line topographies) for distances less than 30 μm. Distance was measured as the length between the center of the cell body to the topography boundary. Scale bars = sem. Two-sample binomial *t*-tests were used to compare the data for statistical significance. χ^2-tests were conducted to determine whether preference was statistically different than a 50% probability distribution. Preference for the 300-nm holes was found to be statistically significant relative to preference on the other topographies; moreover, preferences for all the other topographies were not statistically different relative to one another. *300-nm Holes vs. all other topographies, P < 0.10. §χ^2-tests: 300-nm Holes, *P* < 0.05; preference for all the other topographies did not statistically differ from a 50% probability distribution. Sample sizes (*n* = no. of cells): 2-μm Lines – single, *n* = 11; 2-μm Lines - multiple, *n* = 16; 300-nm Lines – single, *n* = 13; 300-nm Lines – multiple, *n* = 18; 2-μm Holes, *n* = 26; 300-nm Holes, *n* = 14.

114

distribution. Moreover, preference for the 300-nm holes was significant relative to every topography except the 2-μm lines of both boundary-types. Preference numbers between the other topographies did not statistically vary. Overall, the sub-microscale holes were the only features that attracted axon growth considering our sample sizes. Figure 5.5. shows images of cells in competitions between the topographies and smooth surfaces.
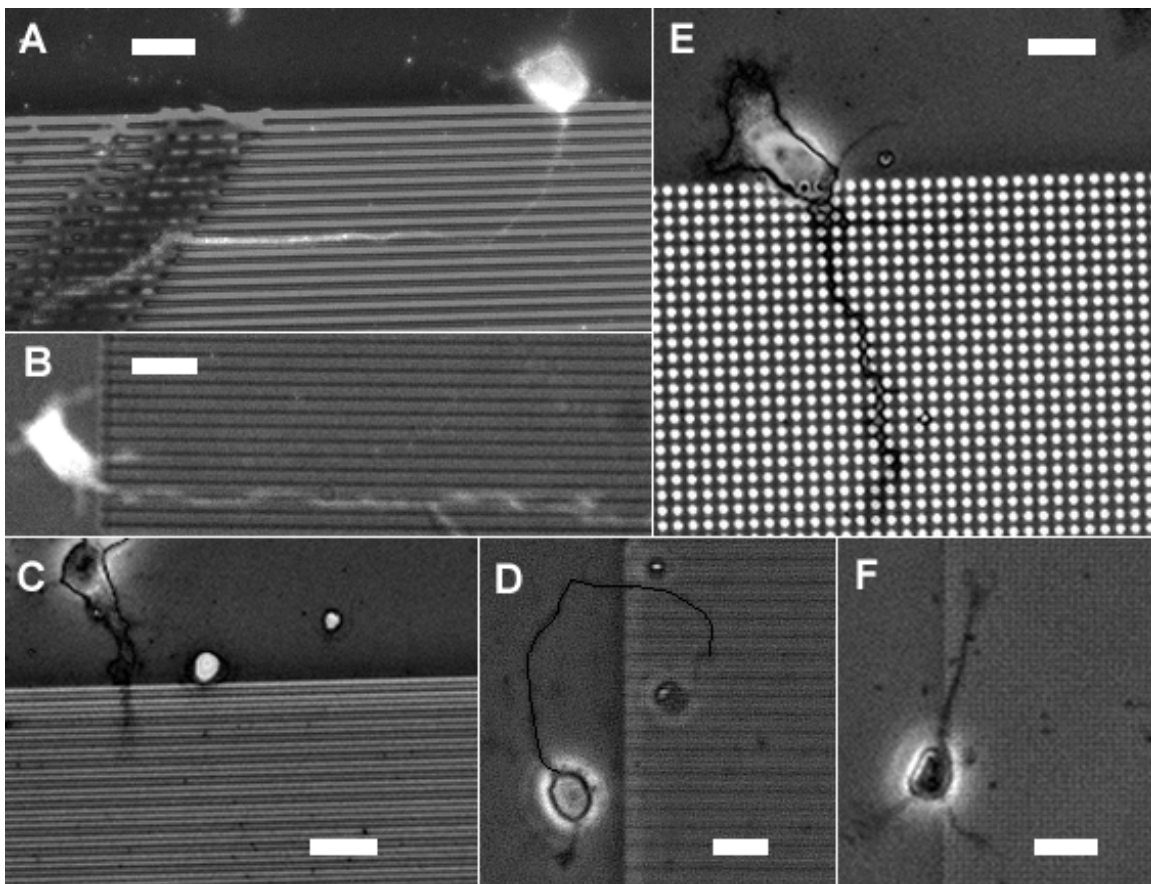
Figure 5.5. Optical images (in some cases labeled with Tau-1 and DAPI) of neurons micropositioned on the outer borders of the topographies in the four-quadrant grid. The images illustrate competitions between bare surface and the (A) 2-μm Lines – single, (B) 2-μm Lines – multiple, (C) 300-nm Lines – single, (D) 300-nm Lines – multiple, (E) 2-μm Holes, and (F) 300-nm Holes. The images show axons established on the topographies. Scale bars = 10 μm. Lines of single-type and multiple-type borders are shown in (A,C) and (B,D), respectively. (Image D has a curve superimposed on the axon to improve visibility)

115

5.4.2 Competitions between topographies

After performing competitions between topography and smooth surface, competition studies were performed between topographies to further evaluate axon preference based on feature size, shape, and boundary type. Individual hippocampal neurons were micropositioned in the unpatterned regions between neighboring topographies and cultured for 24 hours as described in the *experimental* section. For each micropositioned neuron, the pattern drawing the axon to it was counted as the preferred topography (i.e., winner of the competition) (Figure 5.6). Figure 5.7 shows representative images of neurons cultured between two different topographies undergoing competitions.
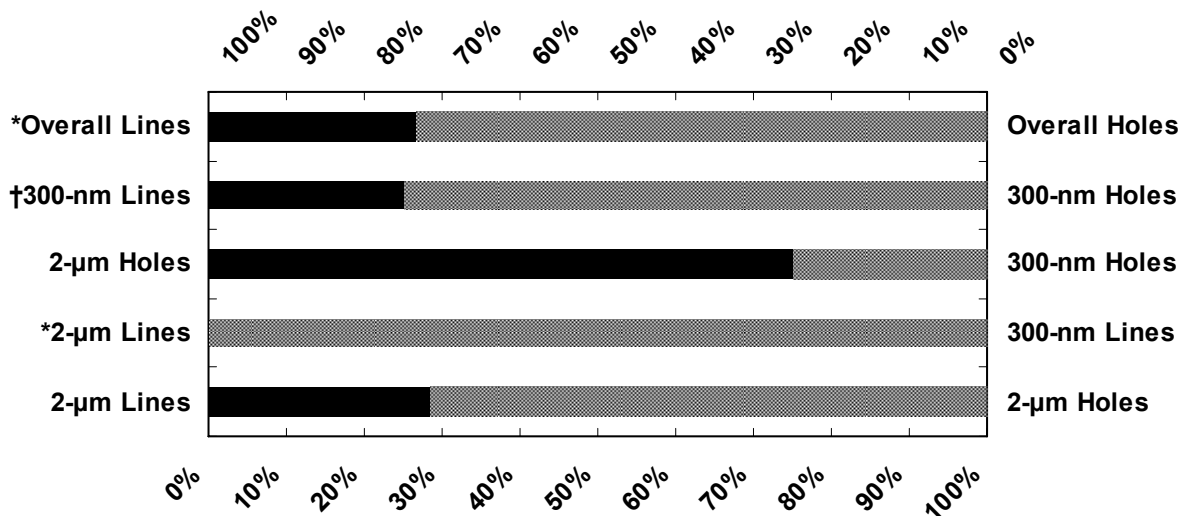
Figure 5.6. Results of the competitions between topographies. The black and dotted bars represent the percentage of cells choosing the topographies on the left and right vertical axes, respectively. One-sample binomial *t*-tests were conducted to determine whether preference was statistically different than a 50% probability distribution. *P < 0.10, †P < 0.15. Sample sizes (*n* = no. of cells): 2-µm Lines vs. 2-µm Holes, *n* = 7; 2-µm Lines vs. 300-nm Lines, *n* = 6; 2-µm Holes vs. 300-nm Holes, *n* = 4; 300-nm Lines vs. 300-nm Holes, *n* = 8; Overall Lines vs. Overall Holes, *n* =15.

116

To investigate preference based on feature size, we compared the 2-μm lines with the 300-nm lines and the 2-μm holes with the 300-nm holes. 100% of neurons extended their axons onto the 300-nm lines rather than the 2-μm lines. 75% of neurons extended their axons onto the 2-μm holes rather than the 300-nm holes. Only preference for the 300-nm lines was significant with respect to our sample sizes, i.e., neurons preferred the 300-nm lines over the 2-μm lines. The data for the lines is in line with results published by Gomez et al. [15] who found that axons preferred smaller lines of 1-μm width over larger lines of 2-μm width. It has been suggested that preference for
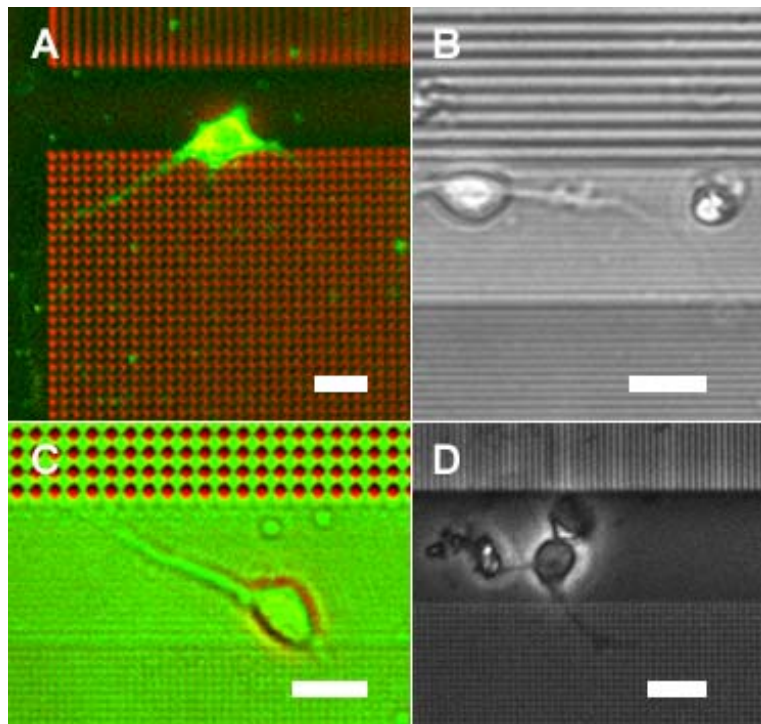
Figure 5.7. Optical images (in some cases labeled with Tau-1 and DAPI) of neurons micropositioned in unpatterned spaces (20-μm wide) between topographies in the four-quadrant grid. The images illustrate competitions between (A) 2-μm Lines and 2-μm Holes, (B) 2-μm Lines and 300-nm Lines, (C) 2-μm Holes and 300-nm Holes, and (D) 300-nm Lines and 300-nm holes. The images show axons establishing themselves on one of the topographies per competition. Scale bars = 10 μm. (Color has been added to images A,C to improve visibility)

117

smaller lines, of 1-μm width or less, may be due to the fact that the particular size-scale mimics the sizes characteristic of neurite fibers found in peripheral nerves *in vivo* [20].

Competitions were studied between holes and lines of similar dimension to determine preference based on feature shape (2-μm holes vs. 2-μm lines and 300-nm holes vs. 300-nm lines). In these cases, lines had the multiple-type boundaries. 71.4% of neurons chose the 2-μm holes over the 2-μm lines, though the result was not statistically significant based on our limited sample size. Also, 75% of neurons chose the 300-nm holes over the 300-nm lines to an 85% confidence ($P = 0.1445$). In compiling the data for the assays comparing morphology, i.e., overall lines versus holes, 73.3% of cells chose holes over lines ($P = 0.0616$), which indicates that neurons appeared to preferentially establish their axons on holes relative to lines. These results appear to be related to our previous findings that axon formation occurred more frequently on holes than lines [21].

Results obtained from the competitions directly comparing the topographies (topography vs. topography) showed different *trends* (not necessarily statistical) than the competitions comparing the topographies with the smooth surfaces. The portions of neurons extending axons to the 300-nm holes (85.7%) over smooth surface was more than those to 2-μm holes (57.5%); however, when neurons were exposed to both the 300-nm holes and 2-μm holes at the same time, neurons chose the 2-μm holes for axonal extension (though the results were not confirmed by statistical measures). Also, the 300-nm lines were preferred over the 2-μm lines in direct comparison, although the 300-nm lines appeared less attractive to the neurons than the 2-μm lines in the competition between topography and the smooth surface.

118

5.5. CONCLUSIONS

In conclusion, competition assays were performed to determine the ability of topography to entice axon formation based on feature size and shape. We designed a four-quadrant topography grid consisting of arrays of holes and lines of 2-μm and 300-nm critical dimension. Single neurons were micro-positioned in gaps between neighboring topographies or at the border of individual topographies juxtaposing unpatterned surface area, and axon preference was determined after a 24-hour culture. We found that small-scale features patterned on biomaterial surfaces appeared to alter the properties of the surface and neuronal recognition, which subsequently induced favorable cellular responses relative to the normal responses observed on smooth surface.

5.6. ACKNOWLEDGEMENTS

5.7. REFERENCES

1.   Fozdar D. Y., Lee J. Y., Schmidt C. E., Chen S., Response of neurons to competing topographical features of various sizes and shapes, *Nano Letters*, 2009; **(submitted)** pp.

2.   Mattson M. P., Establishment and plasticity of neuronal polarity, *Journal of Neuroscience Research*, 1999; **57** pp. 577-589.

3.   Lazic S. E., Barker R. A., The future of cell-based transplantation therapies for neurodegenerative disorders, *Journal of Hematotherapy & Stem Cell Research*, 2003; **12** pp. 635-642.

4.   Schmidt C. E., Leach J. B., Neural tissue engineering: Strategies for repair and regeneration, *Annual Review of Biomedical Engineering*, 2003; **5** pp. 293-347.

5.   Brittis P. A., Canning D. R., Silver J., Chondroitin Sulfate as a Regulator of Neuronal Patterning in the Retina, *Science*, 1992; **255** pp. 733-736.

6.   Liu C. Y., Westerlund U., Svensson M., Moe M. C., Varghese M., Berg-Johnsen J., et al., Artificial niches for human adult neural stem cells: Possibility for autologous transplantation therapy, *Journal of Hematotherapy & Stem Cell Research*, 2003; **12** pp. 689-699.

7.   Stenger D. A., Hickman J. J., Bateman K. E., Ravenscroft M. S., Ma W., Pancrazio J. J., et al., Microlithographic determination of axonal/dendritic polarity in cultured hippocampal neurons, *Journal of Neuroscience Methods*, 1998; **82** pp. 167-173.

8.   Curtis A., Wilkinson C., Topographical control of cells, *Biomaterials*, 1997; **18** pp. 1573-1583.

9.   Dalby M. J., Riehle M. O., Yarwood S. J., Wilkinson C. D. W., Curtis A. S. G., Nucleus alignment and cell signaling in fibroblasts: response to a micro-grooved topography, *Experimental Cell Research*, 2003; **284** pp. 274-282.

10.   Dalby M. J., Topographically induced direct cell mechanotransduction, *Medical Engineering & Physics*, 2005; **27** pp. 730-742.

11.   Teixeira A. I., Abrams G. A., Bertics P. J., Murphy C. J., Nealey P. F., Epithelial contact guidance on well-defined micro- and nanostructured substrates, *Journal of Cell Science*, 2003; **116** pp. 1881-1892.

12.   Teixeira A. I., Abrams G. A., Murphy C. J., Nealey P. F., Cell behavior on lithographically defined nanostructured substrates, *Journal of Vacuum Science & Technology B*, 2003; **21** pp. 683-687.

13.   Rajnicek A. M., Britland S., McCaig C. D., Contact guidance of CNS neurites on grooved quartz: influence of groove dimensions, neuronal age and cell type, *Journal of Cell Science*, 1997; **110** pp. 2905-2913.

14.   Rajnicek A. M., McCaig C. D., Guidance of CNS growth cones by substratum grooves and ridges: effects of inhibitors of the cytoskeleton, calcium channels and signal transduction pathways, *Journal of Cell Science*, 1997; **110** pp. 2915-2924.

15.   Gomez N., Chen S. C., Schmidt C. E., Polarization of hippocampal neurons with competitive surface stimuli: contact guidance cues are preferred over chemical ligands, *Journal of the Royal Society Interface*, 2007; **4** pp. 223-233.

16.   Christensen R., One-way analysis of variance. In *Analysis of Variance, Design and Regression*, Chapman & Hall, Great Britian, 1996, pp. 114-123.

17.   Christensen R., One binomial sample. In *Analysis of Variance, Design and Regression*, Chapman & Hall, Great Britian, 1996, pp. 227-230.

18.   Christensen R., Two independent binomial samples. In *Analysis of Variance, Design and Regression*, Chapman & Hall, Great Britian, 1996, pp. 231-233.

19.   Christensen R., One multinomial sample. In *Analysis of Variance, Design and Regression*, Chapman & Hall, Great Britian, 1996, pp. 233-235.

20.   Nagata I., Kawana A., Nakatsuji N., Perpendicular Contact Guidance of CNS Neuroblasts on Artificial Microstructures, *Development*, 1993; **117** pp. 401-408.

21.   Fozdar D. Y., Lee J. Y., Schmidt C. E., Chen S., Neurons respond uniquely to topographies of various sizes and shapes, *Biomaterials*, 2009; **(submitted)** pp.

Chapter 6: Flash Imprint Lithography Using a Mask Aligner (FILM): a Method for Printing Nanostructures in Photosensitive Hydrogels[1]

6.1. ABSTRACT

Here, a general method for imprinting nanometer-scale features in low-viscosity photosensitive hydrogels using conventional optical mask aligner technology is described. We coin this proprietary method Flash Imprint Lithography using a Mask Aligner (FILM). The FILM process makes it possible to fabricate nanometer-scale features in ultraviolet (UV)-curable hydrogels – quickly, inexpensively, and reproducibly. We believe that the FILM process will be useful in many areas of research but is particularly applicable to tissue engineering. Accordingly, we demonstrate the FILM process by imprinting dense arrays of nanostructures in polyethylene glycol dimethacrylate (PEG-DMA), a material commonly utilized as a substrate in micro- and nanoscale tissue scaffolds; finite element modeling and contact angle analysis are employed to characterize pattern transfer of low-viscosity polymers (e.g., PEGDMA) in the FILM process.

Keywords: Nanopatterning, Nanoimprint Lithography, Mask-Aligner, Polyethylene Glycol, Surface Topography

---

[1] Published in [1].

6.2. INTRODUCTION

Optical lithography is the most widely-utilized process for manufacturing integrated circuits, MEMS and microfluidic devices, and related technologies. Optical lithography prints microscale features in optically-sensitive polymers accurately, precisely, and in high-throughput. A few groups have reported using optical lithography to pattern microscale features in UV-curable PEG hydrogels using conventional photomasks [2, 3]. Unfortunately, because of the desire to pattern nanoscale features in many new applications, particularly in advanced tissue scaffold fabrication, optical lithography is insufficient because of its inability to transfer geometrical information beyond the diffraction limit. While efforts are being made to try to circumvent this limit, it is important to note that solutions to the diffraction-problem have to be amenable to the reproducible and high-throughput requirements inextricably linked to industrial manufacturing and many applications in research. Other widely-utilized nanofabrication technologies, like focused-ion-beam writing (FIB) and electron-beam lithography (EBL), have been able to directly write features down to a few nanometers; however, these serial direct-write techniques are too time-consuming for production at even moderate scales. The future of nanoscale-based engineering will depend largely on the development of innovative nanofabrication processes and technologies that can, accurately and precisely, produce nanometer-scale features with reasonably high throughput.

One such innovative fabrication process, nanoimprint lithography (NIL), introduced by Chou et al. [4], is the process of embossing features from a mechanically hard mold into thermoplastic materials heated above their glass transition temperature. Chou et al. [4] were able to imprint 25 nm holes from a silicon mold into polymethylmethacryate (PMMA). The silicon mold was patterned using

123

EBL and etched using reactive-ion-etching (RIE). A more recently demonstrated process, step-and-flash imprint lithography (S-FIL), introduced by Colburn et al. [5], is the process of imprinting the features of a transparent mold (e.g. quartz) into a photosensitive polymer. The polymer is a low-viscosity liquid that cures upon exposure to ultraviolet (UV) light emanating through the mold. The S-FIL process utilizes a transfer material layer and the nanopatterned UV-curable polymer as etch barriers for the ultimate patterning of the substrate (e.g., silicon) by RIE [5]. The enabling step-and-flash process opened the door to a new genre of imprinting techniques by adapting conventional NIL to use with UV-curable polymers rather than just thermoplastic materials.

Although the S-FIL process has been developed markedly since its inception and, indeed, is a very promising technology, it requires the use of unconventional dedicated nanoimprinting tools (e.g. IMPRIO 55, 100, and 250 by Molecular Imprints, Austin, TX). Such dedicated imprinting tools are typically unavailable in most cleanrooms and require extremely costly imprinting templates and ad hoc drop dispensers to support different UV-curable materials. Other promising variations of UV-based imprinting, like UV Nanoimprint Lithography (UV-NIL), have been demonstrated; however, they either continue to utilize specialized nanoimprinting tools like the S-FIL process or are alternatives that lack the control and automation intrinsic to using nanoimprinting tools [6, 7]. Scheerlinck et al. [8] printed an array of circular pillar structures of approximately 200-300 nm in diameter into a special photoresist using photolithographic equipment; however, their process required the manual removal of the imprint mold, utilized a photoresist not commonly used in tissue engineering applications, did not address critical issues such as mold and substrate surface treatment for optimizing pattern transfer, and did not address issues

124

concerning the filling of features with critical dimension down to around 50 nm where aspect ratios are usually very high. Moreover, torsional forces imparted by manually removing an imprint mold can severely damage nanoscale features patterned in brittle polymers like PEG-based hydrogels. Stuart et al. [9] constructed modules out of 6061-T6 aluminum to outfit conventional mask aligners for automated UV-NIL; however, despite being useful add-ons to conventional mask aligners, their proprietary modules are quite complex. For the quick, reproducible, and completely automated imprinting of nanoscale features into various homemade UV-curable materials, like PEG hydrogels, directly required by many research applications, dedicated nanoimprinting tools or proprietary add-ons to conventional mask aligners are not always necessary; this is especially the case in single-layer fabrication processes where alignment is not crucial.

PEG hydrogels like PEG-diacrylate (PEG-DA) and PEG-dimethacrylate (PEG-DMA) are polymers widely-utilized as substrates in tissue scaffolds for cell-seeding applications. In particular, PEGDA and PEGDMA are ideal substrate materials for adipose and nervous tissue scaffolds used for adipose and nerve cell-studies and tissue restoration for correcting deformities resulting from tumor resections, physical trauma, congenital abnormalities, aging, and other medical conditions; they are nonallergenic, nonpyrogenic, look and feel natural, stable after implantation or injection, and relatively inexpensive [10, 11]. A significant challenge in fabricating adipose and nervous tissue scaffolds in PEGDA and PEGDMA, is having the ability to control the scaffold's physical topography at the nanoscale to closely resemble the topology of the extracellular matrix (ECM) of adipose and nerve cells.

125

In this work, we report a novel nanoimprinting method, called Flash Imprint Lithography Using a Mask Aligner (FILM), capable of imprinting nanoscale features – quickly, inexpensively, and reproducibly – into UV-curable materials using a conventional optical mask aligner without any proprietary add-ons, expensive quartz templates, ad hoc material dispensers, or dedicated imprinting tools while having the control, accuracy, reproducibility, and complete automation of dedicated imprinting technologies. We demonstrate FILM by imprinting a portfolio of nanostructures in PEG-dimethacrylate (PEGDMA), a commonly used material in tissue scaffolds, down to a resolution of 50 nm using an optical aligner from SUSS Microtech (SUSS MA-6, SUSS Microtech, Munich, Germany).

6.3. MATERIALS AND METHODS

6.3.1. Synthesis of PEGDMA biomaterial

PEGDMA prepolymer of MW = 1000 (Polysciences Inc., Warrington, PA, USA, No. 25852-47-5) was dissolved in HPLC-grade demineralized water (Fisher Chemical, Fairlawn, NJ, USA, No. 7732-18-5) to a concentration of 100% (w/v). Irgacure 2959 photoiniator (Ciba Specialty Chemicals, Tarrytown, NY, USA) was added to the PEGDMA/water mixture to a concentration of 0.1% (w/v) relative to the volume of water used (e.g., 0.001 g of Irgacure pure 1 mL of water). The PEGDMA was centrifuged for 30 minutes and refrigerated overnight to allow the mixture to stabilize.

6.3.2. Fabrication of silicon molds

Silicon wafers (NOVA Electronic Materials, Richardson, TX, USA) were diced into 20mm x 20 mm pieces. The silicon pieces were ashed in an O_2-plasma

126

asher (March CS-1701, March Plasma Systems, Concord, CA, USA) to burn off organic contaminants, cleaned in a mixture of 30% H_2O_2 (v/v) in H_2SO_4 (piranha solution) (Hydrogen Peroxide 30% - No. 2190, Sulfuric Acid 96% - No. 9684, J.T. Baker, Phillipsburg, NJ, USA) for 8 minutes, and washed thoroughly in DI water. The wafer pieces were dried thoroughly with N_2 and then dehydration-baked at 200 °C for 5 min on a hot plate to remove all residual moisture. A 20-nm silicon dioxide layer was deposited on the clean silicon using plasma-enhanced chemical vapor depositon (PECVD) (Plasma-Therm 790, Plasma-Therm, Inc., St. Petersburg, FL, USA). ZEP-520A (Zeon Chemicals, Louisville, KY, USA) positive electronic resist was thinned in Anisole to a 1:3 ratio (v/v), respectively; ZEP-520A EBL resist was chosen due to its high resolution and dry-etch resistance. The resist was deposited on the molds by spin-coating at 4000 rpm for 60 sec to a thickness of approximately 100 nm and then soft-baked at 180 °C for 90 sec. The resist was patterned using EBL (JEOL 6000 FSE, JEOL Ltd., Tokyo, Japan; Raith 50, Raith GmbH, Dortmund, Germany) and developed in ZED-N50 solution (Zeon Chemicals, Louisville, KY, USA). The patterned samples were descummed in an O_2-plasma to remove residual resist in the developed regions of the resist. Exposed silicon dioxide was etched through by RIE (Plasma-Therm 790, Plasma-Therm, Inc., St. Petersburg, FL, USA) using the resist as a mask. The resist was subsequently stripped in 30% H_2O_2 (v/v) in H_2SO_4. The exposed underlying silicon was etched with RIE using the patterned silicon dioxide layer as a mask. The silicon dioxide layer was then removed in buffered oxide etchant (BOE) leaving the patterned silicon.

www.manaraa.com

6.3.3. Chemical pretreatment of silicon molds

Silicon molds were chemically treated with Tridecafluoro-1,1,2,2-Tetrahydrooctyl-1 Trichlorosilane (United Chemical Technologies, Inc., Bristol, PA, USA, No. T2492). The silicon molds were ashed in an O_2-plasma asher to burn of organic contaminants and then immersed in a mixture of 30% H_2O_2 (v/v) in H_2SO_4 for 10 minutes, washed thoroughly in DI water, dried thoroughly with N_2, and dehydration-baked at 200 °C for 5 min on a hot plate. The clean silicon molds were then placed in a small container in juxtapose to a small vial containing a few drops of the fluorinated-silane. The container was then covered and stored in a dehumidified nitrogen environment to prevent any reactions between the fluorinated-silane and ambient moisture. After 4 hours, the silicon molds were removed and washed with a mixture of 25% carbon tetrachloride (v/v) in heptane and sequentially sonicated in acetone, methanol, and isopropyl alcohol (IPA) (Acetone Certified ACS, methanol Certified ACS, 2-Propanol Certified ACS, Fisher Chemical, Fairlawn, NJ, USA) for 5 min each. In between imprints using the mask aligner, residual photopolymerized PEGDMA was removed from the silicon molds by sequential immersion in acetone, methanol, and IPA for 1 min each. After being chemically treated with the fluorinated-silane, the silicon molds were dried after each rinse with N_2 but never baked in an effort to preserve the silane layer.

6.3.4. Chemical pretreatment of glass microscope slides

Glass microscope slides were immersed in a mixture of 30% H_2O_2 (v/v) in H_2SO_4 for 10 minutes, washed thoroughly in DI water, dried thoroughly with N_2, and immersed in a 1 mM solution of 3-trichlorosilyl propyl methacrylate (TPM) in a mixture of 25% carbon tetrachloride (v/v) in heptane for 5 minutes. The piranha

solution is a strong oxidizer that cleaned and hydroxylated the microscope slides; the silane attached to the hydroxyl groups (-OH) on the surface of the glass. Since TPM is highly reactive towards water, the microscope slides were meticulously dried before immersion in the silane solution. Because it was extremely difficult to remove all the residual moisture on the microscope slides using N_2 alone, the microscope slides typically formed a powdery-like surface when in contact with the silane solution. The powdery residue formed when the silane reacted with the residual moisture on the microscope slides that was not removed by the N_2. Moreover, unless the silane solution was kept in a dehumidified environment, moisture from the air often caused large particles to form in the silane solution that attached to the microscope slides. To limit the amount of powdery-like residue that formed and attached to the surface of the glass microscope slides, the silane mixture was stirred for the 5-minute duration in which the microscope slides were immersed. Upon removing the microscope slides from the silane mixture, the silanized slides were copiously rinsed with a TPM-free mixture of 25% carbon tetrachloride (v/v) in heptane and then with 1X phosphate buffered saline (PBS). After rinsing, the microscope slides were dried with N_2 and stored in a vacuum dessicator. Carbon tetrachloride served to degrease superfluous silane that did not covalently bond to the silicon surface and remove particulate matter; excess silane was nearly impossible to remove with standard organic solvents like acetone, methanol, and IPA. Pretreated glass slides were dried with N_2 after rinsing but were not dehydration-baked. Baking tended to degrade the tethered methacrylate groups on the glass slides which reduced PEGDMA adhesion.

6.3.5. Examination of PEGDMA topography

Topological features imprinted in PEGDMA were examined using a field-emission scanning-electron microscope (FESEM) (LEO 1530, Carl Zeiss SMT Inc., Peabody, MA, USA) and atomic-force microscope (AFM) (Dimension 3100 with Nanoscope IV controller, Digital Instruments & Veeco Metrology Group, Santa Barbara, CA, USA). AFM images were taken using a silicon tip in tapping-mode (Tap300, Budget Sensors, Sophia, Bulgaria).

6.3.6. Examination of contact angles

Contact angle measurements were taken using a goniometer (FTÅ200, First Ten Angstroms, Inc., Portsmouth, VA, USA). Substrates were placed onto a manually-adjustable sample stage and oriented appropriately; camera lighting, brightness, and contrast were optimized. Small droplets of DI water were electronically dispensed onto the substrates using a syringe pump controlled by computer. Each image was taken a few seconds after a droplet was dispensed. Twelve data points were taken for each measurement to verify accuracy and precision of contact angle data; measurements are reported as mean values with a corresponding standard deviation (SD). The baseline of the droplets was determined using a reflection image produced when the substrates were slightly tilted. The curvature of the droplets were traced using a non-spherical fit model. Information regarding contact angle measurements can be found in the references [12-16].

130

6.4. RESULTS AND DISCUSSION I: EXPERIMENTAL

6.4.1. Imprinting of nanostructures into UV-curable hydrogels

Details of the FILM process are illustrated in Figure 6.1. Figure 6.2 shows images taken by a field-emission scanning electron microscope (FESEM) of arrays of nanostructures of various geometry imprinted into PEGDMA. Figure 6.3 shows images taken by an atomic force microscope (AFM) illustrating the three-dimensional profiles of the nanostructures shown in Figure 6.3.

6.4.1.1. Preparation step (Figure 6.1a). UV-curable PEGDMA was synthesized by the procedure outlined in the materials and methods section. Silicon molds were fabricated using EBL and RIE; complete details of this procedure are also outlined in the materials and methods section. A 2 μL droplet of PEGDMA was deposited on the patterned area of a silicon mold by pipette. The volume of the droplet did not affect pattern transfer; however, droplets of superfluous size resulted in the formation of excessive edge-bead around the edges of the imprinted region.

6.4.1.2. Vacuum step (Figure 6.1b). The silicon mold with the dispensed droplet was put into a container with a flat surface in a vacuum desiccator at room temperature and a pressure of 0.1 Torr. The mold was typically kept under vacuum for 10 min. We found that putting the mold in vacuum was imperative to the consistent transfer of sub-micron patterns where aspect ratios were high; if the mold was not put in vacuum, then very inconsistent high aspect ratio pattern transfer was observed. When imprinting microscale features where aspect ratios were low, the mold did not need to be put in vacuum. Keeping the mold under vacuum too long (>45 min) usually caused the PEGDMA droplet to completely evaporate. On the other hand, while a 10-min time-period was most commonly used in our experiments, the time-period could have probably been reduced further while yielding equivalent

131

results (e.g. to around 5 min). Because the mold is treated to be very hydrophobic, surface tension forces do not naturally pull the interface into the features of the mold. The polymer is pushed into the features during the imprint step as pressure increases when the mold and glass slide are pressed together. We model polymer-filling behavior using finite element analysis; simulation results are presented in the *Results and Discussion II: Simulations* section of this report. The simulations elucidate the effects of nanofeature geometry on pattern transfer and establish the conditions when the vacuum step is necessary.

6.4.1.3. Silicon mold and glass slide alignment (Figure 6.1 c-1, c-2). The features of the silicon mold were imprinted into the PEGDMA using a conventional optical mask aligner – the SUSS MA-6 (SUSS Microtech, Munich, Germany) – typically used for photolithography; in addition to using the MA-6 aligner, the FILM process can be adapted for use with almost any modern mask aligner since, aside from semantics, most aligner's function in the same manner. Using an adhesive, a chemically-treated glass microscope slide was attached to a 5-inch by 5-inch square quartz plate, which was used as a dummy mask. The quartz plate was then attached to a mask holder by suction. The mask holder was inserted into the optical aligner and secured in place. Like with the glass slide, a patterned silicon mold was attached with an adhesive to a substrate holder that fit onto the motorized stage of the optical aligner. Conventional clear double-stick tape worked well as an adhesive for both the glass slide and silicon mold. When the optical aligner is used for optical lithography, its normal mode of operation, an actual quartz-chrome mask is attached to the mask holder instead of the bare quartz plate that we utilized. The mask holder was a standard accessory for the optical aligner. No specially designed components were necessary. Most modern optical aligners use mask holders that support approximately

132

5-inch by 5-inch square quartz-chrome masks; however, like with the SUSS MA-6 and other modern optical aligners, a myriad of mask holders that support different sizes of masks, are available. Any common mask holder can be used in the FILM process.

The motorized stage, where the silicon mold was attached, utilized a substrate holder that is also a common accessory for the mask aligner. Different substrate holders are available to support different sizes of substrates. The substrate holders normally use suction to attach glass or silicon wafers or other substrates in normal photolithography; however, since our silicon molds were small, an adhesive was required. Alignment of the glass slide and mold was manually achieved by eye with little difficulty. Although most optical aligners contain microscopes, which allow for very tight control over alignment in multi-layer fabrication protocols, microscope-precision is not typically necessary in single-layer processing.

6.4.1.4. Imprinting and exposure step (Figure 6.1d). Once the mold and glass slide were positioned, the motorized stage of the optical aligner electronically elevated the silicon mold to the level of the glass slide until reaching some explicitly set gap-spacing; the gap-spacing could be decreased until physical contact was made between the slide and mold or increased to very large spacings of greater than tens of microns. Whether the substrate holder is elevated to the level of the dummy quartz plate or the dummy quartz plate is lowered to the level of the substrate makes little difference in achieving pattern transfer. In absence of the vacuum step, interfacial pressure forces build up and attempt to coerce the polymer into the nanofeatures of the mold as the mold and glass slide come together in imprinting. Simulation results provided by finite element analysis show a direct correlation between polymer-filling and the

133
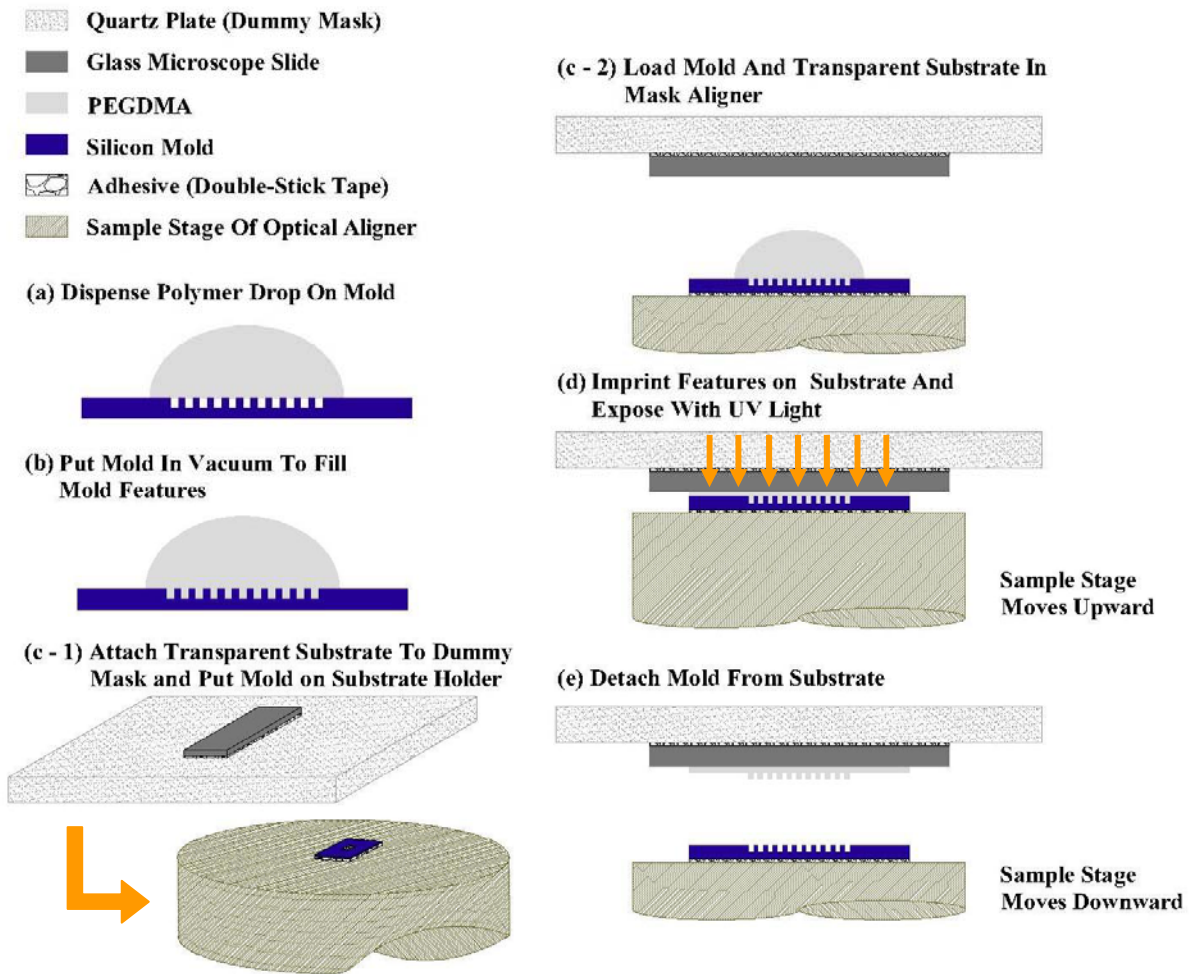
Figure 6.1. A schematic diagram of the FILM process used to imprint nanostructures from a silicon mold into UV-curable PEGDMA (other similar polymers can be utilized) using a conventional optical aligner commonly used in photolithography. (a) A drop of PEGDMA is deposited by pipette on a patterned silicon mold. (b) The mold with the drop is put in vacuum at room temperature and a pressure of 0.1 torr for 10 min. (c-1, c-2) The mold is positioned on the motorized sample stage of the optical aligner using an adhesive. A glass microscope slide is positioned on a quartz dummy plate using an adhesive (the dummy mask in c-1 is inverted). The quartz plate adheres to a mask holder (not drawn) by suction and serves as a transparent dummy photolithographic mask. The mask holder snugly mounts into the optical aligner. The mold and glass slide can be aligned by eye with little difficulty. (d) The motorized sample stage ascends until the mold reaches the level of the glass slide while the mask holder assembly stays fixed; the final gap-spacing between the mold and glass slide can be adjusted. The optical aligner's wedge-error compensation (WEC) feature wobbles the surfaces of the mold and glass slide until they are almost perfectly parallel for optimal pattern transfer. Exposure by UV occurs from the top through the quartz plate and glass slide (see orange arrows). Irradiation time can be set by the user and should be optimized for each particular UV-sensitive material. (e) The motorized sample stage detaches the mold from the slide by descending after exposure.

aspect-ratio of the nanofeatures. Simulation results are presented in the *Results and Discussion II: Simulation* section of this report.aspect-ratio of the nanofeatures. Simulation results are presented in the *Results and Discussion II: Simulation* section of this report.

After the mold was elevated to the glass slide, the PEGDMA was allowed to spread for about 30 seconds and then exposed with 365 nm *i*-line UV-light with an intensity of approximately 12 mW/cm^2. The UV-source of the optical aligner irradiated the PEGDMA from the top through the quartz plate and glass microscope slide for 45 sec. Soft-exposures were performed where a gap-spacing was maintained during exposure; thus, the glass slide and mold were not directly in contact. Gap-spacings of approximately 5 microns routinely achieved high-fidelity pattern-transfer.

Figure 6.2 shows well-defined SEM images of arrays of nanostructures of various geometry imprinted into PEGDMA including (a) approximately 500 nm (short axis is a bit larger) by 4 μm (long axis) nano-wells, (b) 500 nm by 500 nm square pillars with a 1 μm pitch, (c) a square lattice of circular pillars with a 300-nm diameter and pitch of 1.3 μm, (d) a hexagonal lattice of circular pillars with a 150-nm diameter and 1 μm pitch, (e) a hexagonal lattice of circular pillars with 250-nm diameter and 500-nm pitch, (f)-(g) lines of 250-nm and 150-nm width, respectively, with a pitch of 1 μm, and (h) lines of 50-nm width and a pitch of 150 nm. The pitch for the pillar arrays is equal in both the horizontal and vertical directions. As can be seen in Figure 6.2, the imprint process reproducibly printed nanostructures with high-fidelity over large areas. The thickness of the nanostructures was dependent on the thickness of the features in the silicon molds. Additionally, to facilitate good pattern transfer during imprinting, the silicon molds were etched so that the vertical wall-

135
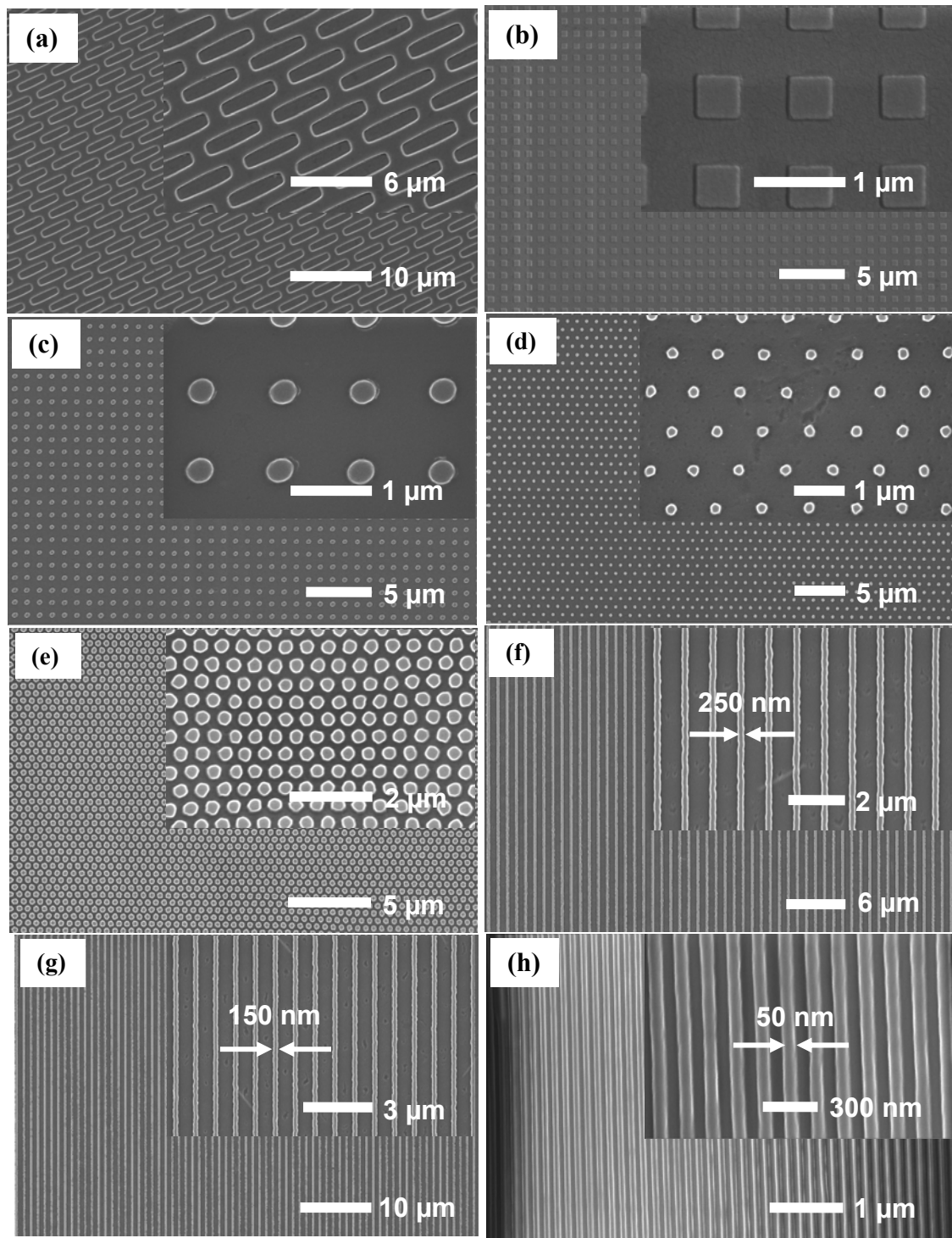
Figure 6.2. SEM images of various patterns imprinted from silicon molds into PEGDMA on glass microscope slides using the FILM process. (a) approximately 500 nm (short axis is a bit larger) by 4 µm (long axis) nano-wells, (b) 500 nm by 500 nm square pillars with a 1 µm pitch, (c) a square lattice of circular pillars of 300 nm diameter with a 1.3 µm pitch, (d) a hexagonal lattice of circular pillars of 150 nm diameter with a pitch of 1 µm, (e) a hexagonal lattice of circular pillars of 250 nm diameter with a pitch of 500 nm, (f),(g) lines of 250-nm and 150-nm width, respectively, with a pitch of 1 µm, and (h) lines of 50-nm width with a pitch of 150 nm. The pitch of the pillar structures is the same in both the horizontal and vertical directions.

136
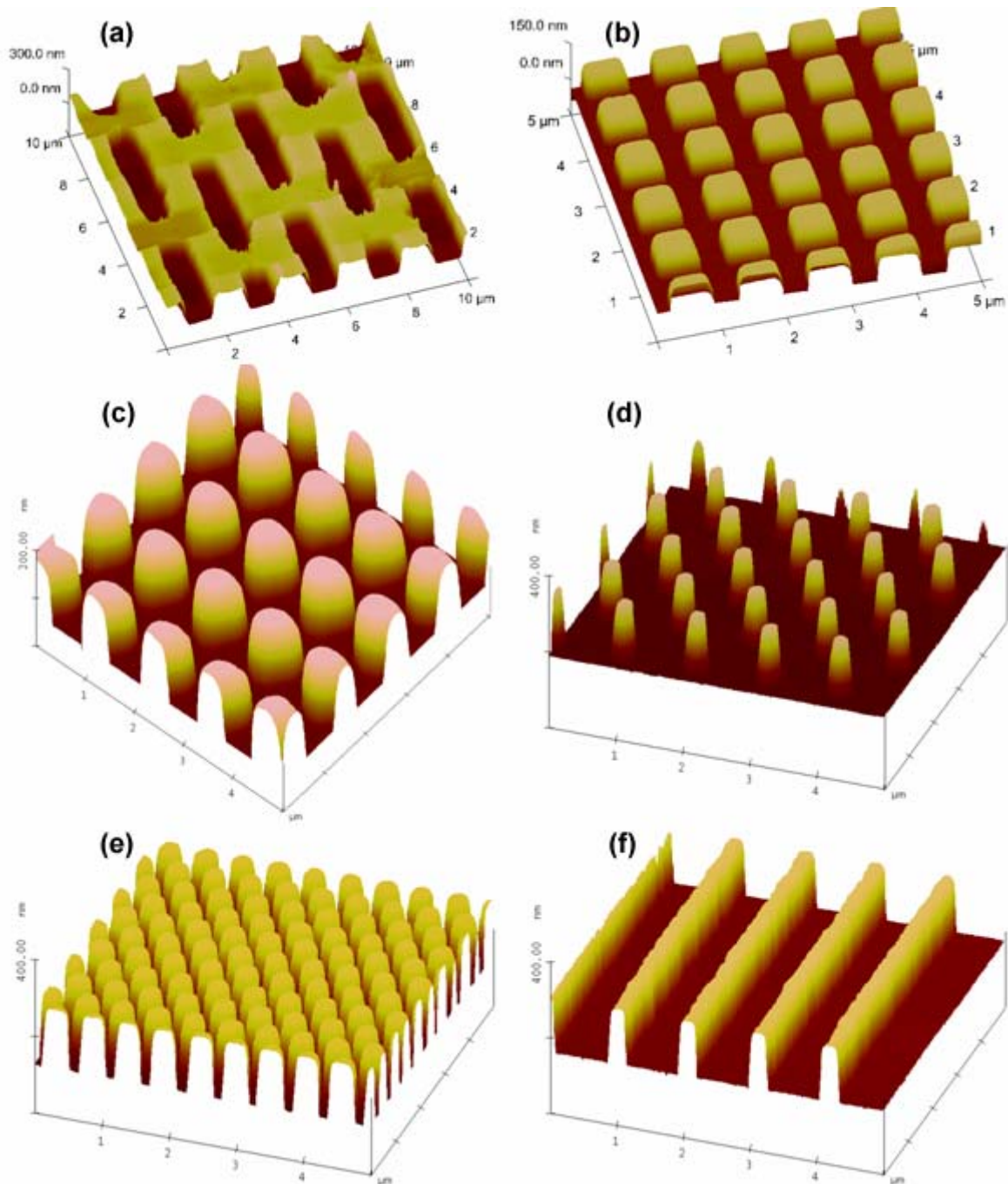
Figure 6.3. AFM images illustrating the three-dimensional topographies of the nanostructures shown in Figure 6.2. (a) approximately 500 nm (short axis is a bit larger) by 4 µm (long axis) nano-wells (b) 500 nm by 500 nm square pillars with a 1 µm pitch, (c) a square lattice of circular pillars of 300 nm diameter with a 1.3 µm pitch, (d) a hexagonal lattice of circular pillars of 250 nm diameter with a pitch of 1 µm, (e) a hexagonal lattice of circular pillars of 250 nm diameter with a pitch of 500 nm, and (f) lines of 150-nm width, respectively, with a pitch of 1 µm. Because the lines of 250-nm and 50-nm width have a nearly identical profiles to that of the 150-nm lines, the AFM images of the 250-nm and 50-nm lines have not been included. All nanostructure arrays were imprinted in PEGDMA using the FILM process.

137

profiles of the features in the mold sloped slightly inward. Thickness and vertical wall-profile angle were controllable by varying parameters of the etch-step during mold fabrication. When non-contact soft-exposures were performed with user-defined gap-spacings between the glass slides and silicon molds, the nanostructures were imprinted on a residual layer having a thickness equal to the gap-spacing (with the exception of the 1 μm by 4 μm holes). Contact imprints, where the glass slide and silicon mold came into direct contact, could also be performed using the optical aligner. Contact imprints minimize the thickness of the residual layer.

Because PEGDMA is a biocompatible material used in substrates for cell-seeding, the residual layer is usually desirable. Figure 6.3 shows AFM images illustrating the three-dimensional profiles of the nanostructures shown in Figure 6.2 including (a) the 500 nm x 4 μm nano-wells, (b) the 500 nm x 500 nm square pillars, (c) the 300-nm circular pillars of 1.3 μm pitch, (d) the 150-nm circular pillars of 1 μm pitch, (e) the 250-nm circular pillars of 500-nm pitch, and (f) the 150-nm lines of 1 μm pitch. Because the vertical profiles of the 50-nm, 150-nm, and 250-nm line structures were almost identical, only the AFM image for the 150-nm has been included. The pillar structures in Figure 6.3(c-e) show that the FILM process can be used to imprint nanostructures of high density and aspect ratio. Structure depth can be altered by adjusting the duration in which the molds are etched.

The mask aligner allowed us to tightly control process variables that are important in imprinting high-fidelity nanometer-scale structures over large areas. First, by using the wedge error compensation (WEC) function on the optical aligner, which is a feature typically found on most modern optical aligners to some variation, the opposing surfaces

138

of the glass slide and the silicon mold could be made to be almost perfectly parallel, which is necessary in achieving pattern transfer, imprinting nearly vertical structures, and in printing a patterned PEGDMA surface of constant thickness. Second, the optical aligner also allowed for a well-controlled exposure protocol. It was possible to perform a non-contact soft-exposure at a user-defined gap-spacing between the mold and glass slide during UV-exposure. Additionally, the UV-source used for polymerizing the PEGDMA produced intense, monochromatic, and uniform UV-radiation over the entire area of the pattern to be printed.

When utilizing opaque materials for the molds, like silicon, it is necessary to utilize a substrate transparent to UV in order to polymerize the UV-curable polymer. Since conventional glass microscope slides are commonly-used transparent substrates for PEG-based scaffolds, we chose to utilize silicon molds due to the highly-characterized properties of silicon with respect to micro- and nanoscale processing. If an opaque substrate is utilized, then the imprinting mold has to be transparent (e.g., quartz. Transparent molds have to be inserted into the aligner such that the UV-radiation can pass through the mold to polymerize the UV-curable material on the opaque substrate; thus, the particular configuration is opposite to the one shown in Figure 6.1c. The transparent mold must be attached to the dummy quartz plate and the opaque substrate must be attached to the substrate holder from the bottom.

6.4.1.5. *Mold detachment (Figure 6.1e).* After exposure, the motorized stage electronically separated the silicon mold from the glass slide. PEG hydrogels printed on unmodified glass do not adhere well during the separating step in the nanoimprinting process and subsequently in the presence of the aqueous buffer solutions used in cell

139

culture. To facilitate adhesion of the PEGDMA to the glass slides, the slides were modified with surface-tethered methacrylate groups. Glass slides were treated with a methacrylated silane, 3-trichlorosilyl propyl methacrylate (TPM); the acrylate-groups of the silane covalently bonded to the PEGDMA upon polymerization to create an acrylate-activate glass surface. The silicon molds were treated with a fluorinated-silane, Tridecafluoro-1,1,2,2-Tetrahydrooctyl-1 Trichlorosilane, to reduce adhesion to PEGDMA. The silane layer on the silicon molds remained intact for several tens of imprints. Details of the procedures used to treat the glass slides and silicon molds can be found in the materials and methods section. From a general perspective, it is important to note that the mold and substrate must be chemically-treated to optimize pattern transfer regardless of the choice of mold and substrate materials; adhesion of the UV-curable material to the mold must be reduced while adhesion to the substrate must be enhanced.

6.5. Contact angle measurements of water on chemically-treated and untreated silicon molds and glass substrates

In order for sufficient pattern transfer to occur, silicon molds and glass substrates have to be chemically-derivatized with various silanes (see sections 6.3., 6.4., and 6.1.5.). To test the efficacy of our protocols used for treating the surfaces of the glass slides and silicon molds, contact angle measurements were taken using a goniometer; contact angles of water in air on glass and silicon are shown in Figure 6.4. The contact angle on untreated glass microscope slides was approximately 9.3° (SD = 3.2°) (Figure 6.4a). The untreated hydroxylated glass slides were extremely hydrophilic having a contact angle of water in air approaching 0°. After silanizing, the contact angle on the glass slides

140

increased to approximately 75.0° (SD = 6.5°) (Figure 6.4b). The contact angle on

untreated silicon with the silicon's native oxide layer was approximately 41.5° (SD =

7.7°) (Figure 6.4c). After silanizing, the contact angle on the silicon increased to

approximately 104.2° (SD = 3.1°) (Figure 6.4d).

In their untreated states, the PEGDMA tended to stick to the glass slides rather

than the silicon; however, if the glass slides were not treated with the acrylated-silane,

delamination always occurred a few minutes after imprinting. Moreover, even when the

(a)   **(b)**

(c)   **(d)**
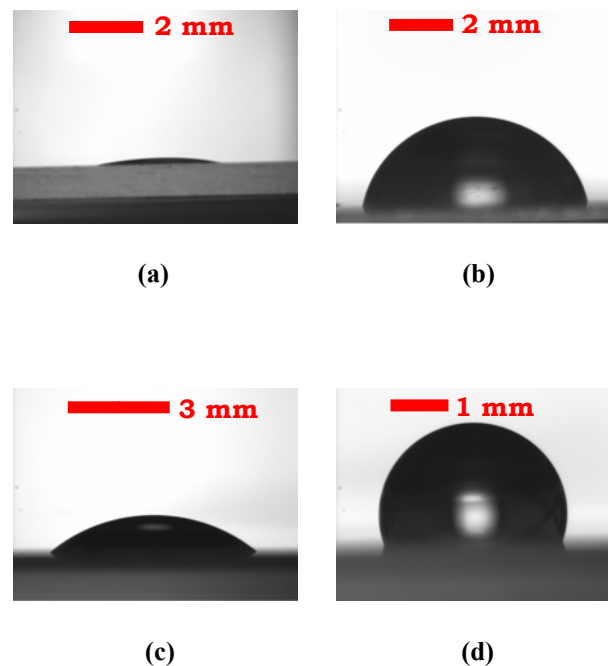
Figure 6.4. Contact angles of water in air on chemically-treated and -untreated glass microscope slides and silicon molds. (a) The contact angle of water on an untreated glass microscope slide. The contact angle is approximately 9.3° (SD = 3.2°). (b) The contact angle of water on a glass microscope slide treated with TPM. The contact angle is approximately 75.0° (SD = 6.5°). (c) The contact angle of water on the native oxide layer of untreated silicon. The contact angle is approximately 41.5° (SD = 7.7°). (d) The contact angle of water on silicon treated with a fluorinated-silane. The contact angle is approximately 104.2° (SD = 3.1°). In general, the mold and substrate must be chemically-treated to optimize pattern transfer despite the choice of mold and substrate materials. Scale-bars are based on the tilt angle of the stage (degrees) and base-width (mm) of the drops.

141

glass slides were treated, adhesion between the PEGDMA and glass decreased significantly when the silicon mold was not treated. We believe that this resulted from the fact that greater tensile forces were required to detach the mold when the mold was not treated.

A significant advantage with using the optical aligner for imprinting was that it mechanically separated the mold from the glass slide without manual intervention. Detaching the mold by hand inevitably introduces torsional forces that can easily crack the silicon mold or destroy the nanostructures imprinted into the PEGDMA. Separating the silicon and glass manually should be avoided to achieve optimal pattern transfer and adhesion between the PEGDMA and glass slide.

6.5. RESULTS AND DISCUSSION II: SIMULATIONS

6.5.1. Finite element modeling of polymer-filling into PEGDMA nanofeatures

Because surface effects are prominent at micron and sub-micron scales and the silicon mold was treated to be very hydrophobic, surface tension forces prevented the PEGDMA from naturally filling the nanofeatures. In absence of the vacuum step, the imprinting step helped to push the polymer into the hydrophobic features of the molds. Whether polymer-filling occurred depended heavily on the aspect ratio of the nanofeatures. To study the relationship between aspect-ratio and polymer-filling due to the imprinting step in the mask aligner, we conducted a finite element analysis using Comsol Multiphysics finite element software (Comsol Multiphysics Version 3.3, Comsol, Inc., Burlington, MA, USA).

142

In simulating the imprinting step, we consider the classical parallel-disk compression viscometer problem [17]. Figure 6.5(a) shows a schematic of a parallel-disk compression viscometer, which is analogous to the mold-substrate configuration in the mask aligner. Two circular disks of radius, R, which share a common axis of symmetry through their centers, are separated by a time-varying height, or gap-spacing $H(t)$. The space between the plates is filled with an incompressible fluid of viscosity μ and density ρ. The upper circular disk moves at a velocity, v_0, towards the lower circular disk which is fixed in place. As $H(t)$ decreases, the fluid is "squeezed" causing an axially symmetrical pressure drop and flow in the outwards radial direction. We can equivalently say that the bottom plate moves upward with velocity, v_0, towards a fixed upper plate, which is similar to the operation of the mask aligner where the mold (lower disk) is elevated at a prescribed velocity towards the fixed dummy plate supporting the glass slide (upper disk). Figure 6.5(b) shows the geometrical domain used in our nanofeature-filling simulations; the domain consists of an individual circular hole initially filled with air and a small region of fluid just above the hole. Two-dimensional axial symmetry has been utilized to reduce computing time; thus, Figure 6.5(b) can be visualized as an extruded cylindrical solid formed by rotating the 2D geometry about the symmetry centerline axis. The height of the fluid region in Figure 6.5(b) is small relative to the gap-spacing between the mold and glass slide. Accordingly, the height of the fluid domain stays constant while the fluid's pressure increases as $H(t)$ decreases. The time-varying pressure distribution from the compression viscometer problem is used as a pressure boundary condition to simulate the effects of the change in $H(t)$. The pressure of the air in the cylindrical hole is set at atmospheric pressure so that, neglecting

143

(a)

*Aspect-Ratio = h/w

(b)
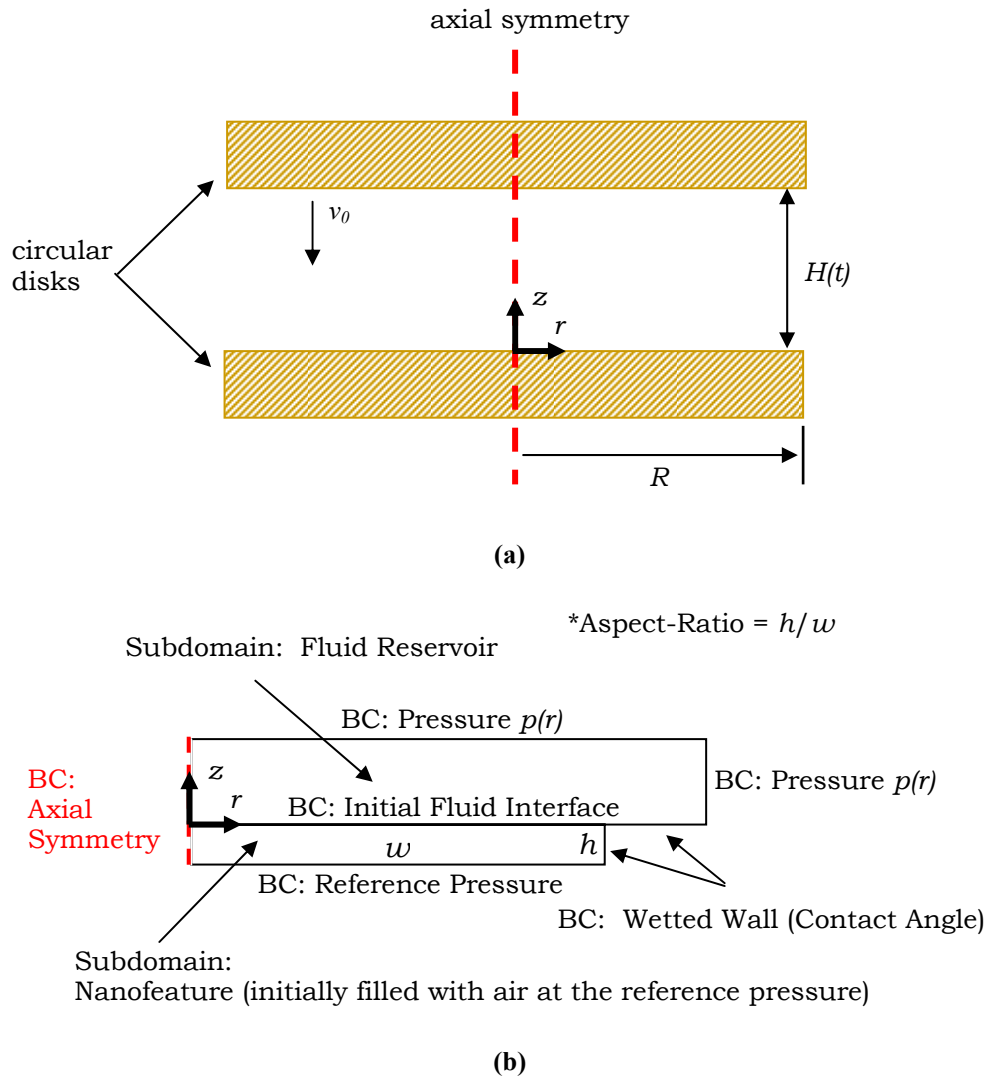
Figure 6.5. (a) A schematic diagram of the classical parallel-disk compression viscometer problem [17]. Two circular disks of radius, *R*, which share a common axis of symmetry through their centers, are separated by a time-varying height, *H(t)*. The space between the plates is filled with an incompressible fluid of viscosity *μ* and density *ρ*. The upper circular disk moves at a velocity, *v₀*, towards the lower circular disk which is fixed in place. As *H(t)* decreases, the fluid is "squeezed" causing a time-varying pressure drop in the radial direction. (b) A schematic diagram of the domain used in our transient nanofeature-filling simulations modeling the convection of polymer into the nanofeatures of the silicon mold. The domain utilizes axial symmetry; the 3D cylindrical domain can be visualized by rotating the 2D domain about the centerline symmetry axis. The domain consists of two subdomains, the fluid reservoir, and the cylindrical nanofeature, which is initially filled with air. The boundary conditions utilized in our simulations are juxtaposed to their corresponding boundaries. The wetted-wall boundary condition applies a frictional force at the walls while simultaneously relating contact angle to surface tension. For high polymer-surface contact angles (i.e. for hydrophobic surfaces), surface tension forces restrict flow.

144

gravitational effects, a balance between interfacial pressure, surface tension, and frictional forces determines whether the hole is filled with the polymer. Because of the low molecular weight of our PEGDMA, which consists of water as its solvent, we model the liquid as being pure water. For higher molecular weight derivatives of PEG, non-Newtonian effects could come into play, and using a power law description of the polymer's viscosity may be more appropriate.

The polymer droplets dispensed onto the patterns of the silicon mold are typically large enough that the polymer spreads to fill the entire gap between the mold and glass slide almost instantly; consequently, we assume that the "squeezing" of the polymer takes place when the gap between the mold and slide is completely filled with polymer in the derivation of the pressure boundary condition. At this point we also assume the following two things: the speed v_0 of the upper plate is slow such that a quasi-steady "squeezing" process can be assumed and the initial starting height of the upper plate, H_0, is much less than the radius of the two disks, i.e., $H_0 \ll R$. In applying the conservation of mass, the rate of decrease in the volume of polymer between the disks must equal the rate of polymer outflow from the disks due to the "squeezing" effect, i.e.,

$$\pi R^2 v_0 = 2\pi R H(t)\langle v_r \rangle_{r=R} \text{ and } \langle v_r \rangle_{r=R} = \frac{R}{2H(t)}v_0 \approx \frac{R}{H(t)}v_0 \quad (6.1)$$

where $\langle v_r \rangle_{r=R}$ is the radial velocity of the polymer at $r = R$. If the polymer velocity in the z-direction, v_z, is assumed to be of the same order of magnitude as v_0 and the polymer

145

velocity in the radial direction, v_r, is of the order of magnitude of $\langle v_r \rangle_{r=R}$, then $v_r >> |v_z|$.

The order of magnitude of the derivatives of the velocities can be estimated to be

$$\frac{\partial v_r}{\partial r} \approx \frac{(R/H(t))v_0 - 0}{R - 0} = \frac{v_0}{H(t)} \text{ and } \frac{\partial v_z}{\partial z} \approx \frac{-v_0 - 0}{H(t) - 0} = -\frac{v_0}{H(t)}. \quad (6.2)$$

Neglecting effects of gravity, the continuity and momentum equations simplify to

$$\frac{1}{r}\frac{\partial}{\partial r}(rv_r) + \frac{\partial v_z}{\partial z} = 0 \qquad \text{(continuity)} \qquad (6.3)$$

$$-\frac{dp}{dr} + \mu\frac{\partial^2 v_r}{\partial z^2} = 0 \qquad \text{(momentum)} \qquad (6.4)$$

with boundary conditions $\begin{cases} \text{BC 1}: v_r = 0; v_z = 0 \text{ at } z = 0 \\ \text{BC 2}: v_r = 0; v_z = -v_0 \text{ at } z = H(t) \\ \text{BC 3}: p = p_{atm} \text{ (atmospheric pressure) at } r = R \text{ (free jet)} \end{cases}$.

(6.5)

From the governing Equations (6.3) and (6.4) and boundary conditions, Equation (6.5), the velocity distributions in the viscometer problem are

$$v_r = \frac{1}{2\mu}\left(\frac{dp}{dr}\right)z[z - H(t)] \text{ and } v_z = \frac{1}{12\mu}\frac{1}{r}\frac{d}{dr}\left(r\frac{dp}{dr}\right). \quad (6.6)$$

Using the velocity distributions, the pressure distribution is derived to be

$$p - p_{atm} = \frac{3\mu v_0 R^2}{[H(t)]^3}\left[1 - \left(\frac{r}{R}\right)^2\right]. \quad (6.7)$$

146

The pressure distribution is a function of radial position and the temporal height of the moving disk relative to the fixed disk, which we coin as the gap-spacing. Values for the radius of the disks, R, and the speed of the moving disk, v_0, are estimated based on our imprinting experiments with the mask aligner; thus, we estimate R based on the usual size of our silicon molds and v_0 by the speed at which either the silicon mold or glass slide moves (in the case of our experiments with the SUSS MA-6, the silicon mold moves upward to the level of the glass slide).

The polymer in the fluid reservoir is allowed to fill the cylindrical hole. Several forces affect whether the fluid will actually convect into the nanofeatures during the imprint step of the FILM process. Surface tension forces that naturally pull a fluid into small recesses with wetting surfaces, in our case, adversely restricts the flow of the polymer because of the high 104.2° (SD = 3.1°) contact angle between the polymer and the silicon surface. To complement the restricting surface tension force, frictional forces aid in retarding fluid motion further. The counterbalancing force is the entrance pressure force that builds as the mold and substrate come together in the imprinting step, and is the result of the pressure drop across the convecting interface. The trapping of air is neglected, which is a mechanism of the assumption that the air is highly soluble in the polymer solution and simply diffuses out of the nanofeature as the polymer monomer enters; consequently, a constant pressure is maintained in the nanofeature as filling occurs. The no gas-trapping assumption is consistent with Reddy et al. [18], who modeled the flow of polymer in the S-FIL process. Assuming a constant air pressure in the nanofeature led us to define a constant pressure condition at the trough boundary in

147

the nanofeature instead of a no-slip wall condition. If filling occurs, the pressure forces trap the polymer in the nanofeature for subsequent curing by UV. For the case of high aspect-ratio features where feature-filling does not occur during the imprinting step, the vacuum step becomes necessary and imprinting and curing in the aligner should be done immediately following the removal of the mold from vacuum. We were unable to imprint high aspect-ratio features even when incorporating the vacuum step if too much time lapsed between the vacuum step and the imprinting step. This could be attributable to the resistive surface-tension forces coercing the polymer out of the nanofeatures.

The Navier-Stokes (N-S) equation, Equation (6.8), describes momentum transport for fluids. In considering the forces affecting the fluid bulk in our geometrical domain, a surface tension force, $\mathbf{F_s}$, is tagged onto the gravitational term on the right-hand-side of the N-S equation. To simplify our problem, gravitational forces are neglected leaving only the surface tension force.

$$\rho\left(\frac{\partial \mathbf{v}}{\partial t} + \mathbf{v} \cdot \nabla \mathbf{v}\right) = \nabla p + \mu \nabla^2 \mathbf{v} + \mathbf{f}$$
$$\mathbf{f} = \rho \mathbf{g} + \mathbf{F_s} \approx \mathbf{F_s} \text{ (gravity neglected)}$$

$$\tag{6.8}$$

The surface tension force acts at the polymer-air interface and is denoted

$$\mathbf{F_s} = \nabla \cdot \mathrm{T}$$
$$\mathrm{T} = \sigma\left[\mathrm{I} - \left(\mathbf{n}\mathbf{n}^T\right)\right]\delta$$

$$\tag{6.9}$$

where I is the identity matrix, $\mathbf{n}$ is the interface normal, and δ is the dirac delta function that equals one only at the air-polymer interface. A level-set two phase computational

148

technique is utilized in Comsol Multiphysics commercial finite element software to model the convection of the air-polymer interface [19]. The software sets up an equation in terms of a level-set function, ϕ, essentially defined as the proportion of polymer in a polymer-air mixture, that tracks the transport of the interface. The stochastic level-set function takes on only three values: $\phi = 1$ in polymer, $\phi = 0$ in air, and $\phi = 0.5$ at the polymer-air interface. The level set function is used to smooth the density and viscosity functions across the polymer-air interface.

As the silicon mold and glass microscope slide approach each other to a prescribed gap-spacing, the polymer droplet spreads to fill the gap between the mold and slide. Polymer spreading occurs because of an asymmetrical pressure drop (Equation 6.7) about the concentric centerline axis of the two substrates. Because the initial pressure of the air in the nanofeature domain is at the reference pressure, the pressure drop across the interface coerces the fluid to enter the features of the mold. As stated earlier, surface tension forces, which are mathematically correlated to the contact angle of the polymer on the silicon, resist feature filling due to the highly hydrophobic nature of the chemically-treated silicon. Combined with a frictional boundary force exerted at the walls of the mold, $\mathbf{F_f}$ (Equation (6.10)), instigated in our Comsol Multiphysics software, a balance of forces determines whether the nanofeatures of the mold fill with polymer.

.

$$\mathbf{F_f} = -\frac{\mu}{l}\mathbf{v} \tag{6.10}$$

149

In Equation (6.10), l is a characteristic slip length that we define to be on the order of the size of our finite elements near the nanofeature-walls in our domain (Figure 6.5(b)).

Figure 6.6 shows time-lapse images of our feature-filling finite element model applied to nanofeatures with an aspect ratio (height / width) of 1/10 and 8. The images plot the level-set function, which indicates either polymer or air. The magenta-colored areas represent polymer, where $\phi = 1$, while the turquoise-colored areas represent air, where $\phi = 0$. As indicative by Figure 6.6, filling occurs on the order of nanoseconds;
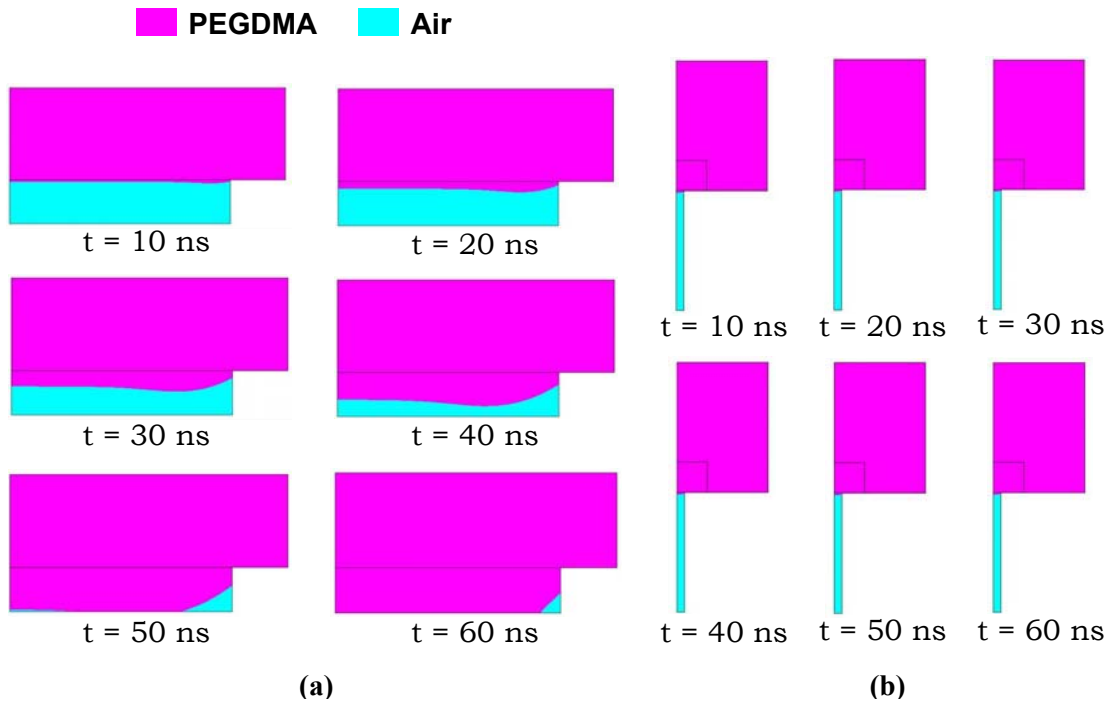
Figure 6.6. Simulated time-lapse images of the filling of cylindrical nanofeatures with a depth of 400 nm and an aspect-ratio of (a) 1/10 and (b) 8 when $H_0 = 5$ μm and $v_0 = 100$ μm/s. The turquoise-colored areas represent air while the magenta-colored areas represent PEGDMA. Polymer-filling occurs for the aspect-ratio of 1/10 but does not occur for the aspect-ratio of 8 (to re-emphasize, the nano-features in both (a) and (b) have a feature depth of 400 nm). Simulation results were obtained using Comsol Multiphysics commercial software.

150

thus, if we assume that the spacing between the silicon mold and glass slide is $H(t) = H_0 - v_0 t$, we can also assume that for very small time-scales, where $t \ll 1\,\text{s}$, that $H(t) \approx H_0$.

By varying H_0 while holding the other parameters of Equation (6.7) constant, including velocity, we can determine if filling will occur. It is important to note that in many applications, it is desirable to have a thick residual layer and to actually delaminate the nanopatterned sheet of PEGDMA from the glass slide. To do this, the value of H_0 should be set much higher since it directly reflects the thickness of the residual layer. If the glass slide is not chemically-treated with TPM, then the PEGDMA will delaminate as a nanopatterned sheet a few minutes after exposure.

Figure 6.7 shows the relationship of H_0 versus aspect-ratio when feature-filling occurs in the nanofeatures. Consistent with our experiments, you can see in Figure 6.6 that as aspect ratio increases, the required gap-spacing for imprinting decreases; moreover, the gap-spacing at which feature-filling occurs decreases with power regression behavior as aspect ratio increases. The power regression curve was generated in Matlab using the least squares curve-fitting technique; in our case, a curve was fitted to the logarithm of the aspect ratio and height-of-filling data to find the constants, a_k, in the general power law form, $y = a_0 x^{a_1}$.

As the gap-spacing decreases, the pressure drop across the polymer-air interface increases providing a greater push for filling to occur. The gap-spacing in the aligner we utilized (SUSS MA-6), could be changed in 1-micron increments; thus, the lowest gap-

151

spacing we could exhibit in our experiments was 1 micron. From our observations, even with a 1-micron setting, the need for the vacuum step (Figure 6.1(b)) became necessary for consistently printing structures with aspect ratios > 1; without the vacuum step, printing high-aspect-ratio structures either did not occur on a consistent basis or did not transfer well over large areas. We believe that trapped air in the features of the mold is released when the silicon mold is put in a low-pressure environment; accordingly, the capillary pressure is somehow overcompensated by mechanical pressure driving the polymer into the feature.

$$H_{Fill} = 4.21 * (AR)^{-0.446}$$
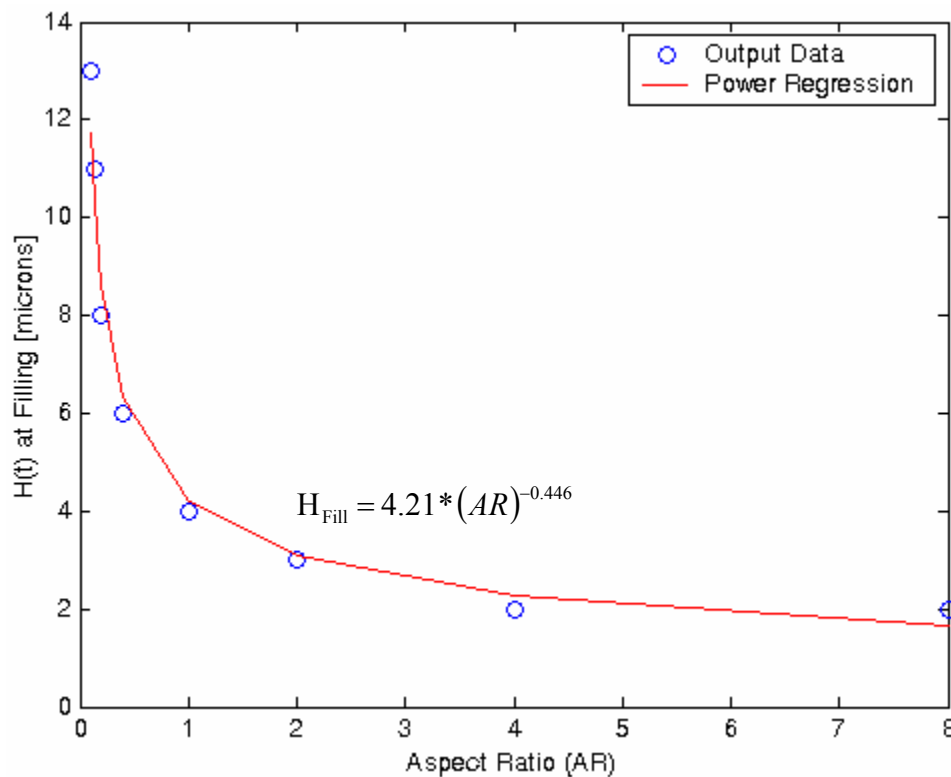
Figure 6.7. A plot of the gap-spacing at which nanofeature-filling occurs versus aspect ratio (AR = h/w). For increasing aspect ratios, the required gap-spacing for filling decreases. Nanofeature-filling behavior follows power regression behavior according to the equation listed in the plot.

152

6.5.2. Verification of finite element modeling methodology

We verify our level-set simulation methodology in Comsol Multiphysics by comparing results obtained for the surface-tension-driven convection of a blood-air interface in a narrow rectangular slit at various contact angles with those obtained by Huang et al. [20]. Figure 6.8 shows plots of the dimensionless position of the blood-air interface as a function of time for the first 0.016 seconds. Our results agree closely with those of Figure 12 in reference [20].
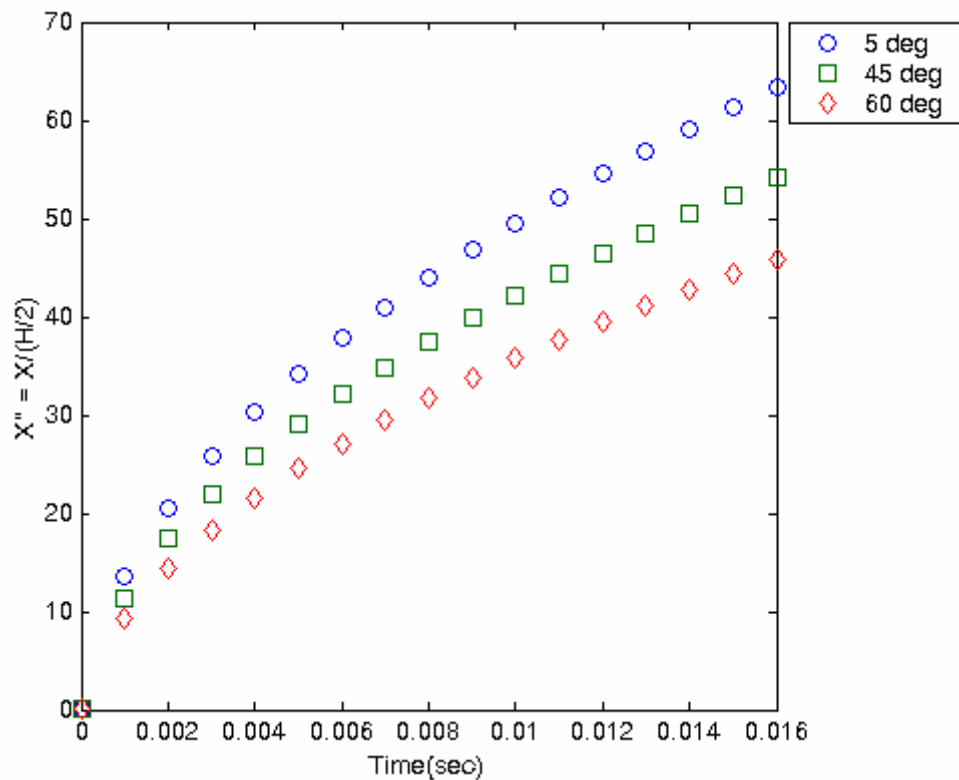
Figure 6.8. The non-dimensional position of a blood-air interface as a function of time and contact angle in a horizontal rectangular slit predicted by our level-set methodology in Comsol Multiphysics. Our results agree closely with those presented by Huang et al. [20]. The height H of the slit is 0.05 mm. Non-dimensional position X'' is given by $X''= X/(H/2)$ where X is position in meters. The chart closely approximates the simulated behavior in Figure 12 of ref. [20].

153

One thing to note is that we utilize the N-S equations to model the physics because we simulated the flow of liquid water. As the size of the nanofeatures reduce to a few nanometers, molecular dynamics (MD) models may be more appropriate. Because we model solely the flow of liquid water, which consists of very tightly packed water molecules, we deemed the N-S equations appropriate for our purposes.

6.6. CONCLUSIONS

We have demonstrated an automated nanoimprinting method, flash imprint lithography using a mask aligner, coined FILM, for transferring nanoscale features from silicon molds into widely-utilized photopolymerizable PEG hydrogels on glass microscope slides using a conventional optical mask aligner. We were able to fabricate nanoscale structures in PEGDMA down to 50 nm without the use of expensive dedicated nanoimprinting tools, quartz templates, and material dispensers, and without any manual intervention.

Mask aligners allow control over many process variables that are important in reproducibly imprinting high-fidelity nanometer-scale structures over large areas. Although we specifically utilized a SUSS MA-6 optical aligner, the FILM process can be adapted for use with many other modern optical aligners since they generally function in the same manner. Additionally, the FILM process can be used to pattern nanostructures in other low-viscosity UV-curable polymers alongside PEG hydrogels without the use of ad hoc material dispensers often required with dedicated nanoimprinting tools. We were also able to utilize cheap silicon molds instead of expensive quartz templates, required by

some imprint tools (e.g. S-FIL), which allowed us to imprint various topographies at very little cost. Moreover, molds of many different materials can be used provided that either the mold or substrate material is transparent to UV. We believe that the generalized FILM process is very well-suited for creating various physical topographies in UV-curable materials like PEG hydrogels for fabricating biomimetic tissue scaffolds used in cell-seeding applications. We are currently working on imprinting sub-50 nm features and using the FILM process to study the effects of physical nanotopography on the adhesion, migration, and differentiation of preadipocytes (fat cell precursors) found in adipose tissues and on axon polarization of hippocampal cells; thus far, the FILM process has vastly improved our ability to do high-throughput studies, which is very important in creating new therapies for adipose and nervous tissue damage.

6.7. ACKNOWLEDGEMENTS

155

6.8. REFERENCES

1.   Fozdar D. Y., Zhang W., Palard M., Patrick C., Chen S., Flash imprint lithography using a mask aligner: a method for printing nanostructures in photosensitive hydrogels, *Nanotechnology*, 2008; **19** pp. 1-13.

2.   Revzin A., Russell R. J., Yadavalli V. K., Koh W. G., Deister C., Hile D. D., et al., Fabrication of poly(ethylene glycol) hydrogel microstructures using photolithography, *Langmuir*, 2001; **17** pp. 5440-5447.

3.   Hahn M. S., Taite L. J., Moon J. J., Rowland M. C., Ruffino K. A., West J. L., Photolithographic patterning of polyethylene glycol hydrogels, *Biomaterials*, 2006; **27** pp. 2519-2524.

4.   Chou S. Y., Krauss P. R., Renstrom P. J., Imprint of Sub-25 Nm Vias and Trenches in Polymers, *Applied Physics Letters*, 1995; **67** pp. 3114-3116.

5.   Colburn M., Johnson S., Stewart M., Damle S., Bailey T., Choi B. J., et al., Step and Flash Imprint Lithography: A New Approach to High-Resolution Patterning, *Proceedings of the SPIE's 24th International Symposium on Microlithography: Emerging Lithographic Technologies III*, Santa Clara, CA, March 1999; **3676**, pp. 379-389.

6.   Kim P., Kim D. H., Kim B., Choi S. K., Lee S. H., Khademhosseini A., et al., Fabrication of nanostructures of polyethylene glycol for applications to protein adsorption and cell adhesion, *Nanotechnology*, 2005; **16** pp. 2420-2426.

7.   Jung G. Y., Ganapathiappan S., Ohlberg D. A. A., Olynick D. L., Chen Y., Tong W. M., et al., Fabrication of a 34 x 34 Crossbar Structure at 50 nm Half-pitch by UV-based Nanoimprint Lithography, *Nano Lett*, 2004; **4** pp. 1225-1229.

8.   Scheerlinck S., Thourhout D. V., Baets R., Nano Imprint Lithography for Photonic Structure Patterning, *Proceedings Symposium IEEE/LEOS Benelux Chapter*, Belgium, 2005; 63-66.

9.   Stuart C., Xu Q., Tseng R. J., Yang Y., Hahn H. T., Chen Y., et al., Nanofabrication module integrated with optical aligner, *Journal of Vacuum Science & Technology B: Microelectronics and Nanometer Structures*, 2006; **24** pp. 539-542.

10.   Patel P. N., Smith C. K., Patrick C. W., Rheological and recovery properties of poly(ethylene glycol) diacrylate hydrogels and human adipose tissue, *Journal of Biomedical Materials Research Part A*, 2005; **73A** pp. 313-319.

11.   Lu Y., Mapili G., Suhali G., Chen S. C., Roy K., A digital micro-mirror device-based system for the microfabrication of complex, spatially patterned tissue engineering scaffolds, *Journal of Biomedical Materials Research Part A*, 2006; **77A** pp. 396-405.

12.   Adamson A. W., *Physical chemistry of surfaces*, John Wiley and Sons, New York, 1982.

13.   Andreas J. M., Hauser E. A., Tucker W. B., Boundary Tension by Pendant Drops, *J Phys Chem*, 1938; **42** pp. 1001-1019.

14.   Adamson A. W., Shirley F. P., Kunichika K. T., Contact angles on molecular solids : I. Ice, *Journal of Colloid and Interface Science*, 1970; **34** pp. 461-468.

15.   Fowkes F. M., Harkins W. D., The State of Monolayers Adsorbed at the Interface Solid--Aqueous Solution, *J Am Chem Soc*, 1940; **62** pp. 3377-3386.

16.   Girifalco L. A., Good R. J., A Theory for the Estimation of Surface and Interfacial Energies. I. Derivation and Application to Interfacial Tension, *J Phys Chem*, 1957; **61** pp. 904-909.

17.   Bird B. R., Stewart W. E., Lightfoot E. N., *Transport Phenomena*, John Wiley and Sons, New York, 2002.

18.   Reddy S., Bonnecaze R. T., Simulation of fluid flow in the step and flash imprint lithography process, *Microelectronic Engineering*, 2005; **82** pp. 60-70.

19.   Sussman M., Fatemi E., Smereka P., Osher S., An improved level set method for incompressible two-phase flows, *Computers & Fluids*, 1998; **27** pp. 663-680.

20.   Huang W., Bhullar R. S., Fung Y. C., The surface-tension-driven flow of blood from a droplet into a capillary tube, *Journal of Biomechanical Engineering-Transactions of the Asme*, 2001; **123** pp. 446-454.

Chapter 7: Micro-well texture printed into PEG hydrogels using the FILM nanomanufacturing process affects the behavior of preadipocytes[1]

7.1. ABSTRACT.

To date, biomaterial scaffolds for adipose tissue engineering have focused on macro- and upper micro-scale fabrication, biocompatibility, and biodegradation, but have failed to recapitulate the sub-micron dimensions of native extracellular matrix (ECM) and, therefore, have not optimized material-cell interactions. Here, we report the findings from a study investigating the effects of a quasi-mimetic sub-micron (< 1 μm) surface texture on the qualitative behavior of preadipocytes (PAs). We found that PAs in contact with tread-like micro-well structures exhibit a different morphology relative to PAs seeded onto control smooth glass surfaces. Additionally, the micro-well topography induced isolated PAs to undergo adipogenesis, which usually occurs in the presence of aggregates of contact-inhibited PAs. The micro-well structures were printed into polyethylene glycol dimethacrylate (PEGDMA) using the recently reported nanomanufacturing process called Flash Imprint Lithography Using a Mask Aligner (FILM). FILM is a simple process that can be utilized to fabricate micro- and nanostructures in UV-curable materials [2]. We demonstrate the utilization of the FILM process for a tissue engineering application for the first time. The micro-well topographical theme is characterized by contact angle and surface energy analysis and the

---

[1] Published in [1].

results were compared with those for smooth glass and unpatterned PEGDMA surfaces. Based on our observations, we believe that the micro-well texture may ultimately be beneficial on implantable tissue scaffolds.

Keywords: Adipose Tissue Engineering; Nanomanufacturing; Polyethylene Glycol; Preadipocyte; Tissue Scaffold

7.2. INTRODUCTION

Adipose tissue engineering, the field of growing new vascularized adipose tissue, has great potential in repairing soft tissue deficits resulting from congenital abnormalities (e.g., hemifacial microsomia, Parry Romberg's syndrome, and Poland's syndrome), trauma, and tumor resection [3]. These contour defects can be psychologically devastating to patients and, in many cases, physical impairments also result (e.g., loss of range of motion). Current reconstructive treatments consist of implanting or injecting synthetic materials or injecting autologous fat tissue (fat tissue removed from other parts of the patient's own body) [3-6]. These treatments are far from ideal. Implanted or injected synthetic materials often induce immune responses dire to the patient, while injected autologous fat tissue is resorbed by the body causing a 40-60% reduction in graft volume [7, 8]. All conventional treatments only correct volume deficits of defects and do not correct for concomitant losses in function (e.g., loss of range of motion). A new promising strategy for treating soft-tissue defects is to fundamentally grow new fully-functioning vascularized adipose (fat) tissue on biomaterial scaffolds. This particular

159

area of research, focused at growing new adipose tissue, is called adipose tissue engineering.

Adipose tissue engineering involves a minimum of three components, a tissue scaffold providing the necessary boundary conditions for tissue formation, pertinent cell types that can be cultured to form new adipose tissue, and a permissive microenvironment [9, 10]. The microenvironment consists of physical and chemical cues that influence the behavior and proliferation of the pertinent cells. To grow new adipose tissue, the appropriate cells are seeded onto a tissue scaffold, which ultimately controls 3D tissue morphology, and the cells proliferate and differentiate into fully-functioning vascularized adipose tissue. To date, biomaterial scaffolds for adipose tissue have focused on macro- and upper micro-scale fabrication, biocompatibility, and biodegradation. They have failed to recapitulate the microscale dimension of native extracellular matrix (ECM) and, therefore, have not optimized material-cell interactions. Significant progress has been made in using preadipocytes (PAs), precursor adipose cells that differentiate into mature fully-differentiated adipose cells, to form new adipose tissue. PAs can readily be expanded *ex vivo*, unlike fully-differentiated adipose cells, and the process by which they differentiate into mature adipose cells, called adipogenesis, is largely understood.

Although the process of adipogenesis is well-understood, physical stimuli causing the onset of adipogenesis and other behavior of preadipocytes, remains largely unknown. *In vivo*, preadipocytes are surrounded by an ECM that is patterned down to sub-micron scales (< 1 μm) [11-13]. Accordingly, mimicking the ECM in implantable biomaterial scaffolds may be very important in elucidating certain responses of PAs that

are important in the development of healthy new adipose tissue. In order to truly harness PA-response, specific topographical schemes have to be strategically designed and manufactured, physically characterized (e.g. contact angle and surface energy analysis), and interactions between the texture and PAs have to be monitored in culture.

Just like tires have tread to help a car gain traction to the road and a bathtub has rubber grips to prevent slipping, we show that periodic tread-like micro-well structures patterned into polyethylene glycol (PEG) hydrogels mediate interactions that affect the morphology of PA's. We chose the micro-well topographical theme based on the idea that the texture would enhance contact with PAs in culture and induce an atypical cell-response. We fabricate the micro-well texture in PEG-dimethacrylate (PEGDMA) by a nanomanufacturing process recently developed by our group called Flash Imprint Lithography using a Mask Aligner (FILM) [2]. PEGDMA is a biocompatible liquid polymer that can be made to solidify upon exposure to ultraviolet light (365 nm *i*-line UV). PEGDMA has optimal material and chemical properties that make it ideal for use in actual three-dimensional implantable adipose tissue scaffolds.

The FILM process is an alternative to Step-and-Flash Imprint Lithography (S-FIL) and other variations of UV-Nanoimprint Lithography (UV-NIL). S-FIL is a very promising technology that is currently being adapted to semiconductor electronics fabrication; however, it requires the use of unconventional dedicated nanoimprinting tools [14]. Such dedicated imprinting tools are typically unavailable in most clean rooms and require extremely costly quartz imprinting templates and ad hoc drop dispensers to support different photosensitive materials. The FILM process requires the use of a common mask aligner normally used for photolithography, cheap silicon imprinting

161

molds, and can be used with any low-viscosity UV-curable biomaterial. FILM was developed as a more suitable alternative for fabricating structures in UV-curable materials with nanoscale resolution (< 100 nm) than conventional technologies like S-FIL and general UV-nanoimprint lithography (UV-NIL), which require dedicated imprinting technologies, and photolithography. Here, we demonstrate the use of the FILM process for a tissue engineering application for the first time.

The interactions observed between PAs and the micro-well topography exemplify the need for incorporating sub-micron strategically designed (< 1 μm) surface textures in implantable biomaterial adipose tissue scaffolds. Furthermore, we believe that the micro-well topography studied in our investigations may be beneficial on implantable adipose tissue scaffolds.

7.3. MATERIALS AND METHODS

7.3.1. Synthesis of PEGDMA biomaterial

PEGDMA prepolymer of MW = 1000 (Polysciences Inc., Warrington, PA, USA, No. 25852-47-5) was dissolved in HPLC-grade demineralized water (Fisher Chemical, Fairlawn, NJ, USA, No. 7732-18-5) to a concentration of 100% (w/v). Irgacure 2959 photoiniator (Ciba Specialty Chemicals, Tarrytown, NY, USA) was added to the PEGDMA/water mixture to a concentration of 0.1% (w/v) relative to the volume of water used (e.g., 0.001 g of Irgacure pure 1 mL of water). The PEGDMA was centrifuged for 30 minutes and refrigerated overnight to allow the mixture to stabilize.

162

7.3.2. Fabrication of silicon molds

Silicon wafers (NOVA Electronic Materials, Richardson, TX, USA) were diced into 20 mm x 20 mm pieces. The silicon pieces were ashed in an O_2-plasma asher (March CS-1701, March Plasma Systems, Concord, CA, USA) to burn off organic contaminants, cleaned in a mixture of 30% H_2O_2 (v/v) in H_2SO_4 (piranha solution) (Hydrogen Peroxide 30% - No. 2190, Sulfuric Acid 96% - No. 9684, J.T. Baker, Phillipsburg, NJ, USA) for 8 minutes, and washed thoroughly in DI water. The wafer pieces were dried thoroughly with N_2 and then dehydration-baked at 200 °C for 5 min on a hot plate to remove all residual moisture. A 20-nm silicon dioxide layer was deposited on the clean silicon using plasma-enhanced chemical vapor deposition (PECVD) (Plasma-Therm 790, Plasma-Therm, Inc., St. Petersburg, FL, USA). ZEP-520A (Zeon Chemicals, Louisville, KY, USA) positive electronic resist was thinned in Anisole to a 1:3 ratio (v/v), respectively; ZEP-520A resist was chosen due to its high resolution and dry-etch resistance. The resist was deposited on the molds by spin-coating at 4000 rpm for 60 sec to a thickness of approximately 100 nm and then soft-baked at 180 °C for 90 sec. The resist was patterned using electron beam lithography (EBL) (JEOL 6000 FSE, JEOL Ltd., Tokyo, Japan; Raith 50, Raith GmbH, Dortmund, Germany) and developed in ZED-N50 solution (Zeon Chemicals, Louisville, KY, USA). The patterned samples were descummed in an O_2-plasma to remove residual resist in the developed regions of the resist. Exposed silicon dioxide was etched through by RIE (Plasma-Therm 790, Plasma-Therm, Inc., St. Petersburg, FL, USA) using the resist as a mask. The resist was subsequently stripped in 30% H_2O_2 (v/v) in H_2SO_4. The exposed underlying silicon was

etched with RIE using the patterned silicon dioxide layer as a mask. The silicon dioxide layer was then removed in buffered oxide etchant (BOE) leaving the patterned silicon.

7.3.3. Chemical pretreatment of silicon molds

Silicon molds were chemically treated with Tridecafluoro-1,1,2,2-Tetrahydrooctyl-1 Trichlorosilane (United Chemical Technologies, Inc., Bristol, PA, USA, No. T2492). The silicon molds were ashed in an O_2-plasma asher to burn of organic contaminants and then immersed in a mixture of 30% H_2O_2 (v/v) in H_2SO_4 for 10 minutes, washed thoroughly in DI water, dried thoroughly with N_2, and dehydration-baked at 200 °C for 5 min on a hot plate. The clean silicon molds were then placed in a small container in juxtapose to a small vial containing a few drops of the fluorinated-silane. The container was then covered and stored in a dehumidified nitrogen environment to prevent any reactions between the fluorinated-silane and ambient moisture. After 4 hours, the silicon molds were removed and washed with a mixture of 25% carbon tetrachloride (v/v) in heptane and sequentially sonicated in acetone, methanol, and isopropyl alcohol (IPA) (Acetone Certified ACS, methanol Certified ACS, 2-Propanol Certified ACS, Fisher Chemical, Fairlawn, NJ, USA) for 5 min each. In between imprints using the mask aligner, residual photopolymerized PEGDMA was removed from the silicon molds by sequential immersion in acetone, methanol, and IPA for 1 min each. After being chemically treated with the fluorinated-silane, the silicon molds were dried after each rinse with N_2 but never baked in an effort to preserve the silane layer.

164

7.3.4. Chemical pretreatment of glass microscope slides

Glass microscope slides were immersed in a mixture of 30% H_2O_2 (v/v) in H_2SO_4 for 10 minutes, washed thoroughly in DI water, dried thoroughly with N_2, and immersed in a 1 mM solution of 3-trichlorosilyl propyl methacrylate (TPM) in a mixture of 25% carbon tetrachloride (v/v) in heptane for 5 minutes. The piranha solution is a strong oxidizer that cleaned and hydroxylated the microscope slides; the silane attached to the hydroxyl groups (-OH) on the surface of the glass. Since TPM is highly reactive towards water, the microscope slides were meticulously dried before immersion in the silane solution. Because it was extremely difficult to remove all the residual moisture on the microscope slides using N_2 alone, the microscope slides typically formed a powdery-like surface when in contact with the silane solution. The powdery residue formed when the silane reacted with the residual moisture on the microscope slides that was not removed by the N_2. Moreover, unless the silane solution was kept in a dehumidified environment, moisture from the air often caused large particles to form in the silane solution that attached to the microscope slides. To limit the amount of powdery-like residue that formed and attached to the surface of the glass microscope slides, the silane mixture was stirred for the 5-minute duration in which the microscope slides were immersed. Upon removing the microscope slides from the silane mixture, the silanized slides were copiously rinsed with a TPM-free mixture of 25% carbon tetrachloride (v/v) in heptane and then with 1X phosphate buffered saline (PBS). After rinsing, the microscope slides were dried with N_2 and stored in a vacuum dessicator. Carbon tetrachloride served to degrease superfluous silane that did not covalently bond to the silicon surface and remove particulate matter; excess silane was nearly impossible to remove with standard organic

165

solvents like acetone, methanol, and IPA. Pretreated glass slides were dried with N_2 after

rinsing but were not dehydration-baked.   Baking tended to degrade the tethered

methacrylate groups on the glass slides which reduced PEGDMA adhesion.

7.3.5. Imprinting of micro-wells in PEGDMA

The micro-well topography was imprinted into PEGDMA using the FILM

process, which is illustrated in Figure 7.1. First, a silicon mold containing a 1 mm x 1

mm area of micro-wells was fabricated using EBL and RIE. The mold was then treated

with a fluorinated silane to increase hydrophobicity and a drop of PEGDMA was

dispensed on the pattern area. The silicon mold with the PEGDMA droplet was put in a

vacuum desiccator at room temperature and a pressure of 0.1 Torr for 10 min to suction

the polymer into the features of the mold. The silicon mold was then loaded onto the

substrate holder in a mask aligner normally used for photolithography (SUSS MA-6,

SUSS Microtech, Munich, Germany) and a 12.7 cm x 12.7 cm blank quartz plate was

loaded into the mask holder in the aligner (instead of a quartz-chrome photomask).

Before loading the dummy plate, a glass microscope slide was treated with a tethered

silane and attached to the quartz dummy plate with double-stick tape. After loading the

silicon mold and glass substrate, the pattern was imprinted as the aligner brought the

mold and glass slide together to a prescribed gap-spacing of 5 µm where the PEGDMA

was allowed to spread.   After letting the PEGDMA spread for about 30 sec, the

PEGDMA is exposed through the quartz dummy plate for 45 sec with 365 nm *i*-line

monochromatic UV-light. Finally, the aligner electronically separated the mold from the

166

A. Dispense polymer drop on mold and put mold in vacuum

B. Load mold and glass slide in aligner

C. Print features in polymer and expose with UV light

Sample stage moves upward

D. Detach mold from glass slide

Sample stage moves downward

Legend:
- Quartz plate
- Glass microscope slide
- PEGDMA
- Silicon mold
- Adhesive
- Sample stage Of optical aligner
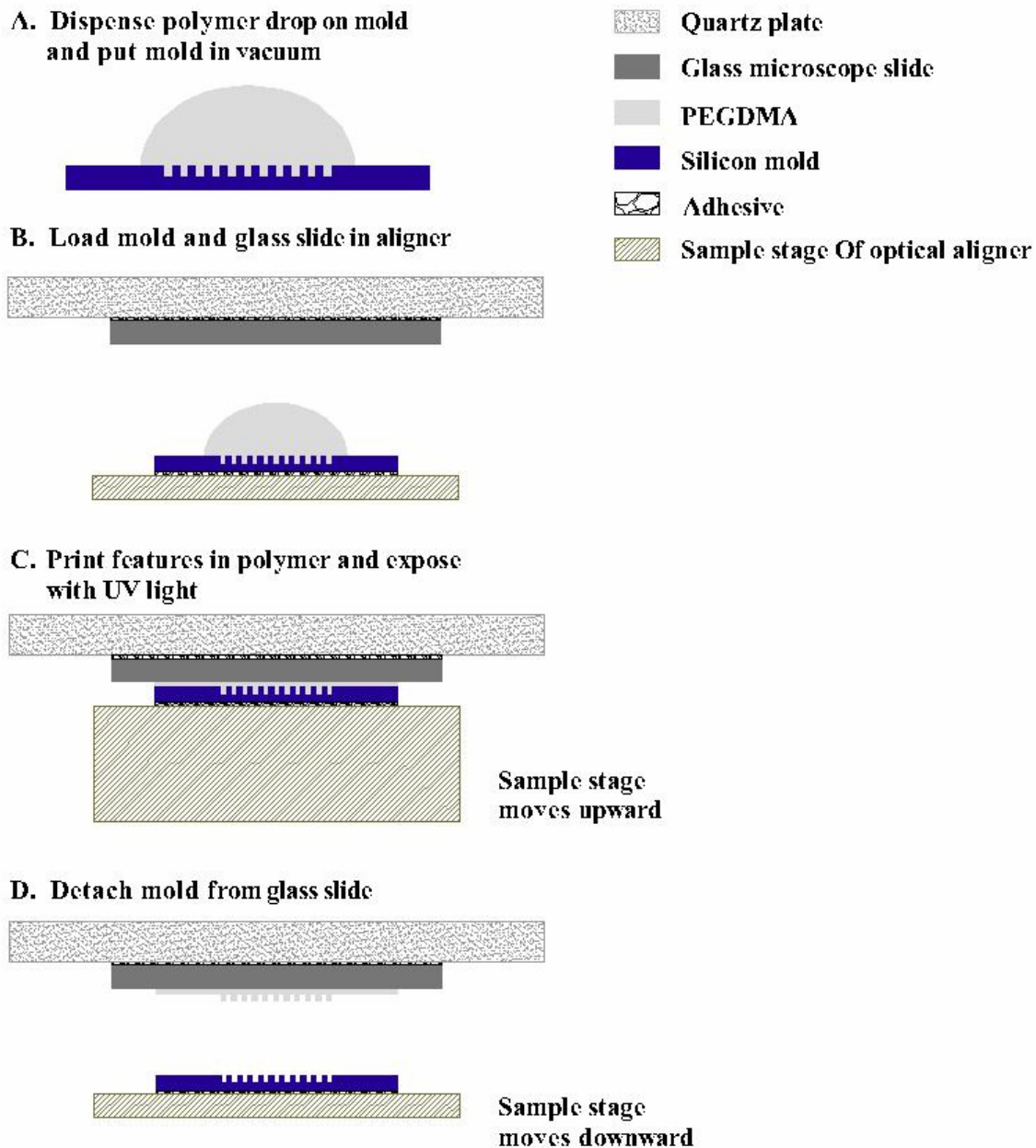
Figure 7.1. A schematic diagram of the FILM process. The FILM process utilizes a common mask aligner to print features from cheap silicon molds onto glass microscope slides. (A) A drop of UV-curable PEGDMA is dispensed onto a silane-treated silicon mold. The mold is placed into a vacuum desiccator at room temperature and a pressure of 0.1 torr for 5-10 min. (B) The mold is positioned on the motorized sample stage of the aligner using an adhesive (e.g., double-stick tape). Likewise, a silane-treated glass microscope slide is positioned on a quartz plate using an adhesive. The quartz plate adheres to a mask holder (not drawn) by suction and serves as a transparent dummy mask. The mask holder mounts into the aligner. (C) The motorized sample stage moves upward until the mold and glass slide come together causing the PEGDMA to spread. The final gap-spacing between the mold and slide can be adjusted depending on the desired gap spacing. Exposure by UV occurs from the top through the quartz plate and glass slide. (D) The motorized sample stage detaches the mold from the glass slide leaving the pattern on the slide.

167

glass slide leaving the patterned PEGDMA on the glass slide. The FILM process is reported in great detail in reference [2].

7.3.6. Examination of micro-wells in PEGDMA

Topological features imprinted in PEGDMA were examined using a field-emission scanning-electron microscope (FESEM) (LEO 1530, Carl Zeiss SMT Inc., Peabody, MA, USA) and atomic force microscope (AFM) (Dimension 3100 with Microscope IV controller, Digital Instruments & Veeco Metrology Group, Santa Barbara, CA, USA). AFM images were taken using a silicon tip in tapping-mode (Tap300, Budget Sensors, Sophia, Bulgaria).

7.3.7. Examination of contact angles

Contact angle measurements were taken using a goniometer (FTÅ200, First Ten Angstroms, Inc., Portsmouth, VA, USA). Substrates were placed onto a manually-adjustable sample stage and oriented appropriately; camera lighting, brightness, and contrast were optimized. Small droplets of DI water were electronically dispensed onto the substrates using a syringe pump controlled by computer. Each image was taken a few seconds after a droplet was dispensed. The baseline of the droplets was determined using a reflection image produced when the substrates were slightly tilted. The curvature of the droplets was traced using a non-spherical fit model. Multiple contact angle measurements were taken on each surface to verify accuracy and precision of contact angle data; the number of contact angle measurements (n) taken on each surface is as follows: n = 12 for glass; n = 8 unpatterned (bare) PEGDMA; n = 30 for PEGDMA

168

micro-well surface. Measurements are reported as mean values with a corresponding standard deviation (SD). Information regarding contact angle measurements can be found in the references [15-19].

7.3.8. Culture of PAs

Rat PAs were harvested and cultured as previously described [20-22]. Control cultures were grown in parallel with all experiments to ensure correct cell phenotype. PAs were not employed greater than passage 2.

7.3.9. Examination of PAs on micro-well surface

The interactions of PAs on patterned surfaces were examined using a JEM 1010 transmission electron microscope (TEM, JEOL USA, Inc., Peabody, MA) equipped with a digital camera and a JSM 5900 scanning electron microscope (SEM, JEOL USA, Inc., Peabody, MA) equipped with electron backscatter detector and digital camera.

7.4. RESULTS AND DISCUSSION

7.4.1. PEGDMA micro-wells and the FILM process

A schematic of the FILM process used to pattern the micro-well texture in PEGDMA on glass microscope slides is shown in Figure 7.1. Figure 7.2 shows SEM and AFM images of the micro-well texture. The micro-wells consist of an offset array of approximately 500 nm x 4 μm wells (the small side is slightly greater than 500 nm). The depth of the micro-wells is approximately 400 nm and the thickness of the residual layer of PEGDMA in Figure 7.2A is approximately 5 μm so that no portion of the glass

169

microscope slide substrate is exposed in the micro-wells. The depth of the micro-wells can be adjusted based on the depth etched into the silicon molds. Though we utilize a residual layer of 5 μm, the residual layer thickness can be set by controlling the final gap-spacing between the silicon mold and transparent substrate (e.g., glass microscope slides); the aligner has the capability of producing a residual layer of negligible thickness (contact print) to thicknesses upwards of tens of microns. As can be seen in Figure 6.2, the FILM process is able to imprint a dense array of high-fidelity microstructures over large areas, which is very important in performing cell studies. The micro-wells have a slightly inward sloping vertical profile, which is a mechanism of the sidewall profile of the silicon mold; sidewall profile is controllable during the silicon etching in mold fabrication. The slightly inward sloping profile helps facilitate the imprinting process.
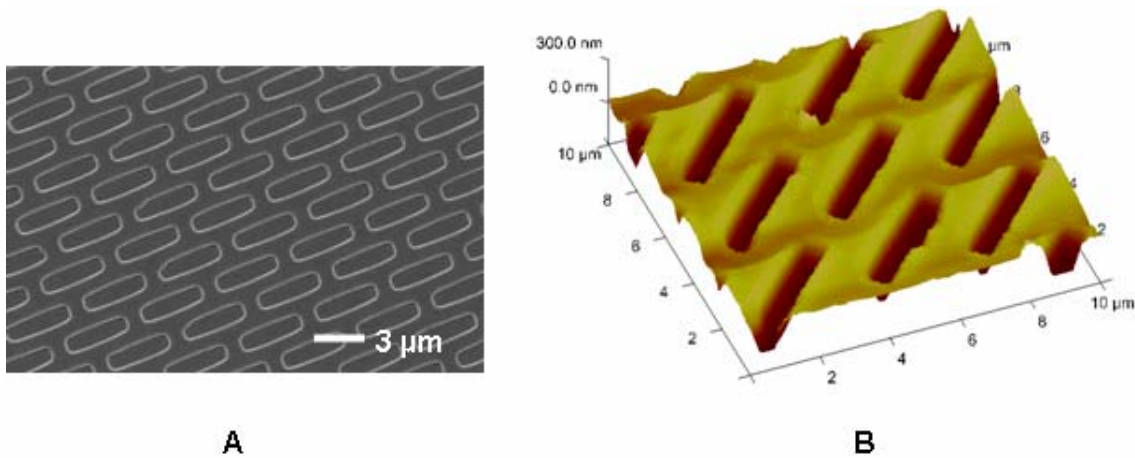
Figure 7.2. An (A) SEM and (B) AFM image of the PEGDMA micro-wells, which consist of an offset array of 500 nm x 4 μm wells. The micro-wells were imprinted using the FILM process.

170

One of the most important aspects of FILM is proper substrate chemical-derivatization (sections 7.3.3. and 7.3.4.). Silicon molds were treated with a fluorinated-silane that made the surface rather hydrophobic (contact angle = 104.2°; SD = 3.1°) to prevent sticking. Glass microscope slides were treated with a tethered silane (contact angle = 75.0°; SD = 6.5°) that attached to the acrylate groups in the PEGDMA upon polymerization by UV. Without proper surface treatment, the PEGDMA almost always delaminated from the glass slides.

As ECM *in vivo* comprises topography at sub-micron scales (< 1 µm), we hypothesized that PAs would respond to our quasi-mimetic micro-well scheme relative to smooth surfaces. The FILM process was very convenient in performing our study because it allowed us to imprint the micro-wells without using proprietary highly-dedicated imprinting technologies (e.g. IMPRIO 55, 100, and 250 by Molecular Imprints, Austin, TX). While dedicated imprinting technology works well, it is usually inaccessible to most tissue engineers and requires the use of expensive add-ons, molds, and polymer drop dispensers. We also found FILM to be cheaper and easier than photolithography since we didn't require an expensive quartz-chrome photomask; accordingly, issues resulting from the contact between a photomask and PEG (or any UV-curable material) is not an issue in FILM. Even if a quartz-chrome photomask is chemically-treated, contact between the photomask and hydrogel would degrade the chrome features of the mask over time as some sticking occurs between the hydrogel and mask. Because spin-coating low-viscosity hydrogels is extremely difficult, especially on chemically-treated substrates (e.g., a chemically modified glass microscope slide), polymer spreading on a substrate for patterning is usually accomplished naturally as the

171

photolithographic mask aligner brings the substrate and photomask together; thus, contact between the hydrogel and photomask is imminent. Additionally, though our tread-like micro-well structures have a sub-micron width (the small side is slightly greater than 500 nm) that isn't quite nanoscale (< 100 nm), FILM has the capability of imprinting nanostructures, which 365 nm *i*-line photolithography cannot produce.

7.4.2. Contact angle of water on PEGDMA micro-well surface

To characterize changes in hydrophobicity due the presence of the physical microstructures in the PEGDMA, we measured the contact angle of water on the microtextured PEGDMA, unpatterned PEGDMA, and a bare glass microscope slide. Figure 7.3 illustrates the results of our contact angle measurements. The contact angle of water on glass was found to be 9.3° (SD ≈ 3.2°; n = 12), but approached 0° when the substrate was hydroxylated by cleaning in a mixture of sulfuric acid and hydrogen peroxide or an oxygen plasma. The contact angle of water on unpatterned PEGDMA was found to be 29.6° (SD ≈ 5.7°; n = 8), which was slightly higher than that reported by Kim et al. [23], who reported a contact angle of water on PEGDMA to be approximately 22.5° (no SD reported); this discrepancy in the contact angle for unpatterned PEGDMA could be due to any number of reasons (e.g. slightly different polymer chemistry, cleanliness of surface, surface hydration, volume of sessile drop, spreading due to drop distance, etc.). The contact angle of water on the micro-well PEGDMA surface was higher at 68.4° (SD ≈ 8.4°), which demonstrates that the presence of the micro-wells makes the surface quite a bit more hydrophobic.

172

As discussed in Kim et al. [23], the increased hydrophobicity of a patterned surface is most likely due to the air pockets that exist in or between structures on a patterned surface (the Cassie state [24]); here, the micro-wells serve as small air pockets between PEGDMA surface area. Cassie et al. [24] reported that the contact angle of a
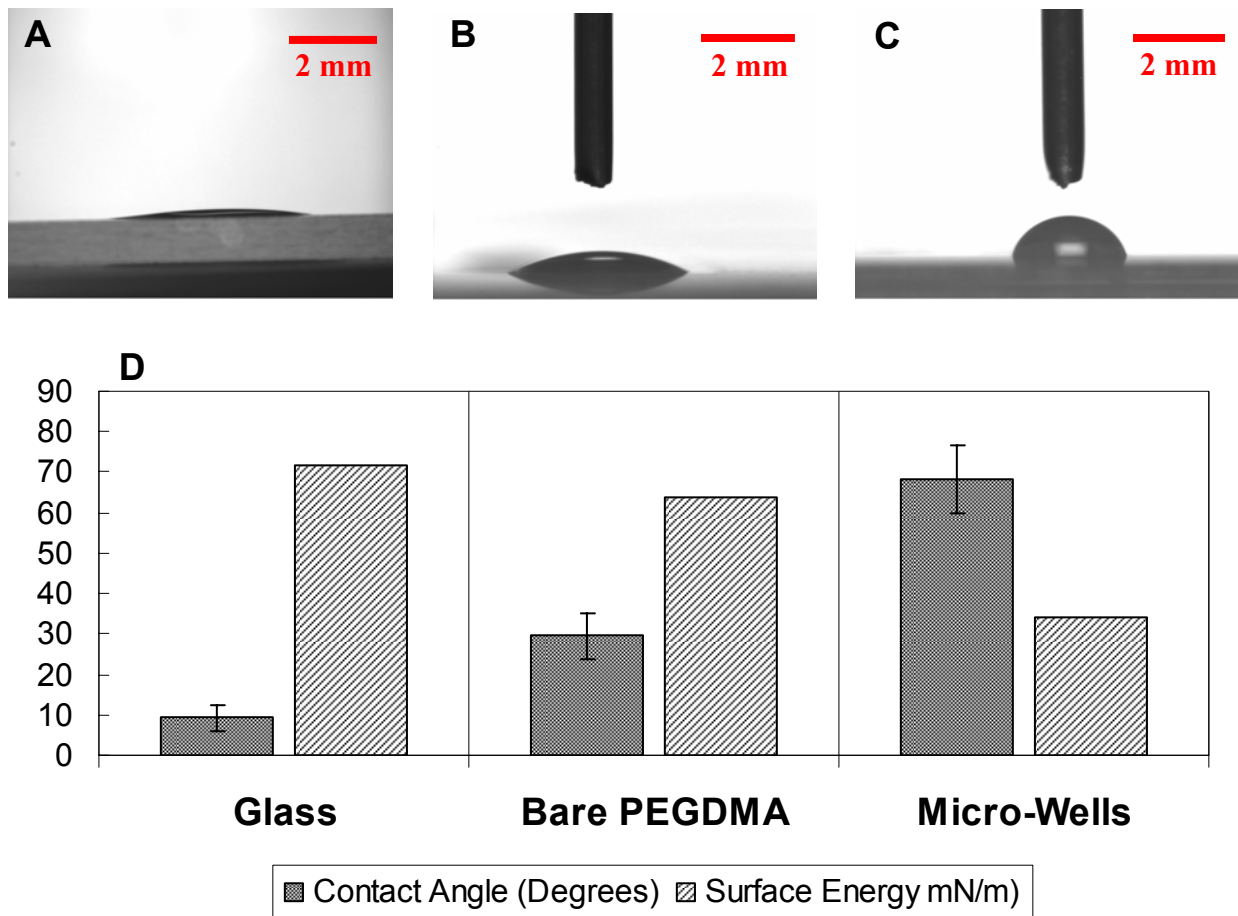
Figure 7.3. Contact angle measurements of water on (A) glass (9.3°; SD ≈ 3.2°; n = 12), (B) unpatterned (bare) PEGDMA (29.6°; SD ≈ 5.7°; n = 8), and (C) PEGDMA patterned with micro-well topography (68.4°; SD ≈ 8.4°; n = 30). Results for contact angle and associated surface energy calculations are summarized in (D); standard deviation for contact angle measurements is illustrated using error bars. The surface energies of glass (γ_{Glass}), bare PEGDMA ($\gamma_{\text{Bare PEG}}$), and the micro-well surface (γ_{Text}) were calculated to be $\gamma_{\text{Glass}} \approx 71.8$, $\gamma_{\text{Bare PEG}} \approx 63.6$, and $\gamma_{\text{Text}} \approx 34.1$ mN/m, respectively. Contact angle values are presented as mean values. Surface energy calculations are based on mean contact angles and were calculated using the GGFY model.

173

porous (micro-patterned) surface is theoretically related to the contact angle of a non-porous surface of the same material by Equation (7.1) (also demonstrated by [23]).

$$\cos\theta_{\text{Text}} = f_1 \cos\theta - f_2 \qquad (7.1)$$

In Equation (7.1), θ_{Text} is the contact angle on a micro-textured surface, θ is the contact angle on a bare unpatterned surface, f_1 is the fractional area of solid surface, and f_2 is the fractional area of air due to the presence of air pockets. It should be noted that $f_1 + f_2 = 1$ [23]. For the micro-well array, f_1 is the fraction of unpatterned PEGDMA and f_2 is the fraction of area consumed by the micro-wells, which represent air pockets or porosity in the surface. If we set $f_1 = 0.68$ and $f_2 = 0.32$ to represent our micro-textured surface and utilize the above reported contact angle $\theta \approx 29.6°$ for bare PEGDMA, we obtain $\theta_{\text{Text}} \approx 74°$, which agrees closely with our measured averaged contact angle of 68.4° and is within one standard deviation (SD = 8.4°, n = 30).

7.4.3. Surface energy of PEGDMA micro-well surface

Contact angle is symbolically related to surface energy as [15]:

surface energy $\gamma_{\text{SV}} = F^{-1}$ (contact angle θ_{S}, surface tension of test liquid γ_{LV})

where F^{-1} represents an inverted functional relationship. If we have a value for the contact angle of a test fluid on a particular solid surface and the surface tension of that test fluid, we can backsolve to find the surface energy of the surface given an appropriate

174

theoretical model. To estimate surface energies for glass, bare PEGDMA, and our microtextured PEGDMA surface, we employ the Girifalco-Good-Fowkes-Young (GGFY) model [17] given by:

$$[1 + \cos(\theta_S)] \cdot \gamma_{LV} = 2\sqrt{(\gamma_{SV}\gamma_{LV})} - \pi \qquad (7.2)$$

π is the vapor pressure, which is assumed to be approximately zero ($\pi \approx 0$) in our calculations, and θ_S = contact angle of the surface in question. Since water is used as the test fluid, we can use the known value for the surface tension of water in air at room temperature, $\gamma_{LV} \approx 72.8$ mN/m. From Equation (7.2), we estimate the surface energy of the micro-textured surface to be $\gamma_{Text} \approx 34.1$ mN/m. In a similar manner, we estimate the surface energy of bare PEGDMA and glass to be $\gamma_{Bare\,PEG} \approx 63.6$ mN/m and $\gamma_{Glass} \approx$ 71.8 mN/m, respectively, based on our contact angle data. Our calculation for the surface energy of glass is consistent with published data and lies between those reported for perfectly clean glass (~ 73 mN/m) and ordinary glass (~ 70 mN/m) [15]. Figure 7.3 summarizes the results of our surface energy calculations. It is important to note that the value for surface energy calculated using the GGFY model is approximate. Employing different models (e.g., Zisman, Owens-Wendt, Wu Harmonic Mean, Lewis Acid-Base Theory) may yield different, yet still approximate, results.

175

7.4.4. PAs interacting with micro-wells

Physical topographical cues within the extracellular microenvironment can influence cellular responses including attachment and adhesion, migration, differentiation, as well as the production of new tissue. Due to the lack of available biological or clinical data in the literature supporting the interaction of PAs with sub-micron (< 1 µm) texture, an initial study was conducted to investigate this interaction. Rat PAs were harvested and cultured as previously described by us [20-22]. The PEGDMA was derivatized with collagen I [25]. Cells were cultured on both glass (control) and the patterned PEGDMA. Figures 7.4(A,B) illustrate a distinct difference in cell morphology between control and microtextured PEG (magnification is the same).

In the control case, the PAs are quite spread out, displaying conventional morphology observed on glass and tissue culture plastic surfaces. In contrast, PAs on the PEG micro-wells are more confined and appear to have cell processes adherent to the micro-well structures. The cell pattern observed in Figure 7.4B is very reminiscent of keratinocyte grown on micro-pillar structures derivatized with fibronectin [26]. The micro-wells seem to provide traction for the PAs to the PEG as the added surface area provides gripping to the cells' processes. The morphological confinement of the cells on the micro-wells relative to those on the control glass is consistent with the surface energy calculations of Figure 7.3. As contact angle decreases or surface energy increases, the PAs cell body tend to spread out; to the contrary, the PAs cell body tend to curl up on surfaces with a low surface energy.

176
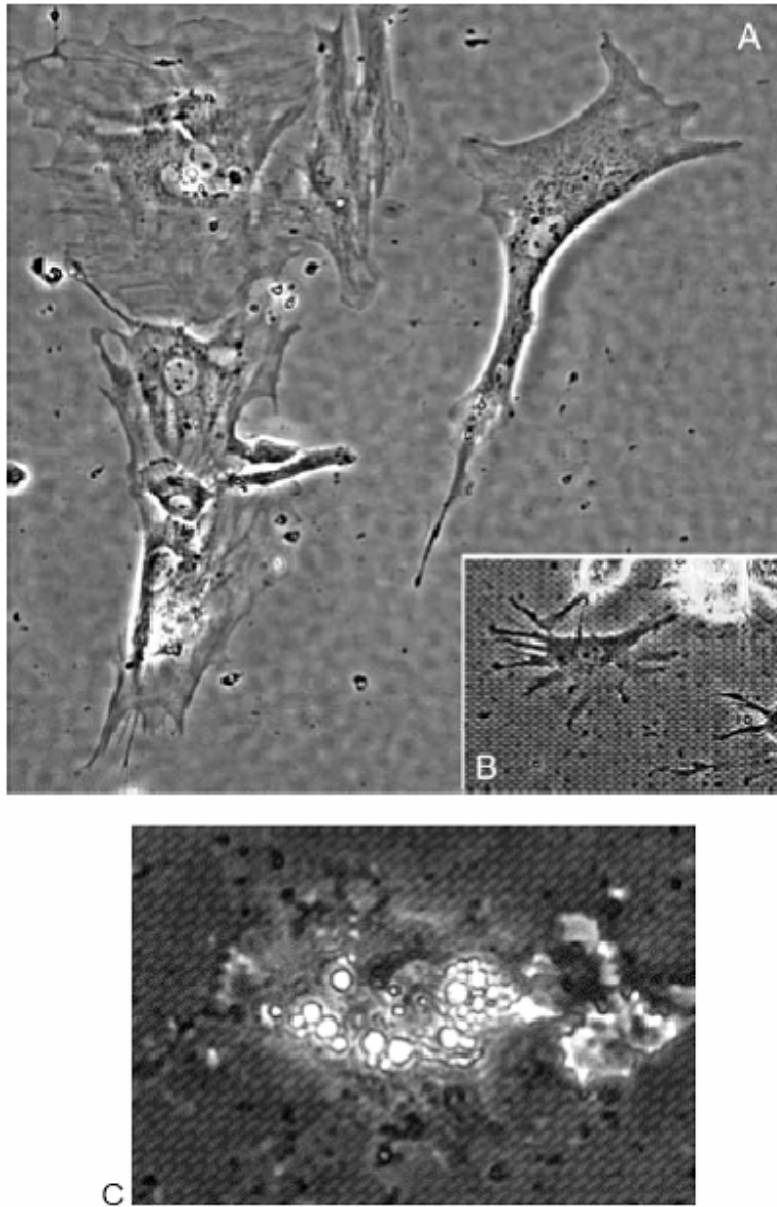
Figure 7.4. PAs seeded on (A) a glass slide and (B) micro-textured PEG (500 nm x 4 μm wells, see Figure 7.2). Both images are at 200x magnification for direct comparison. (C) PA undergoing differentiation as evidenced by lipid loading.

In addition to morphological changes, individual PAs were observed to undergo differentiation (Figure 7.4C), a process that normally occurs only after PAs are surrounded by other PAs. This is evident by lipid-loading or the coalescence of lipid droplets (bright spots) within the PA in Figure 7.4C. The SEM images in Figures 7.5 and 7.6 demonstrate individual cell processes and cell membranes interacting and, in fact, growing into the micro-wells. The white boxes in Figures 7.5 and 7.6 show magnified areas (see figure captions). Because the dimensions of the cell processes of the PAs are smaller than the micro-well structures, decreases in effective surface energy due to the air gaps in the micro-well topography have intrinsically little affect on the processes' conformation; however, changes in surface energy due to the presence of nanoscale topography, where the dimension of the processes is larger than the air gaps in the surface, would seemingly affect the conformation of the cell processes since the nanofeatures are too small for the processes to grow into. For the micro-well surface, the conformation of the cell processes is affected by the added surface area due to the presence of the micro-wells, which effectively increases the density of surface area in the horizontal plane of the PEGDMA surface.

7.5. CONCLUSIONS

Here, we study the qualitative affects of a tread-like micro-well topography in PEGDMA on the morphology and behavior of PAs in culture. The micro-well texture is patterned in the PEGDMA using the FILM nanomanufacturing process. We are the first to employ FILM for a tissue engineering application and found that it was more

178
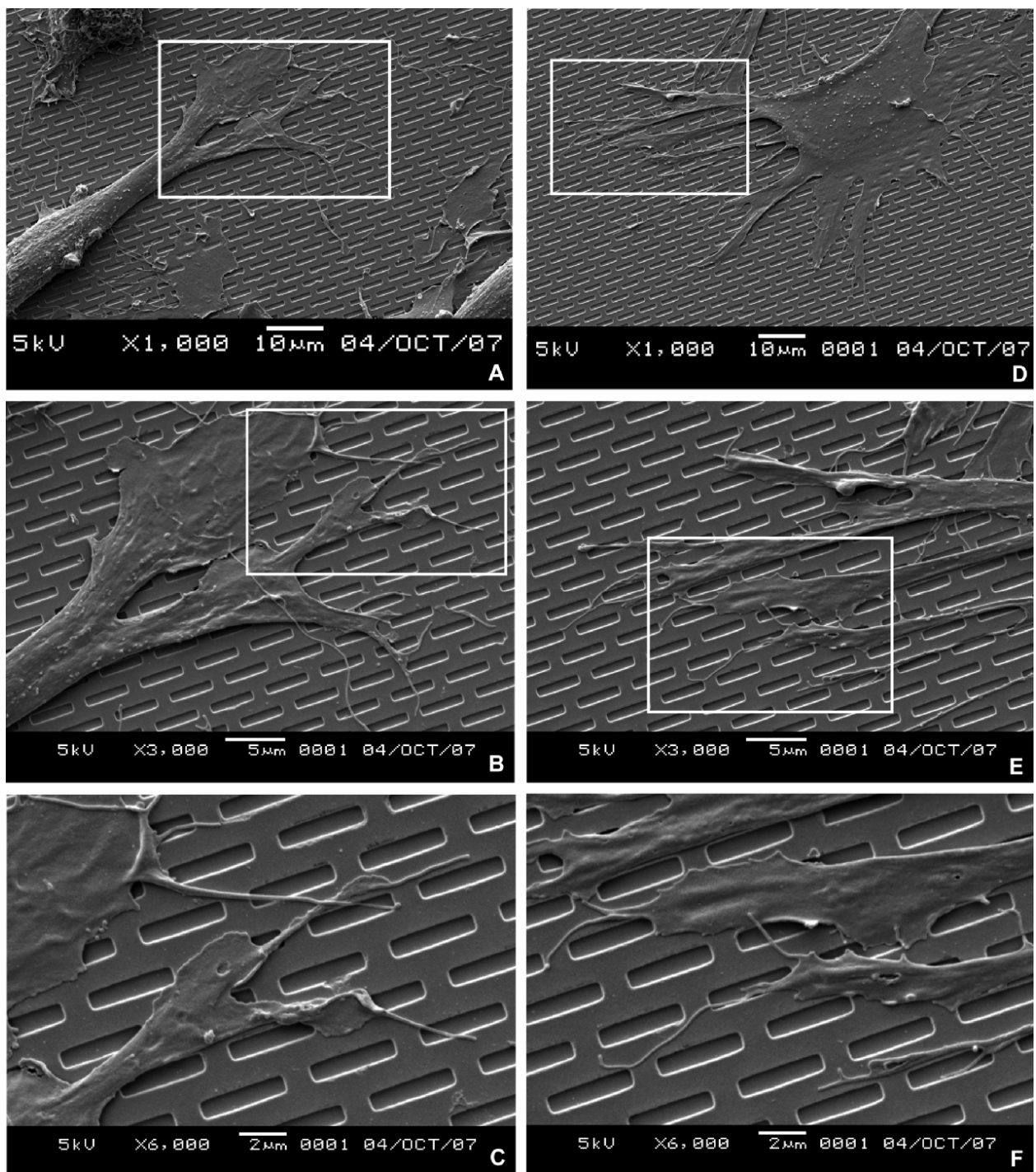
Figure 7.5. SEM images of PAs on the biofunctionalized, PEG micro-well array. Individual cell processes and cell membranes interact with the micro-well topography, growing into the micro-wells. (A-C) and (D-F) depict the same area at different magnifications. White boxes denote magnified area. (A,D) 1,000x. (B, E) 3,000x. (C, F) 6,000x.

179
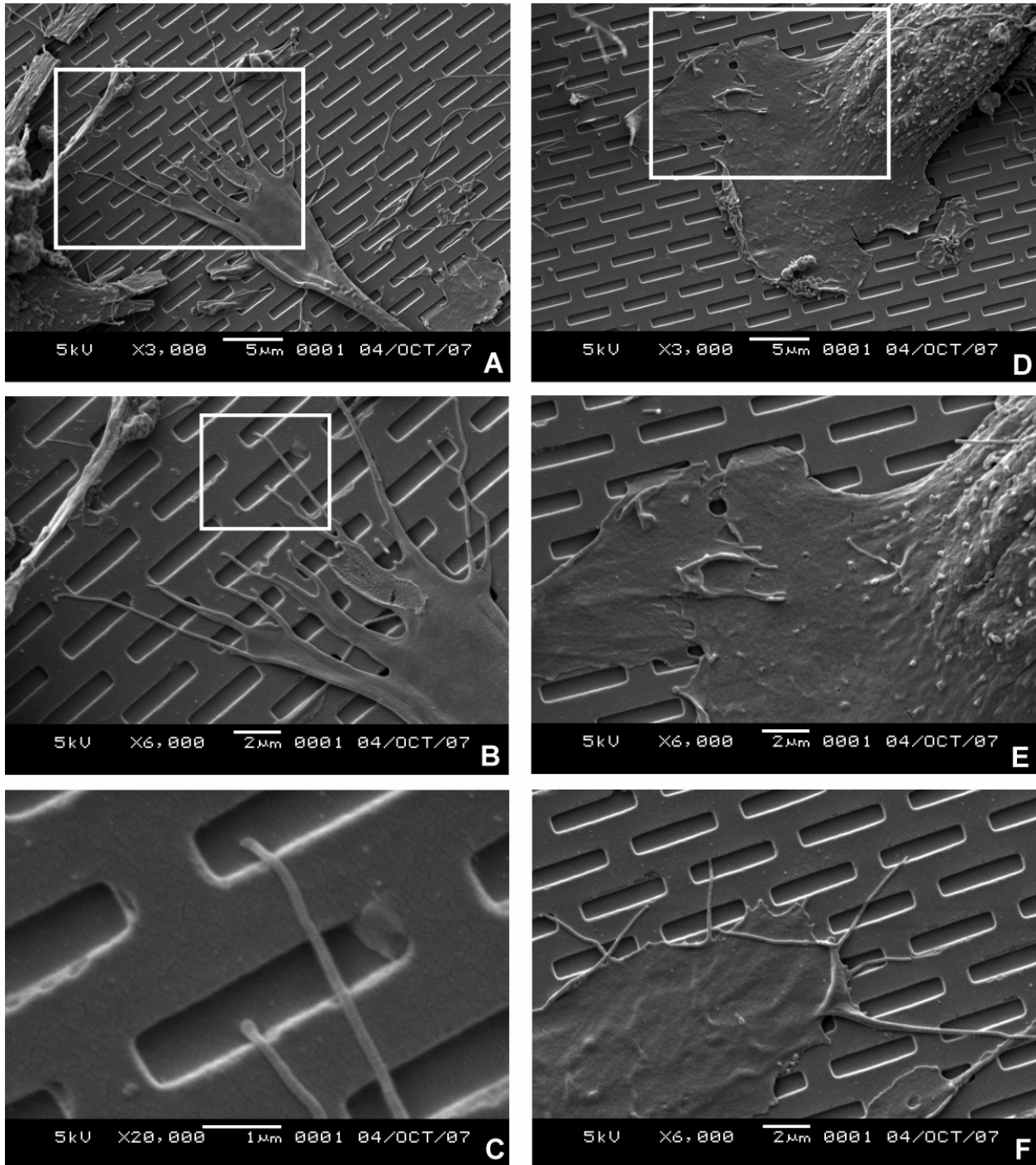
Figure 7.6. SEM images of PAs on a biofunctionalized, PEG micro-well array. Individual cell processes and cell membranes interact with the micro-well topography, growing into the micro-wells. (A-C) and (D-E) depict the same area at different magnifications. White boxes denote magnified area. (A,D) 3,000x. (B, E, F) 6,000x. (C) 20,000x.

180

convenient than other imprinting processes like S-FIL and UV-NIL and 365 nm *i*-line photolithography. The FILM process was able to imprint the micro-well texture with high fidelity over a large area while only requiring the use of common mask aligner technology available in most cleanrooms and a cheap silicon imprinting mold. Contact angle and surface energy analysis were performed to characterize the micro-well scheme; the analyses demonstrated that the presence of the micro-wells in the PEGDMA increases hydrophobicity. According to theory, the increase in hydrophobicity of the micro-well surface is due to the micro-wells mimicking small air pockets in the solid PEGDMA surface.

Our studies demonstrate that PAs uniquely interact with the micro-well PEGDMA surfaces derivatized with Collagen I, and that cell behavior is qualitatively modulated compared with planar control surfaces. Observation from cell culture is consistent with changes in hydrophobicity demonstrated by the surface energy calculations. We believe that the micro-well topography may be useful in implantable adipose tissue scaffolds in modulating PA-response and tissue formation. Our further work will be devoted to performing competition assays to determine the types of physical micro- and nanotopographies that PAs most prefer in an effort to more thoroughly understand the design aspects of implantable adipose tissue scaffold fabrication. We will also be investigating the effects of varying mechanical properties of PEGDMA and the addition of adhesion peptides and other biochemistry (e.g., growth factor) on PA behavior.

7.6. ACKNOWLEDGEMENTS

7.7. REFERENCES

1. Fozdar D. Y., Wu X., Patrick C. W., Chen S., Micro-well texture printed into PEG hydrogels using the FILM nanomanufacturing process affects the behavior of preadipocytes, *Biomedical Microdevices*, 2008; **10** pp. 839-849.

2. Fozdar D. Y., Zhang W., Palard M., Patrick Jr. C. W., Chen S. C., Flash Imprint Lithography Using A Mask Aligner (FILM): A Method for Printing Nanostructures in Photosensitive Hydrogels for Tissue Engineering, *Nanotechnology*, 2008; **19** pp.

3. Wang X. C., Qiao Q., Liu Z. F., Zhao R., Zhang H. L., Yang Y. J., et al., Free anterolateral thigh adipofascial flap for hemifacial atrophy, *Annals of Plastic Surgery*, 2005; **55** pp. 617-622.

4. Hunt J. A., Hobar P. C., Common craniofacial anomalies: Conditions of craniofacial atrophy/hypoplasia and neoplasia, *Plastic and Reconstructive Surgery*, 2003; **111** pp. 1497-1508.

5. Vaienti L., Soresina M., Menozzi A., Parascapular free flap and fat grafts: Combined surgical methods in morphological restoration of hemifacial progressive atrophy, *Plastic and Reconstructive Surgery*, 2005; **116** pp. 699-711.

6. Asai S., Kamei Y., Nishibori K., Katoh T., Torii S., Reconstruction of Romberg disease defects by omental flap, *Annals of Plastic Surgery*, 2006; **57** pp. 154-158.

7. Billings Jr. E., May Jr. J. W., Historical review and present status of free graft autotransplantation in plastic and reconstructive surgery., *Plastic Reconstructive Surgery*, 1989; **83** pp. 368-381.

8. Ersek R. A., Transplantation of purified autologous fat: A 3-year follow-up disappointing, *Plastic Reconstructive Surgery*, 1991; **87** pp. 219-227.

9. Patrick C. W., Tissue engineering strategies for adipose tissue repair, *Anatomical Record*, 2001; **263** pp. 361-366.

10. Patrick C. W., Adipose tissue engineering: The future of breast and soft tissue reconstruction following tumor resection, *Seminars in Surgical Oncology*, 2000; **19** pp. 302-311.

11. Sniadecki N., Desai R. A., Ruiz S. A., Chen C. S., Nanotechnology for cell-substrate interactions, *Annals of Biomedical Engineering*, 2006; **34** pp. 59-74.

12. Abrams G. A., Goodman S. L., Nealey P. F., Franco M., Murphy C. J., Nanoscale topography of the basement membrane underlying the corneal epithelium of the rhesus macaque, *Cell and Tissue Research*, 2000; **299** pp. 39-46.

13. Yim E. K. F., Reano R. M., Pang S. W., Yee A. F., Chen C. S., Leong K. W., Nanopattern-induced changes in morphology and motility of smooth muscle cells, *Biomaterials*, 2005; **26** pp. 5405-5413.

14. Colburn M., Johnson S., Stewart M., Damle S., Bailey T., Choi B. J., et al., Step and Flash Imprint Lithography: A New Approach to High-Resolution Patterning, *Proceedings of the SPIE's 24th International Symposium on Microlithography: Emerging Lithographic Technologies III*, Santa Clara, CA, March 1999; **3676**, pp. 379-389.

15. Adamson A. W., *Physical chemistry of surfaces*, John Wiley and Sons, New York, 1982.

16. Andreas J. M., Hauser E. A., Tucker W. B., Boundary Tension by Pendant Drops, *J Phys Chem*, 1938; **42** pp. 1001-1019.

17. Girifalco L. A., Good R. J., A Theory for the Estimation of Surface and Interfacial Energies. I. Derivation and Application to Interfacial Tension, *J Phys Chem*, 1957; **61** pp. 904-909.

18. Fowkes F. M., Harkins W. D., The State of Monolayers Adsorbed at the Interface Solid--Aqueous Solution, *J Am Chem Soc*, 1940; **62** pp. 3377-3386.

19. Adamson A. W., Shirley F. P., Kunichika K. T., Contact angles on molecular solids : I. Ice, *Journal of Colloid and Interface Science*, 1970; **34** pp. 461-468.

20. Patel P. N., Gobin A. S., West J. L., Patrick C. W., Poly(ethylene glycol) Hydrogel System Supports Preadipocyte Viability, Adhesion, and Proliferation, *Tissue Engineering*, 2005; **11** pp. 1498-1505.

21. Patrick C. W., Chauvin P. B., Hobley J., Reece G. P., Preadipocyte Seeded PLGA Scaffolds for Adipose Tissue Engineering, *Tissue Engineering*, 1999; **5** pp. 139-151.

22. Patrick C. W., Zheng B., Johnston C., Reece G. P., Long-Term Implantation of Preadipocyte-Seeded PLGA Scaffolds, *Tissue Engineering*, 2002; **8** pp. 283-293.

23. Kim P., Kim D. H., Kim B., Choi S. K., Lee S. H., Khademhosseini A., et al., Fabrication of nanostructures of polyethylene glycol for applications to protein adsorption and cell adhesion, *Nanotechnology*, 2005; **16** pp. 2420-2426.

24.   Cassie A. B. D., Baxter S., Wettability of Porous Surfaces, *Transactions of the Faraday Society*, 1944; **40** pp. 546 - 551.

25.   Yim E. K. F., Pang S. W., Leong K. W., Synthetic nanostructures inducing differentiation of human mesenchymal stem cells into neuronal lineage, *Experimental Cell Research*, 2007; **313** pp. 1820-1829.

26.   Steinberg T., Schulz S., Spatz J. P., Grabe N., Mussig E., Kohl A., et al., Early keratinocyte differentiation on micropillar interfaces, *Nano Letters*, 2007; **7** pp. 287-294.

185

Chapter 8: Conclusions

8.1. SUMMARY OF DISSERTATION

8.1.1. Chapter 2 summary

Many advanced patterning and metrology techniques were utilized to fabricate and characterize the nanotextured substrates used in the studies presented in Chapters 4, 5, 6, and 7. Chapter 2 provided an overview of these nanofabrication and nanometrology processeses. Table 8.1 summarizes the techniques that were reviewed.

Table 8.1. Nanofabrication, nanometrology, and nanoprocessing techniques used in the works reported in this dissertation.

Nanolithography
Optical lithography
Soft lithography
Electron beam lithography
Nanoimprint lithography
Nanometrology
Atomic force microscopy
Scanning electron microscopy
Nanoprocessing
Reactive-Ion Etching
Chemical Vapor Deposition
Metal thermal deposition
Metal lift-off

8.1.2. Chapter 3 summary

Statistical methods were utilized to compare the data obtained in the experiments reported in Chapters 4 and 5. Chapter 3 summarizes the statistical methods to give readers a better understanding as to how the data was interpreted, analyzed, and compared. Statistical methods were used to compare two sample means or compare a mean from a single sample with an expected value (null hypothesis). The statistical methods utilized included one and two-sample t-tests for measurement and binomial data (yes / no outcome), one-way balanced ANOVA, and χ^2-tests. Appendix A contains the t- and χ^2-distribution charts used to determine p-values and statistical significance. Unless otherwise noted, a 90% or 95% confidence interval ($\alpha = 0.10$ or 0.05) served as a marker flagging statistical significance. Data that did not meet but approached our criteria for statistical significance, was deemed an interesting trend and noted accordingly.

8.1.3. Chapter 4 summary [1]

Rat hippocampal neurons were cultured on various surfaces consisting of arrays of nanopatterned features with sub-cellular dimensions. Topographies included lines (grooves) of *(1)* 300-nm and *(2)* 2-µm width and holes of *(3)* 300-nm and *(4)* 2-µm diameter. The various shapes and sizes were chosen based upon observations in the literature, which has clearly showed that biological structures contain features with nanoscale dimensions. For example, the basement membrane of organs and ECM proteins like collagen and laminin have been shown to have fibrous (lines) and pores (holes) with dimensions as small as few hundred nanometers [2-8]. After a 24 hour

187

culture, cells were stained with DAPI and Tau-1 and imaged by optical and scanning electron microscopy. The goal of the study was to examine the effects of physical surface structures having sub-cellular dimensions on the differentiation (axon formation) and development of the neurons.

8.1.4. Chapter 5 summary [9]

Using the same shapes and sizes of features introduced in Chapter 4, competition assays were performed to determine the features' relative strengths as physical cues influencing axon differentiation and growth. Arrays of the features were arranged into a rectangular four-quadrant grid where each quadrant consisted of an array of a single feature separated from juxtaposing quadrants by a small gap. The competitions consisted of placing individual hippocampal neurons in the gaps between quadrants using a special micro-positioning system and observing the neurons response after 24 hours in culture. The topography onto which the neurons established their axon was considered the winner of the competition and to influence the neuron more. Competitions were performed between the topographies to determine axon preference based on feature size and shape. Additionally, single neurons micropositioned on the outer border of each of the arrays and competitions were performed between the topographies and bare surface.

8.1.5. Chapter 6 summary [10]

Key to patterning surfaces with features that mimic the ECM of cells is having the nanofabrication tools capable of printing features in biomaterials at the nanoscale. UV-curable hydrogels like polyethylene glycol (PEG) and hyaluronic acid (HA) are thought

to be ideal substrate materials in tissue scaffolds because of their mechanical properties, biocompatibility, and biodegradability. In Chapter 6, we reported a new nanoimprinting technique used to pattern nanoscale features in UV-curable hydrogels using conventional optical mask aligner technology. We coin the process <u>F</u>lash <u>I</u>mprint <u>L</u>ithography Using A <u>M</u>ask Aligner (FILM), and demonstrated FILM by printing arrays of features as small as 50 nanometers in UV-curable polyethylene glycol dimethacrylate (PEG-DMA). A myriad of feature shapes were imprinted including groove-ridges, circular pillars, square pillars, and rectangular wells.

8.1.6. Chapter 7 summary [11]

Preadipocytes (PAs) play a key role in tissue engineering strategies for growing new adipose tissue because they can be readily extracted from a patient and expanded *ex vivo* [12-14]. Though much is known about the molecular biology of PAs, including the differentiation process into mature adipocytes, little is known regarding the interactions of PAs with their native ECM. Like neurons, the ECM of PAs consists of structural proteins and other biochemicals that have textures with nanoscale resolution. Chapter 7 reported a new study conducted examining the effects of a biomimetic nanostructured surface on the behavior of PAs in culture. 500 nm x 4 μm rectangular microwells were fabricated in PEGDMA using FILM (see section 8.1.5 and Chapter 6), and PAs were seeded onto the surface and cultured. The study was the first to utilize the FILM process in a tissue engineering application. Moreover, the PEG surfaces were theoretically characterized by contact angle analysis. Interactions of PAs with the PEG surface were visualized by optical microscopy and SEM.

189

8.2. RESULTS, CONCLUSIONS, AND RECOMMENDATIONS

8.2.1. Chapter 4 results and conclusions

Several aspects of neuron behavior were investigated including *(1)* cell adhesion, *(2)* axon establishment (polarization), *(3)* axon length, *(4)* axon alignment, and *(5)* cell morphology. We found that cell adhesion was not greatly affected by topography though trends showed that adhesion was better on the smaller 300-nm structures than the larger 2-μm structures. Polarization was found to be markedly greater on topography than smooth surface and was greater on the 300-nm features than the 2-μm features; Polarization appeared to be more feature size dependent than feature shape dependent. Axon length was found to be greater on the lines than the smooth surface and holes. In contrary to polarization, elongation appeared to depend more on feature shape than feature size. In agreement with prior published reports [15], we found that axons aligned (Figure 4.4) predominately parallel to the line topographies regardless of feature size; however, we found that alignment was more perpendicular to the 300-nm lines than the 2-μm lines and that complete perpendicular alignment (at 80-90° angle to the grooves) only occurred on the 300-nm lines. By comparing axon alignment with axon elongation, it was found that axons which were perpendicular to the 300-nm lines had markedly longer axons than other alignments; moreover, we found that axons showing extensive elongation (> 100 μm) only occurred when the axons were aligned in some fashion.

8.2.2. Chapter 5 results and conclusions

For the competitions between the smooth surface and the topographies, the distance between the neurons and the topography was found to greatly affect whether the

cells chose topography, moreover, a distance of roughly 30 µm was observed to be a limit over which neurons were unable to sense the nearby topography. For distances under 30 µm, neurons statistically preferred topography over smooth surface. The competitions with bare surface showed that neurons statistically preferred the 300-nm holes relative to all other topographies. For the competitions comparing the topographies, neurons statistically preferred the 300-nm lines over the 2-µm lines but preferred the 300-nm holes over that 300-nm lines. Moreover, neurons were also found to statistically prefer holes over lines.

When deciphering the topography versus smooth data, it was important to distinguish between statistical measurements and trends. Based on trends, the competitions between the topographies and smooth surfaces showed that neurons preferred the 2-µm lines over the 300-nm lines and 2-µm holes, though statistically less than the 300-nm holes; however, the opposite was seen in the experiments conducted between topographies where neurons were found to statistically prefer the 300-nm lines over the 2-µm lines and the 300-nm holes over the 300-nm lines, though trends showed that the neurons preferred the 2-µm holes over the 300-nm holes.

8.2.3. Chapters 4 and 5 recommendation

Results of the studies conducted in Chapters 4 and 5 suggest that incorporating microscale and sub-microscale topography on biomaterial surfaces may enhance biomaterials' ability to influence axon development and regeneration.

8.2.4. Chapter 6 results and conclusions

Using FILM, structures as small as 50 nm were imprinted in PEG consistently. We found several aspects of the FILM process quite convenient. By using the well-controlled UV light source of an optical aligner, an aligner's special wedge error compensation function, and other favorable characteristics of an optical aligner, FILM is able to imprint nanoscale structures with good fidelity over large areas (depends on mold area) with the automation and reproducibility of dedicated nanoimprinting tools. FILM is also capable of handling any UV-curable material, without the need for special material dispensers or other add-ons required by proprietary or dedicated nanoimprinting tools.

8.2.5. Chapter 7 results and conclusions

The study of chapter 7 was the first to utilize FILM for a tissue engineering application. The most difficult aspect of using PEGDMA in cell studies involved maintaining good adhesion of the hydrogel material on the substrate (glass microscope slide) for cultures lasting several days. We also found hydrogel swelling to be problematic for dense arrays of nanoscale structures; however, we were able to limit swelling by changing the hydrogel chemistry. After culturing the PAs and analyzing them with optical microscopy and SEM, we found that PAs showed conformational changes and differences in adhesion on the micro-wells than on smooth surface. PAs were also observed to undergo adipogenesis in isolation.

192

8.2.6. Chapter 6 and 7 recommendation

Like with neurons, PAs appear to interact differently on topography than smooth surface. Results of the studies conducted in Chapters 6 and 7 suggest that incorporating microscale and sub-microscale topography on biomaterial surfaces may enhance biomaterials' ability to influence adipogenesis. The FILM process was also a great tool for fabricating sub-microscale features in UV-curable materials (e.g., hydrogels). FILM was cheap, simple, and quick, making it a useful tool in creating substrates for performing cell studies.

8.3. FUTURE WORK

8.3.1. Investigating sub-100 nm features

Because the ECM of hippocampal cells is patterned down to the nanoscale, *in vivo*, future work will be devoted to investigating the effects of features less than 100 nm in dimension (i.e., size-scales another order of magnitude smaller) on nerve cell maturation. Since sub-100 nm features approach the molecular level in dimensions, these features may optimize cell-biomaterial interactions enhancing the stimulative and adhesive effects of the scaffolds.

8.3.2. Gradients of topography

Gradients are responsible for the movement of various quantities throughout nature, from the flow of heat due to temperature gradients, the flow of current due to voltage gradients, or the flow of fluids due to pressure gradients. Moreover, it is widely known that chemical gradients are vital in influencing cell migration and orientation, *in*

193

vivo. Along these lines, few studies have investigated the effects of gradients of structure-size on the behavior of PAs and neurons to this point. We are interested in fabricating gradients of features ranging in size from several microns down to tens of nanometers.

8.3.3. Axon modeling in response to topography

From a theoretical point of view, we are currently interested in building on work conducted by Forciniti et al. [16] by developing a physical model that can better characterize neurite outgrowth / elongation and alignment on synthetically-patterned surfaces, mainly line arrays. One aspect of our model capitalizes on the fact that a rather large number of physical variables affect cell response, including those referring to substratum geometry and material properties. We are seeking to describe relationships between dimensionless combinations of independent variables affecting polarization, growth, and alignment and the dependent variables directly describing growth / alignment without having to run experiments requiring isolation of the individual independent dimensional variables. Such a model, heuristic and deterministic, simultaneously, could prove to be quite useful in designing scaffolds as certain independent variables seem to be excessively difficult or time-consuming to isolate.

8.4 OVERALL DISSERTATION CONCLUSIONS

Overall, our experiments showed that microscale and sub-microscale (< 1 μm) features affect the behavior of nerve cells and preadipocytes (PAs) relative to smooth

substrates; thus, the inclusion of topography on 2D and 3D nerve and soft tissue scaffolds may be beneficial in restoring damaged tissue.

In the case of the nerve cells, considering the experiments of both Chapters 4 and 5, topography stimulates axon initiation from neurites relative to smooth surfaces; moreover, sub-microscale features appear to stimulate axon initiation more than order-of-magnitude larger microscale features. Results from the competition assays of Chapter 5 showed mixed results if one considers both trends (non-statistical) and statistical results, but statistical measurements showed that axon initation was stimulated greatest on sub-microscale holes. The differences between topography of varying size and shape in stimulating axon initiation appears less decisive than between topography and smooth surface; however, it was clear by the competitions between the topographies and smooth surface, that distance plays a major role in whether topography influences nerve cell behavior.

Line topographies were found to modulate axon alignment. Axons align mostly in parallel to both microscale and sub-microscale lines, but axons become statistically more perpendicular as line size is reduced. Moreover, axons appear to grow longer on lines than holes or smooth surface, though little correlation can be made between alignment and length, except in the case of axons that are aligned almost entirely (completely) perpendicular to lines, which we found to occur only on sub-microscale lines.

Experiments conducted with the PAs on sub-microscale topography showed that the topography makes intimate contact with the PAs altering cytoskeletal conformation and inducing adipogenesis in isolated PAs. The experiments also showed the efficacy of

using the FILM process for fabricating patterned surfaces for cell-based tissue-engineering applications. The FILM process can conveniently print micro- and nanoscale features quickly, easily, and inexpensively, using existing mask aligner technology. FILM can be used to pattern a dense array of features over a large area in PEG or any other UV-curable material. Feature-filling simulations showed that feature-filling in FILM is dependent on the aspect-ratio of the nanofeatures to be printed. Moreover, the vacuum step in FILM (Figure 6.1(b)) is necessary for printing high-aspect ratio features.

196

8.4. REFERENCES

1.   Fozdar D. Y., Lee J. Y., Schmidt C. E., Chen S., Neurons respond uniquely to topographies of various sizes and shapes, *Biomaterials*, 2009; **(submitted)** pp.

2.   Comisar W. A., Hsiong S. X., Kong H. J., Mooney D. J., Linderman J. J., Multi-scale modeling to predict ligand presentation within RGD nanopatterned hydrogels, *Biomaterials*, 2006; **27** pp. 2322-2329.

3.   Sniadecki N., Desai R. A., Ruiz S. A., Chen C. S., Nanotechnology for cell-substrate interactions, *Annals of Biomedical Engineering*, 2006; **34** pp. 59-74.

4.   Abrams G. A., Goodman S. L., Nealey P. F., Franco M., Murphy C. J., Nanoscale topography of the basement membrane underlying the corneal epithelium of the rhesus macaque, *Cell and Tissue Research*, 2000; **299** pp. 39-46.

5.   Yim E. K. F., Reano R. M., Pang S. W., Yee A. F., Chen C. S., Leong K. W., Nanopattern-induced changes in morphology and motility of smooth muscle cells, *Biomaterials*, 2005; **26** pp. 5405-5413.

6.   Abrams G. A., Murphy C. J., Wang Z. Y., Nealey P. F., Bjorling D. E., Ultrastructural basement membrane topography of the bladder epithelium, *Urological Research*, 2003; **31** pp. 341-346.

7.   Curtis A., Wilkinson C., Nantotechniques and approaches in biotechnology, *Trends in Biotechnology*, 2001; **19** pp. 97-101.

8.   Hernandez J. C. R., Sanchez M. S., Soria J. M., Ribelles J. L. G., Pradas M. M., Substrate chemistry-dependent conformations of single laminin molecules on polymer surfaces are revealed by the phase signal of atomic force microscopy, *Biophysical Journal*, 2007; **93** pp. 202-207.

9.   Fozdar D. Y., Lee J. Y., Schmidt C. E., Chen S., Response of neurons to competing topographical features of various sizes and shapes, *Nano Letters*, 2009; **(submitted)** pp.

10.   Fozdar D. Y., Zhang W., Palard M., Patrick C., Chen S., Flash imprint lithography using a mask aligner: a method for printing nanostructures in photosensitive hydrogels, *Nanotechnology*, 2008; **19** pp. 1-13.

11.   Fozdar D. Y., Wu X., Patrick C. W., Chen S., Micro-well texture printed into PEG hydrogels using the FILM nanomanufacturing process affects the behavior of preadipocytes, *Biomedical Microdevices*, 2008; **10** pp. 839-849.

197

12.   Patrick C. W., Adipose tissue engineering: The future of breast and soft tissue reconstruction following tumor resection, *Seminars in Surgical Oncology*, 2000; **19** pp. 302-311.

13.   Hausman G. J., Richardson R. L., Newly recruited and pre-existing preadipocytes in cultures of porcine stromal-vascular cells: Morphology, expression of extracellular matrix components, and lipid accretion, *Journal of Animal Science*, 1998; **76** pp. 48-60.

14.   Entenmann G., Hauner H., Relationship between replication and differentiation in cultured human adipocyte precursor cells, *American Journal of Physiology-Cell Physiology*, 1996; **39** pp. C1011-C1016.

15.   Rajnicek A. M., Britland S., McCaig C. D., Contact guidance of CNS neurites on grooved quartz: influence of groove dimensions, neuronal age and cell type, *Journal of Cell Science*, 1997; **110** pp. 2905-2913.

16.   Forciniti L., Schmidt C., Zaman M., Computational Model Provides Insight into the Distinct Responses of Neurons to Chemical and Topographical Cues, *Annals of Biomedical Engineering*, 2009; **37** pp. 363-374.

Appendix A: Statistical distribution charts[1]

Table A.1. *t*-distribution

				α levels				
Two-sided	.20	.10	.05	.04	.02	.01	.002	.001
One-sided	.10	.05	.025	.02	.01	.005	.001	.0005
					Percentiles			
df	0.90	0.95	0.975	0.98	0.99	0.995	0.999	0.9995
1	3.078	6.314	12.7062	15.8946	31.8206	63.6570	318.317	636.607
2	1.886	2.920	4.3027	4.8487	6.9646	9.9248	22.327	31.598
3	1.638	2.353	3.1824	3.4819	4.5407	5.8409	10.215	12.924
4	1.533	2.132	2.7764	2.9985	3.7470	4.6041	7.173	8.610
5	1.476	2.015	2.5706	2.7565	3.3649	4.0322	5.893	6.869
6	1.440	1.943	2.4469	2.6122	3.1427	3.7075	5.208	5.959
7	1.415	1.895	2.3646	2.5168	2.9980	3.4995	4.785	5.408
8	1.397	1.860	2.3060	2.4490	2.8965	3.3554	4.501	5.041
9	1.383	1.833	2.2622	2.3984	2.8214	3.2499	4.297	4.781
10	1.372	1.812	2.2281	2.3593	2.7638	3.1693	4.144	4.587
11	1.363	1.796	2.2010	2.3281	2.7181	3.1058	4.025	4.437
12	1.356	1.782	2.1788	2.3027	2.6810	3.0546	3.930	4.318
13	1.350	1.771	2.1604	2.2816	2.6503	3.0123	3.852	4.221
14	1.345	1.761	2.1448	2.2638	2.6245	2.9769	3.787	4.140
15	1.341	1.753	2.1315	2.2485	2.6025	2.9467	3.733	4.073
16	1.337	1.746	2.1199	2.2354	2.5835	2.9208	3.686	4.015
17	1.333	1.740	2.1098	2.2239	2.5669	2.8982	3.646	3.965
18	1.330	1.734	2.1009	2.2137	2.5524	2.8784	3.611	3.922
19	1.328	1.729	2.0930	2.2047	2.5395	2.8610	3.579	3.883
20	1.325	1.725	2.0860	2.1967	2.5280	2.8453	3.552	3.850
21	1.323	1.721	2.0796	2.1894	2.5176	2.8314	3.527	3.819
22	1.321	1.717	2.0739	2.1829	2.5083	2.8188	3.505	3.792
23	1.319	1.714	2.0687	2.1769	2.4999	2.8073	3.485	3.768
24	1.318	1.711	2.0639	2.1716	2.4922	2.7969	3.467	3.745
25	1.316	1.708	2.0595	2.1666	2.4851	2.7874	3.450	3.725
26	1.315	1.706	2.0555	2.1620	2.4786	2.7787	3.435	3.707
27	1.314	1.703	2.0518	2.1578	2.4727	2.7707	3.421	3.690
28	1.313	1.701	2.0484	2.1539	2.4671	2.7633	3.408	3.674
29	1.311	1.699	2.0452	2.1503	2.4620	2.7564	3.396	3.659
30	1.310	1.697	2.0423	2.1470	2.4573	2.7500	3.385	3.646
31	1.309	1.696	2.0395	2.1438	2.4528	2.7441	3.375	3.633
32	1.309	1.694	2.0369	2.1409	2.4487	2.7385	3.365	3.622
33	1.308	1.692	2.0345	2.1382	2.4448	2.7333	3.356	3.611
34	1.307	1.691	2.0323	2.1356	2.4412	2.7284	3.348	3.601
35	1.306	1.690	2.0301	2.1332	2.4377	2.7238	3.340	3.591

[1] From [1].

Table A.1 (Cont.). t-distribution

				α levels				
Two-sided	.20	.10	.05	.04	.02	.01	.002	.001
One-sided	.10	.05	.025	.02	.01	.005	.001	.0005
				Percentiles				
df	0.90	0.95	0.975	0.98	0.99	0.995	0.999	0.9995
36	1.306	1.688	2.0281	2.1309	2.4345	2.7195	3.333	3.582
37	1.305	1.687	2.0262	2.1287	2.4314	2.7154	3.326	3.574
38	1.304	1.686	2.0244	2.1267	2.4286	2.7116	3.319	3.566
39	1.304	1.685	2.0227	2.1247	2.4258	2.7079	3.313	3.558
40	1.303	1.684	2.0211	2.1229	2.4233	2.7045	3.307	3.551
41	1.303	1.683	2.0196	2.1212	2.4208	2.7012	3.301	3.544
42	1.302	1.682	2.0181	2.1195	2.4185	2.6981	3.296	3.538
43	1.302	1.681	2.0167	2.1179	2.4163	2.6951	3.291	3.532
44	1.301	1.680	2.0154	2.1164	2.4142	2.6923	3.286	3.526
45	1.301	1.679	2.0141	2.1150	2.4121	2.6896	3.281	3.520
46	1.300	1.679	2.0129	2.1136	2.4102	2.6870	3.277	3.515
47	1.300	1.678	2.0117	2.1123	2.4083	2.6846	3.273	3.510
48	1.299	1.677	2.0106	2.1111	2.4066	2.6822	3.269	3.505
49	1.299	1.677	2.0096	2.1099	2.4049	2.6800	3.265	3.500
50	1.299	1.676	2.0086	2.1087	2.4033	2.6778	3.261	3.496
51	1.298	1.675	2.0076	2.1076	2.4017	2.6757	3.258	3.492
52	1.298	1.675	2.0067	2.1066	2.4002	2.6737	3.255	3.488
53	1.298	1.674	2.0058	2.1055	2.3988	2.6718	3.251	3.484
54	1.297	1.674	2.0049	2.1046	2.3974	2.6700	3.248	3.480
55	1.297	1.673	2.0041	2.1036	2.3961	2.6682	3.245	3.476
56	1.297	1.673	2.0033	2.1027	2.3948	2.6665	3.242	3.473
57	1.297	1.672	2.0025	2.1018	2.3936	2.6649	3.239	3.470
58	1.296	1.672	2.0017	2.1010	2.3924	2.6633	3.237	3.466
59	1.296	1.671	2.0010	2.1002	2.3912	2.6618	3.234	3.463
60	1.296	1.671	2.0003	2.0994	2.3902	2.6604	3.232	3.460
70	1.294	1.667	1.9944	2.0927	2.3808	2.6480	3.211	3.435
80	1.292	1.664	1.9901	2.0878	2.3739	2.6387	3.195	3.416
90	1.291	1.662	1.9867	2.0840	2.3685	2.6316	3.183	3.402
100	1.290	1.660	1.9840	2.0809	2.3642	2.6259	3.174	3.391
110	1.289	1.659	1.9818	2.0784	2.3607	2.6213	3.166	3.381
120	1.289	1.658	1.9799	2.0763	2.3578	2.6174	3.160	3.373
150	1.287	1.655	1.9759	2.0718	2.3515	2.6090	3.145	3.357
200	1.286	1.653	1.9719	2.0672	2.3451	2.6006	3.131	3.340
250	1.285	1.651	1.9695	2.0645	2.3414	2.5956	3.123	3.330
300	1.284	1.650	1.9679	2.0627	2.3388	2.5923	3.118	3.323
350	1.284	1.649	1.9668	2.0614	2.3371	2.5900	3.114	3.319
400	1.284	1.649	1.9659	2.0605	2.3357	2.5882	3.111	3.315
∞	1.282	1.645	1.9600	2.0537	2.3263	2.5758	3.090	3.291

Table A.2. χ^2-distribution

				α levels				
Two-sided	.40	.20	.10	.05	.04	.02	.01	.002
One-sided	.20	.10	.05	.025	.02	.01	.005	.001
				Percentiles				
df	0.80	0.90	0.95	0.975	0.98	0.99	0.995	0.999
1	1.642	2.706	3.841	5.024	5.412	6.635	7.879	10.828
2	3.219	4.605	5.991	7.378	7.824	9.210	10.597	13.816
3	4.642	6.251	7.815	9.348	9.837	11.345	12.838	16.266
4	5.989	7.779	9.488	11.143	11.668	13.277	14.860	18.467
5	7.289	9.236	11.070	12.833	13.388	15.086	16.750	20.515
6	8.558	10.645	12.592	14.449	15.033	16.812	18.548	22.458
7	9.803	12.017	14.067	16.013	16.622	18.475	20.278	24.322
8	11.030	13.362	15.507	17.535	18.168	20.090	21.955	26.125
9	12.242	14.684	16.919	19.023	19.679	21.666	23.589	27.877
10	13.442	15.987	18.307	20.483	21.161	23.209	25.188	29.588
11	14.631	17.275	19.675	21.920	22.618	24.725	26.757	31.264
12	15.812	18.549	21.026	23.337	24.054	26.217	28.300	32.910
13	16.985	19.812	22.362	24.736	25.471	27.688	29.819	34.528
14	18.151	21.064	23.685	26.119	26.873	29.141	31.319	36.124
15	19.311	22.307	24.996	27.488	28.259	30.578	32.801	37.697
16	20.465	23.542	26.296	28.845	29.633	32.000	34.267	39.254
17	21.615	24.769	27.587	30.191	30.995	33.409	35.718	40.789
18	22.760	25.989	28.869	31.526	32.346	34.805	37.156	42.312
19	23.900	27.204	30.143	32.852	33.687	36.191	38.582	43.819
20	25.038	28.412	31.410	34.170	35.020	37.566	39.997	45.315
21	26.171	29.615	32.671	35.479	36.343	38.932	41.401	46.797
22	27.301	30.813	33.924	36.781	37.660	40.290	42.796	48.270
23	28.429	32.007	35.172	38.076	38.968	41.638	44.181	49.726
24	29.553	33.196	36.415	39.364	40.270	42.980	45.559	51.179
25	30.675	34.382	37.653	40.647	41.566	44.314	46.928	52.622
26	31.795	35.563	38.885	41.923	42.856	45.642	48.290	54.054
27	32.912	36.741	40.113	43.195	44.140	46.963	49.645	55.477
28	34.027	37.916	41.337	44.461	45.419	48.278	50.994	56.893
29	35.139	39.087	42.557	45.722	46.693	49.588	52.336	58.303
30	36.250	40.256	43.773	46.979	47.962	50.892	53.672	59.703
31	37.359	41.422	44.985	48.232	49.226	52.192	55.003	61.100
32	38.466	42.585	46.194	49.480	50.487	53.486	56.328	62.486
33	39.572	43.745	47.400	50.725	51.743	54.775	57.648	63.868
34	40.676	44.903	48.602	51.966	52.995	56.061	58.964	65.246
35	41.778	46.059	49.802	53.204	54.244	57.342	60.275	66.622

				α levels				
Two-sided	.20	.10	.05	.04	.02	.01	.002	.001
One-sided	.10	.05	.025	.02	.01	.005	.001	.0005
					Percentiles			
df	0.90	0.95	0.975	0.98	0.99	0.995	0.999	0.9995
36	1.306	1.688	2.0281	2.1309	2.4345	2.7195	3.333	3.582
37	1.305	1.687	2.0262	2.1287	2.4314	2.7154	3.326	3.574
38	1.304	1.686	2.0244	2.1267	2.4286	2.7116	3.319	3.566
39	1.304	1.685	2.0227	2.1247	2.4258	2.7079	3.313	3.558
40	1.303	1.684	2.0211	2.1229	2.4233	2.7045	3.307	3.551
41	1.303	1.683	2.0196	2.1212	2.4208	2.7012	3.301	3.544
42	1.302	1.682	2.0181	2.1195	2.4185	2.6981	3.296	3.538
43	1.302	1.681	2.0167	2.1179	2.4163	2.6951	3.291	3.532
44	1.301	1.680	2.0154	2.1164	2.4142	2.6923	3.286	3.526
45	1.301	1.679	2.0141	2.1150	2.4121	2.6896	3.281	3.520
46	1.300	1.679	2.0129	2.1136	2.4102	2.6870	3.277	3.515
47	1.300	1.678	2.0117	2.1123	2.4083	2.6846	3.273	3.510
48	1.299	1.677	2.0106	2.1111	2.4066	2.6822	3.269	3.505
49	1.299	1.677	2.0096	2.1099	2.4049	2.6800	3.265	3.500
50	1.299	1.676	2.0086	2.1087	2.4033	2.6778	3.261	3.496
51	1.298	1.675	2.0076	2.1076	2.4017	2.6757	3.258	3.492
52	1.298	1.675	2.0067	2.1066	2.4002	2.6737	3.255	3.488
53	1.298	1.674	2.0058	2.1055	2.3988	2.6718	3.251	3.484
54	1.297	1.674	2.0049	2.1046	2.3974	2.6700	3.248	3.480
55	1.297	1.673	2.0041	2.1036	2.3961	2.6682	3.245	3.476
56	1.297	1.673	2.0033	2.1027	2.3948	2.6665	3.242	3.473
57	1.297	1.672	2.0025	2.1018	2.3936	2.6649	3.239	3.470
58	1.296	1.672	2.0017	2.1010	2.3924	2.6633	3.237	3.466
59	1.296	1.671	2.0010	2.1002	2.3912	2.6618	3.234	3.463
60	1.296	1.671	2.0003	2.0994	2.3902	2.6604	3.232	3.460
70	1.294	1.667	1.9944	2.0927	2.3808	2.6480	3.211	3.435
80	1.292	1.664	1.9901	2.0878	2.3739	2.6387	3.195	3.416
90	1.291	1.662	1.9867	2.0840	2.3685	2.6316	3.183	3.402
100	1.290	1.660	1.9840	2.0809	2.3642	2.6259	3.174	3.391
110	1.289	1.659	1.9818	2.0784	2.3607	2.6213	3.166	3.381
120	1.289	1.658	1.9799	2.0763	2.3578	2.6174	3.160	3.373
150	1.287	1.655	1.9759	2.0718	2.3515	2.6090	3.145	3.357
200	1.286	1.653	1.9719	2.0672	2.3451	2.6006	3.131	3.340
250	1.285	1.651	1.9695	2.0645	2.3414	2.5956	3.123	3.330
300	1.284	1.650	1.9679	2.0627	2.3388	2.5923	3.118	3.323
350	1.284	1.649	1.9668	2.0614	2.3371	2.5900	3.114	3.319
400	1.284	1.649	1.9659	2.0605	2.3357	2.5882	3.111	3.315
∞	1.282	1.645	1.9600	2.0537	2.3263	2.5758	3.090	3.291

A.2. REFERENCES

1.   Christensen R., In *Analysis of Variance, Design and Regression*, Chapman & Hall, Great Britian, 1996, pp. 1-587.

Appendix B: Hippocampal and preadipocyte cell culture protocols

B.1. HIPPOCAMPAL CELL MEDIA

B.1.1. Culturing medium: supplemental neurobasal medium

1. 25 ml neurobasal medium
2. 500 µl B-27 supplement
3. 100 µl L-glutamine solution $\left(0.091 \text{ g} \middle/ 5 \text{ ml ddwater} \right)$
4. 10 µl L-glutamic acid solution $\left(0.046 \text{ g} \middle/ 5 \text{ ml of 1M HCL} \right)$
5. 250 µl antibiotic-antimycotic solution

B.1.2. Washing medium

1. 1 ml hibernate media
2. 20 µl B-27 supplement

B.1.3. Digesting medium

1. 4 mg papain
2. 1 ml hibernate medium

B.2. HIPPOCAMPAL CELL PREPARATION

1. Take 1 ml of supernatant from a vial containing the rat brain and store in a fresh tube.
2. Add 1 ml of digesting medium to the tube with the brain.
3. Incubate for 20 min at 30 °C water bath.
4. Remove 1 ml of supernatant from the vial. Do not take out any parts of the brain.
5. Add 1 ml of washing medium.
6. Gently shake the vial.

204

7. Remove 1 ml of solution (with digested brain) from the vial.

8. Titurate with a fire-polished Pateur pipette gently 10 times.

9. Add back 1 ml of medium, taken from initial vial (step 1)

10. Wait 1 min for undissociated pieces of brain to settle.

11. Transfer this 2 ml cell solution into a 15 ml centrifuge tube.

12. Centrifuge for 1 min at 200 g.

13. Remove supernatant leaving ~0.5 ml

14. Add 1 ml of warm neurobasal medium pipetting 1 to 3 times gently.

15. Take out 20 µl of solution and mix with 20 µl of tryphan blue. The tryphan blue shows whether the cells are alive or dead.

16. Count cell density in cell suspension with hemacytometer.

17. Dilute cell suspension if necessary to $5e10^5$ cells/ml.

18. Create the sample solution:
    a. 2 ml neurobasal medium
    b. 200 µl cell suspension ($5e10^5$ cells/ml)

B.3. HIPPOCAMPAL CELL CULTURE

1. Incubate cells at 37 °C with 5% CO_2.

2. Check cells periodically.

B.4. HIPPOCAMPAL CELL FIXING

B.4.1. Fixing media

1. 1.5 ml of 2x PBS

2. 1.5 ml of 8% sucrose

3. 0.12 g of paraformaldehyde

4. 20 µl NaOH (1M)

5. Heat at 60 ° C

B.4.2. Fixing protocol

1. Aspirate medium.

205

2. Wash with warm and sterile PBS.

3. Add 100 μl per cm^2 of fixative onto samples.

4. Incubate at room temperature for 20 min.

5. Wash with PBS

6. Add permeation buffer

   a. 2% BSA

   b. 0.1% Triton-X

   c. PBS

7. Incubate at room temperature for 30 min.

8. Wash with PBS.

9. Add blocking buffer – 2% BSA in PBS (~ 200 μl)

10. Incubate at 37 °C for 1 h.

B.4. HIPPOCAMPAL CELL STAINING

1. Treat samples with BSA

2. Treat with primary antibody dilution (Tau-1) with 2% BSA/PBS (5 μl + 995 μl ~ 1:200 ratio)

B.5. PREADIPOCYTE CELL CULTURE

See section 5.3.8 for references.

Appendix C: Glass Surface Pretreatment for Adhesion of Polyethylene Glycol Dimethacrylate (PEGDMA) - Calculations

C.1. SOLUTION COMPONENT MOLECULAR WEIGHTS[1] AND DENSITIES:

3-trichlorosilyl propyl methacrylate $\{C_7H_{11}Cl_3O_2Si\}$
$$MW = 261.6 \left[\frac{g}{mol}\right]$$
$$Density = 1.239 \left[\frac{g}{mL}\right]$$

Heptane $\{CH_3(CH_2)_5CH_3\}$
$$MW = 100.1 \left[\frac{g}{mol}\right]$$
$$Density = 0.684 \left[\frac{g}{mL}\right]$$

Carbon Tetrachloride $\{CCl_4\}$
$$MW = 153.8 \left[\frac{g}{mol}\right]$$
$$Density = 1.594 \left[\frac{g}{mL}\right]$$

---
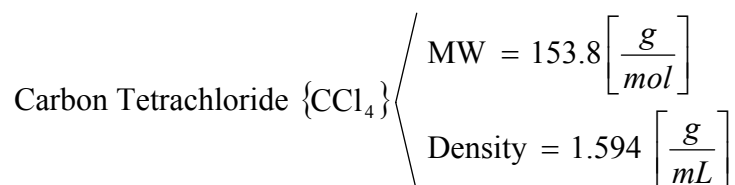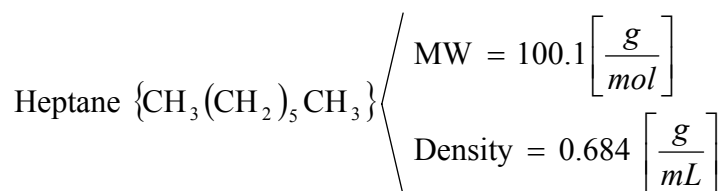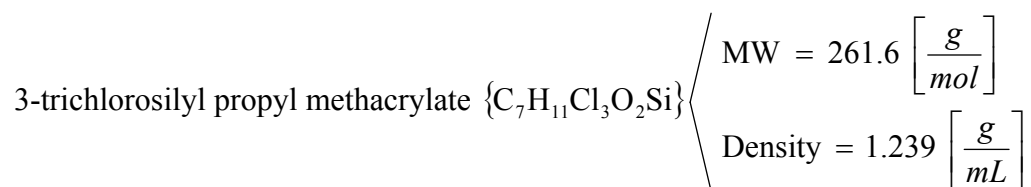
[1] MW ≡ molecular weight [g / mol] or [kg / $kmol$]

C.2. Sample Calculations

Assume 100 mL of a 1 mM solution of 3-trichlorosilyl propyl methacrylate (TPM) in a 4:1 solution of heptane and carbon tetrachloride, respectively.

C.2.1. Determining the amount of 3-trichlorosilyl propyl methacrylate required on a unit mass basis [g]

1. Convert the prescribed volume of solution from milliliters to liters.

$$100 \, [mL]_{\text{solution}} \cdot \frac{1}{1000} \left[\frac{L}{mL} \right]_{\frac{\text{solution}}{\text{solution}}} = 0.100 \, [L]_{\text{solution}}$$

2. Based on the prescribed molarity of 3-trichlorosilyl propyl methacrylate and volume of the mixture (step 1), calculate the amount of 3-trichlorosilyl propyl methacrylate on a unit molar basis [mol].

$$1 \, [mM]_{C_7H_{11}Cl_3O_2Si} = \frac{10^{-3}}{1} \left[\frac{mol}{L} \right]_{\frac{C_7H_{11}Cl_3O_2Si}{\text{solution}}}$$

$$\frac{10^{-3}}{1} \left[\frac{mol}{L} \right]_{\frac{C_7H_{11}Cl_3O_2Si}{\text{solution}}} \cdot 0.100 \, [L]_{\text{solution}} = 1*10^{-4} \, [mol]_{C_7H_{11}Cl_3O_2Si}$$

3. Calculate the amount of 3-trichlorosilyl propyl methacrylate on a unit mass basis [g] by multiplying the amount of 3-trichlorosilyl propyl methacrylate on a unit molar basis (step 2) by the molecular weight of 3-trichlorosilyl propyl methacrylate.

$$1*10^{-4} \, [mol]_{C_7H_{11}Cl_3O_2Si} \cdot 261.6 \left[\frac{g}{mol} \right]_{\frac{C_7H_{11}Cl_3O_2Si}{C_7H_{11}Cl_3O_2Si}} = 0.02616 \, [g]_{C_7H_{11}Cl_3O_2Si}$$

208

4. Calculate the volume $[mL]$ of 3-trichlorosilyl propyl methacrylate by dividing the amount of 3-trichlorosilyl propyl methacrylate on a unit mass basis (step 3) by the density of 3-trichlorosilyl propyl methacrylate.

$$\frac{0.02616\,[g]_{C_7H_{11}Cl_3O_2Si}}{1.239\,\left[\dfrac{g}{mL}\right]_{\frac{C_7H_{11}Cl_3O_2Si}{C_7H_{11}Cl_3O_2Si}}} = 0.02111\,[mL]_{C_7H_{11}Cl_3O_2Si}$$

C.2.2. Determining the volume $[mL]$ and mass $[g]$ of carbon tetrachloride and heptane in the solution

1. Calculate the volume $[mL]$ of heptane and carbon tetrachloride by subtracting the calculated volume of 3-trichlorosilyl propyl methacrylate (previous series of calculations) from the prescribed volume of the solution.

$$100\,[mL]_{solution}\ -\ 0.02111\,[mL]_{C_7H_{11}Cl_3O_2Si}\ =\ 99.98\,[mL]_{CCl_4+CH_3(CH_2)_5CH_3}$$

2. Based on a desired 4:1 ratio of heptane to carbon tetrachloride, respectively, calculate the volume $[mL]$ of carbon tetrachloride by dividing the volume of the mixture of heptane and carbon tetrachloride by a factor of five (see below).

$$1 \cdot V_{CH_3(CH_2)_5CH_3}\ =\ 4 \cdot V_{CCl_4}$$

$$1 \cdot V_{CCl_4}\ +\ 1 \cdot V_{CH_3(CH_2)_5CH_3}\ =\ 1 \cdot V_{CCl_4}\ +\ 4 \cdot V_{CCl_4}\ =\ 5 \cdot V_{CCl_4}\ =\ 99.98\,[mL]_{CCl_4+CH_3(CH_2)_5CH_3}$$

$$V_{CCl_4}\ =\ \frac{99.98}{5}\,[mL]_{CCl_4}\ =\ 19.996\,[mL]_{CCl_4}$$

209

3. Based on a desired 4:1 ratio of heptane to carbon tetrachloride, respectively, and the volume of carbon tetrachloride (step 2), calculate the volume of heptane [*mL*] by multiplying the volume of carbon tetrachloride by a factor of four.

$$V_{CH_3(CH_2)_5CH_3} = 4 \cdot V_{CCl_4} = 4 \cdot 19.996 \, [mL]_{CCl_4} = 79.984 \, [mL]_{CH_3(CH_2)_5CH_3}$$

4. Calculate the mass [*g*] of heptane by multiplying the volume of heptane (step 3) by the density of heptane.

$$79.984 \, [mL]_{CH_3(CH_2)_5CH_3} \cdot 0.684 \left[\frac{g}{mL}\right]_{CH_3(CH_2)_5CH_3} = 54.7091 \, [g]_{CH_3(CH_2)_5CH_3}$$

5. Calculate the mass [*g*] of carbon tetrachloride by multiplying the volume of carbon tetrachloride (step 3) by the density of carbon tetrachloride.

$$19.996 \, [mL]_{CCl_4} \cdot 1.594 \left[\frac{g}{mL}\right]_{CCl_4} = 31.8736 \, [g]_{CCl_4}$$

210

Appendix D: Transferring data from an atomic force microscope into finite element modeling software

Here we describe a novel method for transferring topographical data from an atomic force microscope into finite element software for computational analysis of biomaterial surfaces.

D.1. ABSTRACT

An atomic force microscope (AFM) can map the 3D contour of nanostructured surfaces, which are often too detailed to graphically reproduce in computer-aided drafting software. To date, the AFM has been mostly utilized for taking qualitative images of surfaces, a passive way of utilizing an AFM's powerful capabilities. Active use of topographical data has seemingly been of limited utility in quantitative analysis. Ironically, computational analysis of behavior at nanostructured surfaces has been limited by difficulties in artificially modeling the complex geometries of surfaces of interest. We report a process for transferring AFM data into finite element modeling software for performing computational analysis. We demonstrate our method by transferring data from surfaces consisting of wrinkles in a chromium thin-film on polydimethylsiloxane (PDMS), polystyrene nanospheres on silicon, and the distal tip of a nerve cell axon fixed on nanofabricated lines in quartz. Our method increases capabilities to simulate behavior at nanostructured surfaces.

211

D.2. METHODOLOGY

Finite element modeling (FEM) software is widely-employed for simulating physical phenomenon at the micro- and nanoscale. In particular, Comsol Multiphysics (Comsol Multiphysics version 3.4, Comsol, Inc., Burlington, MA, USA) is becoming increasingly popular FEM software due to its user-friendly graphics user interface and compatibility with computer-aided drafting (CAD) software. Here, we present a method to import AFM data into Comsol without using Comsol's proprietary CAD import modules or by any modification with CAD software. Additionally, our method can be used with any FEM software with little to no modification.

An AFM records height data (z-direction) as a small probe scans a surface at different x- and y- locations (pixels) in the plane of the surface[1]. The recorded data is centered around a particular z-height reference, so it consists of negative values for surface features below the reference (the reference z-height can be changed). The data, consisting of a matrix of z-values whose number of rows and columns depends on the number of pixels scanned per line and the total number of lines scanned by the probe, can be output as a *.txt* text file from an AFM. Typical scans incorporate 256 x 256 pixels (row x column) corresponding to 65,536 height data points.

To manipulate the outputted AFM data, the matrix in the text file (*.txt*) can be imported into a Microsoft Excel spreadsheet. Excel 2007 (and possibly later versions) is preferred over earlier versions since it is capable of handling a greater number of rows and columns, which is imperative for scans incorporating 256 x 256 pixels and greater (e.g., 512 x 512 pixels). Negative z-values can be eliminated from the matrix of data by simply adding the minimum negative value among the data and adding, at least, its

212

absolute value to every point in the matrix. The minimum value can be found by picking a blank cell in the Excel worksheet and using the function *MIN(number 1, number 2, …, → data range)* where the data range is the entire matrix. To add the minimum value determined by the *MIN* function, copy and paste the minimum value to every cell in the matrix using *paste special* (toggle the add option).

In most AFM scans, the *z*-data bordering the image varies. In cases where multiple scans need to be stitched together, manipulating the border data so that it converges to a constant *z*-height can make the stitching process much easier. Since we don't want to eliminate the original data at the border, we incorporate additional rows and columns to the border data in our *z*-data matrix. In the additional rows and columns, we can apply a "convergence" algorithm using the function *IF(criteria, value if true, value if false)*. For example, if we want the numerical values in every cell in the left-most column of our matrix to converge to zero, we could add several columns to the left of the left-most column in the original matrix and input the following logic statement:

=IF(value of cell to the immediate right (*value*) – convergence value (zero) ≤ 10, 0, *value* – 10).

The statement says that if the difference between the value in the cell to the immediate right (starting with the data in the left-most column of the original matrix) and the convergence value (zero) is less than or equal to 10, input zero into the cell immediately to the left; if not, then subtract 10 (units of distance, e.g., nanometers). This particular algorithm will cause the boundary data to converge to zero in an almost linear fashion as the formula is copied to additional columns to the left of the left-most column of the

213

original matrix. More complex algorithms can be used to create a more natural curve-like convergence. A logical algorithm can be simultaneously applied to the border data of the right-most column and top and bottom rows of the original matrix.

After fixing the border data, we must create a point cloud file from the Excel data. A point cloud is a series of *x,y,z* points in space, that make up a complex 3D surface or object. A point cloud file is a *.txt* text file containing three columns with *x*-, *y*-, and *z*-data. We can save the Excel worksheet as a text file in the proper point cloud format. Before this can be done, the matrix (columns) of *z*-data have to be combined into a single column. Because the matrix will usually contain many extended columns of data (e.g., 256 columns for a 256 x 256 pixel scan), combining the columns manually one-after-another is impractical. To our knowledge, Excel lacks a feature capable of automatically combining multiple columns into a single column; however, using a proprietary Excel macros created by Sobolsoft (*Excel Join Multiple Rows or Columns Into One Long Row or Column Software*; www.sobolsoft.com), which costs $30 to download, we could quickly consolidate the columns into a single column.

What we have after combining columns is a single column containing thousands of cells (*n* x 1 column vector). We must cut and past the *z*-data column into the third column (or column *C*) in the spreadsheet and create columns representing the *x*- and *y*-data in columns 1 and 2, respectively (or columns *A* and *B*). Column vectors containing *x*- and *y*- data can be manually inserted by using a simple formula and copying down to the row containing the last cell with *z*-data (usually, the *y*-data repeats for each *x*-value). The *x*- and *y*-data step-sizes (starting with point 0,0) are taken directly by dividing the *x*- and *y*-dimensions of the scan in the appropriate units (usually nanometers) by the number

214

of pixels in x and y. For example, for a 500 x 500 nm scan with 256 x 256 pixels, the x- and y-data step-sizes would be 1.95 nm ($\approx$ 500 / 256 starting with zero). Our spreadsheet will then contain three columns: x-, y-, and z-data in columns 1, 2, and 3, respectively. The spreadsheet can then be saved as a *.txt* point cloud file.

Using special macros, solid modeling software can sometimes import point cloud data and impose a surface on the points. This typically requires that curves be manually drawn through the points in the point cloud to act as constraints so that the solid modeling software knows how to impose a surface. Unfortunately, for AFM scans containing many points, this is not a practical way of creating a surface. Some solid modeling packages, e.g., Solidworks, contain functions that can impose surfaces on meshes created from point cloud data, but we found that these functions had difficulty handling complex scans. Fortunately, we were able to find a relatively inexpensive program called PointCloud 1.0 (www.sycode.com), which runs approximately $200 and can be purchased and downloaded online, that was quite efficient at importing point cloud data and imposing a surface. The software can export 3D surfaces as several useful file types, including standard *.stl* stereolithgraphy files that can be directly imported into many FEM software packages.

The *.stl* surface created by PointCloud can be directly imported into Comsol. In Comsol, the imported surface is really a compilation of knitted-surfaces that can be later combined with other surfaces to form a 3D solid representing a computational domain. When stitching several surfaces together, each component surface has to imported individually and re-positioned within Comsol.

215

Figures 1(a,d) show SEM and AFM images of a 30-nm layer of chromium deposited onto PDMS by thermal deposition. The AFM scan was taken over a 20 μm x 20 μm area (256 x 256 pixels). Wrinkles formed in a maze-like fashion due to a mismatch in thermal expansion coefficients between the PDMS and chromium[2, 3]. The RMS-height and width of the wrinkles are approximately 650 nm and 1.5 μm, respectively. Figures 1(g,h) show the point cloud image generated from our point cloud text file and the surface generated by PointCloud, respectively. Figure 1(i) shows the .stl surface imported into Comsol. If you compare the AFM scan to the final surface, you can see how the border data was refined for potential stitching to juxtaposing imported surfaces.

Figures 1(b,e) show SEM and AFM images of polystyrene spheres of 100-nm diameter coated on a silicon substrate, respectively. The AFM scan was taken over a 1 μm x 1 μm area (256 x 256 pixels). Due to the tightly packed unit-cell structure of the spheres, the AFM tip effectively scanned the upper half of the spheres. Like with the PDMS wrinkles, the edges of the scan were smoothed for stitching. Figures 1(g,h) show the point cloud image and solid surface created in PointCloud, respectively. Figure 1(j) shows the surface imported into Comsol.

Figures 1(c,f) show SEM and AFM images of the distal tip of a hippocampal cell axon extracted from a rat brain. The cell was seeded onto lines of 2-μm width patterned in quartz. The SEM image does not show the same axon as the AFM scan. The AFM scan was taken over a 15 μm x 15 μm area (256 x 256 pixels). Figures 1(g,h) show the point cloud image and surface created in PointCloud, respectively. Figure 1(k) shows the surface imported into Comsol.

216
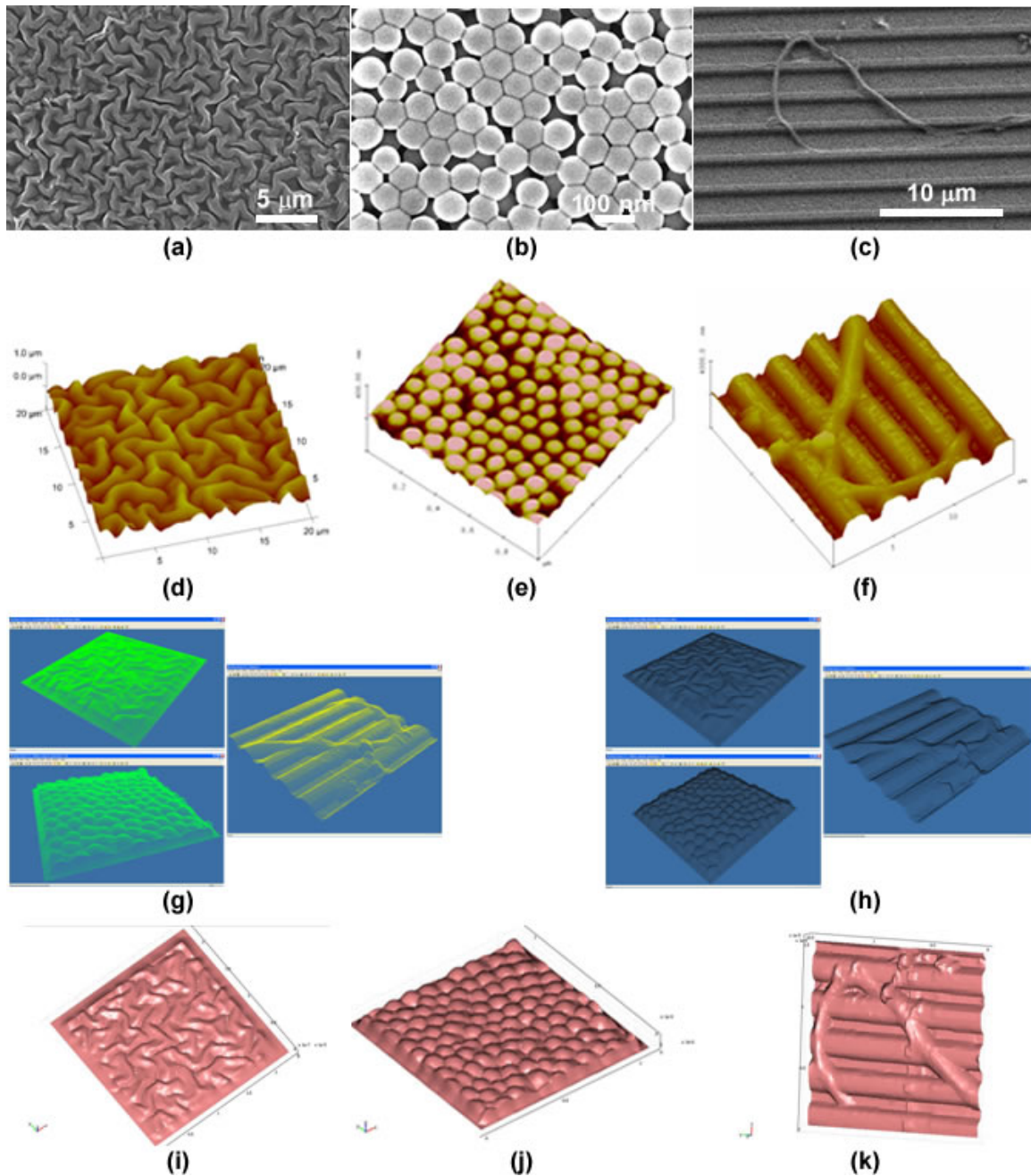
Figure D.1. AFM to FEM conversion. SEM images of (a) maze-like wrinkle structures in polydimethylsiloxane (PDMS) formed by depositing a 30-nm film of chromium by thermal evaporation, (b) a layer of polystyrene nanoparticles of 100-nm diameter spin-coated on silicon, and (c) the distal tip of a hippocampal nerve cell axon fixed on 2-micron lines in quartz, respectively; (d)-(f) AFM scans of the wrinkle structures, layer of polystyrene nanoparticles, and the nerve cell axon, respectively. (g) Point clouds generated in Pointcloud 1.0 from the height data extracted from the AFM images. (h) Surfaces imposed by PointCloud 1.0 from the imported point clouds. The surfaces were exported as *.stl* stereolithography files for importation into FEM software. (i)-(k) The *.stl* surfaces imported into Comsol Multiphysics. The edges of the scans of the wrinkles and the nanoparticles were smoothed at their borders for subsequent stitching to other surfaces.

217

The procedure discussed in this letter provides an interface between the AFM, as a quantitative tool, and FEM. Notably, such an interface should allow us to investigate a wider range of problems at the nanoscale where surface interactions play a prominent role in the governing physics.

D.3. EXPERIMENTAL

D.3.1. AFM and SEM measurements

Topological features were examined using a field-emission scanning-electron microscope (FESEM) (LEO 1530, Carl Zeiss SMT Inc., Peabody, MA, USA) and atomic-force microscope (AFM) (Dimension 3100 with Nanoscope IV controller, Digital Instruments & Veeco Metrology Group, Santa Barbara, CA, USA). AFM images were taken using a silicon tip in tapping-mode (Tap300, Budget Sensors, Sophia, Bulgaria).

D.3.2. PDMS-Chromium wrinkle surface

PDMS prepolymer and curing resin (Sylgard 184, Dow Corning, Midland, MI, USA) were mixed to a 10:1 ratio (v/v). The PDMS was casted on a silicon wafer that was chemically treated with Tridecafluoro-1,1,2,2-Tetrahydrooctyl-1 Trichlorosilane (United Chemical Technologies, Inc., Bristol, PA, USA, No. T2492). The PDMS was cured under vacuum in a vacuum oven for 1 hour at 120 °C. A 30-nm layer of chromium was thermally evaporated onto a small slab of the PDMS.

218

D.3.3. Polystyrene sphere surface

A small 10 mm x 10 mm piece of silicon was hydroxylated in a bath containing a 1:2 mixture of H_2O_2 and H_2SO_4 (v/v) for 10 min. A 10 µl aliquot of an aqueous suspension of polystyrene spheres of 100-nm diameter (company X) was spin-coated at 4000 rpm for 20 sec on the silicon. The solvent naturally evaporated without heating.

D.3.4. Quartz substrate fabrication for nerve cell culture

A 50-nm layer of chromium was thermally evaporated onto a 25 mm x 25 mm quartz substrate. The slow evaporation rate resulted in a film with good mechanical properties. ZEP-520A positive electronic resist was spin-coated onto the chromium layer at 4000 rpm for 40 sec; the resist was soft-baked on a hot plate at 180 °C for 90 sec.

2-micron lines were patterned in the ZEP resist using electron beam lithography (EBL). The resist was developed in ZED-N50 developer for 30 sec and subsequently immersed in IPA for 10 sec. The chromium was dry etched using (recipe) and the underlying quartz was later etched using (recipe). After quartz etching, remaining Cr was stripped with a Cr wet-etchant (Transene Chromium Etch 1020, Danvers, MA, USA). The patterned quartz was thoroughly washed in a 1:2 mixture of H_2O_2 and H_2SO_4 (v/v).

D.3.5. Hippocampal nerve cell culture for axon imaging

Rat hippocampal cells were isolated from commercially available hippocampus tissue, cultured for approximately 20 hours, and fixed according to the protocol reported by Gomez et al. [4] and in Appendix B.

219

D.3.6. Software for AFM to FEM transfer

Microsoft Excel 2007 macro, "Excel Join Multiple Rows or Columns Into One Long Row or Column Software", was downloaded from Sobolsoft (www.sobolsoft.com). Pointcloud 1.0 was downloaded from Sycode (Sycode, Goa, India, www.sycode.com). Comsol Multiphysics FEM software (Comsol Multiphysics v. 3.4., Comsol, Inc., Burlington, MA, USA) was utilized for importing AFM surfaces.

220

D.4. REFERENCES

1. Cohen S. H., Bray M. T., Lightbody M. L., *Atomic Force Microscopy / Scanning Tunneling Microscopy*, Plenum Press, New York, 1994.

2. Bowden N., Brittain S., Evans A. G., Hutchinson J. W., Whitesides G. M., Spontaneous formation of ordered structures in thin films of metals supported on an elastomeric polymer, *Nature*, 1998; **393** pp. 146-149.

3. Zhao X. L., Dong S., An W. W., Sun T., Liang Y. C., Modulated wrinkle patterns in a gold thin film deposited onto an elastomeric polymer, *International Conference on Smart Materials and Nanotechnology in Engineering*, 2007; **6423**, pp. 64230B.

4. Gomez N., Chen S. C., Schmidt C. E., Polarization of hippocampal neurons with competitive surface stimuli: contact guidance cues are preferred over chemical ligands, *Journal of the Royal Society Interface*, 2007; **4** pp. 223-233.

Bibliography

Abrams G. A., Goodman S. L., Nealey P. F., Franco M., Murphy C. J., Nanoscale topography of the basement membrane underlying the corneal epithelium of the rhesus macaque, *Cell and Tissue Research*, 2000; **299** pp. 39-46.

Abrams G. A., Murphy C. J., Wang Z. Y., Nealey P. F., Bjorling D. E., Ultrastructural basement membrane topography of the bladder epithelium, *Urological Research*, 2003; **31** pp. 341-346.

Adamson A. W., *Physical chemistry of surfaces*, John Wiley and Sons, New York, 1982.

Adamson A. W., Shirley F. P., Kunichika K. T., Contact angles on molecular solids : I. Ice, *Journal of Colloid and Interface Science*, 1970; **34** pp. 461-468.

Adamson A. W., The Solid-Liquid Interface - Contact Angle. In *Physical chemistry of surfaces*, John Wiley and Sons, New York, 1982, pp. 338-342.

Andreas J. M., Hauser E. A., Tucker W. B., Boundary Tension by Pendant Drops, *J Phys Chem*, 1938; **42** pp. 1001-1019.

Asai S., Kamei Y., Nishibori K., Katoh T., Torii S., Reconstruction of Romberg disease defects by omental flap, *Annals of Plastic Surgery*, 2006; **57** pp. 154-158.

Bentley D., Toroianraymond A., Disoriented Pathfinding by Pioneer Neuron Growth Cones Deprived of Filopodia by Cytochalasin Treatment, *Nature*, 1986; **323** pp. 712-715.

Berry C. C., Campbell G., Spadiccino A., Robertson M., Curtis A. S. G., The influence of microscale topography on fibroblast attachment and motility, *Biomaterials*, 2004; **25** pp. 5781-5788.

Billings Jr. E., May Jr. J. W., Historical review and present status of free graft autotransplantation in plastic and reconstructive surgery., *Plastic Reconstructive Surgery*, 1989; **83** pp. 368-381.

Bird B. R., Stewart W. E., Lightfoot E. N., *Transport Phenomena*, John Wiley and Sons, New York, 2002.

Bowden N., Brittain S., Evans A. G., Hutchinson J. W., Whitesides G. M., Spontaneous formation of ordered structures in thin films of metals supported on an elastomeric polymer, *Nature*, 1998; **393** pp. 146-149.

Brittis P. A., Canning D. R., Silver J., Chondroitin Sulfate as a Regulator of Neuronal Patterning in the Retina, *Science*, 1992; **255** pp. 733-736.

Cassie A. B. D., Baxter S., Wettability of Porous Surfaces, *Transactions of the Faraday Society*, 1944; **40** pp. 546 - 551.

Chen W. Y. J., Abatangelo G., Functions of hyaluronan in wound repair, *Wound Repair and Regeneration*, 1999; **7** pp. 79-89.

Chou S. Y., Krauss P. R., Renstrom P. J., Imprint lithography with 25-nanometer resolution, *Science*, 1996; **272** pp. 85-87.

Chou S. Y., Krauss P. R., Renstrom P. J., Imprint of Sub-25 Nm Vias and Trenches in Polymers, *Applied Physics Letters*, 1995; **67** pp. 3114-3116.

Christensen R., In *Analysis of Variance, Design and Regression*, Chapman & Hall, Great Britian, 1996, pp. 1-587.

Christensen R., One binomial sample. In *Analysis of Variance, Design and Regression*, Chapman & Hall, Great Britian, 1996, pp. 227-230.

Christensen R., One multinomial sample. In *Analysis of Variance, Design and Regression*, Chapman & Hall, Great Britian, 1996, pp. 233-235.

Christensen R., One-way analysis of variance. In *Analysis of Variance, Design and Regression*, Chapman & Hall, Great Britian, 1996, pp. 114-123.

Christensen R., Two independent binomial samples. In *Analysis of Variance, Design and Regression*, Chapman & Hall, Great Britian, 1996, pp. 231-233.

Christensen R., Two independent multinomial samples. In *Analysis of Variance, Design and Regression*, Chapman & Hall, Great Britian, 1996, pp. 235-239.

Christensen R., Two independent samples with unequal variance. In *Analysis of Variance, Design and Regression*, Chapman & Hall, Great Britian, 1996, pp. 95-98.

Cohen S. H., Bray M. T., Lightbody M. L., *Atomic Force Microscopy / Scanning Tunneling Microscopy*, Plenum Press, New York, 1994.

Colburn M., Johnson S., Stewart M., Damle S., Bailey T., Choi B. J., et al., Step and Flash Imprint Lithography: A New Approach to High-Resolution Patterning, *Proceedings of the SPIE's 24th International Symposium on Microlithography: Emerging Lithographic Technologies III*, Santa Clara, CA, March 1999; **3676**, pp. 379-389.

Comisar W. A., Hsiong S. X., Kong H. J., Mooney D. J., Linderman J. J., Multi-scale modeling to predict ligand presentation within RGD nanopatterned hydrogels, *Biomaterials*, 2006; **27** pp. 2322-2329.

Curtis A. S., Varde M., Control of cell behavior: Topological factors, *Journal of the National Cancer Institute*, 1964; **33** pp. 15-26.

Curtis A., Wilkinson C., Nantotechniques and approaches in biotechnology, *Trends in Biotechnology*, 2001; **19** pp. 97-101.

Curtis A., Wilkinson C., Topographical control of cells, *Biomaterials*, 1997; **18** pp. 1573-1583.

Dalby M. J., Riehle M. O., Yarwood S. J., Wilkinson C. D. W., Curtis A. S. G., Nucleus alignment and cell signaling in fibroblasts: response to a micro-grooved topography, *Experimental Cell Research*, 2003; **284** pp. 274-282.

Dalby M. J., Topographically induced direct cell mechanotransduction, *Medical Engineering & Physics*, 2005; **27** pp. 730-742.

Dotti C. G., Sullivan C. A., Banker G. A., The Establishment of Polarity by Hippocampal-Neurons in Culture, *Journal of Neuroscience*, 1988; **8** pp. 1454-1468.

Duffy D. C., McDonald J. C., Schueller O. J. A., Whitesides G. M., Rapid prototyping of microfluidic systems in poly(dimethylsiloxane), *Analytical Chemistry*, 1998; **70** pp. 4974-4984.

Elias K. L., Price R. L., Webster T. J., Enhanced functions of osteoblasts on nanometer diameter carbon fibers, *Biomaterials*, 2002; **23** pp. 3279-3287.

Emmelius M., Pawlowski G., Vollmann H. W., Materials for Optical-Data Storage, *Angewandte Chemie-International Edition in English*, 1989; **28** pp. 1445-1471.

Entenmann G., Hauner H., Relationship between replication and differentiation in cultured human adipocyte precursor cells, *American Journal of Physiology-Cell Physiology*, 1996; **39** pp. C1011-C1016.

Ersek R. A., Transplantation of purified autologous fat: A 3-year follow-up disappointing, *Plastic Reconstructive Surgery*, 1991; **87** pp. 219-227.

Firkowska I., Olek M., Pazos-Perez N., Rojas-Chapana J., Giersig M., Highly ordered MWNT-based matrixes: Topography at the nanoscale conceived for tissue engineering, *Langmuir*, 2006; **22** pp. 5427-5434.

Forciniti L., Schmidt C., Zaman M., Computational Model Provides Insight into the Distinct Responses of Neurons to Chemical and Topographical Cues, *Annals of Biomedical Engineering*, 2009; **37** pp. 363-374.

Fowkes F. M., Harkins W. D., The State of Monolayers Adsorbed at the Interface Solid--Aqueous Solution, *J Am Chem Soc*, 1940; **62** pp. 3377-3386.

224

Fozdar D. Y., Lee J. Y., Schmidt C. E., Chen S., Neurons respond uniquely to topographies of various sizes and shapes, *Biomaterials*, 2009; **(submitted)** pp.

Fozdar D. Y., Lee J. Y., Schmidt C. E., Chen S., Response of neurons to competing topographical features of various sizes and shapes, *Nano Letters*, 2009; **(submitted)** pp.

Fozdar D. Y., Lu Y., Shao D. B., Chen S., Nano/Microfabrication Techniques for Organic Electronics and Photonics. In *Handbook of Organic Electronics and Photonics*, American Scientific Publishers, Valencia, CA, 2008, pp.

Fozdar D. Y., Wu X., Patrick C. W., Chen S., Micro-well texture printed into PEG hydrogels using the FILM nanomanufacturing process affects the behavior of preadipocytes, *Biomedical Microdevices*, 2008; **10** pp. 839-849.

Fozdar D. Y., Zhang W., Palard M., Patrick C., Chen S., Flash imprint lithography using a mask aligner: a method for printing nanostructures in photosensitive hydrogels, *Nanotechnology*, 2008; **19** pp. 1-13.

Gheith M. K., Sinani V. A., Wicksted J. P., Matts R. L., Kotov N. A., Single-walled carbon nanotube polyelectrolyte multilayers and freestanding films as a biocompatible platformfor neuroprosthetic implants, *Advanced Materials*, 2005; **17** pp. 2663-+.

Giordano G. G., Thomson R. C., Ishaug S. L., Mikos A. G., Cumber S., Garcia C. A., et al., Retinal pigment epithelium cells cultured on synthetic biodegradable polymers, *Journal of Biomedical Materials Research*, 1997; **34** pp. 87-93.

Girifalco L. A., Good R. J., A Theory for the Estimation of Surface and Interfacial Energies. I. Derivation and Application to Interfacial Tension, *J Phys Chem*, 1957; **61** pp. 904-909.

Goldner J. S., Bruder J. M., Li G., Gazzola D., Hoffman-Kim D., Neurite bridging across micropatterned grooves, *Biomaterials*, 2006; **27** pp. 460-472.

Goldstein J., Newbury D., Echlin P., Joy D., Jr. A. D. R., Lyman C., et al., *Scanning Electron Microscopy and X-Ray Microanalysis: A Text for Biologists, Materials Scientists, and Geologists*, Plenum Press, New York, 1992.

Gomez N., Chen S. C., Schmidt C. E., Polarization of hippocampal neurons with competitive surface stimuli: contact guidance cues are preferred over chemical ligands, *Journal of the Royal Society Interface*, 2007; **4** pp. 223-233.

Gomez N., Lu Y., Chen S.C., Schmidt C., Immobilized Nerve Growth Factor and Microtopography Have Distinct Effects on Polarization Versus Axon Elongation in Hippocampal Cells in Culture, *Biomaterials*, 2006; **Accepted** pp.

225

Guenard V., Kleitman N., Morrissey T. K., Bunge R. P., Aebischer P., Syngeneic schwann-cells derived form adult nerves seeded in semipermeable guidance channels enhance peripheral-nerve regeneration, *Journal of Neuroscience*, 1992; **12** pp. 3310-3320.

Hahn M. S., Taite L. J., Moon J. J., Rowland M. C., Ruffino K. A., West J. L., Photolithographic patterning of polyethylene glycol hydrogels, *Biomaterials*, 2006; **27** pp. 2519-2524.

Hausman G. J., Richardson R. L., Newly recruited and pre-existing preadipocytes in cultures of porcine stromal-vascular cells: Morphology, expression of extracellular matrix components, and lipid accretion, *Journal of Animal Science*, 1998; **76** pp. 48-60.

Hernandez J. C. R., Sanchez M. S., Soria J. M., Ribelles J. L. G., Pradas M. M., Substrate chemistry-dependent conformations of single laminin molecules on polymer surfaces are revealed by the phase signal of atomic force microscopy, *Biophysical Journal*, 2007; **93** pp. 202-207.

Huang W., Bhullar R. S., Fung Y. C., The surface-tension-driven flow of blood from a droplet into a capillary tube, *Journal of Biomechanical Engineering-Transactions of the Asme*, 2001; **123** pp. 446-454.

Hudson T. W., Evans G. R. D., Schmidt C. E., Engineering strategies for peripheral nerve repair, *Clinics in Plastic Surgery*, 1999; **26** pp. 617-+.

Hunt J. A., Hobar P. C., Common craniofacial anomalies: Conditions of craniofacial atrophy/hypoplasia and neoplasia, *Plastic and Reconstructive Surgery*, 2003; **111** pp. 1497-1508.

Ikeda K., Yamauchi D., Osamura N., Hagiwara N., Tomita K., Hyaluronic acid prevents peripheral nerve adhesion, *British Journal of Plastic Surgery*, 2003; **56** pp. 342-347.

Jung G. Y., Ganapathiappan S., Ohlberg D. A. A., Olynick D. L., Chen Y., Tong W. M., et al., Fabrication of a 34 x 34 Crossbar Structure at 50 nm Half-pitch by UV-based Nanoimprint Lithography, *Nano Lett*, 2004; **4** pp. 1225-1229.

Kallinger C., Hilmer M., Haugeneder A., Perner M., Spirkl W., Lemmer U., et al., A flexible conjugated polymer laser, *Advanced Materials*, 1998; **10** pp. 920-+.

Kim E., Xia Y. N., Whitesides G. M., Polymer Microstructures Formed by Molding in Capillaries, *Nature*, 1995; **376** pp. 581-584.

Kim E., Xia Y. N., Zhao X. M., Whitesides G. M., Solvent-assisted microcontact molding: A convenient method for fabricating three-dimensional structures on surfaces of polymers, *Advanced Materials*, 1997; **9** pp. 651-654.

Kim P., Kim D. H., Kim B., Choi S. K., Lee S. H., Khademhosseini A., et al., Fabrication of nanostructures of polyethylene glycol for applications to protein adsorption and cell adhesion, *Nanotechnology*, 2005; **16** pp. 2420-2426.

Langer R., Tissue engineering, *Molecular Therapy*, 2000; **1** pp. 12-15.

Lawes G., *Scanning Electron Microscopy and X-Ray Microanalysis*, John Wiley and Sons, Hoboken New Jersey, 1987.

Lawrence J. R., Turnbull G. A., Samuel I. D. W., Polymer laser fabricated by a simple micromolding process, *Applied Physics Letters*, 2003; **82** pp. 4023-4025.

Lazic S. E., Barker R. A., The future of cell-based transplantation therapies for neurodegenerative disorders, *Journal of Hematotherapy & Stem Cell Research*, 2003; **12** pp. 635-642.

Lee J. Y., Bashur C. A., Gomez N., Goldstein A. S., Schmidt C. E., Enhanced polarization of embryonic hippocampal neurons on micron scale electrospun fibers, *Journal of Biomedical Materials Research - Part A*, 2009 (in press); pp.

Lehmann H. W., Widmer R., Ebnoether M., Wokaun A., Meier M., Miller S. K., Fabrication of Sub-Micron Crossed Square-Wave Gratings by Dry Etching and Thermoplastic Replication Techniques, *Journal of Vacuum Science & Technology B*, 1983; **1** pp. 1207-1210.

Li G. N., Hoffman-Kim D., Tissue-engineered platforms of axon guidance, *Tissue Engineering Part B-Reviews*, 2008; **14** pp. 33-51.

Liliensiek S. J., Campbell S., Nealey P. F., Murphy C. J., The scale of substratum topographic features modulates proliferation of corneal epithelial cells and corneal fibroblasts, *Journal of Biomedical Materials Research Part A*, 2006; **79A** pp. 185-192.

Liu C. Y., Westerlund U., Svensson M., Moe M. C., Varghese M., Berg-Johnsen J., et al., Artificial niches for human adult neural stem cells: Possibility for autologous transplantation therapy, *Journal of Hematotherapy & Stem Cell Research*, 2003; **12** pp. 689-699.

Lu L. C., Kam L., Hasenbein M., Nyalakonda K., Bizios R., Gopferich A., et al., Retinal pigment epithelial cell function on substrates with chemically micropatterned surfaces, *Biomaterials*, 1999; **20** pp. 2351-2361.

Lu L. C., Yaszemski M. J., Mikos A. G., Retinal pigment epithelium engineering using synthetic biodegradable polymers, *Biomaterials*, 2001; **22** pp. 3345-3355.

Lu Y., Mapili G., Suhali G., Chen S. C., Roy K., A digital micro-mirror device-based system for the microfabrication of complex, spatially patterned tissue engineering scaffolds, *Journal of Biomedical Materials Research Part A*, 2006; **77A** pp. 396-405.

Macdougald O. A., Lane M. D., Adipocyte Differentiation - When Precursors Are Also Regulators, *Current Biology*, 1995; **5** pp. 618-621.

Macdougald O. A., Lane M. D., Transcriptional Regulation of Gene-Expression During Adipocyte Differentiation, *Annual Review of Biochemistry*, 1995; **64** pp. 345-373.

Madou M. J., *Fundamentals of Microfabrication: The Science of Miniaturization*, CRC Press, Boca Raton, 2002.

Mandrup S., Lane M. D., Regulating adipogenesis, *Journal of Biological Chemistry*, 1997; **272** pp. 5367-5370.

Mattson M. P., Establishment and plasticity of neuronal polarity, *Journal of Neuroscience Research*, 1999; **57** pp. 577-589.

Miller D. C., Haberstroh K. M., Webster T. J., Mechanism(s) of increased vascular cell adhesion on nanostructured poly(lactic-co-glycolic acid) films, *Journal of Biomedical Materials Research Part A*, 2005; **73A** pp. 476-484.

Miller D. C., Thapa A., Haberstroh K. M., Webster T. J., Endothelial and vascular smooth muscle cell function on poly(lactic-co-glycolic acid) with nano-structured surface features, *Biomaterials*, 2004; **25** pp. 53-61.

Nagata I., Kawana A., Nakatsuji N., Perpendicular Contact Guidance of CNS Neuroblasts on Artificial Microstructures, *Development*, 1993; **117** pp. 401-408.

Nagata I., Nakatsuji N., Rodent Cns Neuroblasts Exhibit Both Perpendicular and Parallel Contact Guidance on the Aligned Parallel Neurite Bundle, *Development*, 1991; **112** pp. 581-590.

Norman J., Desai T., Methods for fabrication of nanoscale topography for tissue engineering scaffolds, *Annals of Biomedical Engineering*, 2006; **34** pp. 89-101.

Patel P. N., Gobin A. S., West J. L., Patrick C. W., Poly(ethylene glycol) Hydrogel System Supports Preadipocyte Viability, Adhesion, and Proliferation, *Tissue Engineering*, 2005; **11** pp. 1498-1505.

Patel P. N., Smith C. K., Patrick C. W., Rheological and recovery properties of poly(ethylene glycol) diacrylate hydrogels and human adipose tissue, *Journal of Biomedical Materials Research Part A*, 2005; **73A** pp. 313-319.

228

Patrick C. W., Adipose tissue engineering: The future of breast and soft tissue reconstruction following tumor resection, *Seminars in Surgical Oncology*, 2000; **19** pp. 302-311.

Patrick C. W., Chauvin P. B., Hobley J., Reece G. P., Preadipocyte Seeded PLGA Scaffolds for Adipose Tissue Engineering, *Tissue Engineering*, 1999; **5** pp. 139-151.

Patrick C. W., Tissue engineering strategies for adipose tissue repair, *Anatomical Record*, 2001; **263** pp. 361-366.

Patrick C. W., Zheng B., Johnston C., Reece G. P., Long-Term Implantation of Preadipocyte-Seeded PLGA Scaffolds, *Tissue Engineering*, 2002; **8** pp. 283-293.

Rajnicek A. M., Britland S., McCaig C. D., Contact guidance of CNS neurites on grooved quartz: influence of groove dimensions, neuronal age and cell type, *Journal of Cell Science*, 1997; **110** pp. 2905-2913.

Rajnicek A. M., McCaig C. D., Guidance of CNS growth cones by substratum grooves and ridges: effects of inhibitors of the cytoskeleton, calcium channels and signal transduction pathways, *Journal of Cell Science*, 1997; **110** pp. 2915-2924.

Reddy S., Bonnecaze R. T., Simulation of fluid flow in the step and flash imprint lithography process, *Microelectronic Engineering*, 2005; **82** pp. 60-70.

Revzin A., Russell R. J., Yadavalli V. K., Koh W. G., Deister C., Hile D. D., et al., Fabrication of poly(ethylene glycol) hydrogel microstructures using photolithography, *Langmuir*, 2001; **17** pp. 5440-5447.

Riechel S., Kallinger C., Lemmer U., Feldmann J., Gombert A., Wittwer V., et al., A nearly diffraction limited surface emitting conjugated polymer laser utilizing a two-dimensional photonic band structure, *Applied Physics Letters*, 2000; **77** pp. 2310-2312.

Rodia C. M., Precision Electroforming for Optical Disk Manufacturing, *Proceedings of the Society of Photo-Optical Instrumentation Engineers*, 1985; **529** pp. 69-75.

Sapelkin A. V., Bayliss S. C., Unal B., Charalambou A., Interaction of B50 rat hippocampal cells with stain-etched porous silicon, *Biomaterials*, 2006; **27** pp. 842-846.

Scheerlinck S., Thourhout D. V., Baets R., Nano Imprint Lithography for Photonic Structure Patterning, *Proceedings Symposium IEEE/LEOS Benelux Chapter*, Belgium, 2005; 63-66.

Schlereth K. H., Bottner H., Embossed Grating Lead Chalcogenide Distributed-Feedback Lasers, *Journal of Vacuum Science & Technology B*, 1992; **10** pp. 114-117.

229

Schmidt C. E., Leach J. B., Neural tissue engineering: Strategies for repair and regeneration, *Annual Review of Biomedical Engineering*, 2003; **5** pp. 293-347.

Schmidt C. E., Shastri V. R., Vacanti J. P., Langer R., Stimulation of neurite outgrowth using an electrically conducting polymer, *Proceedings of the National Academy of Sciences of the United States of America*, 1997; **94** pp. 8948-8953.

Seckel B. R., Jones D., Hekimian K. J., Wang K. K., Chakalis D. P., Costas P. D., Hyaluronic-Acid through a New Injectable Nerve Guide Delivery System Enhances Peripheral-Nerve Regeneration in the Rat, *Journal of Neuroscience Research*, 1995; **40** pp. 318-324.

Seidlits S. K., Lee J. Y., Schmidt C. E., Nanostructured scaffolds for neural applications, *Nanomedicine*, 2008; **3** pp. 183-199.

Sniadecki N., Desai R. A., Ruiz S. A., Chen C. S., Nanotechnology for cell-substrate interactions, *Annals of Biomedical Engineering*, 2006; **34** pp. 59-74.

Steinberg T., Schulz S., Spatz J. P., Grabe N., Mussig E., Kohl A., et al., Early keratinocyte differentiation on micropillar interfaces, *Nano Letters*, 2007; **7** pp. 287-294.

Stenger D. A., Hickman J. J., Bateman K. E., Ravenscroft M. S., Ma W., Pancrazio J. J., et al., Microlithographic determination of axonal/dendritic polarity in cultured hippocampal neurons, *Journal of Neuroscience Methods*, 1998; **82** pp. 167-173.

Stuart C., Xu Q., Tseng R. J., Yang Y., Hahn H. T., Chen Y., et al., Nanofabrication module integrated with optical aligner, *Journal of Vacuum Science & Technology B: Microelectronics and Nanometer Structures*, 2006; **24** pp. 539-542.

Sussman M., Fatemi E., Smereka P., Osher S., An improved level set method for incompressible two-phase flows, *Computers & Fluids*, 1998; **27** pp. 663-680.

Teixeira A. I., Abrams G. A., Bertics P. J., Murphy C. J., Nealey P. F., Epithelial contact guidance on well-defined micro- and nanostructured substrates, *Journal of Cell Science*, 2003; **116** pp. 1881-1892.

Teixeira A. I., Abrams G. A., Murphy C. J., Nealey P. F., Cell behavior on lithographically defined nanostructured substrates, *Journal of Vacuum Science & Technology B*, 2003; **21** pp. 683-687.

Vaienti L., Soresina M., Menozzi A., Parascapular free flap and fat grafts: Combined surgical methods in morphological restoration of hemifacial progressive atrophy, *Plastic and Reconstructive Surgery*, 2005; **116** pp. 699-711.

Wang J., Sun X. Y., Chen L., Chou S. Y., Direct nanoimprint of submicron organic light-emitting structures, *Applied Physics Letters*, 1999; **75** pp. 2767-2769.

Wang X. C., Qiao Q., Liu Z. F., Zhao R., Zhang H. L., Yang Y. J., et al., Free anterolateral thigh adipofascial flap for hemifacial atrophy, *Annals of Plastic Surgery*, 2005; **55** pp. 617-622.

Wilbur J. L., Kumar A., Kim E., Whitesides G. M., Microfabrication by Microcontact Printing of Self-Assembled Monolayers, *Advanced Materials*, 1994; **6** pp. 600-604.

Winter J. O., Schmidt C. E., Biomimetic strategies and applications in the nervous system. In *Biomimetic Materials and Design: Biointerfacial Strategies, Tissue Engineering, and Targeted Drug Delivery*, 2002, pp.

Xia Y. N., Zhao X. M., Whitesides G. M., Pattern transfer: Self-assembled monolayers as ultrathin resists, *Microelectronic Engineering*, 1996; **32** pp. 255-268.

Xia Y., Whitesides G. M., Soft lithography, *Angewandte Chemie International Edition*, 1998; **37** pp. 551-575.

Yaji N., Yamato M., Yang J., Okano T., Hori S., Transplantation of tissue-engineered retinal pigment epithelial cell sheets in a rabbit model, *Biomaterials*, 2009; **30** pp. 797-803.

Yim E. K. F., Pang S. W., Leong K. W., Synthetic nanostructures inducing differentiation of human mesenchymal stem cells into neuronal lineage, *Experimental Cell Research*, 2007; **313** pp. 1820-1829.

Yim E. K. F., Reano R. M., Pang S. W., Yee A. F., Chen C. S., Leong K. W., Nanopattern-induced changes in morphology and motility of smooth muscle cells, *Biomaterials*, 2005; **26** pp. 5405-5413.

Zhang L. J., Webster T. J., Nanotechnology and nanomaterials: Promises for improved tissue regeneration, *Nano Today*, 2009; **4** pp. 66-80.

Zhao X. L., Dong S., An W. W., Sun T., Liang Y. C., Modulated wrinkle patterns in a gold thin film deposited onto an elastomeric polymer, *International Conference on Smart Materials and Nanotechnology in Engineering*, 2007; **6423**, pp. 64230B.

Zhao X. M., Xia Y. N., Whitesides G. M., Fabrication of three-dimensional micro-structures: Microtransfer molding, *Advanced Materials*, 1996; **8** pp. 837-&.

Vita

David Yash Fozdar was born in Columbus, Ohio, USA on June 27th, 1981, to Connie and Yash Fozdar. He has a brother, Michael Fozdar, and a sister, Julie Rindler. He received his high school diploma from Edmond North High School in Edmond, Oklahoma in 1999.

From 1999 to 2003, he attended the University of Oklahoma where he received a B.S. in Mechanical Engineering conferred by the faculty with special distinction. In 2003, he pursued his graduate studies in Mechanical Engineering at The University of Texas at Austin. He joined Dr. Shaochen Chen's research group in Thermal-Fluids Systems area within the Department of Mechanical Engineering. He received an M.S. in Mechanical Engineering in 2005 and continued his graduate studies to pursue his Ph.D. He joined the Doctoral Nanotechnology Portfolio program at The University of Texas at Austin and graduated with a Certification in Nanotechnology in 2009.

David is first author on six journal and review papers and has co-authored several additional journal papers and conference proceedings. He presented at a national conference and workshop and later served as a session chair at an international conference.

Parmanent address: 1220 Olde Bridge Road, Edmond, Oklahoma 73034.

This dissertation was typed by David Yash Fozdar.

232